Analysis and evaluation of multi-strand beams under static and dynamic loading

A thesis submitted to the University of Sheffield

for the degree of Doctor of Philosophy in the Faculty of Engineering

by

Haval Kamal Asker

Department of Mechanical Engineering

University of Sheffield

September 2017

Abstract

Multi-strand systems include, but are not limited to, beam-like structure (special composites) or wire-like structure (mechanical cables and electrical wires), constructed from many long strands that are constrained rather than bonded, can provide appreciable levels of damping through the friction in the interfacial surfaces between the individual strands. These systems are generally metallic to provide dry friction damping over significantly wider working temperature ranges than is typical for common damping materials such as viscoelastic polymers.

This work proposes an analytical model that describes the frictional damping behaviour of multi-strand system constructed from strands that have square and circular cross-sections. The analytical models predict the frictional system stiffness under simply supported configuration. This is followed by systematic quasi-static experiments and numerical investigations using standard finite element analyses. Simple Coulomb friction is assumed at the interfaces.

Dynamic loss factors for multi-strand beams and multi-strand wires are obtained by performing forced vibration tests and are found (the loss factors) to be insensitive of the frequency. The analytical models in this study show preference in describing multi-strand systems due to some limitations in the experimental and numerical representations. This thesis provides a vital and necessary insight into the physics for stranded structures and materials that are largely prevalent in mechanical (e.g. cables) and electrical (e.g. wires) elements.

Acknowledgment

List of publications from this work

[1] H.K. Asker, J.A. Rongong, C.E. Lord, Stiffness and loss factor of unbonded , multi-strand beams under flexural deformation, in: Int. Conf. Eng. Vib., Ljubljana, Slovenia, 2015: pp. 1518–1529.

[2] H. Asker, J. Rongong, C. Lord, Mathematical and numerical evaluation of the damping behaviour for a multi- strand bar, in: EACS 2016 – 6th Eur. Conf. Struct. Control., 2016: pp. 1–10.

[3] H. Asker, J. Rongong, C. Lord, Dynamic properties of unbonded, multi-strand beams subjected to flexural loading, Mechanical systems and signal processing journal, 101 (2018) 168-181.

List of contents

List of figures

xvii

List of tables

Nomenclature

A	Cross-section area.
A_w	Area in the interface.
b	Width of the individual strands.
b_w	Width of the interface.
d	Distance from neutral axis.
dA	Segment area.
db	Configuration label for diagonal multi-strand beam.
d_{sl}	Displacement resulted from slip force.
dW	Energy dissipation per cycle.
DMSB	Diagonal multi-strand beam.
E	Modulus of elasticity.
f	Frequency (Hz).
F	Applied force.
F_c	Normal force.
F_d	Frictional force.
F_l	Flexural load.
F_{sl}	Slip force.
h	Height of the individual strands.
h_{any}	Height of multi-strand bar or wire.
I	Second moment of area.
I_0	Second moment of area for individual strands.
I_{bond}	Second moment of area with bonded contact.
I_f	Frictional Second moment of area.
$I_{frictionless}$	Second moment of area with frictionless contact.
K	System stiffness.
l	Span length.
l_r	Length of each heat shrink ring.
L	Free length.
m	Mass.

m_{eff}	Effective mass.
msr	Configuration label for multi-strand bar.
msw	Configuration label for multi-strand wire.
M	Bending moment about neutral axis.
MSB	Multi-strand beam.
MSR	Multi-strand bar.
MSW	Multi-strand wire.
n	Number of surfaces in contact.
N	Number of strands.
N_r	Number of heat shrink rings.
N_y	Number of strands in vertical direction.
P_{eq}	Equivalent pressure applied to individual strands.
P_f	Interface pressure.
Q	First moment of area.
r	Radius of individual strands.
r_f	Nominal radius.
r_i	Inner radius of the multi-strand wire.
r_o	Outer radius of the heat shrink ring.
R	Orbit radius.
s	Half width of sheared area.
sb	Configuration label for multi-strand beam.
U_1	Strain energy in the positive part of hysteresis loop.
U_2	Strain energy in the negative part of hysteresis loop.
U_{max}	Maximum strain energy.
v	Velocity.
x	System displacement.
X_{-i}	Decayed amplitude at the end of half cycle.
X_i	Maximum amplitude when velocity is zero.
X_{i+1}	Amplitude of the next cycle.
y'	Distance between sheared area and the neutral axis.
y_t	Location of the geometric centroid.

y_w	Thickness of the strands involved in the slip.
α	Pitch angle between the strands centre.
$\varDelta u$	Relative displacement between the surfaces in contact.
δ	Displacement under sliding friction at maximum force.
δ_{bond}	Total displacement in a bonded system.
$\delta_{frictionless}$	Total displacement in a frictionless system.
δ_r	Radial interface displacement.
δ_{rm}	Radial displacement of the multi-strand wire.
δ_{rr}	Radial displacement of the heat shrink ring.
ε_f	Flexural strain.
ζ	Damping ratio.
η	Loss factor.
λ	Dimensionless parameter.
μ	Coefficient of friction.
μ_w	Coefficient of friction at the interface.
v	Poisson's ratio.
ρ	Density.
σ	Maximum stress.
σ_{fri}	Frictional stress.
τ	Shear stress.
τ_w	Shear stress at the interface.
φ	Angle of rotation.
ω	Excitation frequency (rad/s).
ω_n	Natural frequency (rad/s).

Chapter 1

Introduction

Vibration control in machinery and mechanical structures is considered a subject of interest to many researchers. The presence of dry metal friction in a system can provide significant levels of damping over a large range of working temperatures. Unlike viscoelastic materials, which are well known for providing damping, metallic dry frictional systems are temperature independent systems, which has caused them to be of considerable interest in some industry sectors. The main source of damping in these systems is the energy dissipated as heat due to the relative movement between mating surfaces that have frictional contact.

1.1 Multi-strand systems

Multi-strand systems comprise individual strands having frictional contact on the interfacial surfaces. The individual strands in this study are made of mild steel. These strands are kept together by means of clamping that applies the normal force required to provide frictional forces. Multi-strand systems of square and circular cross-sectional construction are shown in Figure 1.1.
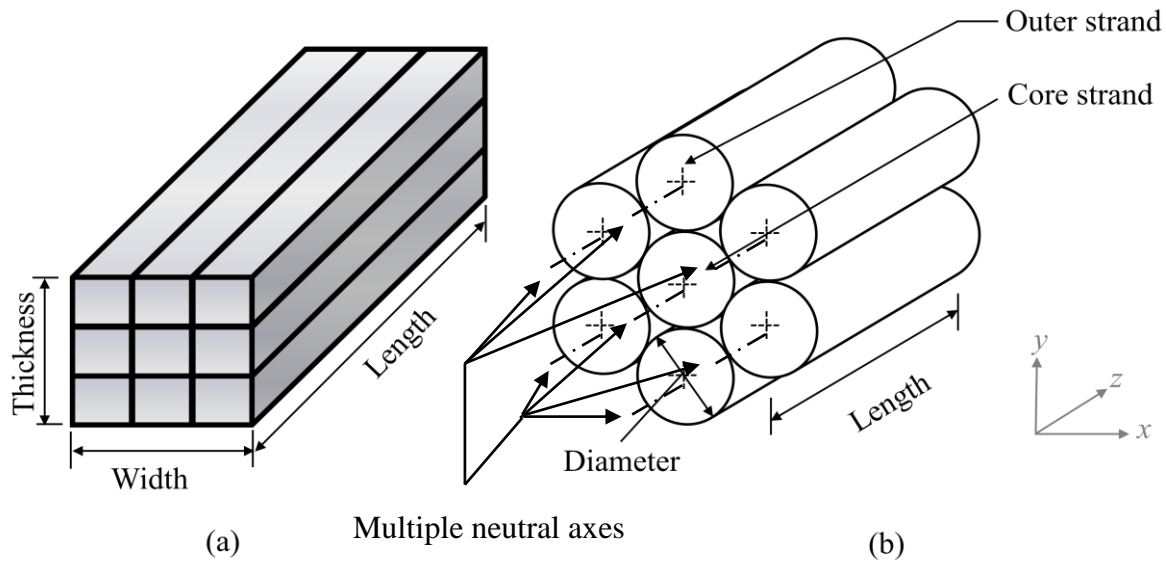
Figure 1.1 Multi-strand systems comprising (a) nine-strand beam with square cross-section and (b) seven-strand wire with circular cross-section

Multi-strand systems are distinguished as having multiple neutral axes due to the strands being frictionally connected rather than bonded to each other. This means that, during flexure, the individual strands flex independently of each other, thereby making relative displacement possible between strands. Optimising relative motion between the strands, whilst considering the change in flexural stiffness of the system is the key to improving damping levels.

One of the benefits of these systems is that they can be implemented in machines as a part of the system itself to control vibrations through the dissipating vibrational energy. Another benefit is that these systems are not expensive and are widely available.

The challenge in these systems is that the mechanism is not well understood and therefore it is difficult to optimise the frictional behaviour in order to provide certain damping levels. To achieve understanding of these systems, the overall stiffness of the system experiencing frictional behaviour should be identified accurately when the system is in slide contact condition. This stiffness is termed frictional stiffness in this study. The ability to describe the stiffness of a frictional system analytically can provide scope for new research as there is currently a lack of research describing the stiffness of a system where friction behaviour is involved during flexural loading.

1.2   Aims and contributions

The work in this study aims to provide understanding of the frictional behaviour of multi-strand beams (MSB), diagonal multi-strand beams (DMSB), multi-strand bars (MSR) and multi-strand wires (MSW) that comprise square and circular cross-sectioned strands. This is achieved through introducing analytical models that describe the frictional behaviour in these systems. These models are able to predict the flexural stiffness of the system. The effects of various parameters such as the length of strands, the number of strands, the cross-section size, the normal force, the amplitude of the forcing and the frequency of excitation on the damping levels are investigated in order to explain and optimise the damping behaviour of multi-strand systems.

This work addresses the damping behaviour in such multi-strand systems with frictional contact between individual strands. This is carried out by introducing analytical models to predict the system's stiffness and damping when subjected to flexural deformations. The analytical models are validated by experimental and numerical work.

To some extent, the experimental tests along with the numerical analyses are used to validate the analytical modelling. However, when the structure is more complex, the experimental set-up becomes more difficult, especially in a multi-strand wires comprising more than thirty-seven wires. On the other hand, the finite element analyses had limitations in simulating complex structures as the finite element package was limited to constructing multi-strand wire systems comprising seven wires, without taking into account the time expense. Therefore, it is desirable to have analytical models that can predict and describe the

frictional damping behaviour in these complex systems in a significantly shorter time and with less preparation.

1.3   Thesis layout

Various multi-strand systems are involved in this study, including multi-strand beams, multi-strand bars and multi-strand wires. Full description of the frictional behaviour during the sticking and the sliding phases are illustrated in this thesis. This thesis is divided into eight chapters.

Chapter 2 presents a literature review of previous research. The literature was selected to cover the different aspects of the study. Discussions and explanations of the previous and current research are conducted to clarify the knowledge gaps in these topics.

Chapter 3 focuses on the analytical and numerical models developed to describe the frictional behaviour in multi-strand beams (MSB) in which the individual strands are square cross-sectioned. The effects of the studied parameters such as length of individual strands, number of strands involved in the system, the clamp force, the size of individual strands and the amplitude of the displacement on the damping are described. The experimental investigation of material properties is discussed. The chapter describes the experiments performed to identify the static and dynamic coefficients of friction. Prediction of the frictional stiffness of the system is modelled analytically. The analytical models produce hysteresis loops which are then compared against hysteresis loops that are obtained numerically. Numerical models are built to investigate the effect of changing the number of individual strands while keeping the overall cross-section of the system the same.

Chapter 4 deals with the experimental tests performed on multi-strand beams (MSB) to investigate the same parameters considered in Chapter 3. Comparisons of the damping parameters and hysteresis loops obtained analytically, numerically and experimentally are presented.

Chapter 5 concentrates on the experimental, analytical and numerical investigations of diagonal multi-strand beams (DMSB) in. This chapter considers the effects of parameters such as the length of individual strands, the number of the strands involved in the system, the clamp force and the amplitude of the applied displacement on the damping behaviour of the

system. The effect of rotation of the system on the system stiffness and on the frictional forces is investigated. The thermal effect that occurred during the experimental work due to the friction is investigated and the hysteresis loops and the damping parameters obtained experimentally, analytically and numerically are compared together.

Chapter 6 explores multi-strand bars (MSR) and multi-strand wires (MSW) experimentally, analytically and numerically. Material properties are identified experimentally. This involves manufacturing special clamps to clamp the MSR and calibrate the clamp forces, while heat shrink rings are used to clamp the MSW. After explaining the experimental work performed on MSR and MSW the chapter focuses on the analytical models developed to predict the frictional stiffness of the system and to describe the hysteresis loops. The effects of parameters such as the number, the diameter and the length of individual strands as well as amplitude of the applied displacement on the damping characteristics are considered. The chapter presents comparisons of the damping parameters and the hysteresis loops obtained analytically, experimentally and numerically.

Chapter 7 deals with the dynamic experiments conducted on multi-strand beams (MSB) and multi-strand wires (MSW). These experiments were designed to illustrate the effect of vibration on the damping levels in these systems. The damping parameters are presented over the range of the tested frequencies.

Chapter 8 presents the main conclusions drawn from the work described above.

Chapter 2

Literature Review

2.1 Dry friction

To discuss dry friction sensibly, some definitions are defined upfront.

Dry friction can be defined as the friction induced from the relative movement of two or more mating surfaces in the absence of lubrication. Dry friction comprises two possible generalized regimes. The first regime is the static friction, sometimes known as "stiction", where there is no movement between mating surfaces. The second regime is the dynamic friction, which occurs when slip is present at the mating surface. These regimes are used to define the friction coefficients. The slip takes place at two phases. The first phase is microslip where some asperities break and others remain depending on the force level, ratio of shear force to normal force, applied to the system causing relative movement between the two surfaces in contact at the micro-scale level. The second phase is the macroslip where slip starts at all surface asperities causing the two bodies in contact start to slide relative to each other.

Therefore, static and dynamic coefficients of friction are used to estimate the frictional force.

An early attempt to study friction phenomena scientifically was made by Amontons in 1699 through his three laws of friction which were verified later by Coulomb in 1785. These three friction laws state that the normal force has a direct effect on the friction force, the friction force is independent of the area of the contact, and the kinetic friction is independent of the sliding velocity. Several analytical models were later proposed. The types of model used to describe static dry friction may include the Coulomb model, Static Friction model and Karnopp model.

The Coulomb model (Equation 2.1),which has been adopted by many researchers, states that the friction force is independent of the contact area, has a direct proportion to the normal force and opposes the direction of movement, while the friction force is dependent on the direction of the velocity (assuming no zero velocity).

$$F_{Coul} = \mu F_N \, \text{sgn}(v)$$ 2.1

where, F_{Coul} is Coulomb friction force, μ is coefficient of friction, F_N is the normal force and v is the velocity.

The Static friction, stiction, model, which was studied by Rabinowicz [1], stated that the external force needed to overcome the stiction force for a system that has static contact would be greater than the external force needed to overcome Coulomb friction force due to the fact that Coulomb model did not count for zero velocity contact. Static friction model assumes that the static friction is dependent on the external force (the force that can cause the slipping if it was high enough to overcome the stiction force) as shown in Equation 2.2 in addition to the independency of the velocity.

$$F_{Stat} = \begin{cases} F_{ex} & \text{if } v = 0 \text{ and } |F_{ex}| < \mu F_N \\ \mu F_N \, \text{sgn}(F_{ex}) & \text{if } v = 0 \text{ and } |F_{ex}| \geq \mu F_N \end{cases}$$ 2.2

where, F_{Stat} is Static friction force and F_{ex} is the external force.

For some control applications, zero velocity contact can cause some computational problems therefore Karnopp [2] introduced a friction model in which he introduced the friction force as a function of velocity and defined a region for low velocity, and whereas outside this region the friction force has an arbitrary value, inside the low velocity region the friction force is found by other forces in the system.

Stick-slip behaviour is a 'jerking' relative motion between surfaces alternating between a relative velocity of zero (stick) and nonzero (slip). This occurs when either the tangential force fluctuates between less than and greater than (or equal to) the frictional force, or the statistical 'locking' of the asperities changes spatially alternating between lock and unlock conditions.

Stick-slip phenomenon was first given its name "stick-slip" by Bowden and Leben [3] during their experimental work to investigate the effect of sliding on alternation between

sticking and sliding the frictional force where they assumed values for the static and the kinetic coefficients of friction. This investigation was extended by the experimental work of Antoniou et al [4] who specified magnitudes for the coefficient of friction at each stick-slip cycle as the stick-slip oscillates. More stick-slip studies can be found in the references [5–9].

Since earthquakes are generated by stick-slip between the tectonic plates, geophysicists needed a model that could describe the time history of the friction force magnitude. The Dahl model [10], which was introduced in 1968, was supposed to cover the static and the dynamic dry friction contact stages. Dahl provided a description for the elastic and plastic distortions of the asperities during the microslip by transforming the stress-strain curve of each contact pair into a force-displacement curve analytically. Dahl friction force is a function of velocity and displacement which is represented empirically as

$$\frac{dF_{Dahl}}{dx} = \sigma_0 \left(1 - \frac{F_{Dahl}}{\mu F_N} \text{sgn}(v) \right) \qquad\qquad 2.3$$

where, F_{Dahl} is Dahl friction force, σ_0 is stiffness parameter at equilibrium point where $F_{Dahl}=$ 0. Dahl friction force can be written in a time derivative as

$$\frac{dF_{Dahl}}{dt} = \frac{dF_{Dahl}}{dx} \cdot \frac{dx}{dt} = \left[\sigma_0 \left(1 - \frac{F_{Dahl}}{\mu F_N} \text{sgn}(v) \right) \right] v \qquad\qquad 2.4$$

Coulomb model (Equation 2.1) was considered as a special case of Dahl's model, representing the steady-state case of the Dahl model (Equation 2.4).

Stribeck effect is friction behaviour whereby friction force decreases due to increasing the velocity in contacts and due to a lubrication film, and many researchers have used this effect to describe the stick-slip at its initial conditions. The sliding contact for Coulomb, viscous, combination of Coulomb and viscous and Stribeck friction models have been investigated analytically by Andersson et al [11] in terms of their performance conditions and contact type. However, they argued that the friction force in the case of zero sliding cannot be found, and this case may require the use of micro-slip models like Dahl, Lu-Gre and combinations of "Coulomb, viscous and Stribeck" friction models. Basically, models depend on the occurrence of local slip of some particles inside the contact area while other particles are still stacked without slipping. They suggested that if these models were connected together to

construct a system model, this system model could be used in the simulation and analysis of different contact conditions.

To mimic the unequal distribution of asperities in the contact region, Haessig and Friedland [12] introduced the Bristle model (Equation 2.5) which was considered a dynamic friction model as the model counted for the velocity. In this model, the friction is created by large numbers of random bristles that come into contact. Each bristle is considered as a spring and friction force is counted by summing the total forces resulting from the presumed springs. This model was found to be inefficient as the complexity of the model is increased by increasing the number of the bristles.

$$F_{Bris} = \sum_{i=1}^{M} \sigma \ (x_i - s_i) \qquad\qquad 2.5$$

where, F_{Bris} is Bristle friction force, M is the number of bristles, σ is the stiffness of bristles, x_i is the relative location of bristles and s_i is the connection position of the mating bristles.

Later, scientists from the Lund control group and the Grenoble control group started to propose a dynamic friction model called the Lu-Gre model [13, 14]. Basically, this model was a combination of the Dahl model and Stribeck effect along with the Bristle model but with averaging of the friction forces resulting from the total bristles in contact. Lu-Gre friction model described as

$$F_{Lu-Gre} = \sigma_0 z + \sigma_1 \dot{z} + \sigma_2 v \qquad\qquad 2.6$$

Where, F_{Lu-Gre} is Lu-Gre friction force, z has been introduced by Dahl and considered the bristles deformation in Lu-Gre model and is described as

$$z = \frac{F_{fri}}{\sigma_0} \qquad\qquad 2.7$$

where, F_{fri} is the friction force, σ_1 is the microscopic damping, $\dot{z}$ is obtained through substituting Equation 2.7 into Equation 2.4 which results

$$\frac{dz}{dt} = \dot{z} = \frac{1}{\sigma_0} \cdot \frac{dF_{Bris}}{dx} \cdot \frac{dx}{dt} = v - \sigma_0 \frac{|v|}{F_{Coul}} z. \qquad\qquad 2.8$$

In Lu-Gre friction model, the constant friction force F_{Coul} is replaced with a velocity-dependent function $g(v)$ which leads to

$$\dot{z} = v - \sigma_0 \frac{|v|}{g(v)} z, \qquad\qquad\qquad 2.9$$

σ_2 is the viscous friction coefficient. The advantage of Lu-Gre model is the preslide and slide stages are included in the model.

2.1.1 Dry friction in delaminated and multi layered beams

In many cases delamination may be considered as a phenomenon of failure in composites. This happens when the layers start to separate from each other. Friction induced between the delaminated layers can be utilized in vibration control. Most research papers deal with the delamination status theoretically. Additionally, multi-layered beams can give similar behaviour to the delamination.

The free vibration of composite laminates with a single central delamination was investigated by Saravanos and Hopkins [15]. In their work, they obtained natural frequencies and modal damping values experimentally, and they also developed an analytical model to help explain the effect of delaminations. In the model, a kinematic assumption was introduced to describe the crack as an additional degree of freedom in the laminate theory. Accordingly, the generalized stiffness, mass and damping matrices were formulated. It was found that the natural frequency decreases with increasing the delamination length. The effect of friction in the delamination interface on the damping performance was not considered. The dynamic behaviour of a composite beam with a single delamination has also been studied by Kargarnovin et al [16] but with a moving contact force on the surface. The dynamic response was obtained analytically through modal analysis and the effects of the velocity of the moving force, location of the single delamination and the delamination length were considered; however, the effect of friction between the delaminated layers was neglected. Li and Crocker [17] examined the effect of the delamination length, position and whether the delamination occurred on one side or both sides of a honeycomb-foam sandwich beam. They pointed out that the delamination can cause friction which would in turn increases the damping; however, the friction between the delaminated layers was not studied.

The vibration of a beam with two delaminations was studied analytically by Della and Shu [18]. They divided the beam into five interconnected strands and applied classical beam

theory in their work. The vibration modes of the beam were investigated when the strands were free (global), partially constrained (mixed) and fully constrained (local) – see Figure 2.1. They studied the effect of slenderness ratio on the fundamental frequency of the beam. Only equal delamination lengths were used in their study. They found that in the case of the constrained mode the strands were vibrating together, while in the case of the free mode the beams were vibrating independently. On the other hand, they found that vibration of the beam depended on the thickness of the delaminated layer in the case of the partially constrained mode. The drawback of their work is that, the effects of friction were not taken into consideration despite obvious frictional contact.

(a)

(b)

(c)
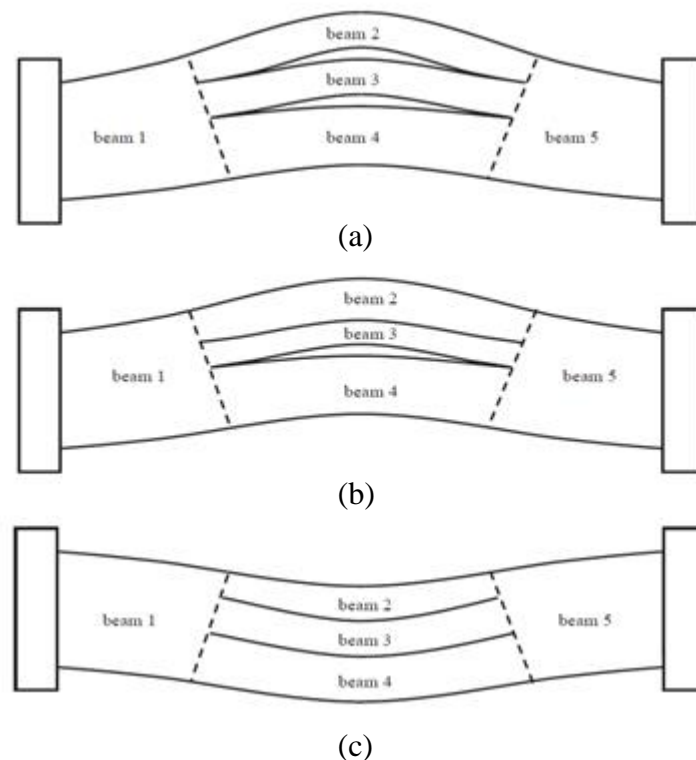
Figure 2.1 Beam vibration modes (a) free mode, (b) partially constrained mode and (c) constrained mode (Source [18])

The influence of the size and location of the delamination on the fundamental frequency and mode shape in a beam with two overlapping delaminations were investigated by Della et al [19]. An analytical study of the free vibrations was conducted. They found that the fundamental frequency and the mode shape were affected by the second overlapping delamination of a clamped beam. Also, the length of the delamination had a significant effect

on the fundamental frequency and the mode shapes. However, the study focused on the dynamic behaviour of the delaminated beams and ignored the frictional effect between the laminates and its effects on the response. A similar study, conducted by Andrews et al [20], used a cantilever beam that was loaded at its end and the beam end was divided into segments (delaminations with different lengths). They showed that the short and long delaminations can reduce or increase the rate of energy release depending on the geometry of the system. The contact between the segmented beams was assumed to be non-frictional and the study suggested that future researches should study the effects of friction. Other studies that analysed the response of composites experiencing interlayer slip [21–24] ignored the presence of friction in the interlayer region.

A leaf spring system (shown in Figure 2.2), often used in the automotive industry, can show dry friction at the interfaces between the leaves. An approach was introduced by Osipenko et al [25] to investigate the shape of bent leaves where each leave has different lengths with un-bonded frictionless contact. The model was simplified into spring of two straight leaves under bending. The leaves were constrained from one end and was free from the other end. To simplify the problem of getting the shape for the bent leaf, they calculated the density of the interfacial loads. The hysteresis behaviour of the leaf spring system of a truck was studied experimentally and numerically by Yum [26]. The experimental part of this study focused on the effect of friction that may result from the shackle (that lies at one of the leaf ends) on the hysteresis loops. Shackle friction effect was neglected in the numerical analysis, in addition to the friction between the leaves, which resulted in some differences in the hysteresis behaviour compared with the experimental results.

Blok [27] showed in his thesis that the energy dissipation by a Coulomb model in a stick condition is at similar levels to the energy dissipated by a Stribeck model or Viscous model of stick status. Blok built an experimental model for a mass which was sliding on a base depending on the basis of Coulomb friction model. The results were compared with those from theoretical analysis based on the Coulomb friction model.

2.1.2 Dry friction between fibres

Fibrous materials involve metallic and non-metallic materials such as steel fibres, entangled metal wire, yarns and paper. Under load these materials experience dry friction as slip can
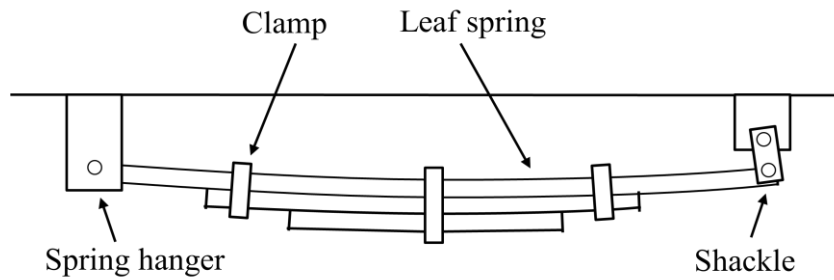
Figure 2.2 Leaf spring system

occur at interfaces. The dry friction between the contact surfaces will cause non-linear behaviour and at the same time will resist relative motion between the moving parts. This resistance can be considered as a dissipation of the energy which can be utilized in vibration control.

The first studies to investigate fibres and their twisting methods started in the 1950s. An apparatus was developed by Lindberg and Gralen [28] to evaluate the coefficient of friction between two twisted fibres in experiments using fibres made of nylon and wool. The method involved twisting two fibres together, applying a force at one of the four ends while holding the other ends and then starting the slip. Because the applied forces were known, the frictional forces could then be found. This method was applicable to two fibres in contact only.

The friction between yarns and a cylinder was studied experimentally by Howell [29], using yarn and a cylinder produced from different materials. A formula was developed for the Capstan contact which was represented as line contact between the fibres and the cylinder or as point contact between the fibres themselves. The effect of the cylinder diameter was studied in terms of the resulting contact with the yarn and its effect on the friction coefficients. The tension of a fibre around a cylinder was found as

$$T = T_o e^{\mu \theta \left(\frac{\rho}{T_0} \right)^{(1-n)}}$$

2.10

where, T is the tension of a fibre around a cylinder for non-metallic materials and is found experimentally, T_o is the initial or the restraining tension, μ is the coefficient of friction, ρ is

the radius of the cylinder, θ is the angle of the twist of the fibre around the cylinder and n is the friction index. Then the coefficient of friction is estimated as

$$F = \mu T^n \qquad\qquad 2.11$$

Howell stated that the repeatability of the experimental results depended on the level of the cylinder's surface cleaning. The fibres and the cylinder were non-metallic materials.

Gupta and El-Mogahzy [30] attempted to generalize a model that can work on viscoelastic fibres, identifying the parameters a and n of the empirical formula

$$F = aN^n \qquad\qquad 2.12$$

where, a represented the effect of the stiffness and n represented the shape factor. They believed that the surface morphology has an effect on the coefficient of friction as the number of asperities increases if the surface is rough. They studied fibres made of materials with viscoelastic deformation as these materials do not follow the standard friction law because these materials partially deform plastically. They assumed that neither the contact area nor the normal force affects the specific shear strength. The study was concerned to find a general formula for the true area of contact in terms of the number of asperities at the contact area. Through generalizing the pressure distribution on the asperities in the contact area and assuming some forms of stress distribution for the asperities, they were able to derive the formula. Line contact for in-line fibres and the point contact for across fibres were implemented.

The experimental work conducted by El-Mogahzy and Gupta [31] was an attempt to connect their study with the results of a previous theoretical study [30]. They used both line contact method (twist method) [28] and point contact method (Capstan method) [29]. Both of which methods can be classified as inter-fibre contact. The parameters under study were the coefficient of friction in addition to a and n indices in the friction formula for viscoelastic materials Equation 2.12. They examined the effect of the cross-section shape of the fibre as well as the effects of the type of the fibre used in the experiments and whether the fibres were annealed or not. Generally, the parameters under study took the structural effects and the shape effects into account. They noticed that n was not affected by wet contact but was affected by the shape factor and a was a factor of material properties. The previous two

studies were limited to investigating the effect of the morphology of the contact area on the friction for fibres.

Depending on the structural similarity between the yarn/fabric and the fibrous material in terms of both having friction in their fibres, Ngoc et al [32] adopted Dahl's model to describe the hysteresis loops of woven materials. A comparison was made between the simulated results and data measured in the lab. Based on the results of this study, they suggested that more research is needed to describe and simulate the friction behaviour in fibres as the simulated model was empirical-data dependent.

A review of models used to represent the behaviour of dry fibrous materials was conducted by Syerko et al [33] within different conditions. The study concluded that models at macro-scale (whole component) can process any type of fibrous material as these models do not depend on the micro structure of the material; however, this procedure is used at the expense of the accuracy. Models at the meso-scale (yarn) can analyse some statuses like crushing and sliding in fibres, but input data will be needed to simulate these models. In order to obtain the input data, models at the micro-scale (fibre) will be needed to illustrate the exact internal behaviour of the adjacent fibres and how they affect the whole model. In the work of Raoof and Hobbs [34] and Raoof and Roger [35], multilayered strands experiencing axial load were studied analytically where the ends of the strands were assumed fixed. In their work, zero friction was assumed for the full slip stage as they considered that the frictional force is negligible compared to the force changes in the wires themselves due to the axial load.

2.1.3 Microslip in balls and cylinders

The normal contact between two elastic curved bodies was first analytically introduced by Hertz in 1882. The assumptions of the Hertz theorem are that the deformations are within the elastic limit, the contact area is much smaller compared with the dimensions of the bodies in contact, the bodies are elastic half-space, and the contact is frictionless. Hertzian contact includes only normally loaded (normal to the longitudinal axis of the bodies in contact) contact.

Later, the contact of two elastic half space bodies that were loaded normally and tangentially was studied by Cattaneo in 1938 and by Mindlin in 1949 by extending the Hertzian theory of contact to include a slip condition that may occur due to tangential loading. Mindlin

simplified the analysis by introducing the following assumptions: 1- the two spheres in contact are identical in shape. 2- the contact area resulting from the normal load is independent of the tangential loading. 3- tangential loading causes the contact interface to start slipping and increase of the tangential load causes the slip to spread radially as an annulus starting from the edge of the contact area. The inner radius of the annulus (*c*) was defined as

$$c = a\sqrt{1 - \frac{P}{\mu N}} \qquad\qquad 2.13$$

where, *a* is the Hertzian half width contact area, *N* is the contact normal force and *P* is the non-constant tangential load. 4- the direction of the shear stress generated on the annulus is parallel to the direction of the tangential load.

The Mindlin concept regarding the slip generated from tangential loading has been used widely by researchers in an attempt to describe frictional contact in elastic half-space bodies.

Goodman and Brown [36] compared the results of their experimental work, using a steel ball constrained by two steel surfaces opposite to each other where the ball was exposed to normal load and cyclic tangential load, with analytical prediction depending on the Mindlin concept, and they were able to describe the hysteresis loop for the stick-slip condition. Similar work was presented by Dini and Hills [37]. Pires and Oden [38] studied numerically the deformations of the asperities when subjected to constant normal and oscillating tangential loading. They limited their work to the assumption that the normal pressure distribution on the asperities is independent of the effect of the oscillation of the tangential load. A similar assumption, that normal deformations are independent of the tangential stresses, was applied to the numerical work of Nowell et al [39], which used two dissimilar elastic bodies that came into contact. Their results agreed with the analytical prediction of the Mindlin concept.

In the above research, it was assumed that the tangential stress would not cause sliding between the mating surfaces and that the tangential stress was applied in the lateral direction. In the work of this thesis, the contact was allowed to extend to full slide condition. In addition, the system was exposed to flexural loading creating tangential stresses along the length of the system (longitudinal direction).

Although the Hertzian theorem of contact states that the contact is frictionless and that the normal pressure is Hertzian, some researchers have attempted to utilize this theorem in frictional contact systems.

Kalker [40] studied two cylinders in contact numerically and it was assumed that there was no distinction between the slip and no slip cases. The tangential stress was supposed not to affect the distribution of the normal Hertzian pressure on the contact area. The shape of the contact area of two cylinders pressed over each other where their longitudinal axes were parallel, was described by Kalker [41]; however, he pointed out that the error in the results, when compared to an exact Hertz solution, increases when the ratio of the length of the contact area to the width of the contact area increases. Similar work was conducted by Ahmadi et al [42] that attempted to relate the effect of friction to the contact area. They stated that the contact area might change slightly due to friction, but provided no actual calculations. In an attempt to model the tangential contact stiffness of the asperity in the frictional contact area, Shi et al [43] considered the contact area of the asperity as a parameter instead of using the major and minor axes, because they believed that the asperity contact area is stochastic. They showed that the tangential contact stiffness decrease with increasing the tangential force and increase with increasing the normal force. In line with the previous, Mulvihill et al [44] were not able to measure the true contact area in their study to investigate the friction between carbon fibres in composites and they used a Hertzian formula to calculate the contact area instead.

Researchers have utilized simplified Mindlin concepts to describe the rolling contact of two half space bodies experiencing friction in terms of distribution of tangential stress along the contact area and prediction of the contact area dimensions.

The tangential stress resulting from rolling of two normally loaded elastic spheres and its distribution along the contact area was proposed mathematically by Goodman [45] and Mossakovskii [46]. The friction effects were inserted as frictional stresses into Hertzian pressure. The contact status was limited to stick in their study. Similar work was done by Zhupanska and Ulitko [47]. The shear modulus of elasticity was denoted to μ in Goodman's work, which makes it difficult for the reader to follow the insertion of the friction effect in the analytical equations, especially since no clear evidence was shown for the use of the coefficient of friction in their work. Their solution was simplified by presuming normal

displacements independent of tangential stress. Normal displacements dependent on tangential stress were studied by Spence [48] in a full stick contact problem and by Spence [49] in a partial stick contact problem. The adhesion contact area of bodies, in a Hertzian problem, experiencing rolling contact was predicted by Haines and Ollerton [50] in their work. They described the adhesion contact area experimentally through photoelasticity technique which was followed by analytical work using simple strip theory; however, there was a difference between the experimental and predicted contact area. Kalker, referring to this difference in his review of the Haines and Ollerton work, explained that strip theory can hardly be used in this type of problem as this theory cannot explain rolling and tangential slip as it is a two dimensional theory. Haines then presented similar work [51] based on photoelastic experiments and computer programming. He found that it is difficult to describe the system when it starts to slide under the rolling and tangential actions. A model was built by Vu-Quoc et al [52] to describe the normal and tangential stresses in elastoplastic spheres. However, their model depended majorly on data such as the radius of the contact area, radius of curvature, stresses and force-displacement curves that were obtained from finite element simulation. They pointed out that in elastoplastic spheres the contact area is not expected to be circular as Mindlin assumed for elastic spheres in contact. An elastoplastic sphere normally loaded on a flat surface was also studied by Brizmer et al [53] to investigate the effect of different materials under slip and stick conditions. The analytical model adopted the Hertzian theorem to measure the radius of the contact area for slip, while numerical methods were used to describe the stick condition. The stick and slip in rolling bodies and its effect on subsurface cracks was explored by Liu et al [54]. In their research, the radius of contact area was defined based on the Mindlin formula (Equation 2.13).

Most of the research discussed above dealt with the rolling action in normally loaded cylinders and spheres and depended on the Mindlin formula to predict the slip contact area, with the slip contact area assumed to be in the shape of an annulus, in sphere contact, that surrounds the stick contact area with the inner radius of annulus c as shown in Equation 2.13. Examination of this equation leads to the conclusion that even though the outer radius was not specified in the Mindlin formula, it is impossible that the inner radius (c) will have a value greater than the radius of contact of a frictionless case where it is assumed to represent the radius of contact in stick contact in the Mindlin formula. The current study

retains this formula used in the previous researches described above as the author believes that the radius of contact in stick contact is much larger than the radius of contact in frictionless contact.

2.2   Damping from interfacial friction

2.2.1   Interfacial damping

One source of interfacial damping is the damping generated from the frictional slip at the interfacial contact area. Some mechanical structures that are beam-like utilize interfacial frictional behaviour to reduce vibrations. This section reviews some of the work in this area.

Goodman and Klumpp [55], presented a model of a double leaf cantilever beam that estimated theoretically the dissipation of energy from two beams in contact. They compared the obtained data with results derived from experimental work. Experimental data are important in designing frictional damper systems as Griffin [56] showed in his review because some mechanisms that can affect the dynamic response of the system are difficult to predict in advance in addition to that the experimental work can validate the analytical models. A review of the mathematical methods used to describe the dry frictional behaviour in turbine blades was introduced by Rizvi et al [57]. They pointed out that most of the available models can only describe and analyse problems through limited cases that adopt the boundary conditions of these models. In the study of Menq et al [58], two dimensional friction damper was added to a blade mass and the damper was assumed to be massless with a constant stiffness. Coulomb model was adopted to represent the friction behaviour in the system. The purpose of this study was to find an estimated method to analyse problems with two dimension frictional contact. Three cases were included in the solution and a mathematical form was built for each case; full stick, full slip and microslip. They used receptance method as a methodology to separate the effects of the external load and the damping force from each other. The effect of the ramp angle of a displacement dependent damper on the damping characteristics of a beam was investigated by Whiteman and Ferri [59]. They studied a beam-like structure attached to displacement dependent damper (Figure 2.3). In their study, the normal force causing the dry friction was set to increase linearly in relation to the transverse beam deflection through the use of ramp configuration. The study tried to find an

optimal value for the ramp angle to give a maximum damping ratio. It was found that the more the ramp angle increased, the lower the equivalent damping ratio.
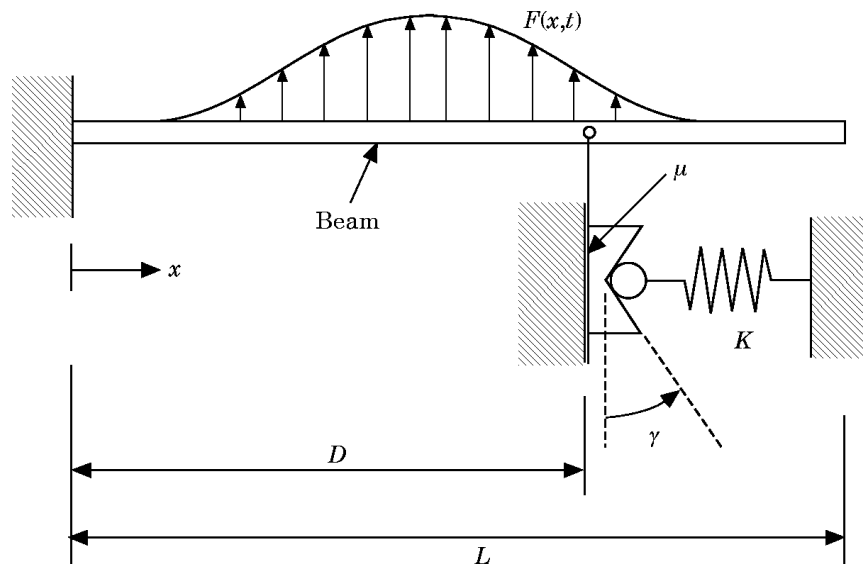
Figure 2.3 Transverse frictional interfaces to represent variable normal load (Source [59])

Damping can be effected by the geometrical characteristics. The effect of the interface length on the loss factor was investigated by Singh and Nanda [60] through experimental study of the dynamic behaviour of two beams held together by a tack weld and having slip in the interface. During dynamic loading, the amount of energy dissipated decreased when compared with the microslip case. The half-power method was used to obtain the damping ratio. The contact pressure between the two beams was considered as a uniform pressure. It was found that the energy dissipation increased with increasing the length of the beams, whereas it decreased with increasing the thickness of the beams.

The effect of the damping caused by interfacial friction in a composite of silicone rubber and steel rods was investigated by Nelson and Hancock [61]. Tensile experiments were performed for three main types of contact: bonded fibre matrix, lightly bonded fibre matrix and matrix alone. Their study showed that a matrix with lightly bonded fibres can give a much greater energy dissipation than those with fully bonded fibres because of the existence of interfacial slip. Hysteresis loops were used to estimate the difference between the three cases. The purpose of their study was to design a composite with targeted values of stiffness and damping. Research on the damping mechanism in fibre reinforced composites and the

methods applied to analyse the damping was described and reviewed by Chandra et al [62]. The damping studies were categorised as based on three main types of method: macromechanical, micromechanical and viscoelastic. Meanwhile, the levels of interfacial bonding were classified as soft, ideal and sturdy. It was reported that the maximum damping could be obtained from the matrix of the composite, which is controversial with regard to the work of Nelson and Hancock [61] which concluded that the maximum damping in composite was obtained from the fibres.

Other researchers have developed empirical models to describe the damping in composites. For example, the damping properties of laminate composite materials with interleaved viscoelastic layers were investigated experimentally through a cantilever beam test by Berthelot et al [63]. The obtained damping data were modelled under the consideration of laminate theory, taking into account the transverse shear effect. This model was applied to a simple structure comprising different materials. The loss factor of those materials was derived from the experimental damping data. On the same lines, Mahi et al [64] investigated the damping characteristics in some types of unidirectional and orthogonal composites. The stored strain energy was used in their study to determine the damping behaviour of the composites generated from the material. The results of their analytic analysis were fitted to the experimental results. The loss factor found from the analysis was considered to derive from the material damping. It was concluded that composites with higher friction behaviour, such as taffeta composite, will produce a higher loss factor as the friction is greater between the wrap and weft fibres.

Some researchers have attempted to simplify the problem through systems with lower degrees of freedom. The analytical work of Dowell [65] investigated a linear single degree of freedom system damped by a dry friction element attached to the system, following Coulomb theory. Some cases were introduced to examine the effect of location of the dry friction element within the system. It was found that if the exciting force and the threshold force (the force at which the dry friction element has no motion) were in the same position, the threshold force was not affected by the exciting frequencies or by the geometrical parameters (stiffness, mass and damping). Meanwhile, if they were positioned in different places, the threshold force was affected by all those parameters previously mentioned above. In a theoretical and experimental study introduced by Dowell and Schwartz [64, 65], three

different configurations for the attached dry friction setting were assumed and the equation of motion was derived for these settings . They compared the results of their study with the results obtained previously by Dowell [65] and a similar behaviour was obtained as they used a cantilever beam and Dowell used a simply supported beam.

2.2.2 Loss factor

The loss factor is one of the most convenient indicators for the level of damping that exists in a system. This is proportional to the ratio between the energy loss and the maximum vibrational energy in a system.

$$Loss\ factor = \frac{energy\ loss}{\max.energy}$$
<div align="right">2.14</div>

Some researchers have investigated the loss factor generated from material damping.

Carfagni et al [68] presented methods to calculate the loss factor η. They proposed the loss factor as the comprehensive parameter to describe the damping in a system and the reason is that loss factor can describe the damping in nonlinear cases. Similar work was presented by Carfagni and Pierini [68, 69]. A dynamic study on thick cross-plied composite configured as cantilever was carried out by Koo and Lee [71] to investigate the natural frequency and damping factors. Experimental and numerical analyses were carried out using graphite/epoxy composite. The dependence of the material on the frequency was investigated by calculating the modulus of elasticity from the natural frequency. The effect of the natural frequency on the material properties of the composite was explored and it was found that at higher frequencies, there was a reduction in the values of the modulus of elasticity.

Other researchers have investigated the loss factor obtained from structural damping.

Srinivasan and Cutts [72] related the damping in turbine blades of jet engines to rubbing at the shroud interface and to platform dampers. They considered the frictional damper to be of macroslip type in their experimental and analytical work and they expressed the effects of friction as loss factor. Sherif and Omar showed in their experimental and analytical work [73] that there is inverse proportion between the damping and the relative amplitude in the microslip region. The structure consisted of two simple elastic bodies experiencing dry friction and the two bodies were moving at the same direction but with different forcing

values. Wang et al [74] attributed the dissipation of energy in their experimental and analytical work to the friction on a cantilever beam that had pressure distributed along the length and was constrained with a frictional layer. Yuan et al [75] examined the frictional damping in blades using a two dimensional model. Lacing and shroud structures (see Figure 2.4) were used and their effect on the blade stiffness and blade damping was investigated. A three dimensional model of two asperities in rough contact was presented by Pan et al [76]. Although they used Hertz theory to describe the dry frictional contact problem, they showed that the loss factor increased with increasing the dynamic coefficient of friction.

(a)

(b)
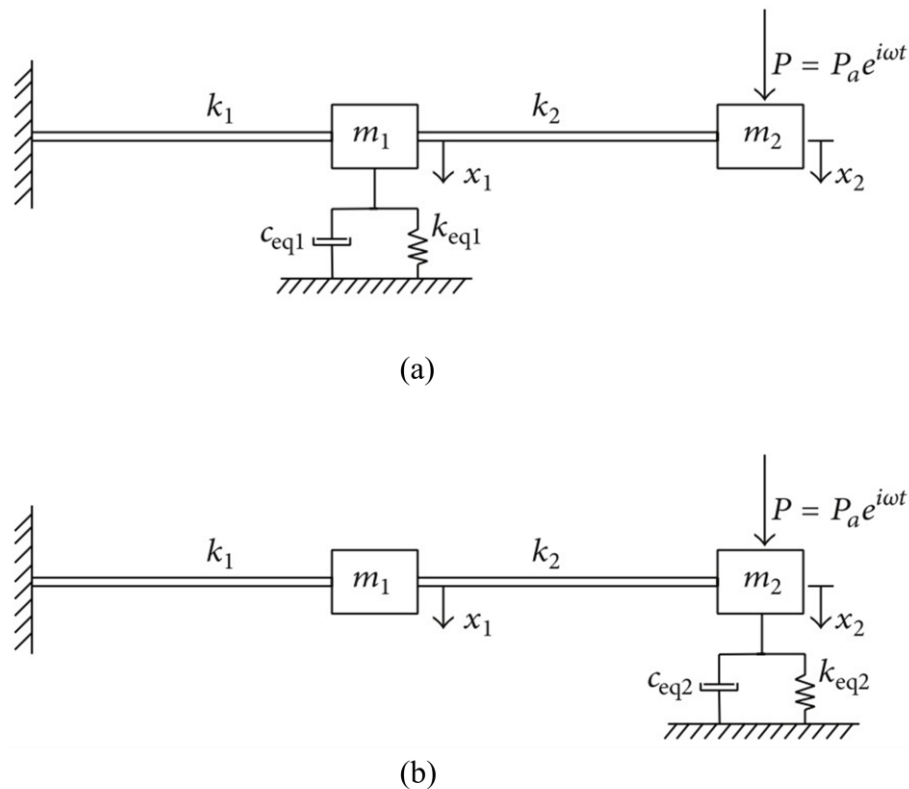
Figure 2.4 Simplified blade model showing (a) Lacing structure and (b) Shroud structure
(Source [75])

2.2.3 Microslip friction

The general concept of micro-slip friction is that within a certain contact area, slip movement could occur between some particles or asperities while at the same time other

asperities in the same contact area may be in a stick condition. This phenomenon can be considered the main source for damping in some systems

There is interest in the capabilities of nanotubes technique and one benefit cited is that they have the potential to increase damping in composites. In the work of Zhou et al [77], a single wall carbon nanotube was used as filler in polymer resin in addition to the other filler types in order to enhance the damping characteristics. A micromechanical model was introduced. The microslip interfacial friction was considered between the resin and the nanotubes. Experimental work was compared to the analytical data and showed enhancement in the damping features when single wall nanotube was added (η=0.08) compared to other filler types (η=0.01–0.02). They used a finite element model to estimate the damping ratio in order to be able to compare the results of the analytical model against the experimental work, which means that the model could not predict damping. The friction effect between the nanotubes and the resin and between the nanotubes themselves on the damping was studied theoretically in a nano-composite with carbon nanotubes by Lin and Lu [78]. The contact between the nanotubes themselves was assumed to be similar to a dry friction condition in beams. A vibration analysis was performed analytically on a mass–spring system to account for the effect of the two friction types in the system. The effect of some parameters on the loss factor was explored, for example, volume fraction (loss factor increase with increasing volume fraction) and resin modulus of elasticity (loss factor decrease with increasing resin modulus). They found that damping level increased for higher modes, with a more complicated mode shape, can result in more strain and then more damping in the system. Similar work was presented by Formica and Lacarbonara [79] where they found the microslip to be one of the factors that increased the damping in their study on nanocomposites. The dynamic behaviour at the interfacial contact area, particularly the energy dissipation during the microslip phase, was described by Asadi et al [80]. An analytical model was built to estimate the energy dissipation in a beam with frictional support at the root region. Stick, microslip and slip cases were studied. The contact between the fixed support and the beam was frictional. Experimental work was performed on a beam and the results were compared with the analytical model. The contact parameters for the analytical model were obtained from the experimental work; therefore, their model can be considered as an empirical model rather than an analytical model. They compared hysteresis

24

loops that were obtained analytically and experimentally at frequencies above and below the fundamental natural frequency region. It is interesting to see the good match between the hysteresis loops even though that the inertial effect was not removed from the results, as exciting a system at frequencies near and beyond the fundamental frequency would certainly produce inertial effects. The above research shows that the analytical models were dependent on parameters obtained either numerically or experimentally.

2.3   Modelling with finite element method

Using finite element models in some vibrational problems can save time and expense in addition to providing the ability to study the effects of many parameters during the simulation.

The use of FE models can sometimes dispense with the need for experimental work, as stated by Boisse et al [81] who used the three dimensional finite element package as an alternative to experimental work in the case of the unit woven cell. They determined the mechanical behaviour of woven materials, the transverse compaction, in biaxial tension and in-plane shearing. The woven yarn was assumed as a two directional fabric (warp and weft) instead of using the yarn as a straight or curved beam. During the experimental comparative study, a camera processed with software was used when performing the in-plane shear test, the displacement and strain region being obtained by the use of an image correlation method. Coulomb friction with master/slave technique was adopted to represent the contact between the yarns when making the 3-D finite element model, in addition to the use of elastic orthotropic material. For the solving process, they depended on the large strain theory due to the displacements and strains being high. For the simulation of the woven fabric in the case of in-plane shearing, an implicit method was used because it was sufficient up to the case of locking angle, while in the case of biaxial tension simulation an explicit approach was used to implement the generality of formulation that they introduced.

Chen and Deng [82] used a FE model to simulate the micro-slip and the damping behaviour induced in the interfacial friction in beams with two types of contact: press-fit joint and lap-shear joint. They compared their results with two previous experimental studies. They called the first experimental data G-K, deriving from the Goodman and Klumpp model [55], and

the second experimental data was called the M-D, referring to the Metherell and Diller model [83]. They found that the FE model was capable of predicting the damping behaviour and could simulate the slip damping. Several important parameters were compared including the effects of clamping pressure, vertical applied force, coefficient of friction, and the height of the beams on the energy loss per loading cycle.

Two models of simply supported plates were dynamically studied by Burlayenko and Sadowski [84]. The first model was designed with de-bond in the middle of the plate (penny shape debonded), while the second model had no de-bond. The plate was considered as a type of laminate. Commercial FE code was used to simulate the models. Their study found that the contact was a source of the non-linearity in the structure and that the existence of the delamination had the effect of increasing the amplitude and reducing the natural frequency. They reported that the FE code was capable of predicting the dynamical characteristics.

Some researchers have attempted to model wire rope systems through the use of finite element packages. Most of these studies reduced a system with a complex wire rope structure with several wires helically wound around a core (including systems with nineteen wires and more) to a simple straight wire system with a core wire and six outer wires.

In the work of Ghoreishi et al [84, 85] and Ramteke and Yenarkar [87], a simple straight wire rope (1+6) comprising six outer wires placed radially around a core wire was modelled using a finite element package. The system was subjected to axial loads in order to predict mechanical behaviour. Friction was not included in their analysis, but they suggested that it should be included in future work. Similar work was presented by Kastratovic and Vidanovic [88] and Shibu et al [89] but with a bonded contact and no separation.

Some researchers altered the size of the wires in order to minimise the effect of friction during the modelling. In the work of Gerdemeli et al [90] and Foti and Luca [91] it was ensured that the size of the core wire was larger than the outer wires in such a way that only frictional contact between the core wire and the outer wires existed. Coefficient of friction of 0.115 was used for the wires with modulus of elasticity of 188 GPa, and that no friction existed between the outer wires themselves.

Models of simple straight wire rope where friction was included between the wires during the simulation of axial loading were presented by Kastratovic and Vidanovic [92] and Imrak

and Erdonmez [93] and Erdonmez and Imrak [94] and Shi et al [95], with coefficient of friction values between 0.1 and 0.2 for wires and with modulus of elasticity in the range of 188 GPa and 190 GPa.

2.4 Summary

The study in this thesis focuses on the macroslip behaviour in multi-strand structure experiencing flexure loading. Here, the Coulomb model is adopted to represent friction as the damping is found to be independent of the frequency.

Most of the research shown in Section 2.1.1 that dealt with multi-strand beams neglected frictional effects. In the work presented in this thesis, the effects of friction are included in an analytical work in order to describe stiffness in the presence of friction.

It can be seen that the studies reviewed in Section 2.1.2 did not present effective methods to describe the frictional behaviour in multi-layered systems composed of steel bars or steel wires. In the study presented in this thesis, the frictional behaviour of multi-strand bars and wires and the frictional system stiffness are described with sufficient accuracy to be compared with quasi-static tests and numerical analyses.

Most studies of frictional behaviour between two mating cylinders shown in Section 2.1.3 depend on the Hertzian theorem for frictionless contact in their description of frictional behaviour and actual measurements for the contact area experiencing dry friction were not presented. In the work of this thesis, the analytical model used to describe the frictional behaviour of multi-strand bars and multi-strand wires counted for the real frictional contact area and was eliminated analytically.

In this thesis, the interfacial frictional behaviour between the mating strands was utilized to provide damping levels under different parametric characteristics. Similar behaviour regarding the effect of beam length and thickness on the loss factor that has been shown by other research in Section 2.2.1 is obtained and is presented in Chapters 3, 4 and 5. The analytical model presented in this thesis is purely analytical and does not depend on any experimental or numerical data to describe the damping behaviour in multi-strand systems. This model is ensured to be is simple and accurate, having taken into consideration many

parameters during model design. The results from the analytical model agree with the experimental and numerical results when compared together.

In the work of this thesis, the loss factor, the ratio of dissipated energy per cycle to the stored strain energy, is considered as indicator of the damping amount in the multi-strand system.

In this study, finite element models of the multi-strand beams and bars are used to simulate the flexural loading during frictional contact between all the strands involved in the system. These FE models are used to verify the analytical and experimental work to an extent because the finite element package has been not capable of obtaining solutions in the case of multi-strand bars and wires with large number of strands (nineteen strands and more) due to the complexity that the line-to-line contact, between the mating bars and wires, add to the solution process. This can be referred to the fact that for line-to-line contact, finite element package uses nodal detection scheme rather than Gauss integration points used in a surface-to-surface contact. Using nodes as contact detection technique can cause convergence complications such as node slipping in which the node slips off the edge of the targeted surface.

The aim of this study is to describe the frictional damping behaviour of multi-strand systems constructed from strands that have square and circular cross-sections.

The objectives of this study can be summarized as:

- Propose analytical models to estimate the frictional stiffness and damping in multi-strand systems such as multi-strand beams, diagonal multi-strand beams, multi-strand bars and multi-strand wires.
- Validate the analytical models through experimental and numerical studies at several different configurations and loadings.
- Investigate the effect of vibration on the damping levels in multi-strand systems.
- Examine the sensitivity of the obtained damping to parameters such as length, cross-section, clamp force, loading amplitude and number of strands.

Chapter 3

Modelling of damping behaviour for meso-scale multi-strand beams

3.1 Introduction

In this chapter, damping behaviour in systems comprising multi-strand square steel beams experiencing dry frictional behaviour at metal-to-metal surfaces is investigated numerically and analytically at the meso-scale.

Analytical models were built to describe the damping behaviour of multi-strand beams. These models are independent of both the experimental data and the numerical results. Instead, damping is estimated from the energy dissipated during cyclic loading by plotting the force-displacement curves.

The analytical modelling followed the numerical studies, the purpose being to validate the analytical work. For this reason, the specifications of the individual strands (width, thickness and height) are identified as described in the next section in order to expose the multi-strand beams to different loading levels and configurations (Table 3.1). The work in this chapter is followed by experimental work in the next chapter (Chapter 4) to compare the hysteresis loops for the different loadings and configurations obtained from the analytical, numerical and experimental work.

3.2   Description of the multi-strand beams

The multi-strand beam (MSB) used in this work is defined as a beam-like structure comprising individual strands. These strands considered were square cross-section, key steel beams. The length of each strand was 300 mm and they were constructed from BS4235 mild steel. A three-point bend configuration was adopted for the analysis and two span distances between the supports, 250 mm and 200 mm, were chosen. MSBs were constructed from four and nine individual strands. The overall cross-section of each MSB was set to have a square profile by placing the individual strands equally in the vertical and horizontal directions; therefore, nine-strand beams (see Figure 3.1) comprised three rows and three columns of individual strands. Individual strands with square cross-section of 3×3 mm and 4×4 mm were used and each MSB configuration, detailed in Table 3.1, was made up of strands with the same cross-section size. The method of choosing the values of the clamp forces and applied displacements used in Table 3.1 will be explained later in Sections 3.4.1 and 4.2.3 respectively.

Normal forces applied to surfaces that experience frictional contact are essential to create frictional forces; therefore, clamp forces were applied to the MSB during the analytical and numerical work. For the analytical work, the clamp force utilized to calculate the frictional stress was one of the requirements for the modelling process. For the numerical study, the clamp effect was applied as an equivalent pressure on the outer surfaces of the individual strands.
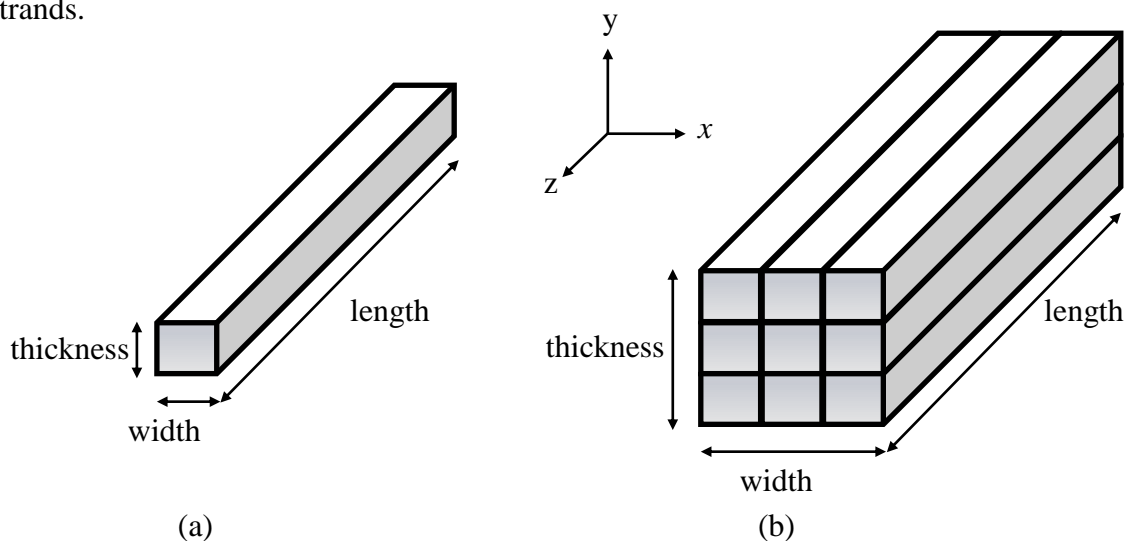
Figure 3.1 Geometric nomenclature for an (a) individual strand and (b) nine-strand beam

The MSB was subjected to flexural deformations and as the beam flexed, if the load was large enough, slip between individual strands occurred along the length of the beam. This is shown in Figure 3.2.
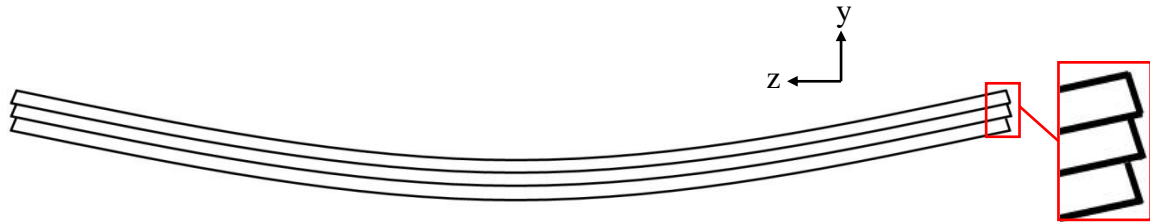
Figure 3.2 Typical multi-strand beam undergoing flexure (nine-strand beam system shown).

Table 3.1 Loading levels and configurations for the MSB

Test Configuration No	Span distance, mm	No of beams	Cross-Section size, mm	Clamping force, N	Peak displacement, mm×Sin(ωt)			
					1	1.7	2.5	1
sb01	250	4	3×3	100	✓	✓	✓	✓
sb02	250	4	3×3	190	✓	✓	✓	✓
sb03	250	4	3×3	250	✓	✓	✓	✓
sb04	250	4	4×4	100	✓	✓	✓	✓
sb05	250	4	4×4	190	✓	✓	✓	✓
sb06	250	4	4×4	250	✓	✓	✓	✓
sb07	250	9	3×3	100	✓	✓	✓	✓
sb08	250	9	3×3	190	✓	✓	✓	✓
sb09	250	9	3×3	250	✓	✓	✓	✓
sb10	250	9	4×4	100	✓	✓	✓	✓
sb11	250	9	4×4	190	✓	✓	✓	✓
sb12	250	9	4×4	250	✓	✓	✓	✓
sb13	200	4	3×3	100	✓	✓		✓
sb14	200	4	3×3	190	✓	✓		✓
sb15	200	4	3×3	250	✓	✓		✓
sb16	200	4	4×4	100	✓	✓		✓
sb17	200	4	4×4	190	✓	✓		✓
sb18	200	4	4×4	250	✓	✓		✓
sb19	200	9	3×3	100	✓	✓		✓
sb20	200	9	3×3	190	✓	✓		✓
sb21	200	9	3×3	250	✓	✓		✓
sb22	200	9	4×4	100	✓	✓		✓
sb23	200	9	4×4	190	✓	✓		✓
sb24	200	9	4×4	250	✓	✓		✓

3.3   Evaluating material properties

Knowledge of the modulus of elasticity and material density of the individual square key steel strands was considered of importance due to their influence on the dynamic behaviour of the MSB. At the same time, identification of these mechanical properties was one of the requirements for building the numerical and analytical models. As the beam strands were flat key steel, accurate information relating to the material properties was unavailable.

3.3.1   Measurement of density

In order to estimate the density, six strands (three with cross-section 3×3 mm and three with 4×4 mm) were weighed on electronic scales. Accurate dimensional measurements were made to calculate the volume and, using Equation 3.1, the average density was found to be approximately 7802 kg/m^3 for beams with 3×3 mm and 7808 kg/m^3 for beams with 4×4 mm.

$$m = \rho\,AL \qquad\qquad\qquad 3.1$$

where, m is the mass of a strand, ρ is the density, A the cross-sectional area and L is the free length. For simplicity, a common value of 7800 kg/m^3 was used in the subsequent work.

3.3.2   Measurement of Young's modulus from beam free vibration

Free vibration tests were carried out to estimate the natural frequency of the first vibration mode of a strand held in a cantilevered configuration. The Young's modulus was then obtained using the well-known natural frequency formula for Euler-Bernoulli beams with rectangular cross-sections.

Strands with cross-section size of 3×3 mm and 4×4 mm were used in the experiment. With both cross-section sizes, the free length of the strand was 212 mm. Each experiment was repeated five times for consistency and repeatability purposes. During the experiments, the strand was clamped at one end using a block and fasteners. Two torque values, 40 N.m and 50 N.m, were used on the fasteners and it was noticed that changing the torque values did not affect the results, which means that the clamp condition in the holder was acceptable. A Laser Optical Displacement Sensor (MicroEpsilon LD1605-10) with a sensitivity of 2 V/mm was used to read the displacement response. The sample rate on the data acquisition system was 50000 sample/sec and the duration of the signal was 1.8 sec (see Figure 3.3). To calculate the modulus of elasticity, Equation 3.2 was used [96].

$$f = \frac{\lambda^2}{2\pi L^2} \sqrt[2]{\frac{EI}{\rho A}}$$ 3.2

where, f is the frequency in Hz, λ is a dimensionless parameter (1.875 for the first mode of a clamped – free beam), I is the second moment of area.

The natural frequencies (ω_n) obtained from the experiments and their corresponding modulus of elasticity values (E) are shown in Table 3.2. Noting that the scatter in the results was relatively small, the average values for the modulus of elasticity taken forward from this work were 180 GPa for the 3×3 mm strands and 190 GPa for the 4×4 mm strands. This enabled the assignment to reflect better representation for the material properties, especially at the numeric and mathematic stages. Although the tested values of modulus of elasticity for each cross-section (Table 3.2) are considered repeatable however the modulus of elasticity for the 3×3 mm strands differed from those for the 4×4 mm strands. The reason of obtaining different values of the modulus of elasticity for different cross-sections might be because of the manufacturing process and the cutting technique used to prepare these key steel strands was different between these cross-sections which resulted in different levels of residual stresses in the material.
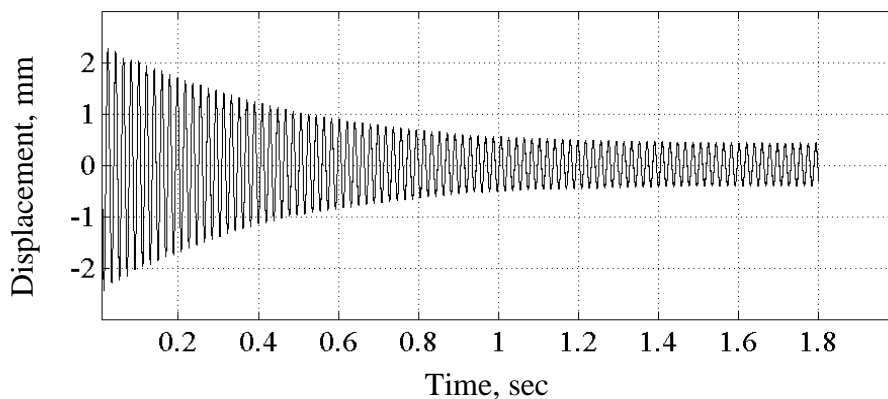
Figure 3.3 Time domain free decay signal for a 3×3×212 mm beam.

Table 3.2 Material properties obtained experimentally for strands with dimensions of
3×3×212 mm and 4×4×212 mm

	strands of dimensions 3×3×212 mm		strands of dimensions 4×4×212 mm	
	f, Hz	E, GPa	f, Hz	E, GPa
	51.90	180.6	71.07	190.5
	51.82	180.0	71.24	191.4
	51.69	179.1	70.93	189.7
	51.88	180.5	71.15	190.9
	51.72	179.3	71.00	190.1
Average	51.80	179.9	71.07	190.5
Standard deviation	0.093	0.681	0.121	0.664

3.4 Friction estimation experiments

Friction is typically classified as lubricated friction, dry friction, fluid friction or internal friction. Lubricated friction exists when a lubricant is present between the mating surfaces, whereas dry friction occurs if there is no lubricant. Fluid friction is the motion resistance between the layers of a viscous fluid. The resistance to the deformations between the material particles at the molecular level is called internal friction. This study considers only dry friction that occurs between the strands of a multi-strand beam.

Several models have been built and developed in order to describe the frictional behaviour between two surfaces in contact as shown in Chapter 2. Some of these models count for the static behaviour of the contact condition as Coulomb friction models and others count for the dynamic behaviour in the contact region, such as the Dahl model, Bristle model and LuGre model. In the Coulomb friction model, only the direction of the velocity is taken into account and is independent of the area of the contact. The Coulomb friction model assumes that the friction force opposes the direction of the relative motion and is dependent on the amount of normal force, which is perpendicular to the shear force direction. Dynamic friction models are used to identify the value of the friction amount between the two surfaces in contact. For instance, in a steady-state condition, the Dahl friction model would take exactly the same form as the Coulomb friction model.

Specifically, for a multi-layer beam, the above models showed similar trends in terms of the resulting waveforms when subjected to a free vibration excitation as shown in the work presented by Lord [97] therefore, the Coulomb friction model is adopted for numerical and analytical models presented here and henceforth. The Coulomb friction model is presented as

$$F_d = F_c \mu \operatorname{sgn}(v)$$ 3.3

where, F_d is the frictional force, F_c is the normal force, μ is the coefficient of friction which is a ratio between the frictional force and the normal force and sgn(v) is the sign of the velocity which is considered a signum function to identify the direction of the frictional force as

$$\operatorname{sgn}(v) = \begin{cases} -1, & v > 0 \\ 0, & v = 0 \\ +1, & v < 0 \end{cases}$$ 3.4

This section describes free vibration tests conducted to estimate the coefficient of friction between the steel strands used in this work. This includes experiments to calibrate the normal force values that were applied to the specimens during the friction experiments.

3.4.1 Torque-force calibration for clamps

The normal (clamping) force, or pressure, in any frictional system has a significant effect on the magnitude of the frictional forces, see Equation 3.3, and hence the amount of energy that can be dissipated. For this reason, it was important to use a repeatable and accurate method to apply the normal force. As the experimental work described in Chapter 4 would require the strands to be clamped together during the flexural experiments, the same type of clamps and fasteners were used during the friction measurements. The clamp set comprised two halves, each of which had a circular cross-section that was attached to the load cell, while the opposite face of the clamp was flat to accept fasteners that connected the two clamp halves together.

The clamping force was applied as a torque to the two fasteners connecting the clamp halves. It was assumed that the clamping force could be set by altering the torque applied to the fasteners. A test rig (see Figure 3.4) was used to measure the force from the applied torque. The test setup contained a load cell (Loadstar Sensor MFD-050-100) sandwiched between a

pair of clamps. Various levels of torque were applied to the clamp's two fasteners, and the resulting equivalent force was measured. The tests were repeated five times and the average force for each torque level was taken as the nominal value for subsequent work. The results of the torque-load calibration experiments are shown in Figure 3.5. Note that the torque values quoted were those applied directly to each fastener. List of the torque values and the equivalent reaction force is presented in Appendix A.
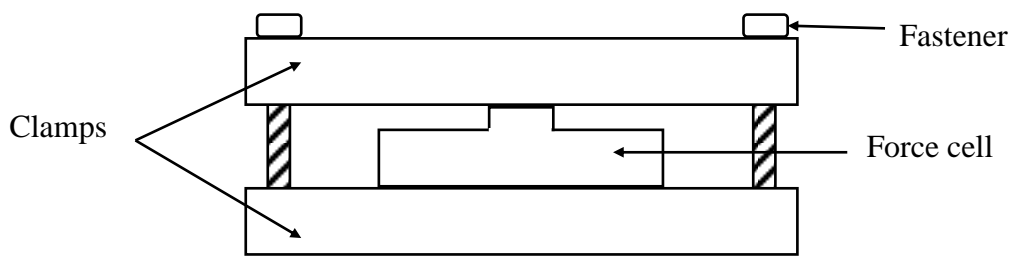
Figure 3.4 Normal force calibration test rig
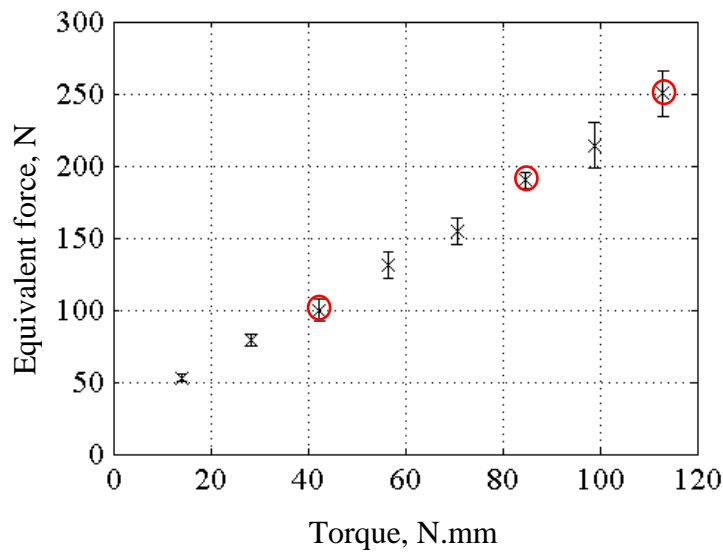
Figure 3.5 Equivalent clamping force values, red circles indicate the clamp forces used in the tests (error bars show one standard deviation)

3.4.2 Coefficient of friction experiments

This section describes static and dynamic experiments conducted to estimate the coefficient of friction values.

It was shown in Section 3.3 that material properties differed somewhat for the two strand types. It was also assumed that friction between the strands could differ and hence the static test was performed on both sizes of strands with cross-section of 3×3 mm and 4×4 mm. The length of the strands was 300 mm. The static test (referred to here as the tilt test) involved attaching one strand to a surface and a laying second strand on top of it. The surface was gradually tilted from one end until the upper strand started moving. Figure 3.6 shows the setup of the tilt test. At the tilt position where slide commences, the vertical height (y projection) and the horizontal width (x projection) were measured to calculate the angle of the inclination. Finally, the coefficient of friction was calculated from the tangent of the inclination angle. A different upper beam was used in each of the five trials conducted, while the lower beam was kept unchanged. The coefficient of friction values that were estimated by the tilt test were considered as static coefficients of friction.

Table 3.3 shows the estimated coefficient of friction values for strands of both cross-section sizes, 3×3 mm and 4×4 mm. The average values for the coefficient of friction were 0.24 and 0.33 for the strands with cross-section size of 3×3 mm and 4×4 mm respectively.
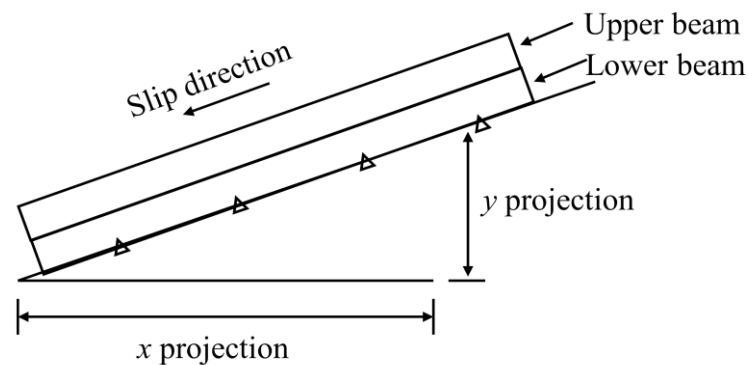
Figure 3.6 Setup of the tilt test

Table 3.3 Estimation of the coefficient of friction values obtained from the tilt test for strands with cross-section of 3×3 mm and 4×4 mm

Trials	Cross-section of 3×3 mm			Cross-section of 4×4 mm		
	x proj.	y proj.	μ	x proj.	y proj.	μ
1	150	32.0	0.21	150	50.0	0.33
2	150	42.0	0.28	150	52.0	0.34
3	150	33.0	0.22	150	45.0	0.30
4	150	37.0	0.24	150	53.0	0.35
5	150	40.0	0.26	150	51.0	0.34
Average			0.24			0.33
Standard deviation			0.02			0.01

Experiments were also carried out to measure friction during dynamic loading. Testing was conducted on the 4×4 mm strand interfaces using a modified version of Lord's base-excited, single degree-of-freedom oscillator test rig [97] that is shown in Figure 3.7b. The oscillator is formed from a mass block and a linear spring that sit within the rig frame through which base motion is applied. The test interfaces are constructed from two pairs of pads, each of which are segments cut from the key steel strands with cross-section of 4×4 mm. In this work, the length of the pads that were attached to the test rig was 15 mm and the length of the pads that were attached to the mass was 35 mm. The general methodology of the experiment was to provide a pulse excitation to the base of the test rig and to then let the resulting motion decay freely. Then, the difference between any two subsequent peaks in the relative displacement signal between the test rig body and the mass was used to estimate the coefficient of friction. The instrumental setup for the experiment is shown in Figure 3.7a.
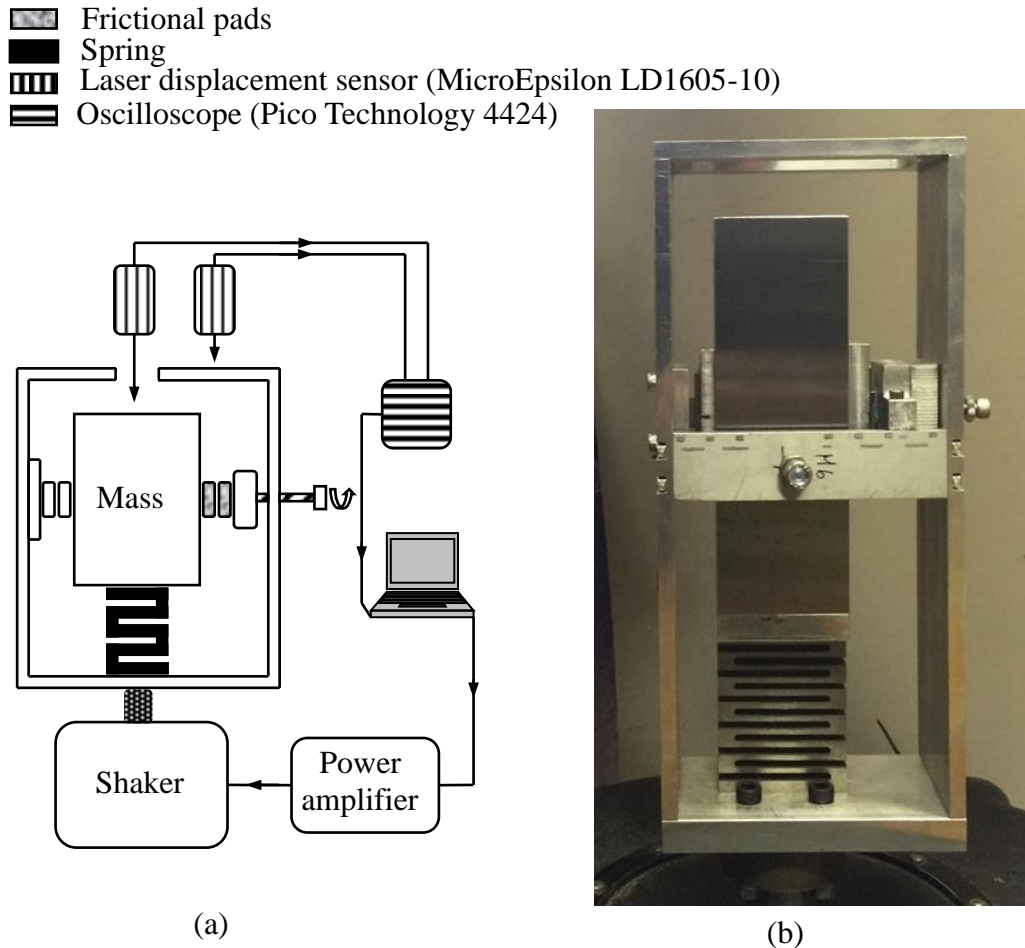
Figure 3.7 Friction experiment showing (a) instrumentation layout and (b)the test rig

The attachment process was conducted carefully to ensure that there would be no unexpected movement of the pads during the experiment: first, interfacial groove seats were machined where the pads attached to both the test rig body and the mass; second, ceramic strain gauge adhesive was used to fix the pads into their positions. The length and width of the grooves were such that the pads would not move once they were fitted.

The mass was maintained in the centre of the test rig by the linear spring attached to the base of the mass and also by the frictional pairs on both sides of the mass. A fastener (M6) was attached to the side of the test rig body through a threaded hole with an open end to the outer frictional pad. The fastener was exposed to various levels of clamp force. The clamp force was applied in the shape of a torque on the fastener, causing the fastener in turn to press the outer frictional pad towards the other mating pad. As this connection was the same as that

used in the clamps discussed in Section 3.4.1, the clamp forces were estimated from the torque applied to the fastener. Forces were therefore obtained using Figure 3.5 although the actual force values had to be halved because the data shown in Appendix A involved two fasteners being loaded simultaneously, while in the coefficient of friction experiment only one fastener was used to clamp the pads. Clamp torques of 14.1 N.mm, 28.2 N.mm, 42.3 N.mm, 56.5 N.mm and 70.6 N.mm were applied to the fastener to produce applied clamping forces of 27 N, 40 N, 50 N, 65 N and 78 N respectively to the mild key steel pads. For each clamping force level, the relative displacement signal was recorded and analysed.

A half sine signal of a frequency 20 Hz was generated through the software Audacity and transferred from the sound card of the PC into the power amplifier (1000VA capacity). The signal was used to excite the test rig through the use of an electrodynamic shaker with peak force capacity of 500 N (Ling Dynamic Systems V455) attached to the base of the test rig. As the test rig was excited, two laser displacement sensors were used to measure the displacements of the test rig body and the mass respectively. The resulting displacement signals were acquired using a digital oscilloscope (Pico Technology 4424) operating at a sample rate of 14000 sample/sec. Relative displacement between the mass and the base was then calculated as the difference between the two displacement signals.

The Coulomb friction model assumes that the friction force is independent of the velocity and that the friction force opposes the velocity direction as shown in Equation 3.4 and hence the sign of the friction force changes every half cycle. When undergoing free vibration, the energy lost by the system over one half-cycle can be obtained from the difference in strain energy (stored in the spring) at the two extreme displacement points where the velocity is zero. The dissipated energy is equal to the work done by the friction force [98] as

$$\frac{1}{2}K(X_i^2 - X_{-i}^2) = F_d(X_i + X_{-i}) \qquad\qquad 3.5$$

where, K is the system stiffness, X_i is the maximum amplitude when the velocity is zero, X_{-i} is the decayed amplitude at the end of the half cycle and F_d is the frictional force.

Rearranging Equation 3.5 in terms of the amplitude decrease over a half cycle,

$$(X_i - X_{-i}) = \frac{2F_d}{K}. \qquad\qquad 3.6$$

Then the amplitude reduction for a whole cycle is given by

$$(X_i - X_{i+1}) = \frac{4F_d}{K} \qquad\qquad 3.7$$

where, X_{i+1} is the amplitude of the next cycle.

Noting that in this experiment, two interface pairs act in parallel, substitution of Equation 3.3 into Equation 3.7 results in,

$$\mu = \frac{K(X_i - X_{i+1})}{4F_c n} \qquad\qquad 3.8$$

where, n is the number of the surfaces which are in contact and F_c is the normal force.

The total mass of the moving parts in the test rig was 2.415 kg including the mass block and the fasteners used to attach these parts together. Using the relationship of the natural frequency to the stiffness and the mass, the stiffness of the spring in this test rig was 37.8 N/mm.

A typical result is shown is Figure 3.8. The apparent distortion of the signals when they exceeded +1 mm was caused by the range limit on the lasers rather than by a physical effect. Where this occurred, the "negative peaks" (extreme values below 0 mm) were used instead. The difference between two peaks in the relative displacements for different clamping force levels is shown in Table 3.4.
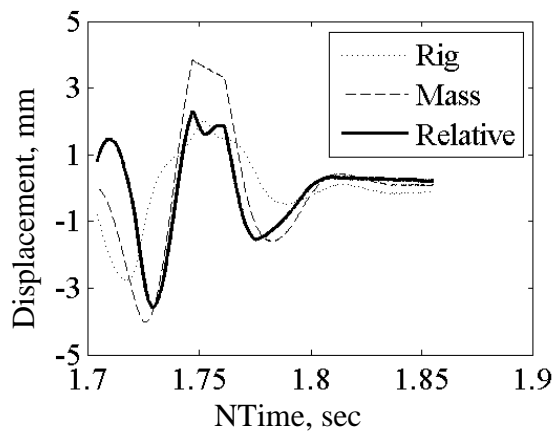
Figure 3.8 The test rig, mass block and relative displacement unfiltered signals with clamp force of 26.5 N are shown

Table 3.4 The difference between two subsequent peaks in the relative displacement signals
for different clamp forces

Clamp force, N	Selected peak, mm	Following peak, mm	Difference between two peaks (x_i-x_{i+1}), mm	μ
26.5	3.07	1.61	1.46	0.26
39.5	2.55	0.35	2.20	0.26
46.0	2.51	0.16	2.35	0.23
64.6	3.28	0.11	3.17	0.23
77.5	5.05	0.80	4.25	0.26

From Table 3.4 it can be seen that the average coefficient of friction obtained from the dynamic tests on the 4×4 mm strands was approximately 0.25. The static coefficient of friction values from the tilt test for the same strand cross-section were around 0.33. This reduction of around 24% from static to dynamic behaviour is as expected. While dynamic testing was not carried out for the 3×3 mm strands, assuming the same ratio between static and dynamic coefficients of friction would give a dynamic friction coefficient value of 0.18.

3.5   Quasi-static numerical analyses

Finite element (FE) models are used to simulate the response of the multi-strand beams that were defined in Table 3.1. Quasi-static force or quasi-static displacement means that the change of the force or displacement with time is very slow. This variation should be much less than the value of the first natural frequency of the system to which the force or displacement is applied to. It also may mean that, the system can be analysed as several static states and the change in the force or displacement will not affect the dynamic characteristics of the system.

The coefficient of friction used at the interfacial surfaces was 0.25 and 0.18 for the multi-strand beams of cross-section size 4×4 mm and 3×3 mm respectively and the equivalent modulus of elasticity was 190 GPa and 180 GPa. The selection of these values was based on the experimental results obtained from Section 3.3 and Section 3.4. Each configuration was constrained and loaded as a beam subjected to three-point flexure with a sinusoidal displacement loading. The FE models were constructed using ANSYS and involved 20 node brick elements for the body representation and the contact pairs represented using 3-D, 8

node surface-surface contact (CONTA174) and 3-D, target segment (TARGE170). A Coulomb friction model was used where sliding occurs if the tangential force exceeds the limiting force defined as the product of normal force and coefficient of friction. The number of potential slip zones meant that convergence was not easily achieved. To help with this, an augmented Lagrange contact formulation was used along with a contact stiffness factor of 0.075. The element size was decided to be 2.0 mm for strands of cross-section 4×4 mm and 1.5 mm for strands with cross-section of 3×3 mm. The selection of the element size was based on a mesh density study performed on Configuration sb06. Two factors were considered, the first was the consistency of the predicted forcing value and the second was the computational expense − see Figure 3.10a and Figure 3.10b. The validation study is presented in Figure 3.9 and it is clear that the element size of 2.0 mm should not affect the accuracy of the numerical analyses. The element size for strands with cross-section of 3×3 mm was reduced to 1.5 mm to provide suitable meshing as this number is the half of the cross-section sides.
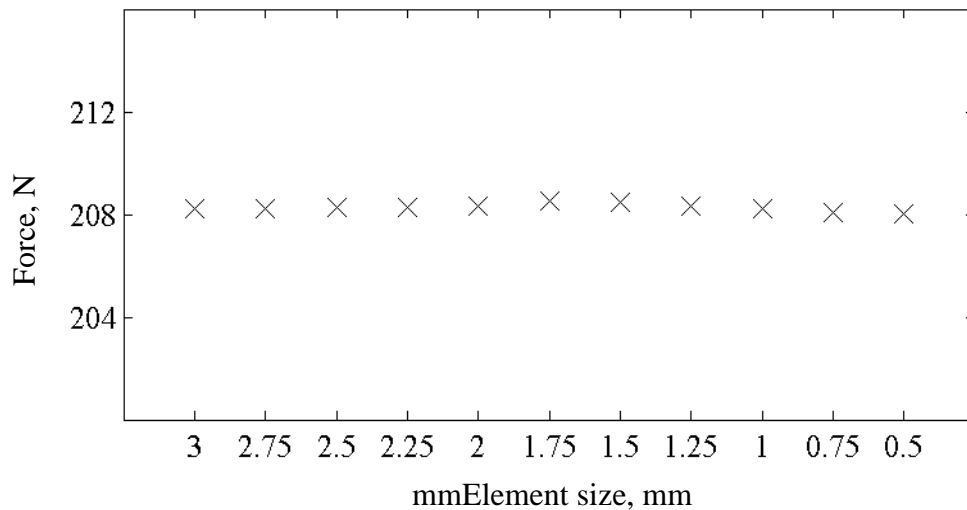
Figure 3.9 Validation of the Element size

It is worth to mention here that during the mesh density study, the contact status was assumed bonded for the ease of the simulation as this condition was considered not to affect the validation process. The model was subjected to a ramp displacement loading of 1.0 mm during the validation study.

(a)

(b)
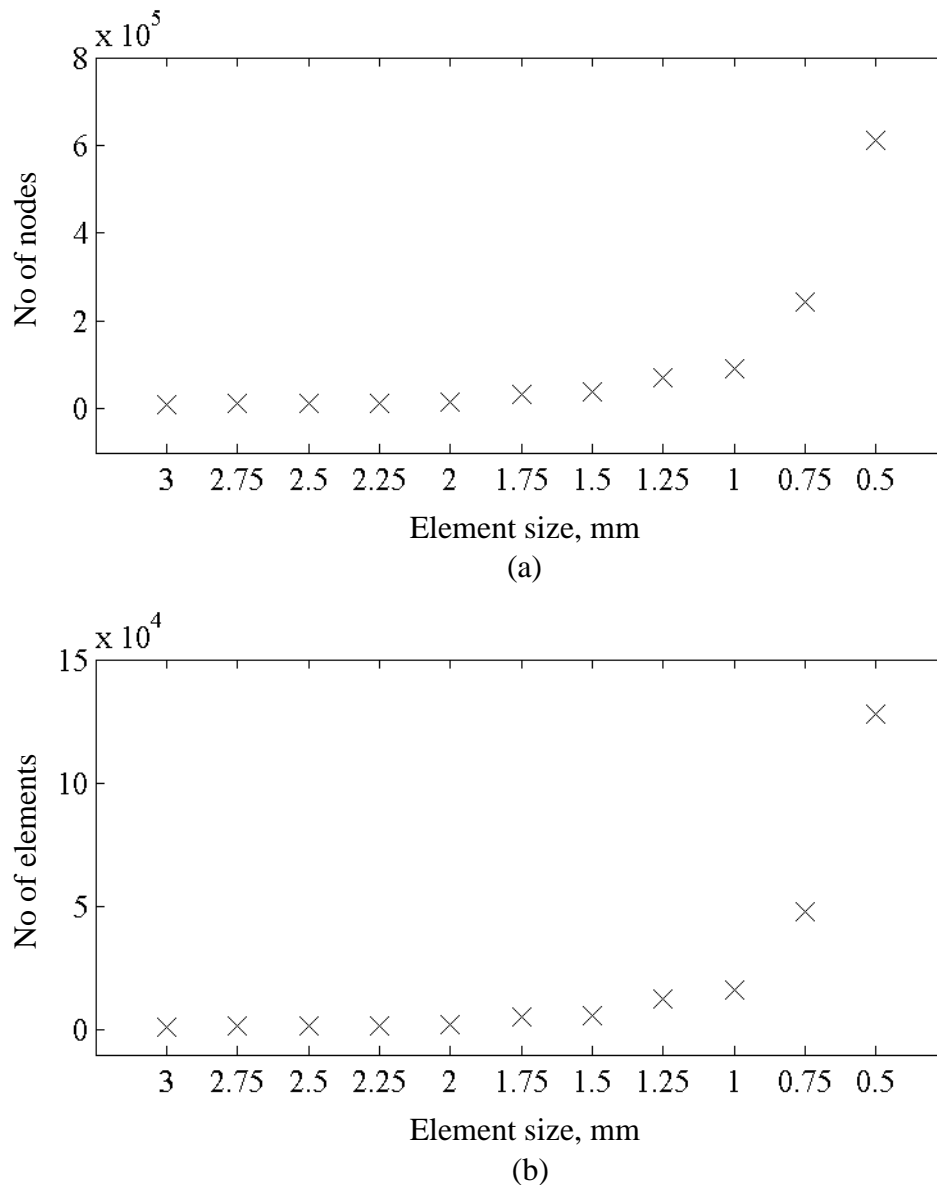
Figure 3.10 Effect of element size on the number of (a) nodes and (b) elements – showing FE statistics of Configuration sb06

Table 3.5 displays information about of the FE models used to simulate Configurations sb01 through sb24. The deformed FE models for Configurations sb06 and sb12 are shown in Figure 3.11. The clamp effect was simulated as a distributed pressure on the outer surfaces of the multi-strand beam. Loading was applied at the middle of the beam as a prescribed sinusoidal displacement with a frequency of 1 Hz. The response was calculated using 150 substeps involving the implicit iterative solver built into the FE software. The simulated

force-displacement hysteresis loops for Configurations sb06, sb12, sb18 and sb24 are presented in Figure 3.12.

Table 3.5 Statistic data of the FE models for Configurations sb01 through sb24

Configuration	No of strands	Length, mm	cross-section, mm	Element size, mm	No of nodes	No of elements
sb01-sb03	4	250	3×3	1.5	15204	2016
sb04-sb06	4	250	4×4	2	15204	2016
sb07-sb09	9	250	3×3	1.5	34209	4536
sb10-sb12	9	250	4×4	2	34209	4536
sb13-sb15	4	200	3×3	1.5	12084	1600
sb16-sb18	4	200	4×4	2	12084	1600
sb19-sb21	9	200	3×3	1.5	27189	3600
sb22-sb24	9	200	4×4	2	27189	3600

(a)

(b)
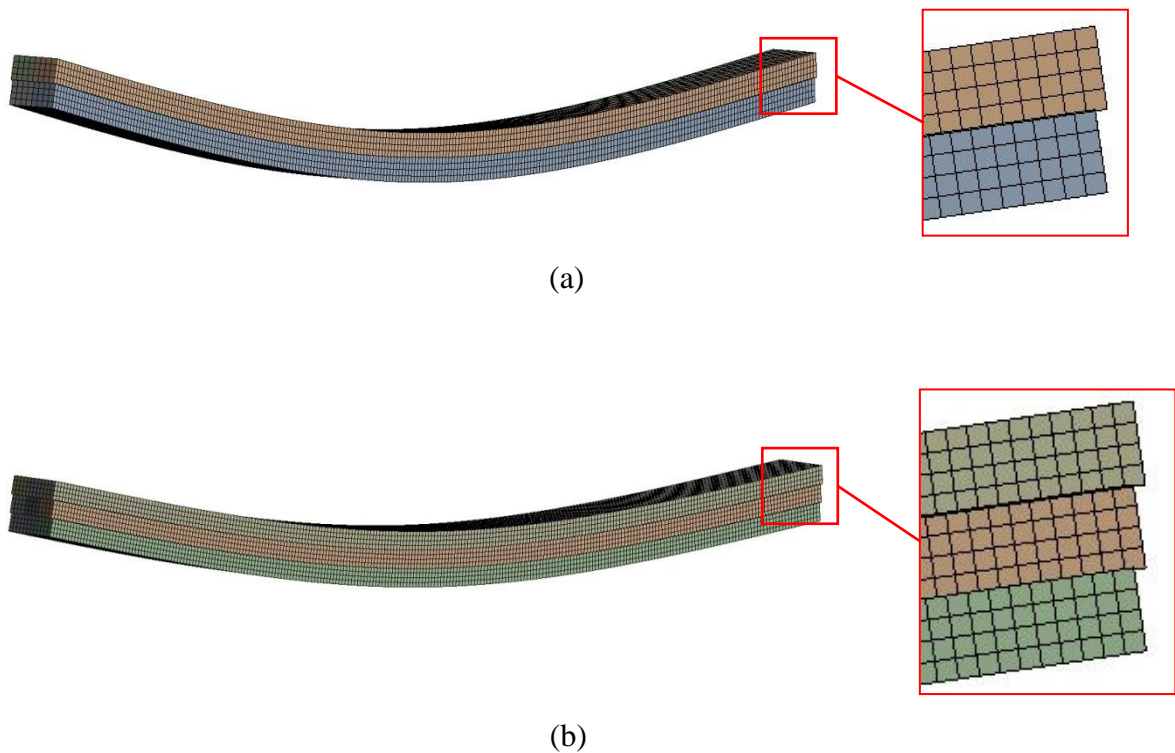
Figure 3.11 Flexural deformation of the FE models for Configurations (a) sb06 and (b) sb12
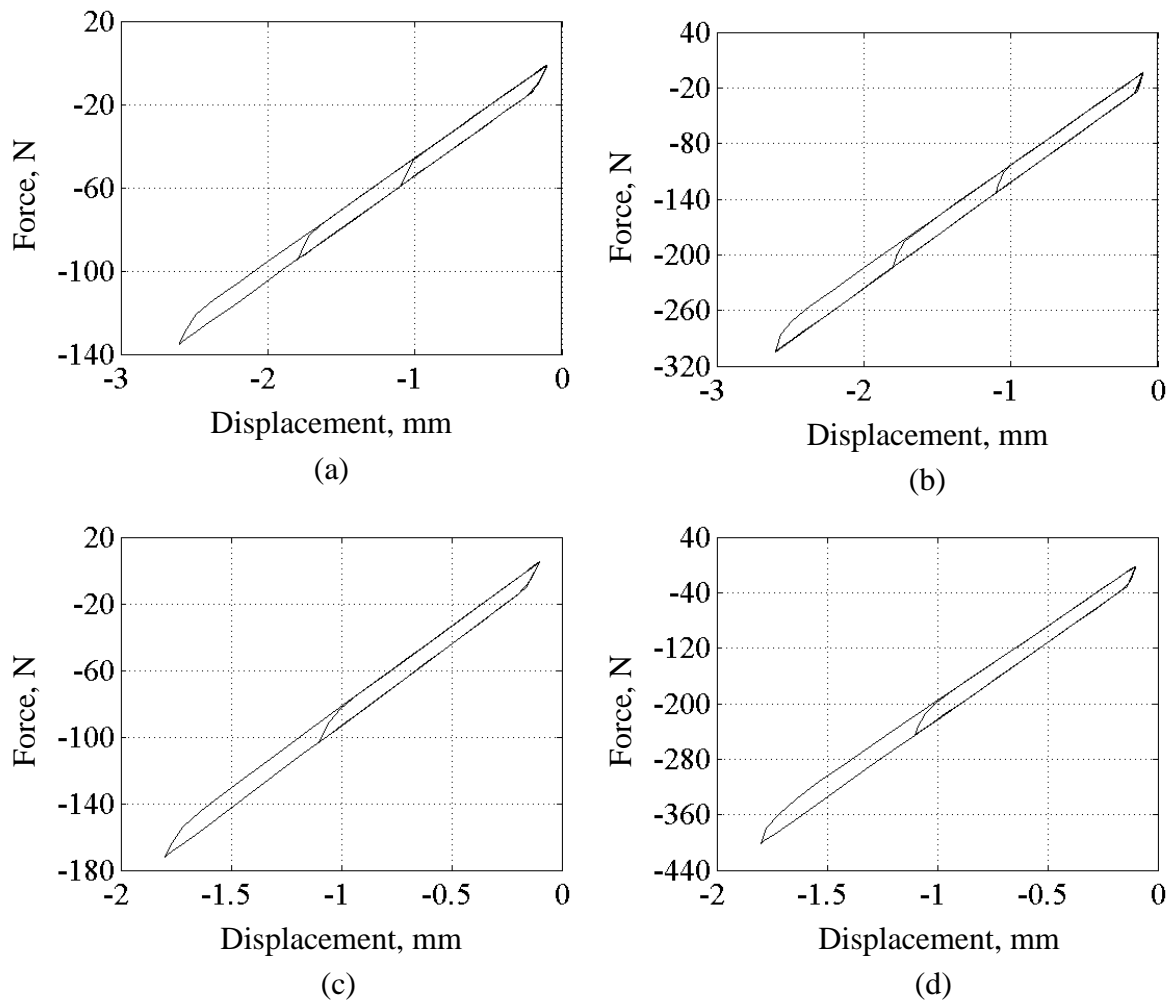
Figure 3.12 Numerical hysteresis loops at different displacement loading levels for Configurations (a) sb06, (b) sb12, (c) sb18 and (d) sb24

3.6 Analytical modelling

The system considered in this section consisted of multi-strand beams undergoing flexural deformations and experiencing frictional contact between the mating strands, with each strand being a perfect Euler-Bernoulli beam. The analytical model developed in this section takes into account the frictional effects by introducing them directly into the system stiffness. The interfaces of the strands are allowed to slide against each other once the friction force at the interface is exceeded. This results in a reduction of stiffness for the system.

3.6.1 The frictional second moment of area

The flexural stiffness of a multi-strand beam (MSB) can be represented using the frictional second moment of area. The term "frictional second moment of area" in this work refers to an effective second moment of area that accounts for friction-dependent slip and stick in an MSB such that it can be treated as a Euler-Bernoulli beam. When the contact between strands is either bonded or frictionless, the second moment of area can be calculated using the parallel axis theorem,

$$I = \sum_{n=1}^{N} (I_0 + Ad^2)_n \qquad 3.9$$

where I is the second moment of area for the system, I_0 is the second moment of area for an individual strand, A *is* the cross-section area, N is the number of strands and d is neutral axis that it deforms around.

When the bond between the strands is perfect, d is the distance from the centroid of the strands to the centroid of the beam, where the neutral axis is located. For a frictionless contact, d is equal to zero (as shown in Figure 3.13b) as each strand flexes around its own neutral axis. The absence of friction decouples the axial stretching of strands and hence two separate systems. In a frictional case, the transfer distance (d) increases as the coefficient of friction μ, increases as shown in Figure 3.13c.

This section introduces an analytical method used to predict the frictional second moment of area at any magnitude of μ up to the limiting of the equivalent of the strands being bonded. This was achieved firstly by estimating the deformation relationship, over a range of μ magnitudes, extending from frictionless contact to bonded contact. Second, the estimated deformation magnitudes were used to predict the frictional second moment of area at any specific μ magnitude.
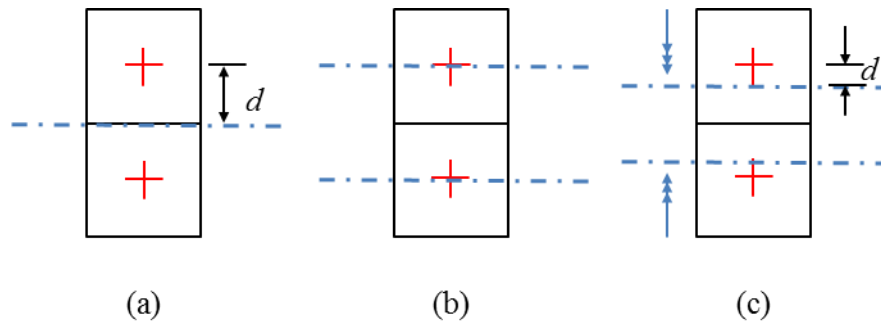
Figure 3.13 Transfer distance, d, for strands that are (a) bonded, (b) frictionless, and (c) frictional – dashed lines represent the neutral axes

To provide upper and lower bounds for the frictional second moment of area, two cases were considered: perfectly bonded strands and strands with frictionless contact. Equation 3.10 was used to calculate the second moment of area for a system with frictionless contact

$$I_{frictionless} = \frac{Nbh^3}{12}$$ 3.10

where N is the number of strands involved in the system, b and h are the cross-section dimensions of the individual strands. The total deformation in a frictionless system for a simply supported beam is,

$$\delta_{frictionless} = \frac{Fl^3}{48EI_{frictionless}}$$ 3.11

where E is the modulus of elasticity, l is the span distance, and F is the applied force at the centre of the multi-strand beam. For the bonded case, the second moment of area can be calculated from,

$$I_{bond} = \frac{N_y b (N_y h)^3}{12}$$ 3.12

where N_y is the number of strands in the vertical direction. The total deformation can be calculated by

$$\delta_{bond} = \frac{Fl^3}{48EI_{bond}}.$$ 3.13

A multi-strand beam contains many interfaces along which slip can occur. The basic assumption made in developing this model is that an interface will remain stuck as long as the magnitude of the shear stress at the interface is less than the frictional stress. Therefore, the last moment that the interface is considered stuck is when the shear stress (τ_w) induced by the applied load, equals the frictional stress.

$$\tau_w = \sigma_{fri}. \qquad\qquad 3.14$$

The frictional stress can be expressed as

$$\sigma_{fri} = \frac{F_c \mu_w}{A_w} \qquad\qquad 3.15$$

where, F_c is the clamping force, μ_w is the coefficient of friction at the interface, A_w is the area of the interface. The expression for shear stress in a rectangular beam [99], with simply supported boundary conditions, can be written as,

$$\tau_w = \frac{F}{4I}((y_t)^2 - (y_t - y_w)^2) \qquad\qquad 3.16$$

Where τ_w, is the shear stress at the interface, F is the force applied to the system, y_t is the location of the geometric centroid of the multi-strand beam and is expressed as

$$y_t = \sum_{n=1}^{N_y} \frac{t_n}{2} \qquad\qquad 3.17$$

where, N_y is the number of the strands in the vertical direction and y_w is the thickness of the strands involved in the slip and is described as

$$y_w = \sum_{n=1}^{w} t_n. \qquad\qquad 3.18$$

where, w is the number of strand involved in the slip. For given loading therefore, the coefficient of friction at the critical condition can be obtained by substituting Equations 3.15 and 3.16 into 3.14, to get,

$$\mu = \frac{F N_y A_w}{4I_{bond} F_c} \left[(y_t)^2 - (y_t - y_w)^2 \right] \qquad\qquad 3.19$$

Thus, for a given applied load, the deflection under frictionless conditions is given by Equation 3.11. The deflection where strands remain stuck together is given by Equation 3.13 and the corresponding minimum coefficient of friction is given by Equation 3.19.

For each interface of interest, the analytical model is used to find two key points in the load-deflection behaviour. The first is the point at which slip begins and the second is when the maximum load is reached. These points are represented graphically in Figure 3.15 as points 1 and 2 respectively.
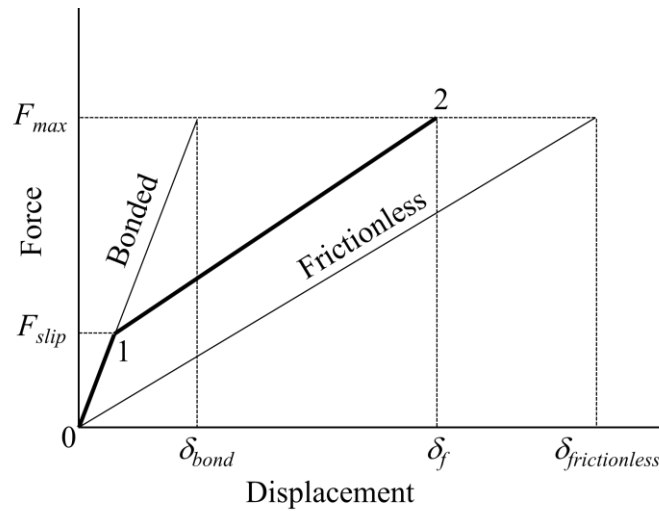
Figure 3.14 Key points on the force-displacement plot for the analytical model

For a given coefficient of friction, F_{slip} for any interface can be obtained by rearranging Equation 3.19. The corresponding displacement (at point 1) can be obtained by substituting this force value in Equation 3.13.

To obtain the δ_f, the displacement under sliding friction at maximum force (point 2), the assumption is made that its position between the bonded and frictionless cases (shown in Figure 3.14) is linearly related to the coefficient of friction. Figure 3.15 shows the relationships between the displacement (δ) and the coefficient of friction (μ) for Configurations sb01 to sb06 that are obtained using this approach. Equivalent results for Configurations sb07 to sb24 are presented in Appendix B. Note that the left end of each line represents the frictionless case (at displacement $\delta_{frictionless}$) while the right end, represents the limiting bonded condition (at displacement δ_{bond}). The value of δ_f is defined by the value of each of these lines at the friction coefficient of interest.
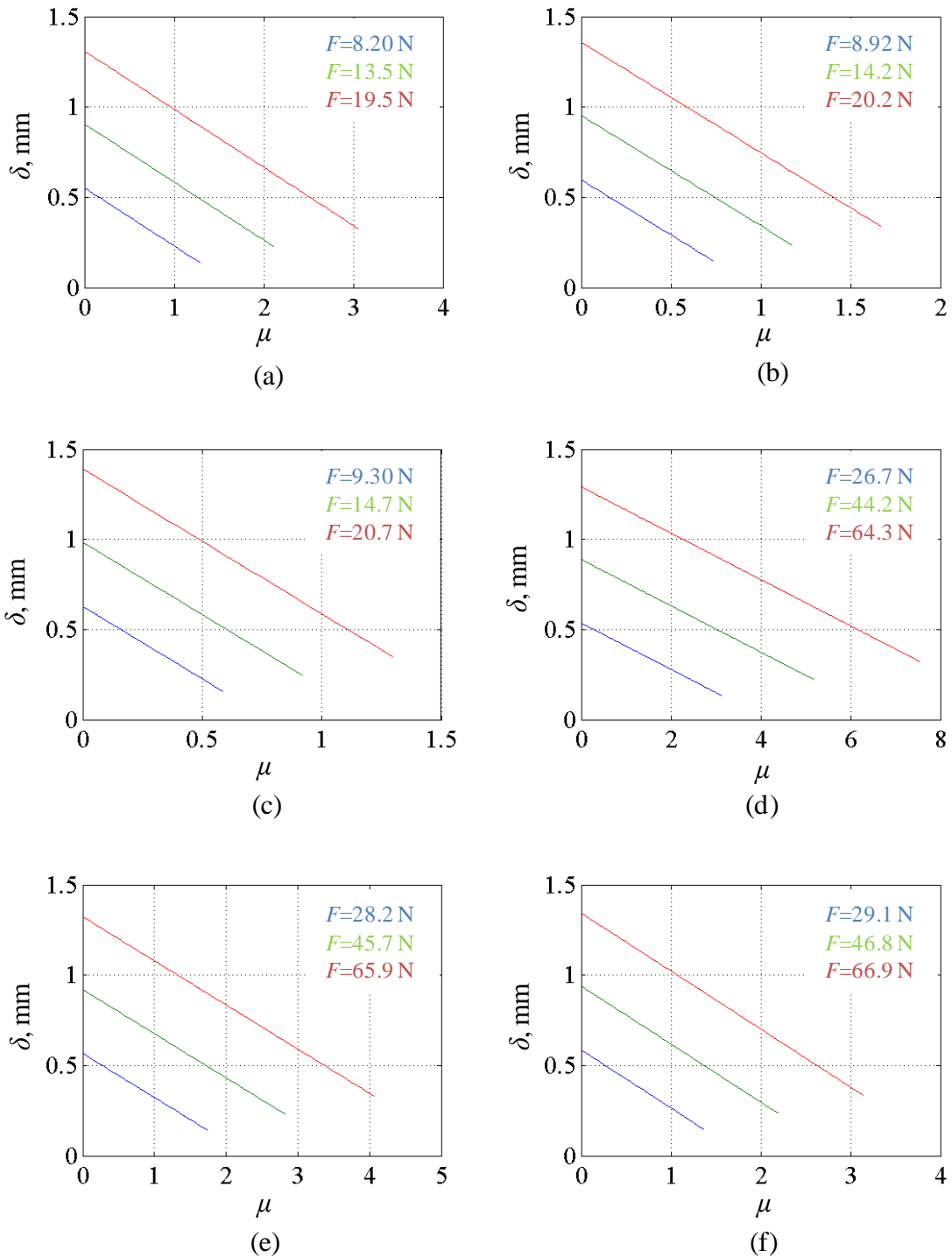
Figure 3.15 Deformations versus coefficient of friction for Configurations (a) sb01 through (f) sb06 respectively

51

It was crucial to investigate the validity of the linear relationship between the displacement and μ, therefore, a finite element model (described in Section 3.5) was built for Configuration sb06 to compare with the analytically predictions. Results from the two approaches, for an applied load of 29.1 N, is depicted in Figure 3.16. From the FE result, it can be seen that the relationship is approximately linear, hence the assumption used in the analytical model can be considered acceptable.
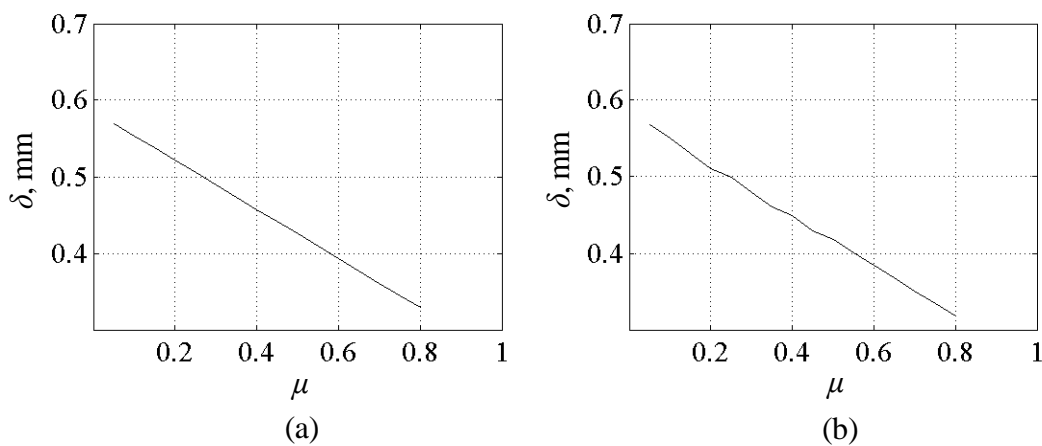
Figure 3.16 Deformation versus coefficient of friction for (a) analytical model and (b) FE model – Configuration sb06 is shown

It is often convenient to obtain a linear approximation of the stiffness of a system. The analytical model allows this by using the concept of the frictional second moment of area I_f which has a similar form to the bonded and frictionless cases, hence,

$$I_f = \frac{Fl^3}{48E\delta}.$$ 3.20

For a given maximum applied force therefore, the linear approximation can therefore be made the desired friction condition – as indicated in Figure 3.17.
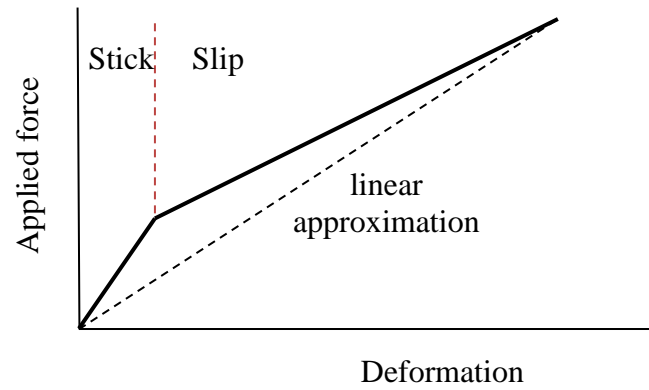
Figure 3.17 Effect of applied load intensity on the system stiffness

Figure 3.18 depicts this second moment of area Configurations sb01 to sb06 under different loading conditions.
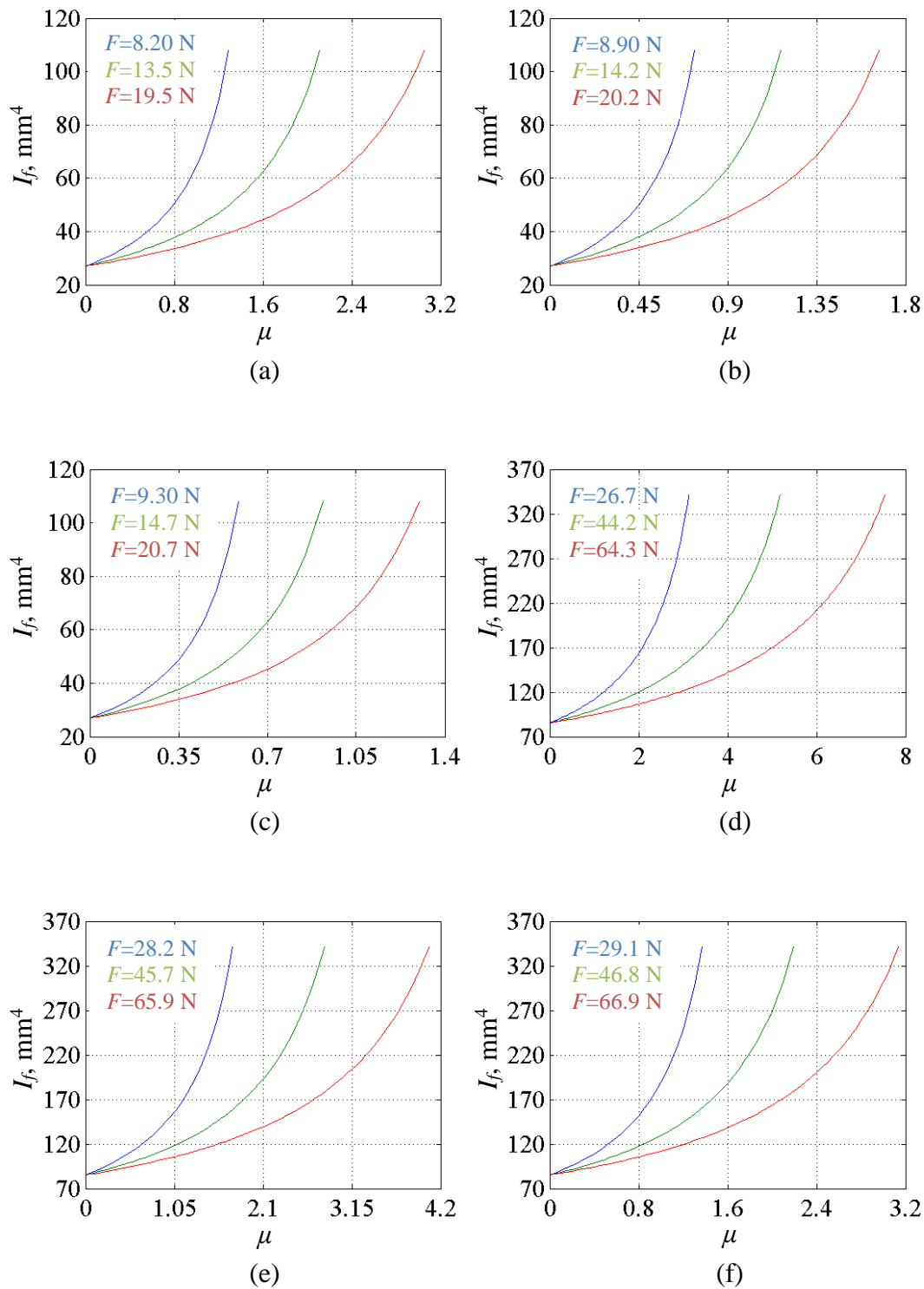
Figure 3.18 Second moment of area versus coefficient of friction for Configurations (a) sb01 through (f) sb06 respectively

The frictional second moment of area for Configurations sb07 to sb24 are presented in Appendix C.

54

3.6.2 Frictional second moment of area – finite element analysis

Finite element (FE) models were used to investigate the significance of local stretching (resulting in microslip) for this type of system. Typical load-deflection behaviour is shown in Figure 3.19 where it can be seen that there is little evidence of significant microslip.
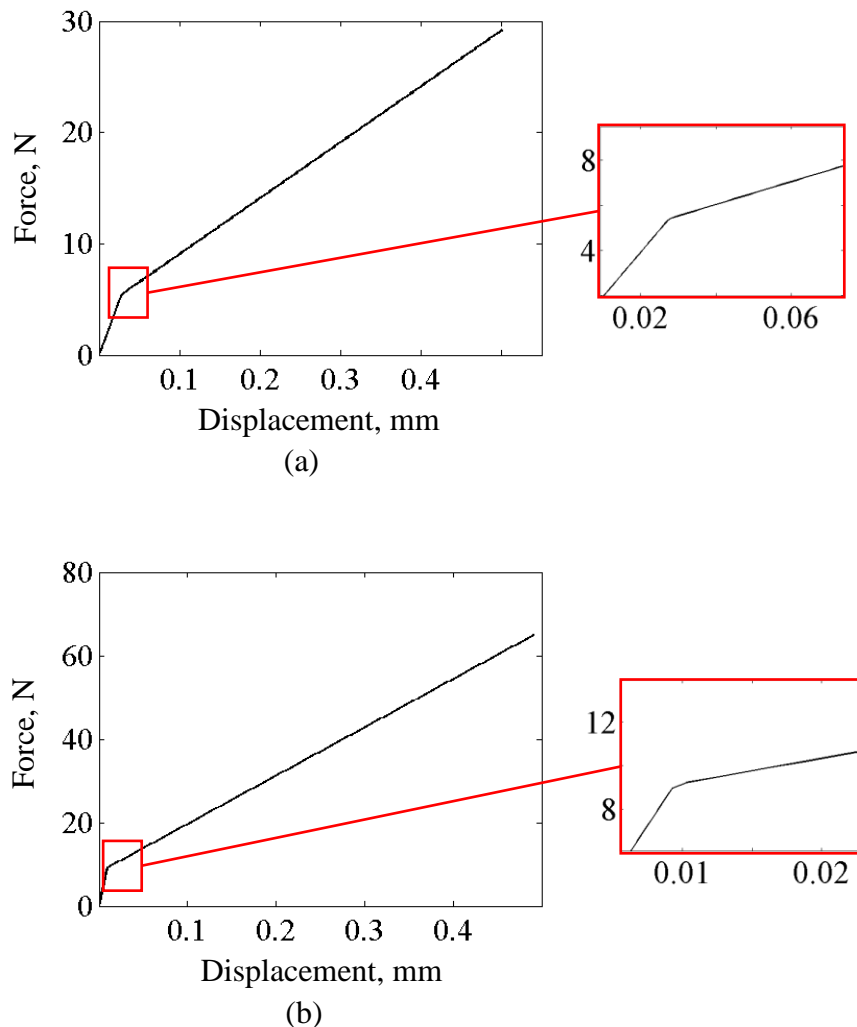
Figure 3.19 Microslip region (red boxes indicate upper and lower bounds) of the multi-strand beams for (a) sb06 and (b) sb12

The sensitivity of the frictional second moment of area to the applied force was also investigated. This was calculated by substituting the load and deflection values obtained from the FE analysis into Equation 3.20. Results are shown in Figure 3.20.

(a)

(b)
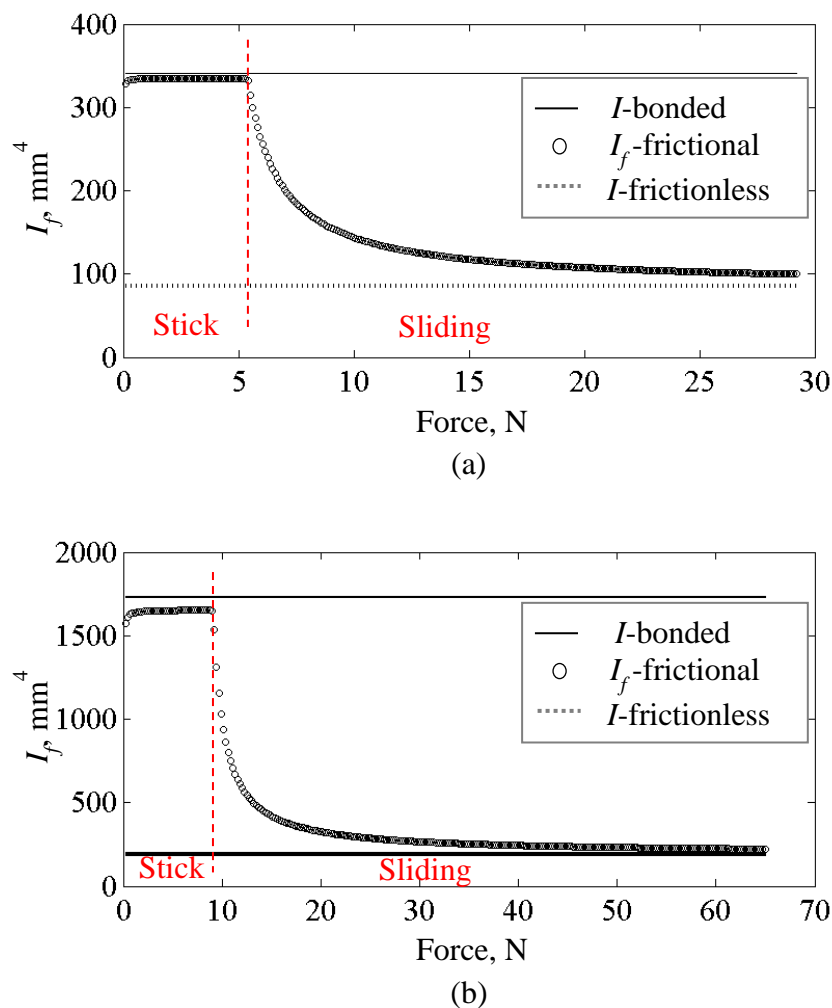
Figure 3.20 Behaviour of the frictional second moment of area (I_f) during system transition through sticking, microslip and sliding regions for Configurations (a) sb06 and (b) sb12

3.6.3 Analytical hysteresis loops

The previous section presented the prediction of both the frictional second moment of area (the stiffness) for the multi-strand beams for the loading levels and configurations presented in Table 3.1.

The analytical model produces a force-displacement response. This can be extended into a force-displacement hysteresis loop to estimate the system loss factor (damping levels).

Figure 3.21 shows the various loading and unloading stages for the hysteresis loop. The starting point for the hysteresis loop is the origin, point(0). Point (1) defines the commencement of the sliding stage during the loading phase, which ends at point (2).
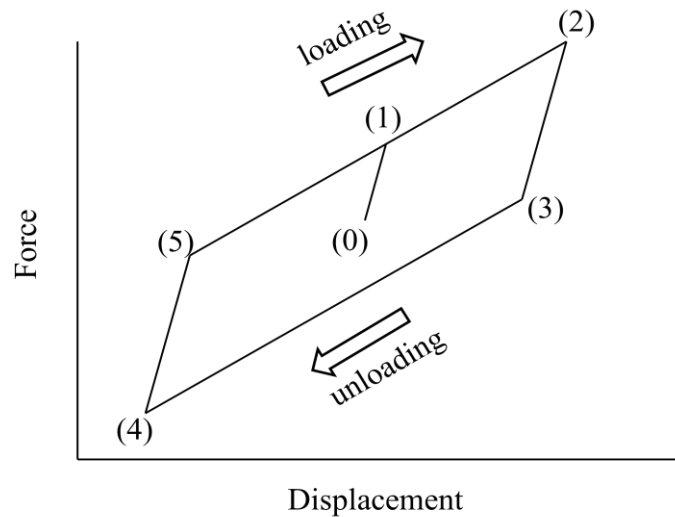
Figure 3.21 Hysteresis loop stages

To describe the force-displacement hysteresis loop, the shear stress and the frictional stress at the contact regions were used to determine the force required to start the slipping in the multi-strand beams. At the moment when slide starts at an interface, the frictional stress equals the shear stress that tries to initiate the slipping (Equation 3.14). By substituting Equations 3.15 and 3.16 into Equation 3.14 and rearranging in term of the force F, the force needed to start slip [100] can be described as

$$F_{slip} = F_1 = \frac{4F_{d1}\mu I_{bond}}{A[(y_t)^2 - (y_t - y_w)^2]}.$$
                                                                                                    3.21

The deformation resulting from the slip force can be calculated through

$$\delta_1 = \frac{F_{slip}l^3}{48EI_{bond}}.$$
                                                                                                    3.22

The third stage is the damping stage and it represents the transition from the sticking region into the sliding region. Damping stage starts from point (2) which represents the maximum force and displacement applied on the system and ends at point (3). This stage determines

the damping amount in the produced hysteresis loop. Depending on the peak force F, the maximum resulting deformation is calculated by,

$$\delta_2 = \frac{Fl^3}{48EI_f}.$$
                                                                                                    3.23

The force and deformation at the end of the damping stage are calculated as

$$F_3 = F - 2\left[\frac{4F_c\,\mu I_{bond}}{A[(y_t)^2 - (y_t - y_w)^2]}\right],$$
                                                                                                    3.24

$$\delta_3 = \frac{F_3 l^3}{48EI_{bond}}$$
                                                                                                    3.25

The fourth stage is the sliding stage during the unloading phase. The fourth stage starts from point (3) and travels all the way to the position of the maximum force and loading on the other side of the hysteresis loop, the bottom left side, to end up at point (4).

It is worth mentioning that in most of experimentally obtained hysteresis loops, the maximum force counts for the calculations of the average peak strain energy because it is rare that a point on the hysteresis loop will have both the force and displacement at its maximum values.

The analytical model in this study assumes the sides of the hysteresis loop are symmetric. Therefore, the force and displacement of point (4) are found as follows,

$$F_4 = -F_2,$$
                                                                                                    3.26
$$\delta_4 = -\delta_2.$$
                                                                                                    3.27

The sliding stage during the loading phase starts from point (5) and ends at point (2). The force and displacement at the start of the sliding stage are calculated through,

$$F_5 = F_4 - 2\left[\frac{4F_{d2}\,\mu I_{bond}}{A[(y_t)^2 - (y_t - y_w)^2]}\right],$$
                                                                                                    3.28

$$\delta_5 = \frac{F_5 l^3}{48EI_{bond}}.$$
                                                                                                    3.29

F_{d1} and F_{d2} present the frictional forces including the flexural loading effect at the required levels.

The average effective stiffness was defined by bisecting the distance between the loading and unloading stages. The energy dissipated per cycle was measured as the area inside the hysteresis loop. The stored strain energy was calculated as the area contained between the average effective stiffness and the displacement axis. The general description for the loss factor can be expressed as

$$\eta = \frac{dW}{2\pi U_{max}}$$ 3.30

where, η is the loss factor, dW is the energy dissipation per cycle and U_{max} is the maximum strain energy.

For a symmetric hysteresis loop, Equation 3.30 can be used to calculate the loss factor of a system as it counts for one half of the hysteresis loop by finding the maximum stored strain energy (U_{max}). However for the reasons of the asymmetric hysteresis loop (see Figure 3.22) that present in this work, the previous equation cannot determine accurately the amount of the damping in the system since this equation assumes the both ends of the hysteresis loop are symmetric. In order to accurately calculate the hysteresis loop in a system that has asymmetric hysteresis loop, the total strain energy should be considered to count for the two halves of the hysteresis loop. Equation 3.31 used to calculate the loss factor in a system with asymmetric hysteresis loop [101].

$$\eta = \frac{dW}{\pi(U_1 + U_2)}$$ 3.31

where, U_1 and U_2 are the strain energy in the positive and negative parts of the hysteresis loop and they are not equal.
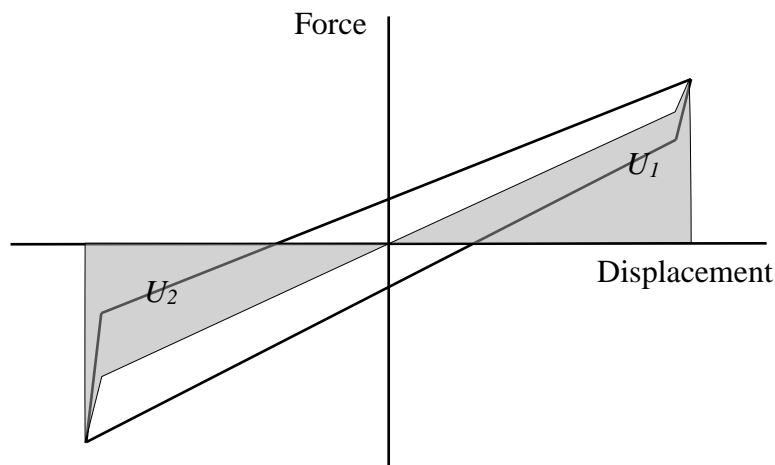
Figure 3.22 Hysteresis loop for stored strain energy

3.7   Modelling results and discussion

This section presents the obtained hysteresis loops, compares the damping levels gained from the multi-strand beams using different analyses methods and discusses the analytical and numerical results. Force-displacement curves obtained at each loading stage for Configuration sb01 to Configuration sb24, (see Table 3.1) were used to plot the numerical hysteresis loops. Configurations sb01–sb12 had three loading stages (1.0 mm, 1.7 mm and 2.5 mm) while Configurations sb13–sb24 had only two loading stages (1.0 mm and 1.7 mm) because they were shorter in length and a 2.5 mm loading can cause permanent deformations (more explanation is provided in Section 4.2.3). Analytical models were used to estimate the system stiffness and to describe the analytical hysteresis loops for the parameters shown in Table 3.1.

Comparison between the analytical and numerical hysteresis loops were presented in Figure 3.23 at different loading levels for Configuration sb22 through sb24. Comparison for Configuration sb01 through Configuration sb21 is presented in Appendix D. The hysteresis loops obtained analytically and numerically were in good agreement for all configurations. The analytical models followed the sliding stages accurately. The numerical models described the transition from the stick stage to the slide stage while the analytical models were designed to provide general description for the damping behaviour in the MSB and despite this fact, the analytical models were able to define the start and end of the stick and slide regions accurately enough to describe the general damping behaviour.
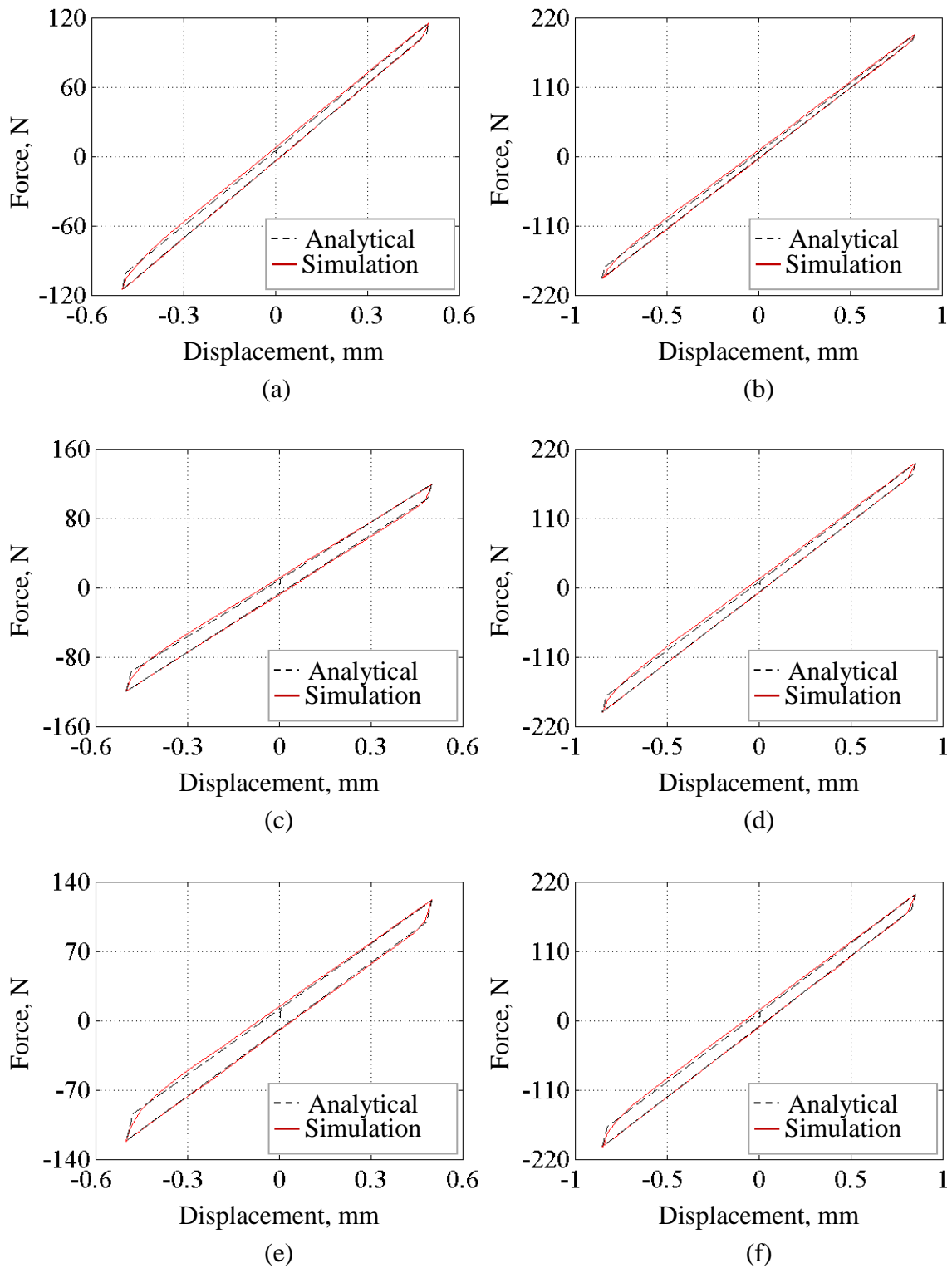
Figure 3.23 Comparison of analytical and numerical hysteresis loops for Configuration sb22 at PK-PK loading of (a) 1.0 mm, (b) 1.7 mm and for Configuration sb23 at PK-PK loading of (c) 1.0 mm, (d) 1.7 mm and for Configuration sb24 at PK-PK loading of (e) 1.0 mm and (f) 1.7 mm

This study considers the loss factor values an indication for the damping levels that the multi-strand beams (MSB) achieved during the flexural loading. For the damping parameters that were obtained analytically and numerically, the energy dissipation per cycle was calculated by counting for the area inside the hysteresis loops. The stored strain energy was calculated by defining the average system stiffness and measuring the area contained between the average stiffness and the displacement axis.

Analytical and numerical damping parameters such as the loss factor, energy dissipation per cycle, strain energy and the system stiffness for Configuration sb01 to sb24 are presented in Appendix E.

The stored strain energy was not affected by the change of clamp force values or the change of the loading levels while the energy dissipation per cycle showed increase in the values with increasing the clamp force however it (energy dissipation) was reduced with increasing the loading levels. As a result, the loss factor values increased by increasing the clamp force levels while the loss factor decreased by increasing the loading levels. These results are in line with previous research [60,73,74].

In order to investigate the effect of the loading levels and the geometrical parameters on the obtained damping levels for the MSB without taking into account the effect of variation of both the material properties of the strands and the coefficient of friction values, it was decided to use the analytical models to describe the hysteresis loops for strands that had the same material properties, E=190 GPa, and the same coefficient of friction, μ=0.25 for all configurations, sb01–sb24, shown in Table 3.1. This procedure should shed light purely on the effect of the cross-section size, the loading displacement levels, the clamping force, the span length and the number of strands involved in the multi-strand beams. Figure 3.24 shows the loss factor values for all the configurations at different peak-to-peak loading levels, 1.0 mm, 1.7 mm and 2.5 mm. Figure 3.25a shows that the loss factor is directly proportional to the clamp force level. The reason behind this was that clamp force had a direct relation to the frictional forces induced between the mating strands therefore the increase of the clamp force led to the increase of the frictional forces which in turn increased the energy dissipation levels. While the loss factor has inverse proportion to the loading levels as shown in Figure 3.25b. The direct proportion between the loss factor and the span length is shown in Figure 3.26a. Shorter strands had higher stiffness, similar to the effect of the cross-section

on the loss factor, which led to increase the strain energy resulted from each flexural loading and in turn decrease the loss factor values. The cross-section size of the individual strands has inverse proportion to the loss factor as shown in Figure 3.26b. This behaviour is referred to that the stiffness levels were lower in systems with smaller cross-sections which means in theory, that less force needed to dissipate energy per cycle than those with larger cross-sections for same energy dissipation level. Figure 3.27 depicts the effect of the number of strands involved in the multi-strand beams on the loss factor values where the cross-section size of the individual strands kept unchanged. Interestingly, there was approximately no change in loss factor values during changing the number of strands in the MSB for systems with the same cross-section size but different number of strands. This behaviour was not true when the change of the strands number was synced with the change of the cross-section size as shown in Figure 3.27b were increasing the number of strands with increasing the strands cross-section led to a reduction in the loss factor values.
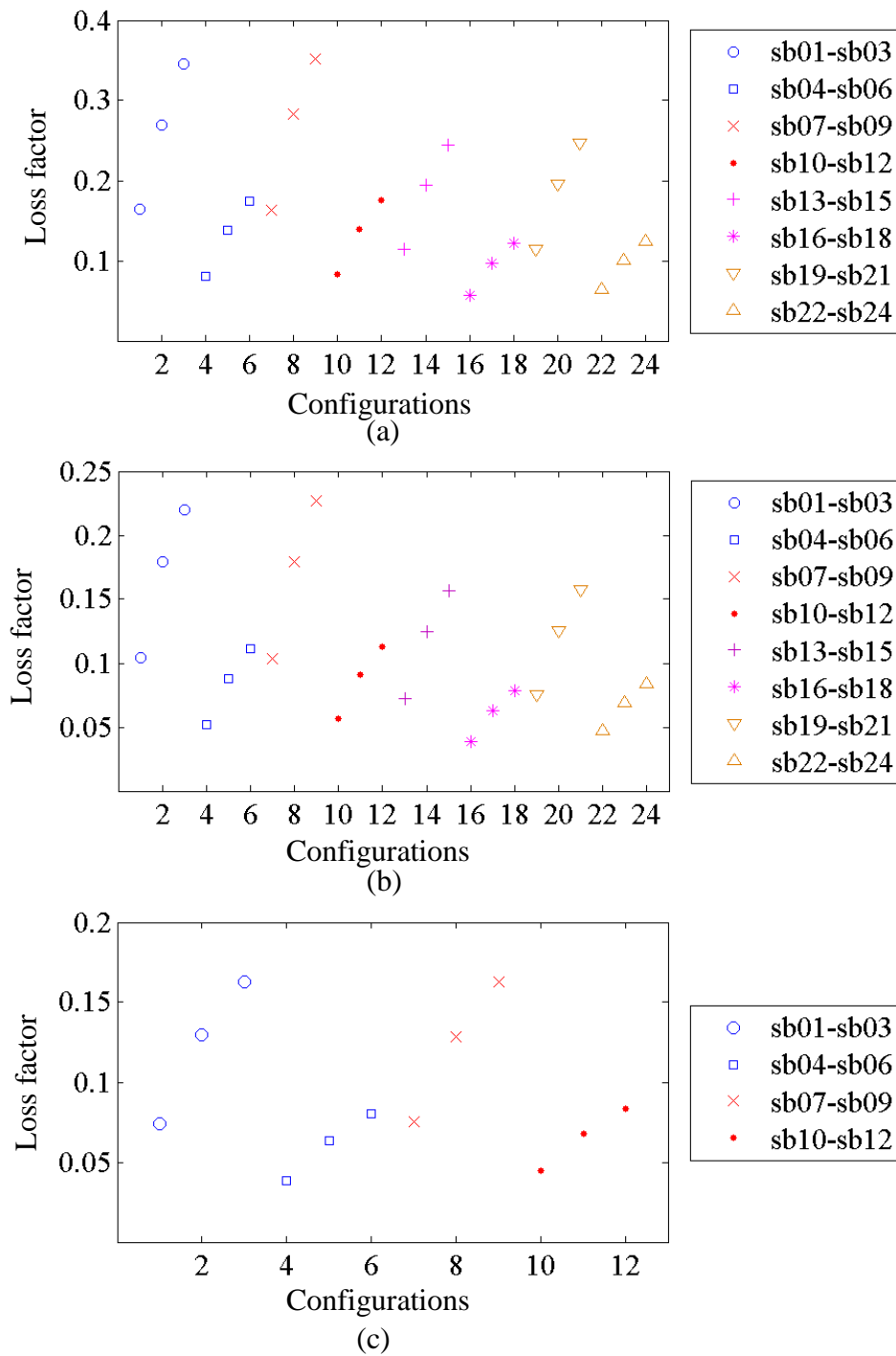
Figure 3.24 Loss factor values for the configurations shown in Table 3.1 at PK-PK loading levels of (a) 1.0 mm, (b) 1.7 mm and (c) 2.5 mm
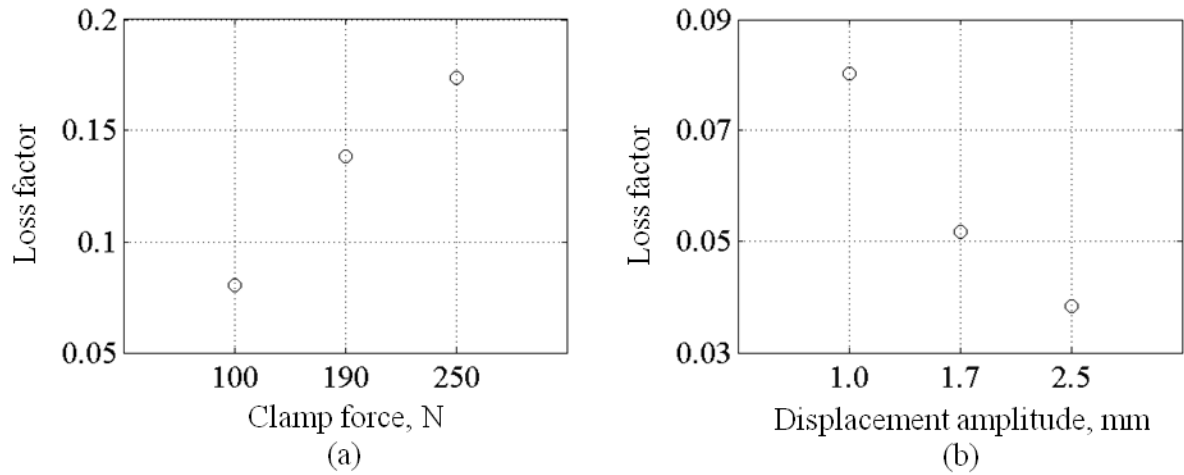
Figure 3.25 Loss factor versus (a) clamp force for Configurations sb04-sb06 at PK-PK loading level of 1.0 mm and loss factor versus (b) loading levels (Displacement amplitude) for Configuration sb04
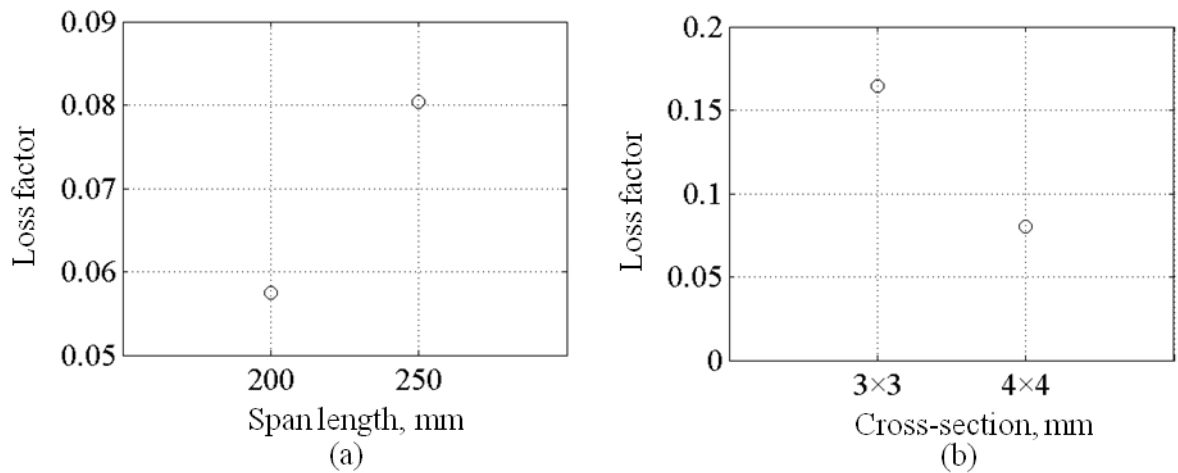
Figure 3.26 Loss factor versus (a) span length for Configurations sb04 and sb16 and loss factor versus (b) cross-section size for Configurations sb01 and sb04 at PK-PK loading level of 1.0 mm
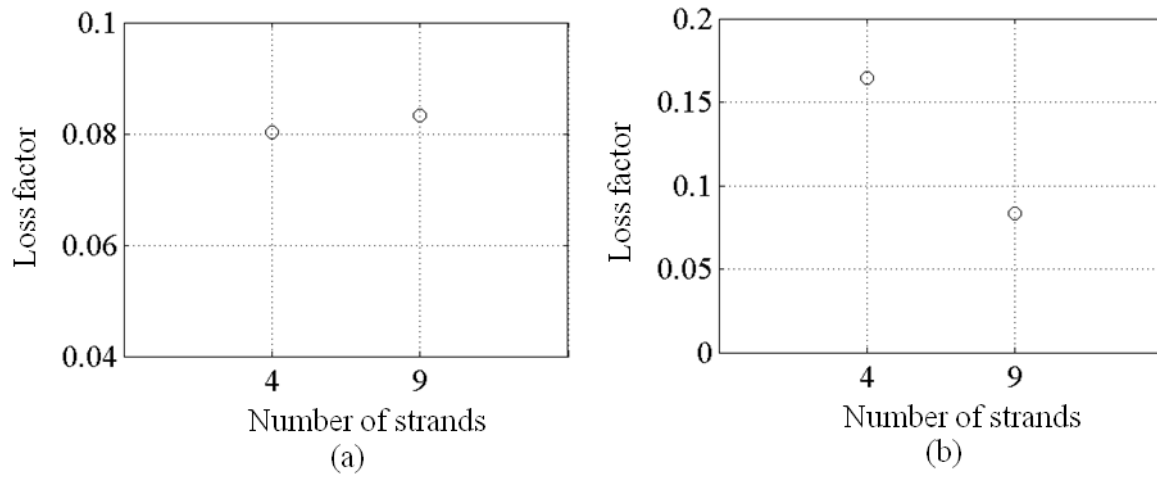
Figure 3.27 loss factor versus number of individual strands where in (a) the number of strands increased from four strands (each strand cross-section is 4×4 mm) to nine strands (each strand cross-section is 4×4 mm) while in (b) the number of strands increased from four strands (each strand cross-section is 3×3 mm) to nine strands (each strand cross-section is 4×4 mm) at PK-PK loading levels of 1.0 mm

3.8   Numerical stiffness study

In the previous sections, the effect of the number of strands was considered, however the size of each strand was maintained and hence the overall cross-section of the MSB changed. This section is devoted to investigate the effect that the number of strands involved in the MSB have on the loss factor and the energy dissipation levels whilst maintaining the overall cross-section.

This section adopted numerical models for analysis purposes. Finite element models were built for the MSB which was constructed from different numbers of square sectioned strands. The overall dimensions of the MSB were fixed at $12 \times 12 \times 300$ mm for all configurations, which are defined in Table 3.6 and described in Figure 3.28.

The numerical models were expected to simulate the behaviour of the MSB that was exposed to a quasi-static peak-to-peak (PK-PK) cyclic sinusoidal displacement loading of 1.0 mm at a frequency of 1.0 Hz. Clamp force levels of 100 N, 190 N and 250 N were applied to hold the individual strands together during flexural loading. The clamp force effect was applied as an equivalent distributed pressure along both the outer upper and outer lower surfaces of the MSB. The modulus of elasticity for the numerical work in this section was 190 GPa and the coefficient of friction between the individual mating strands was 0.25.

Table 3.6 Configuration of the MSB for the numerical stiffness study

Configuration no.	Total no. of strands	Individual cross-sectional strand width and thickness, mm	No. of strands per row and column
mb01	4	6	2
mb02	9	4	3
mb03	16	3	4
mb04	36	2	6
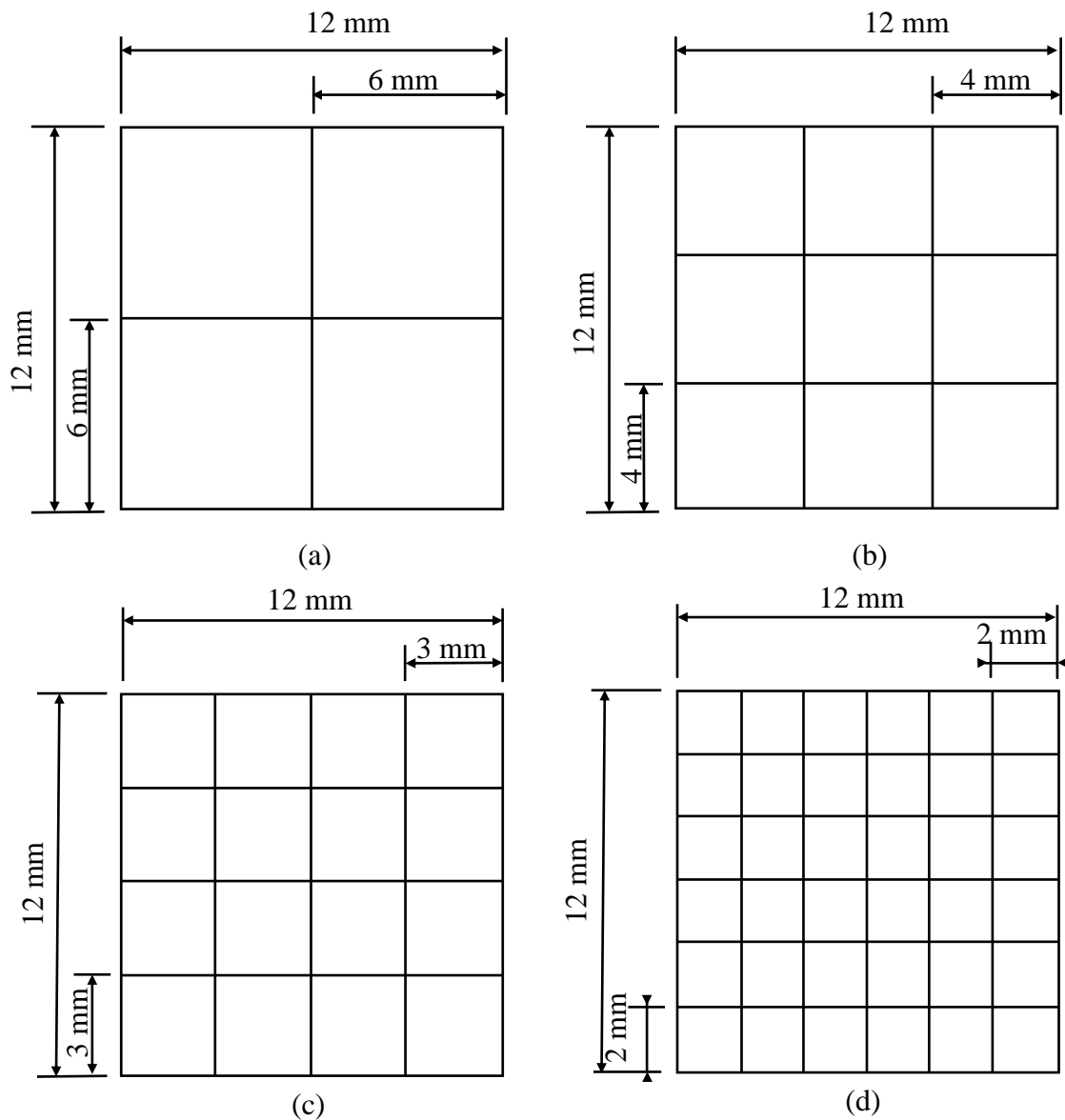
Figure 3.28 Layout of the MSB containing (a) four strands (mb01), (b) nine strands (mb02), (c) sixteen strands (mb03) and (d) thirty-six strands (mb04)

The average effective stiffness was estimated by a polynomial fit applied to the numerical hysteresis loop. The energy dissipation per cycle was measured by numerical integration of the force-displacement curve. The loss factor was calculated from the hysteresis loop from the energy dissipation and the stored strain energy using Equation 3.31 [99, 100].

Figure 3.29 shows hysteresis loops for Configurations mb01 through mb04. It can be observed that increasing the number of strands reduces the underlying gradient of the

hysteresis loops and therefore the system stiffness. The energy dissipation per cycle (i.e. the area of each hysteresis loop) however, is approximately the same for all configurations (shown in Figure 3.30). The peak strain energy (shown in Figure 3.31) is directly proportional to the stiffness and therefore reduces as the number of strands increases. The loss factor is shown in Figure 3.32.
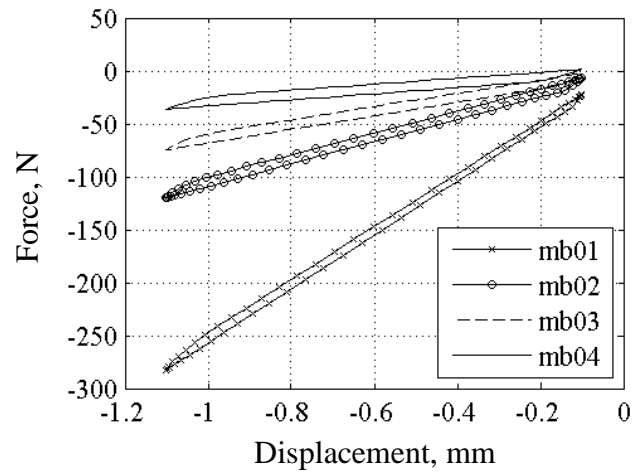
(a)
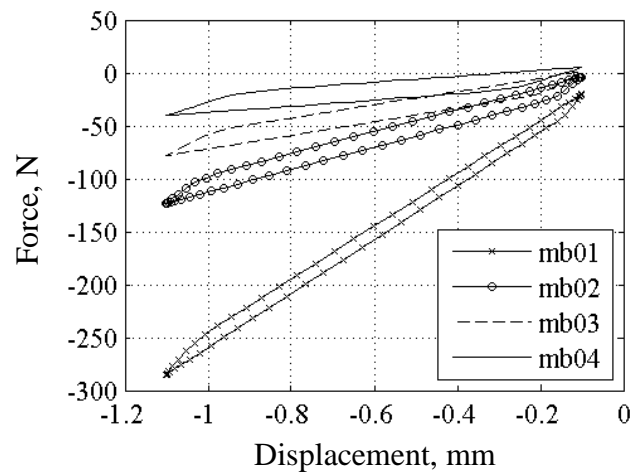
(b)
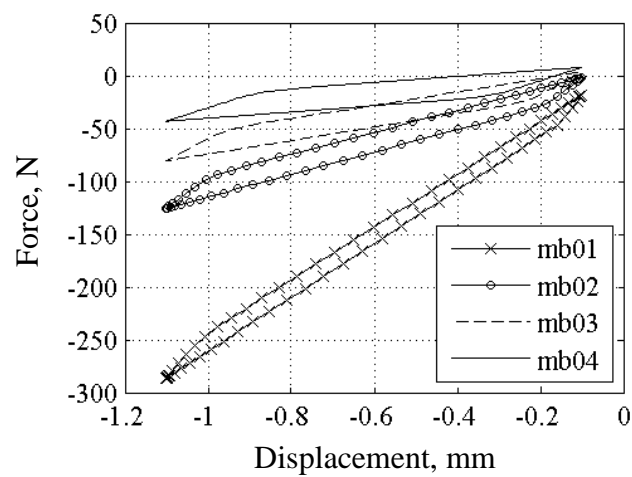
(c)

Figure 3.29 Numerical force-displacement curves for Configurations mb01–mb04 at PK-PK
displacement of 1.0 mm and a clamp force of (a) 100 N, (b) 190 N and (c) 250 N
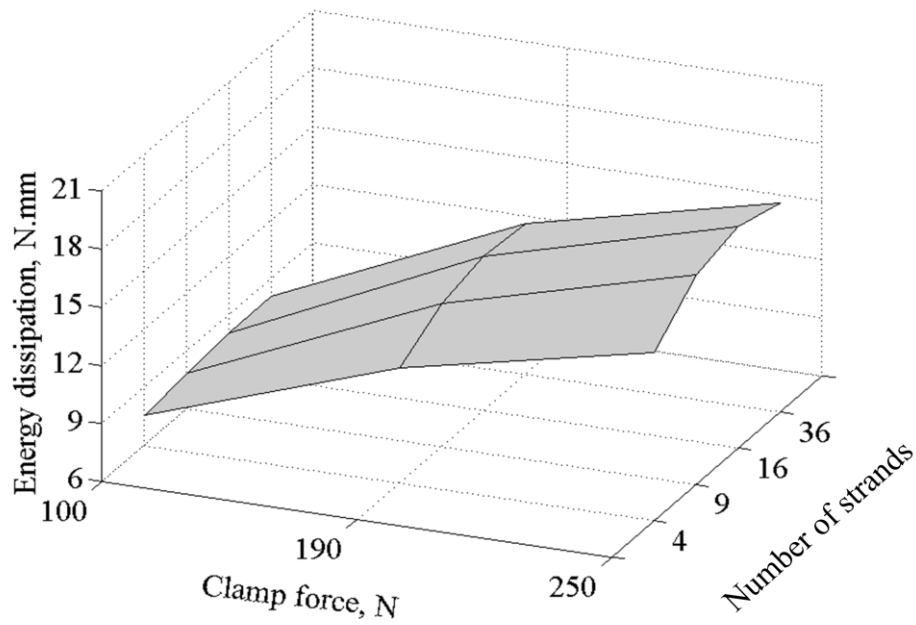
Figure 3.30 The relationship between the energy dissipation, clamp force, and number of strands for Configurations mb01−mb04 at 1.0 mm PK-PK displacement
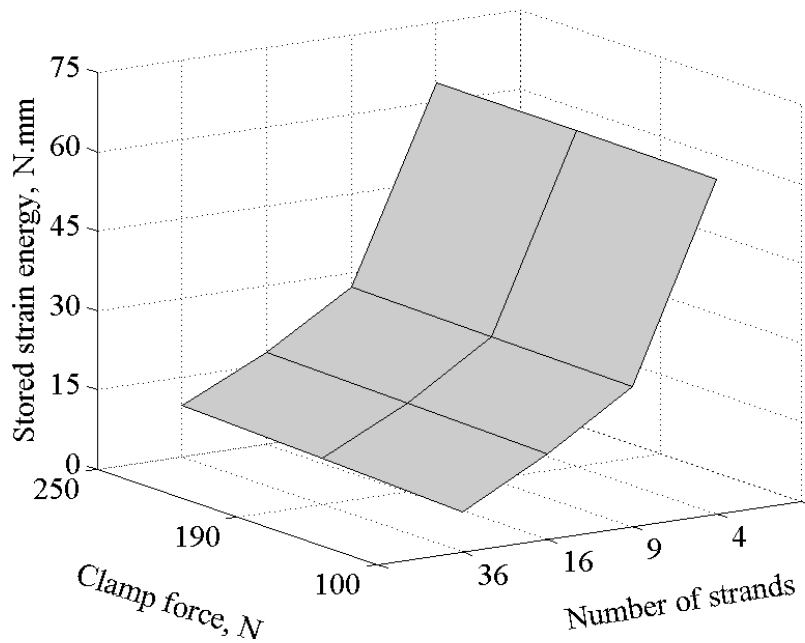
Figure 3.31 The relation between the stored strain energy, clamp force and number of strands for Configurations mb01−mb04 at 1.0 mm PK-PK displacement

71
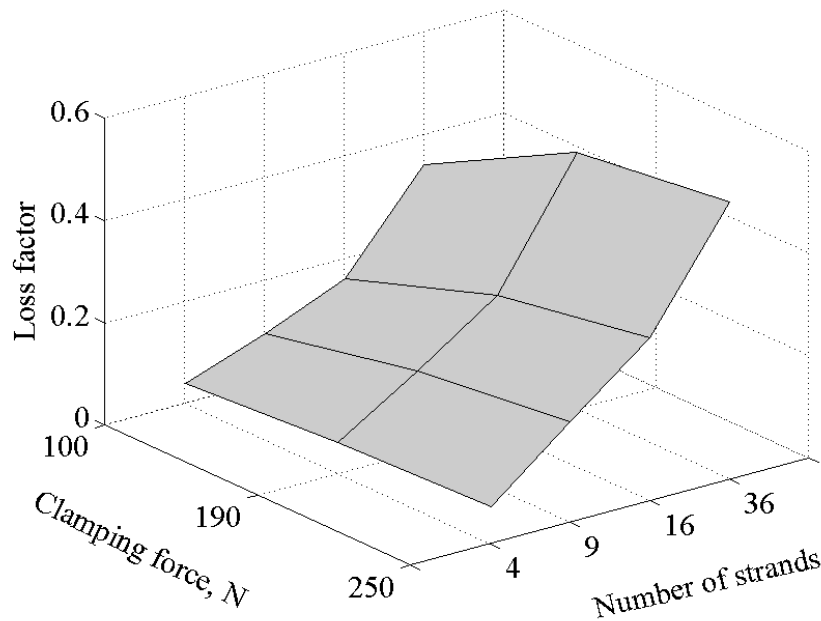
Figure 3.32 The relationship between the loss factor, clamp force, and number of
strands for Configurations mb01–mb04 at 1.0 mm PK-PK displacement

3.9   Conclusions

Several conclusions can be drawn from the results obtained in this chapter. The main
conclusions are:

- Conclusions on loss factor level,

  ➢ The loss factor values are independent to the number of strands in the multi-strand
  beams if the cross-section size of the individual strands kept unchanged. This is not
  true when strands with different cross-section size are used in the MSB.

  ➢ The energy dissipation remains approximately at same levels when increasing the
  number of strands in the MSB if the overall cross-section area of the MSB kept
  unchanged while the loss factor tends to increase.

  ➢ The loss factor is highly dependent on the clamp force levels. Larger clamp forces
  result in higher loss factor values.

  ➢ Increasing the loading level can reduce the loss factor values. Also, decreasing the
  length of the individual strands can cause to reduce the loss factor values.

➢ The loss factor is dependent on the cross-section size of the individual strands. Larger cross-sections may reduce the loss factor values.

- Conclusions on the modelling level,

  ➢ The finite element models were able to simulate the flexural behaviour that was performed on the multi-strand beams.

  ➢ The analytical model was able to predict the stiffness for a system experiencing frictional behaviour during flexural loading.

  ➢ The analytical model follows the numerically computed force-displacement response over most stages of loading and unloading.

- Conclusions of the effect of the coefficient of friction,

  ➢ The relationship between the frictional second moment of area and the coefficient of friction is highly nonlinear.

  ➢ The relationship between the system deformation and the coefficient of friction is linear.

- The transition region between the stick and slip stages plays an important role in changing the system stiffness from being bonded to frictional to being frictionless.

Chapter 4

Quasi-static experiments on multi-strand beams

4.1 Introduction

This chapter describes the experimental work conducted on the set of multi-strand beams (MSBs) introduced in Chapter 3. The purpose of the work was to investigate the effects of various parameters on the system loss factors and to provide experimental validation of the analytical and numerical models. Testing involved exposing each MSB to sinusoidal loading using a three point bend configuration. Hysteresis loops were generated from the resulting force and displacement signals.

4.2 Methodology

Testing was conducted at low loading rates using a servo-hydraulic test machine (MTS 858 Table Top System). The arrangement for each test is shown in Figure 4.1. Mechanical clamps (A) were used to hold the strands together to form a beam (B). Each beam was supported on 25 mm diameter rollers (D) while loading was applied as displacement controlled motion of the central roller (C), which was also of the same diameter. The parameters under study were: the span distance between the two supporting rollers, the number of strands in the MSB, the cross-section size of the tested strands, the clamping force and the applied vertical displacement at the middle of the MSB.
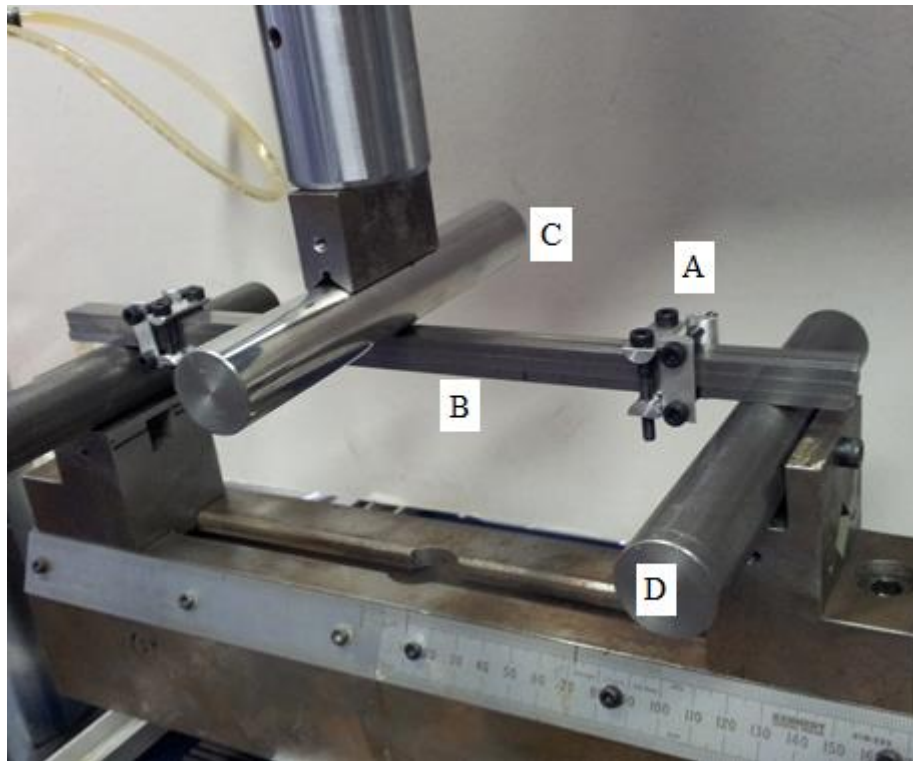
Figure 4.1 Test configuration showing (A) clamps, (B) beam, (C) loading roller and (D) support roller

4.2.1 Clamping

The clamp sets had a semicircular cross-section with the curved side positioned to face the outer strands to reduce the contact region between the clamps and the strands (see Figure 4.2) to minimise friction at this contact, a PTFE lubricant was inserted into the interface between the clamps and the strands. Each clamp set had two threaded fasteners which were torqued to apply the required clamping force on the MSB. Conversion and calibration of the clamp torque into equivalent clamp force were described in Section 3.4.1. Using Appendix A, torques of 42.3 N.mm, 84.7 N.mm and 112.9 N.mm were applied on each of the two fasteners that were used to connect the two halves of the clamp set to produce equivalent clamp forces of 100 N, 190 N and 250 N applied through the clamp sets against the MSB.
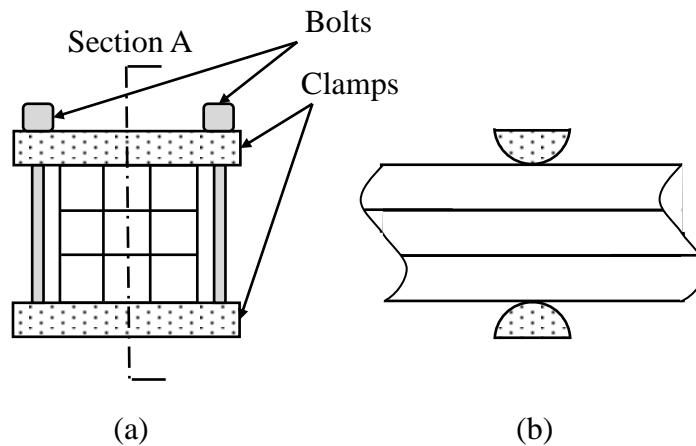
Figure 4.2 Clamp configuration on multi-strand beam for (a) side view and (b) front view

The method employed in this study involved four pairs of clamps which provided clamping forces in the horizontal (width) and vertical (thickness) directions. The clamps were located approximately 25 mm from each stationary roller at each end of the beam.

4.2.2 Test procedure

First, the span between the supports was set according to the test configuration – as defined in Table 3.1. Testing was carried out at different amplitude levels of peak-to-peak sinusoidal displacement loading. Loading was applied in the thickness direction through the loading roller. At the start of each experiment, the loading roller was lowered until an initial contact (observed as an increase in the force signal) was made with the beam. From this point, the loading roller was lowered a further 0.1 mm to induce a light compressive load to ensure contact was maintained at all times between the loading roller and the beam. A sinusoidal displacement at a frequency of 1.0 Hz was then used to load the beam from the 0.1 mm initial displacement to additional peak-to-peak (PK-PK) displacements of 1.0 mm, 1.7 mm, and (for configurations with the span of 250 mm) 2.5 mm. The reason for selecting these loading levels are explained in Sections 4.2.3 and 4.2.4. A repeat test at the lowest amplitude (1.0 mm) was carried out at the end of each set of tests and was compared with the equivalent original test. In this way it was shown that significant permanent change did not occur in any of the strands or interfaces during testing. Force and displacement signals were

recorded at a rate of 100 sample/sec and the time for each loading stage was 15 sec with a dwell time of 1 sec between each stage.

4.2.3 Estimation of the loading displacement levels

It was important to deform the MSBs sufficiently, in order to activate slip at the interfaces. However, it was also important to avoid deforming strands beyond their plastic limits in the absence of available material data on yield strains, testing of individual strands were necessary.

For flexural loading under prescribed displacement, it was noted that the highest stress would occur on the outer surfaces of the thickest beam if inter-strand slip did not occur. considering this as the worst case, for a square section beam of thickness h, Euler-Bernoulli bending theory [99] gives

$$\sigma = \frac{6M}{h^3},$$ 4.1

where, σ is the maximum stress and M is the bending moment about the neutral axis.

For a centrally loaded, simply supported beam, the maximum bending moment is,

$$M = \frac{Fl}{4}$$ 4.2

while the deflection is,

$$\delta = \frac{Fl^3}{48EI}$$ 4.3

Combing these equations, it can be shown that the maximum strain is,

$$\varepsilon_f = \frac{6\delta h}{l^2},$$ 4.4

where, ε_f is the flexural strain.

The stress-strain relation for the material was obtained through a three point bend test on a single strand of 2×2×300 mm. The maximum displacement applied by the test machine was 30 mm which corresponded to a static forcing equal to approximately 15 N. The feed rate of the servo-hydraulic machine was 1.0 mm/min with sampling frequency of 100 Hz.

The resulting stress-strain plot for the material can be seen in Figure 4.3, although no sudden yield point is noticeable, relatively linear behaviour can be seen up to 0.3% strain. Consequently, this was used as the "worst case" strain that beams under testing would be allowed to experience.
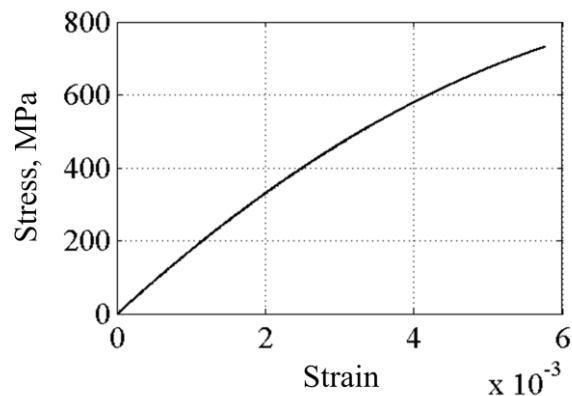
Figure 4.3   Stress-strain behaviour under flexural loading

For a 12 mm thick beam (i.e. Configuration sb12 and sb24 under bonded conditions) a maximum strain of 0.3% is reached at deflections of 1.7 and 2.5 mm for spans of 200 and 250 mm respectively. These values were therefore used as the maximum deflections for loading.

4.2.4 Estimation of slip initiation force

While no slip was assumed to find the deflection limits, it was important to ensure that slip did actually take place. The likelihood of this occurring was predicted using the analytical model developed in Chapter 3. The force required for slip to commence, is given by Equation 3.21. Certain assumptions were adopted: the clamping force was assumed to be 250 N, the coefficient of friction, μ ,was 0.25, modulus of elasticity 190 GPa.

The force required to initiate the slip was 0.50 N and 0.62 N for Configurations sb12 and sb24 respectively. This was equivalent to deformations of 0.004 mm and 0.003 mm respectively. This indicates that the chosen range of the applied displacements can initiate the slip in the system.

4.3   Results and discussion

4.3.1   Experimental results

During the three-point bend test, closed-loop control was employed to ensure that the displacement signal had a sinusoidal shape. The effect of friction between the strands could be seen in the force trace as a small phase difference (from damping) and a distortion of the waveform (from nonlinearity). A typical pair of signals is shown in Figure 4.4.
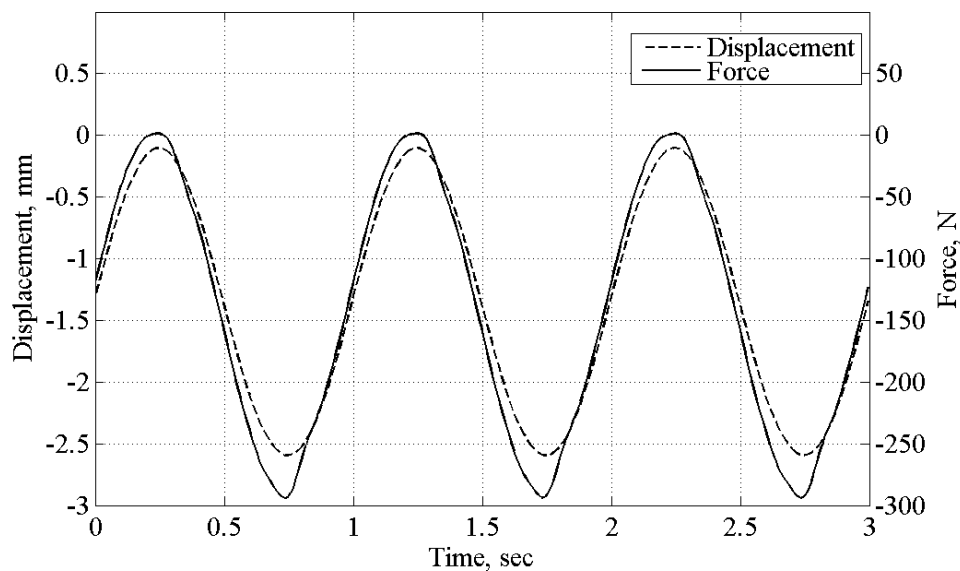
Figure 4.4   Force and displacement histories for Configuration sb12 at PK-PK displacement of 2.5 mm

Configurations sb01–sb12 experienced four displacement loading stages (1.0 mm, 1.7 mm, 2.5 mm and 1.0 mm) while Configurations sb13–sb24 were exposed to three loading stages (1.0 mm. 1.7 mm and 1.0 mm). The damping behaviour was presented through plotting the hysteresis loops for the force and displacement time histories. In this section, not all the test Configurations results are presented however, Figure 4.5 shows the unfiltered hysteresis loops for Configurations sb06, sb12, sb18 and sb24.
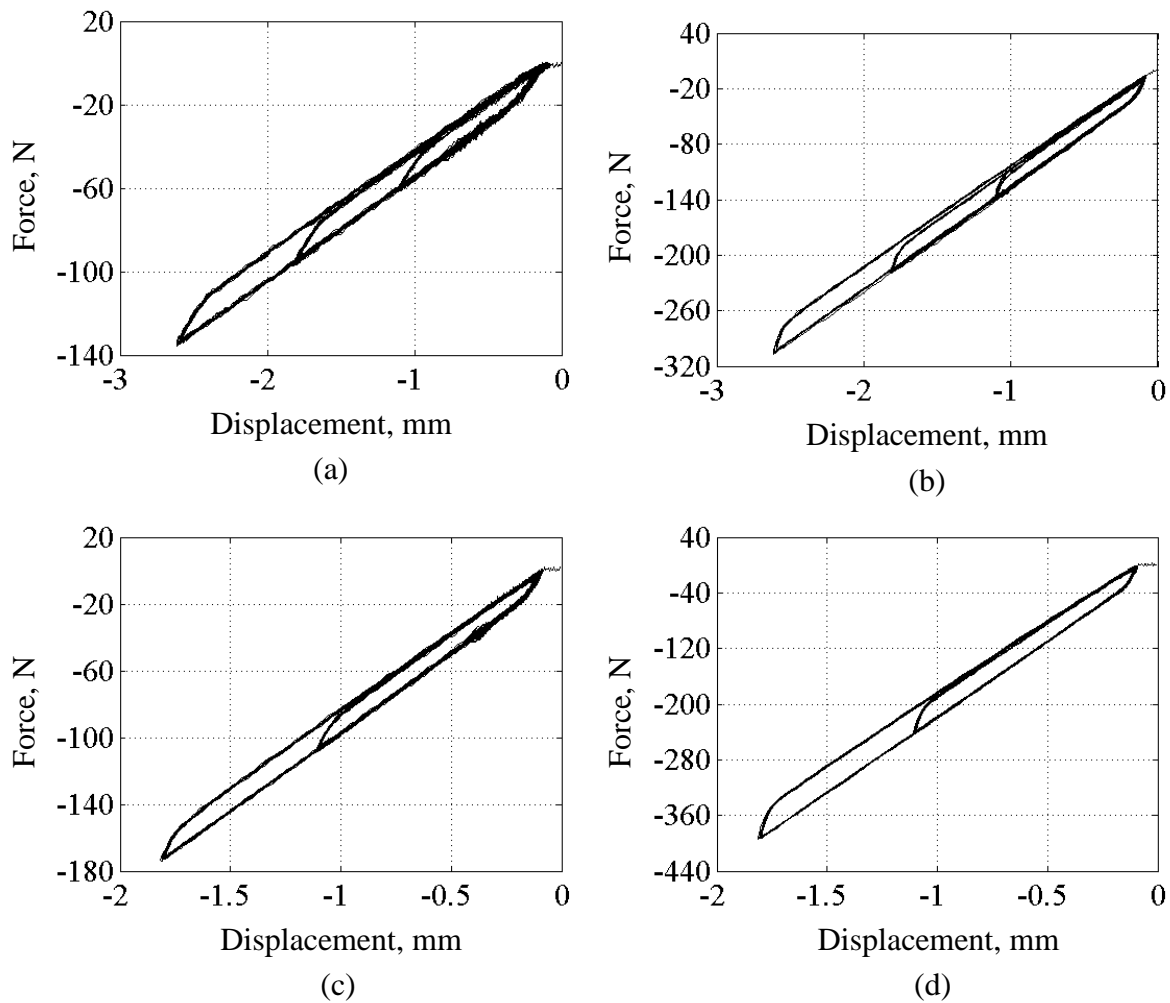
Figure 4.5 Experimental hysteresis loops at different displacement loadings levels for Configurations (a) sb06, (b) sb12, (c) sb18 and (d) sb24

The displacement loading for test Configurations sb13 through sb24 was limited to 1.7 mm due to the analytical prediction results obtained in Section 4.2.3 which suggested that the maximum displacement loadings should be maintained at under 80% of the maximum allowable flexural displacement (2.2 mm) for multi-strand beams with individual strands length 200 mm. Therefore, the hysteresis loops for test Configurations sb18 and sb24 show only three displacement loadings, 1.0 mm 1.7 mm and 1.0 mm, as can be seen in Figure 4.5c and Figure 4.5d.

It is worth mentioning at this stage that the maximum loading forces achieved during the experiments agreed well with the analytical estimation of allowable forces obtained in Section 4.2.3 for test Configurations sb12 and sb24 as shown in Table 4.1.

Table 4.1 Comparison of analytically estimated and experimentally obtained forces values

Test set	Estimated maximum forcing, N	Experimental maximum forcing, N
sb12	307	296
sb24	384	391

The behaviour of the hysteresis loops agrees well with the damping behaviour in a dry frictional system as reported by [103].

The force measurement contained some noise, as seen in Figure 4.5. The reason for this was that the load cell range was 10 KN while the measurements rarely exceeded 500 N. It was considered beneficial to remove the noise using digital filtering techniques. Generally, a signal is digitally filtered for two reasons: first to restore a distorted signal: second, to separate two or more combined signals that are contained in the unfiltered signal. The filtering in this work adopts the separation of two or more combined signals as the noises contained in the unfiltered signal can be considered as the combined signals.

In order to select the best approach, three techniques were considered: averaging, Fast Fourier Transform (FFT) filtering and a harmonic fitting approach. A brief description of each technique is provided below.

Averaging: the signal is divided into individual cycles and the average taken. In this work, eight averages were used. For this approach to work, the noise would have to be random.

FFT filter: the signal is converted from time domain into frequency domain using the algorithm. In the frequency domain, spectral data above a cut-off is set to zero before inverse transforming back to the time domain. The cut-off frequency is chosen to be 25 times the natural frequency.

Harmonic fitting: a series of sine waves, corresponding to multiples of the test frequency, are fitted to the measured force signal over eight cycles in the time domain.

Figure 4.6 shows the effects of using these three techniques to filter the experimental results for Configuration sb06.

For convenience, this work adopts the Fourier transform technique which is shown in Figure 4.6c.
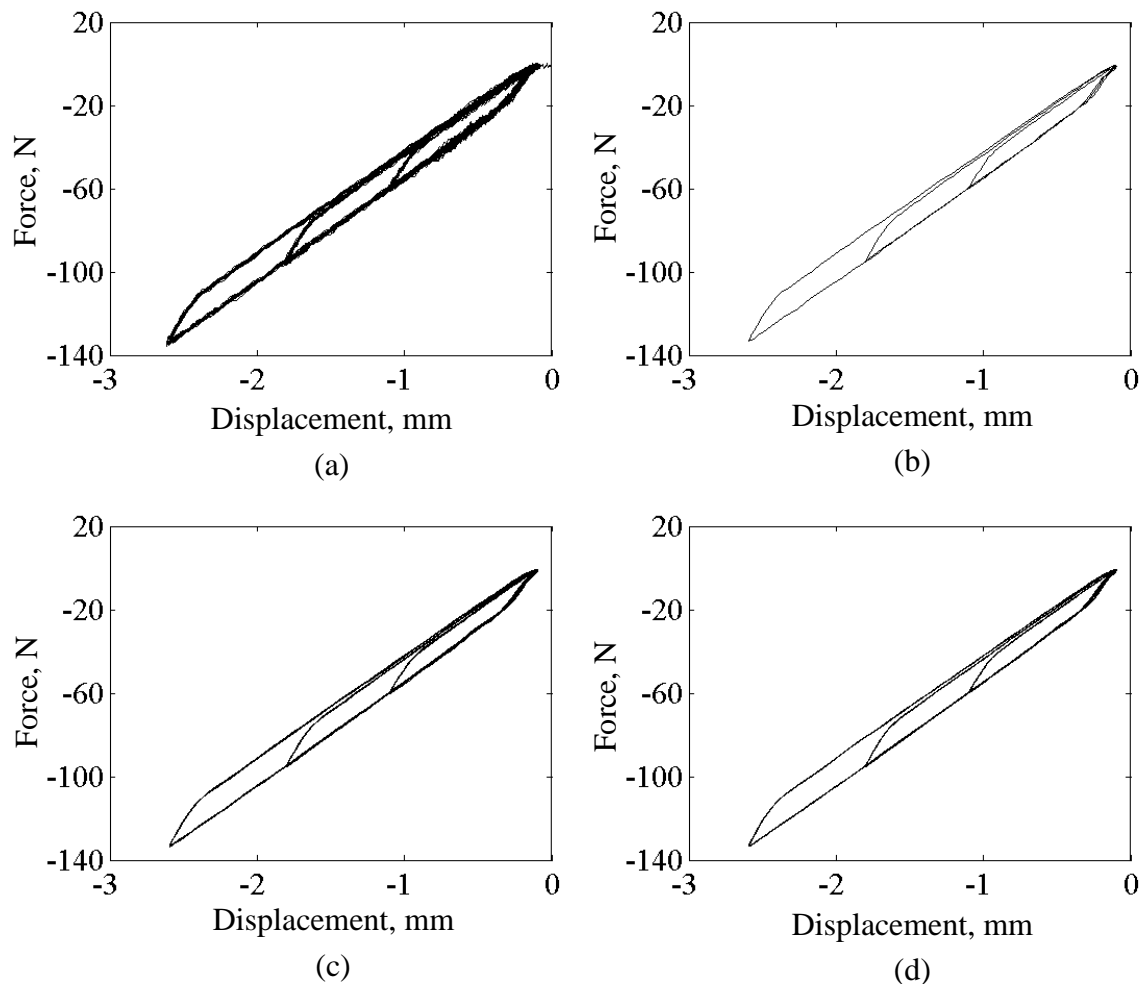
Figure 4.6 Hysteresis loops for test Configuration sb06 with (a) no filtering, (b) averaging, (c) Fast Fourier Transform and (d) Harmonic fitting

The work in this chapter and the later chapters utilizes the loss factor values as an indication for the amount of damping that the multi-strand beams achieved during the flexural behaviour in line with the different parameters that have been studied. A Matlab script was developed to calculate the loss factor and system average stiffness for all the displacement loading stages.

Differences were found between the trends of the loading stage and unloading stage in the experimentally obtained hysteresis loops which means that these hysteresis loops were asymmetric, with the hysteresis loop appearing to be thicker near the region of the maximum loading than at the start of the loading. The reason for this behaviour could relate to the

amount of loading differing between the loading and unloading stages, as the unloading stage starts after the system has reached its maximum position that comprises both the clamping force and the maximum loading level. At this particular moment, the system restoration process is greater than at the start of the loading stage where the system restores from the effect of the clamping force only. This behaviour seemed to be more noticeable in the nine-strand beams than in the systems with four-strand beams due to the increased number of surfaces in contact inside the system.

The average effective stiffness was estimated by applying a polynomial fit (third order) to the experimental hysteresis loop. The energy dissipation per cycle (i.e. the area enclosed in the loop) was measured by numerical integration of the force-displacement curve. The loss factor was calculated from the experimentally obtained hysteresis loop through counting the energy dissipation and the stored strain energy using Equation 3.31.

Table 4.2 and Table 4.3 show the experimental damping parameters for Configurations sb01–sb12 and Configurations sb13–sb24 respectively. Findings regarding the effect of the parameters presented in Table 3.1on the loss factor were obtained in a similar way to the modelling results presented in Chapter 3. The average effective stiffness was not affected by change in either the clamp force values or the loading levels, whereas increasing the clamp force led to an increase in the energy dissipation per cycle, and increasing the loading levels reduced the energy dissipation. For further details about the effect of the parameters on the loss factor values please read Section 3.7 (Figure 3.24–Figure 3.27).

Table 4.2 Experimental damping characteristics for Configuration sb01 through
Configuration sb12

Configuration	Loading, mm	Experimental			
		Loss factor	Energy dissipation / cycle, mJ	Strain energy, mJ	Stiffness, N/mm
sb01	1.000	0.074	0.798	3.437	14.56
	1.700	0.047	1.575	10.73	15.43
	2.500	0.042	3.115	23.63	15.33
sb02	1.000	0.102	1.111	3.474	12.97
	1.700	0.065	2.166	10.67	15.17
	2.500	0.051	3.791	23.53	15.49
sb03	1.000	0.161	1.786	3.521	13.87
	1.700	0.099	3.330	10.69	15.09
	2.500	0.075	5.572	23.63	15.92
sb04	1.000	0.062	2.428	12.50	49.83
	1.700	0.048	5.402	35.65	49.54
	2.500	0.045	10.74	75.95	48.58
sb05	1.000	0.158	6.371	12.80	49.77
	1.700	0.103	11.82	36.43	49.96
	2.500	0.092	22.26	77.12	49.25
sb06	1.000	0.178	7.557	13.48	50.24
	1.700	0.136	15.97	37.32	49.62
	2.500	0.117	28.58	77.86	47.84
sb07	1.000	0.103	2.737	8.446	34.15
	1.700	0.063	4.968	25.09	34.74
	2.500	0.048	8.143	54.26	35.79
sb08	1.000	0.170	4.820	9.018	34.67
	1.700	0.118	9.586	25.89	36.61
	2.500	0.091	15.75	55.32	35.71
sb09	1.000	0.203	5.624	8.831	34.35
	1.700	0.125	10.06	25.63	36.19
	2.500	0.092	15.98	55.18	36.58
sb10	1.000	0.061	5.320	27.57	111.9
	1.700	0.051	12.65	79.71	110.7
	2.500	0.063	33.87	171.3	112.1
sb11	1.000	0.115	10.18	28.13	114.5
	1.700	0.086	21.86	80.79	113.1
	2.500	0.086	46.48	171.4	112.6
sb12	1.000	0.173	15.54	28.66	114.0
	1.700	0.121	30.69	80.97	112.1
	2.500	0.098	52.92	172.6	113.4

Table 4.3 Experimental damping characteristics for Configuration sb13 through
Configuration sb24

Configuration	Loading, mm	Experimental			
		Loss factor	Energy dissipation / cycle, mJ	Strain energy, mJ	Stiffness, N/mm
sb13	1.000	0.046	1.074	7.385	29.49
	1.700	0.040	2.681	21.56	29.69
sb14	1.000	0.109	2.601	7.628	30.14
	1.700	0.072	4.983	22.09	30.08
sb15	1.000	0.109	2.632	7.689	30.56
	1.700	0.078	5.467	22.31	31.20
sb16	1.000	0.073	5.472	23.79	95.93
	1.700	0.059	12.60	68.26	96.09
sb17	1.000	0.120	8.961	23.85	93.91
	1.700	0.089	19.02	68.24	95.18
sb18	1.000	0.130	9.833	24.10	94.63
	1.700	0.096	20.61	68.46	95.38
sb19	1.000	0.068	3.630	16.95	69.36
	1.700	0.045	7.028	49.25	68.12
sb20	1.000	0.120	6.574	17.37	70.77
	1.700	0.084	13.19	49.99	69.58
sb21	1.000	0.145	7.805	17.09	68.76
	1.700	0.091	14.13	49.46	69.16
sb22	1.000	0.087	14.67	53.47	216.8
	1.700	0.072	35.02	154.0	215.9
sb23	1.000	0.136	23.27	54.32	218.0
	1.700	0.094	45.70	154.8	218.2
sb24	1.000	0.144	24.50	54.23	218.5
	1.700	0.109	52.99	154.8	218.3

4.3.2 Comparison of results

The results in Chapter 3 that were obtained from the analytical and numerical modelling comprised the entire range of configurations shown in Table 3.1. As the experimental work involved performing tests on the same configurations that were used for the work presented in Chapter 3, this enabled comparisons to be conducted between results from the experimental work of this chapter and those from the analytical and numerical modelling work of Chapter 3.

Comparison between the experimental, numerical and analytical hysteresis loops are presented in Figure 4.7 and Appendix F for the studied parameters shown in Table 3.1 at different loading levels. Most of the comparisons showed good agreement, particularly when the stiffness of the multi-strand beams was at higher levels – for example Figure 4.7. The hysteresis loops obtained numerically and analytically were in good agreement with each other for all the configurations. The analytical model followed the sliding stages accurately. The hysteresis loops obtained experimentally using square strands with cross-section of 3×3 mm produced slightly different results compared with the hysteresis loops that were obtained numerically and analytically. The reason was that these strands seem to have different specifications from the square strands with cross-section of 4×4 mm, also the cross-section size of the 3×3 mm strands, *b* and *h* (Figure 3.1a), was not consistent along the length of the strands which might have caused instability during the frictional flexural loading. Meanwhile, the cross-section for strands of 4×4 mm showed a consistent profile along the strands' length, as shown in Table 4.4, The experimental hysteresis loops' behaviour at the start of the unloading stage, discussed earlier in Section 4.3.1, where the thickness of the experimental hysteresis loop increased, appeared visually clear when compared with the numerical and analytical hysteresis loops. This was related to the system at that region, the end of the loading stage, restoring from a higher forcing level where this forcing effect comprised both the clamp force and the maximum loading force applied to the system while only the clamp force was involved in the restoration process at the start of the loading stage.
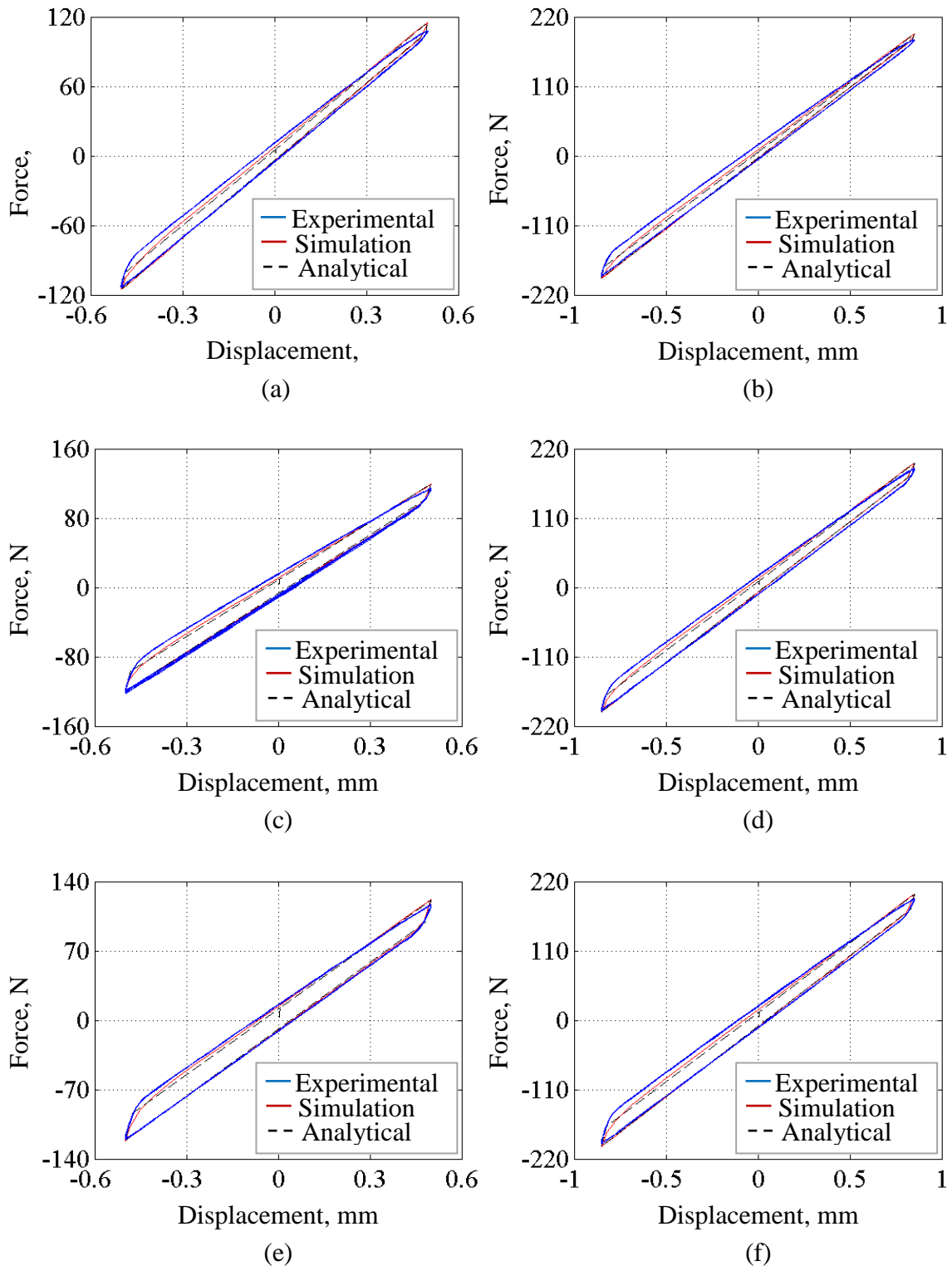
Figure 4.7 Comparison of experimental, numerical and analytical hysteresis loops for Configuration sb22 at PK-PK loading of (a) 1.0 mm, (b) 1.7 mm and for Configuration sb23 at PK-PK loading of (c) 1.0 mm, (d) 1.7 mm and for Configuration sb24 at PK-PK loading of (e) 1.0 mm and (f) 1.7 mm

Table 4.4 Profile of a square strand cross-section of 3×3 and 4×4 mm along the length of the strand presented as the width (b) and the height (h)

Length, mm	Cross-section of 3×3 mm		Cross-section of 4×4 mm	
	b, mm	h, mm	b, mm	h, mm
0.00	2.99	2.99	3.99	3.99
20.0	2.99	2.98	3.99	3.99
40.0	2.99	2.99	3.99	3.99
60.0	2.99	2.99	3.99	3.99
80.0	2.99	2.99	3.99	3.99
100	2.99	2.99	3.99	3.99
120	2.99	2.99	3.99	3.99
140	2.98	2.98	3.99	3.99
160	2.99	2.99	3.99	3.99
180	3.00	2.98	3.99	3.99
200	2.99	2.98	3.99	3.99
220	2.99	2.99	3.99	3.99
240	2.99	2.99	3.99	3.99
260	2.99	2.99	3.99	3.99
280	2.98	2.98	3.99	3.99
300	2.99	2.99	3.99	3.99

Comparison of the loss factor and the stiffness obtained analytically, numerically and experimentally are represented in Table 4.5 for Configurations sb01–sb12 and Table 4.6 for Configurations sb13–sb24.

Table 4.5 Comparison of analytically, numerically and experimentally obtained damping
characteristics for Configurations sb01–sb12

Configuration	Loading, mm	Analytical		Numerical		Experimental	
		Loss factor	Stiffness, N/mm	Loss factor	Stiffness, N/mm	Loss factor	Stiffness, N/mm
sb01	1.000	0.109	16.48	0.116	14.86	0.074	14.56
	1.700	0.067	15.90	0.072	15.20	0.047	15.43
	2.500	0.048	15.63	0.051	15.28	0.042	15.33
sb02	1.000	0.188	17.86	0.201	14.50	0.102	12.97
	1.700	0.119	16.74	0.128	14.86	0.065	15.17
	2.500	0.084	16.22	0.090	15.15	0.051	15.49
sb03	1.000	0.233	18.78	0.248	14.84	0.161	13.87
	1.700	0.151	17.30	0.162	14.71	0.099	15.09
	2.500	0.107	16.61	0.115	15.01	0.075	15.92
sb04	1.000	0.080	53.40	0.085	50.57	0.062	49.83
	1.700	0.052	52.07	0.054	50.70	0.048	49.54
	2.500	0.038	51.46	0.039	50.53	0.045	48.58
sb05	1.000	0.139	56.38	0.147	48.99	0.158	49.77
	1.700	0.088	53.85	0.092	50.20	0.103	49.96
	2.500	0.064	52.71	0.066	50.87	0.092	49.25
sb06	1.000	0.174	58.36	0.184	48.29	0.178	50.24
	1.700	0.111	55.04	0.117	49.68	0.136	49.62
	2.500	0.080	53.54	0.084	50.57	0.117	47.84
sb07	1.000	0.105	36.79	0.110	35.02	0.103	34.15
	1.700	0.066	35.62	0.068	34.59	0.063	34.74
	2.500	0.048	35.10	0.049	34.31	0.048	35.79
sb08	1.000	0.187	39.52	0.196	34.09	0.170	34.67
	1.700	0.116	37.28	0.122	35.08	0.118	36.61
	2.500	0.082	36.25	0.086	34.91	0.091	35.71
sb09	1.000	0.237	41.35	0.251	33.78	0.203	34.35
	1.700	0.148	38.39	0.156	34.63	0.125	36.19
	2.500	0.105	37.00	0.110	35.11	0.092	36.58
sb10	1.000	0.083	120.0	0.085	114.7	0.061	111.9
	1.700	0.057	117.4	0.056	113.9	0.051	110.7
	2.500	0.045	116.2	0.043	113.3	0.063	112.1
sb11	1.000	0.139	126.0	0.145	115.7	0.115	114.5
	1.700	0.091	120.9	0.092	115.5	0.086	113.1
	2.500	0.068	118.7	0.068	114.7	0.086	112.6
sb12	1.000	0.175	129.9	0.182	113.6	0.173	114.0
	1.700	0.113	123.3	0.116	116.3	0.121	112.1
	2.500	0.083	120.3	0.084	115.6	0.098	113.4

Table 4.6 Comparison of analytically, numerically and experimentally obtained damping characteristics for Configurations sb13–sb24

Configuration	Loading, mm	Analytical		Numerical		Experimental	
		Loss factor	Stiffness, N/mm	Loss factor	Stiffness, N/mm	Loss factor	Stiffness, N/mm
sb13	1.000	0.074	31.18	0.078	29.46	0.046	29.49
	1.700	0.046	30.44	0.048	29.71	0.040	29.69
sb14	1.000	0.130	32.90	0.136	28.75	0.109	30.14
	1.700	0.081	31.53	0.085	29.37	0.072	30.08
sb15	1.000	0.164	34.05	0.171	28.36	0.109	30.56
	1.700	0.103	32.21	0.109	29.15	0.078	31.20
sb16	1.000	0.057	102.6	0.060	98.43	0.073	95.93
	1.700	0.039	100.4	0.039	98.43	0.059	96.09
sb17	1.000	0.097	105.9	0.102	96.61	0.120	93.91
	1.700	0.063	102.7	0.065	98.66	0.089	95.18
sb18	1.000	0.122	108.3	0.127	95.94	0.130	94.63
	1.700	0.078	104.2	0.081	98.12	0.096	95.38
sb19	1.000	0.073	69.91	0.076	67.58	0.068	69.36
	1.700	0.048	68.46	0.048	66.85	0.045	68.12
sb20	1.000	0.127	73.34	0.132	66.85	0.120	70.77
	1.700	0.080	70.57	0.083	67.74	0.084	69.58
sb21	1.000	0.162	75.62	0.168	66.09	0.145	68.76
	1.700	0.101	71.93	0.105	67.99	0.091	69.16
sb22	1.000	0.065	230.8	0.064	222.4	0.087	216.8
	1.700	0.048	227.4	0.045	221.4	0.072	215.9
sb23	1.000	0.101	238.3	0.103	225.9	0.136	218.0
	1.700	0.069	231.9	0.068	223.9	0.094	218.2
sb24	1.000	0.125	243.2	0.127	222.9	0.144	218.5
	1.700	0.084	234.9	0.083	224.9	0.109	218.3

4.4 Conclusions

Three point bend tests were performed on multi-strand beams (MSB) at different configurations and different loading levels (Table 3.1). The conclusions drawn from the work in this chapter can be summarised as

➢ The damping behaviour of the MSB that was obtained experimentally followed the analytical and numerical damping behaviour for most of the configurations that were shown in Table 3.1.

➢ Changing the clamp force and loading levels had approximately no effect on the systems stiffness.

➢ The clamp force and loading levels were directly proportional to the energy dissipation per cycle and the loss factor.

➢ The experimental damping characteristics results (Table 4.2 and Table 4.3) were in good agreement with the findings from Chapter 3 regarding the effect of the parameters under study (Table 3.1) on the damping behaviour of the MSB.

➢ The visual observation of the experimentally obtained hysteresis loops validated the experimental estimations of the coefficient of friction and the modulus of elasticity performed in Sections 3.3 and 3.4 respectively.

Chapter 5

Quasi-static damping behaviour of multi-strand diagonal beams

5.1 Introduction

The work presented in Chapter 3 and Chapter 4 investigated the damping levels in multi-strand beams (MSB) where the system was at an angle of 0° with the horizontal axis. This chapter will present work on multi-strand beams positioned at different angles with the horizontal axis. This configuration was used for two reasons: first, to explore the effect of the angle of rotation (φ) on the system's stiffness; second to investigate the effect of φ on the frictional forces that are induced between the mating surfaces in such a system and on the amount of the slip deformations which in turn affect the energy dissipation levels.

A series of experiments were conducted on the diagonal multi-strand beams, which studied parameters such as the length of the individual strands, the number of strands, the clamp force levels, and the loading displacement levels. During the experiments, the DMSB was placed at 45° with the horizontal axis.

Analytical models were built, first, to estimate the stiffness of a system that experiences frictional behaviour and, second, to describe the damping behaviour of the DMSB during the flexural loading. The analytical models were developed to include the effect of the angle of rotation (φ) into the calculations.

Finite element (FE) models were built to simulate the flexural behaviour of the DMSB that was placed at 45° where frictional contact presents between the individual mating strands.

This was followed by building FE models for Configurations db3 and db6 (see Table 5.1) to describe the damping behaviour where the angle of rotation changes in the range of 0°–45° with the horizontal axis at an angle step of 5°.

Subsequently, analytical models were built to take the change of the angle of rotation from 0° through 45° into consideration.

A comparison was performed between the hysteresis loops that were obtained experimentally, numerically and analytically for different configurations where the angle of rotation was at 45°. The results from Chapter 3 were used for studying the multi-strand beams at angle of rotation of 0° for specific configurations.

A comparative study was then conducted in order to compare the damping characteristics of the DMSB through the range of the angles of rotation (0°–45°).

Thermal effect (temperature rise) was studied to investigate if there was a major increase that might change the strands properties as shown in Appendix G.

5.2 Quasi-static experiments on the diagonal multi-strand beams

This section is dedicated to the quasi-static tests performed on the diagonal multi-strand beams. The effect of various parameters on the damping levels in the DMSB was considered during the tests. The various set-ups of the DMSB were exposed to cyclic quasi-static displacement loading. For the purposes of this study the system was constructed of individual key steel square strands to form a beam-like structure.

5.2.1 Methodology

Quasi-static tests were conducted on the diagonal multi-strand beams and the three point bend configuration was adopted for the experiments. The experiment set-up is shown in Figure 5.1. Various parameters such as the length of the individual strands, the number of strands in the system, the loading displacement levels and the clamp force levels, shown in Table 5.1, were considered during the tests and their effects on the damping levels of the DMSB were investigated. The DMSB was placed diagonally at an angle of rotation (φ) of 45°, see Figure 5.1a, during the experiments to minimize any potential of twisting.

A servo-hydraulic test machine (MTS 858 Table Top System) was used to conduct the tests on the DMSB through applying a displacement controlled quasi-static load. The dimensions of the individual strands were 4×4×300 mm and the span distance varied between 250 mm and 200 mm. Four strand and nine strand configurations were used to form the DMSB.

(a)   (b)
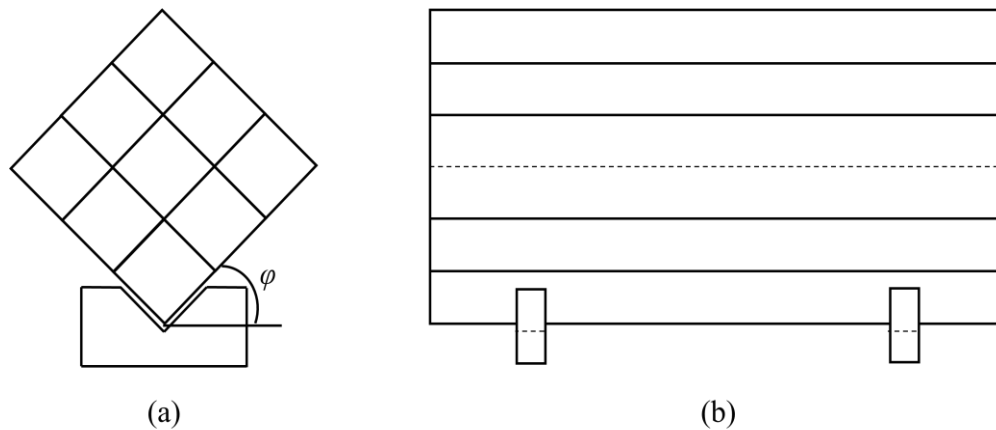
Figure 5.1 Experimental set-up for diagonal nine-strand beam showing (a) the side view and (b) the front view.

Tests were carried out on Configuration db01 through db12 as shown in Table 5.1 and the DMSB was positioned between two stationary supports and the test machine's non-rotating, uniaxial motion, loading roller. Special supporters were manufactured to maintain the DMSB horizontal during the experiment. Figure 5.2 shows the specially manufactured support. One supporter was located at 125 mm and the other at 100 mm from the centre of the DMSB in order to form span distances of 250 mm and 200 mm respectively. The loading roller was positioned at the centre.

A clamping mechanism was used to hold the individual strands together during the experiments. The rotation of the DMSB at angle of 45° necessitated applying four pairs of clamps to provide the required clamp force on the entire outer surfaces of the DMSB. The clamp units were the same as those used in Chapter 3 because the strands used in these experiments resembled the strands used in the Chapter 3 experiments; therefore, the calibration of the normal forces applied to the clamps in Section 3.4.1 was used for this section as well. The clamps were located at 25 mm from each stationary supporter on each side.

Figure 5.3 shows the diagonal multi-strand beams (DMSB) for Configuration db06 during the flexural loading with the clamps attached. Three clamp force levels were used to clamp the system 100 N, 190 N and 250 N.

Table 5.1 Test parameters for the DMSB

Test Configuration No	Span distance, mm	No of strands	Clamping force, N	Peak displacement, mm×Sin(ωt)		
				1.00	1.70	1.00
db01	250	4	100	✓	✓	✓
db02	250	4	190	✓	✓	✓
db03	250	4	250	✓	✓	✓
db04	250	9	100	✓	✓	✓
db05	250	9	190	✓	✓	✓
db06	250	9	250	✓	✓	✓
db07	200	4	100	✓	✓	✓
db08	200	4	190	✓	✓	✓
db09	200	4	250	✓	✓	✓
db10	200	9	100	✓	✓	✓
db11	200	9	190	✓	✓	✓
db12	200	9	250	✓	✓	✓

Figure 5.2 Stationary supporter
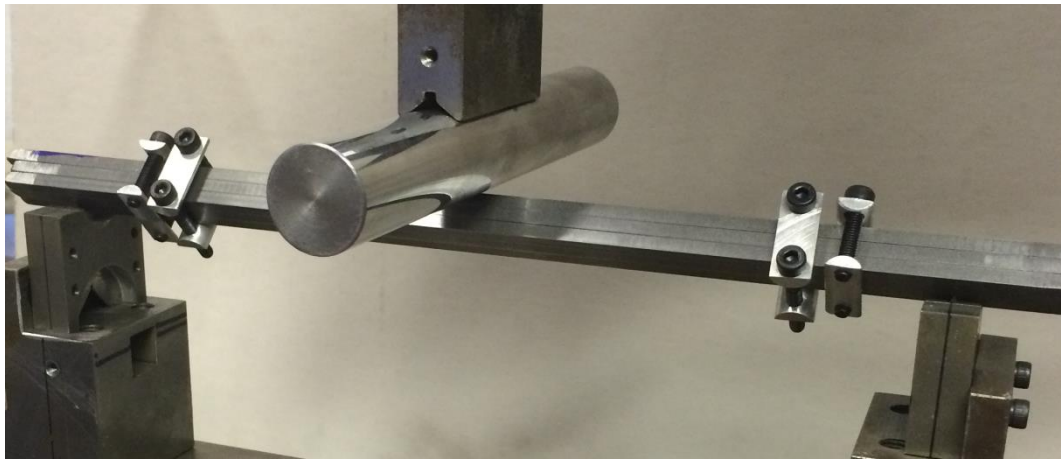
(a)

(b)

Figure 5.3 Diagonal nine-strand beam (a) under flexural loading (b) with clamps attached

Experiments were carried out at two amplitude levels of peak-to-peak (PK-PK) sinusoidal displacement loading of 1.0 mm and 1.7 mm. These values and the force needed to initiate the slip were calculated in a prior investigation in Sections 4.2.3 and 4.2.4. The test procedure adopted to test the DMSB is similar to the procedure performed on the (MSB) in Section 4.2.2 but with a pre-displacement of 0.2 mm that was applied to the loading roller where visual increase in the force signal was observed. Peak-to-peak (PK-PK) sinusoidal displacements of 1.0 mm and 1.7 mm was applied for each configuration followed by further displacement at the lowest amplitude (1.0 mm) at the end of each loading displacement (1.7 mm).

5.2.2 Experimental results

The displacement and the force signals were recorded via a closed-loop controller during the flexural loading to trace the expected sinusoidal shape for the displacement. The pair of signals shown below in Figure 5.4 show the phase difference (from damping) in the force signal which relates to the friction effect between the strands and a distortion of the waveform that is derived from the nonlinearity.
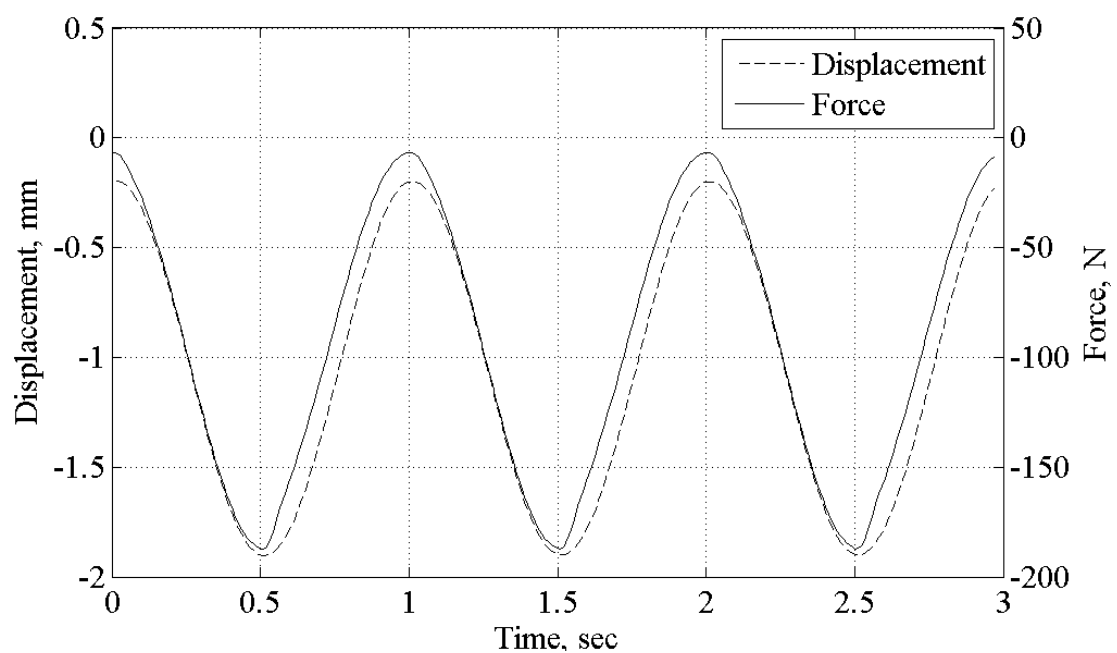
Figure 5.4 Force and displacement histories for Configuration db06 at PK-PK displacement of 1.7 mm.

Configurations db1–db12, Table 5.1, experienced three sinusoidal displacement loading stages (1 mm, 1.7 mm and 1 mm) during the flexural tests. In section 3.4.2, the maximum PK-PK displacement amplitude for multi-strand beams was limited to 1.7 mm for systems where the span distance between the individual strands was 200 mm, corresponding to the investigations performed in that section. However, to examine the effect of the loading levels on the damping behaviour in the multi-strand beams, the maximum loading was set at 1.7 mm for the entire configurations in this chapter.

 The damping behaviour was obtained by plotting the hysteresis loops from the force and displacement time histories. Unfiltered hysteresis loops for Configurations db03, db06, db09

and db12 are shown in Figure 5.5. Each hysteresis loop contained the two displacement loadings (1 mm and 1.7 mm). In Figure 5.5, it can be seen that the start of the loading stage, upper right corner on the hysteresis loop, is narrower than the start of the unloading stage, lower left corner on the hysteresis loop. This behaviour can be related to the larger amount of loading at the end of the loading stage, where the loading is at its maximum value, and this causes the system to restore from higher deformation levels at the start of the unloading stage than at the start of the loading stage.

Generally, at the microslip region, in the transition from stick to slide, at the start of both the loading and unloading stage, the diagonal multi-strand beams (DMSB) appeared to take a longer distance to transit from sticking to sliding than the multi-strand beams (MSB), which was discussed in Chapter 3, and the reasons for this behaviour are twofold. First, the loading condition during the experiment necessitated that the loading roller of the servo-hydraulic test machine had a point contact with the upper-top diagonal strand in the DMSB, which means that the flexural loading started at the single upper-top strand, then the loading transited to the next layers of the diagonal strands, and so on. Second, interestingly, the arrangement of the strands in the DMSB and the fact that the vertical loading from the test machine was no longer perpendicularly distributed on the contact regions, as was the case for the multi-strand beams (MSB) in chapter 3, allowed creation of diagonal contact regions. This means that each strand in the DMSB had two of its surfaces experiencing dry frictional contact, which was double the number of strand surfaces with frictional contact in the MSB. Bearing this fact in mind and knowing that the contact intensity may vary between the different couples of strands that are in contact, this would lead to some diagonally placed strand couples deforming separately from other couples instead of deforming simultaneously, as seen visually during the experiment, and this could be the major reason for the extension in microslip distance.
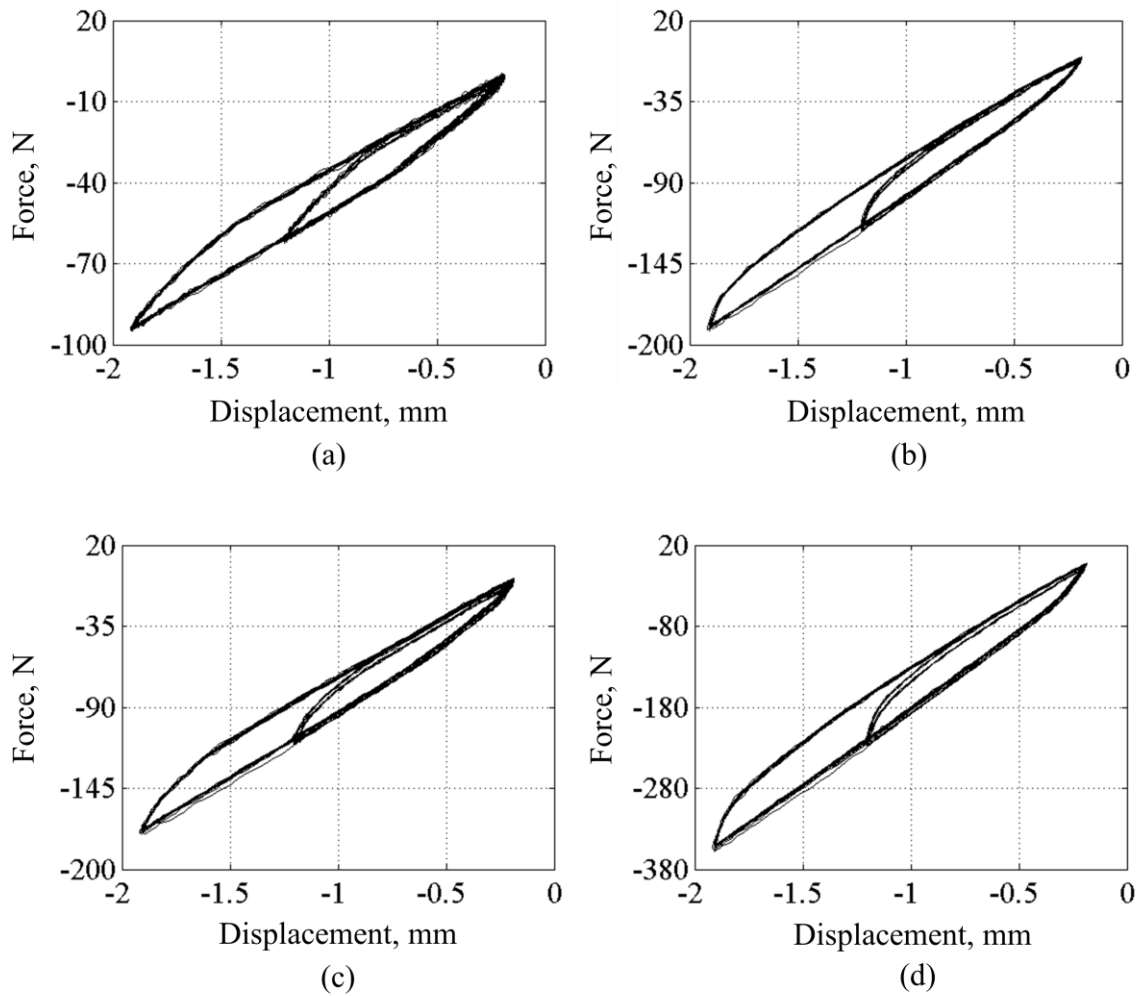
Figure 5.5 Unfiltered hysteresis loops at PK-PK displacement loading of 1 mm and 1.7 mm for Configuration (a) db03, (b) db06, (c) db09 and (d) db12

The unfiltered force traces contained noise in the range of 2N–4N. The most likely cause for this is the relatively low sensitivity of the force sensor as its maximum range was 10 KN.

As with the work in Chapter 4, the Fourier transform was used to filter the data. Figure 5.6 shows the filtered experimentally obtained hysteresis loops for Configurations db03, db06, db09 and db12.
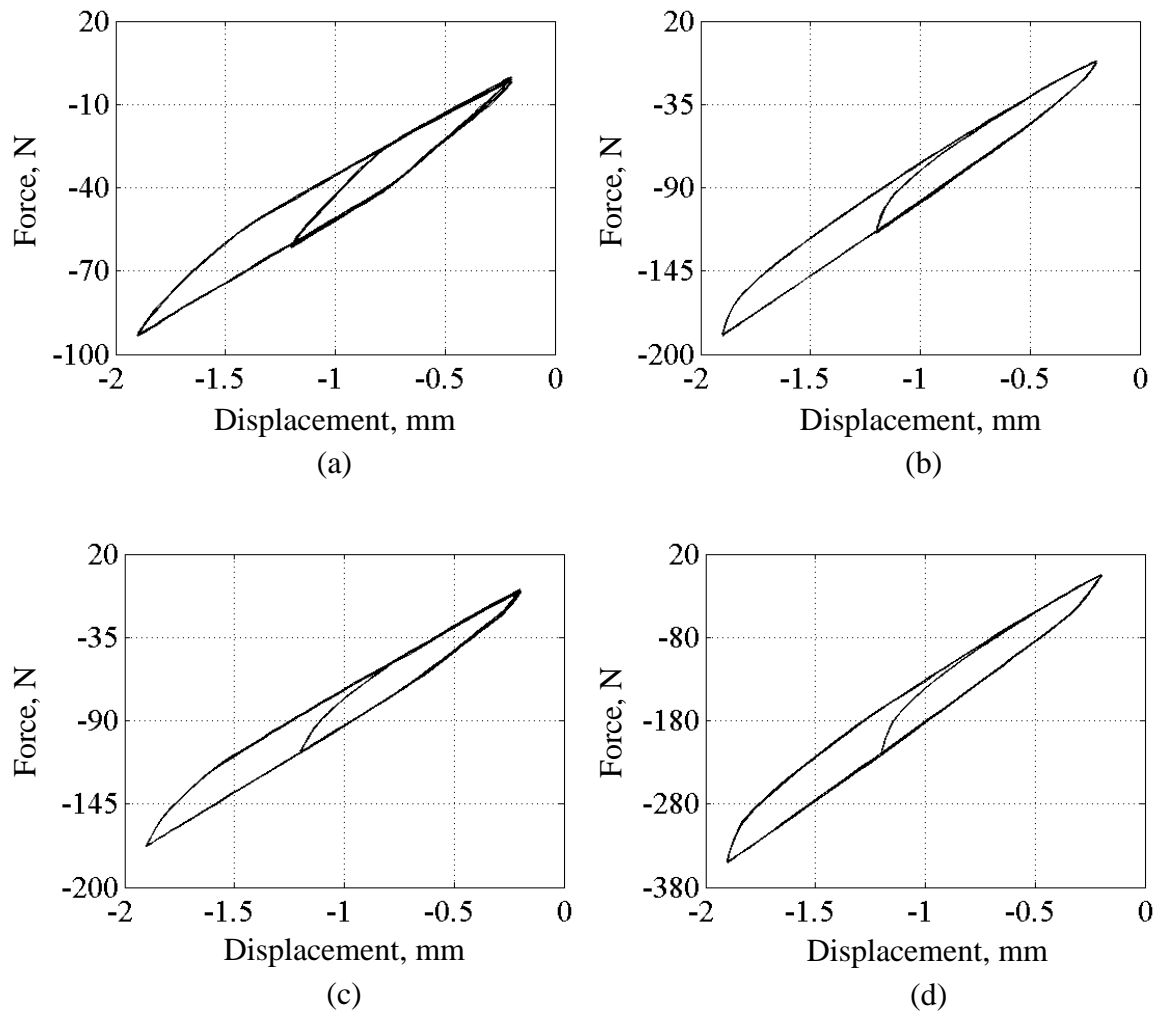
Figure 5.6 Filtered hysteresis loops at PK-PK displacement loading of 1 mm and 1.7 mm for Configuration (a) db03, (b) db06, (c) db09 and (d) db12

5.3   Analytical modelling

The aim of the work described in this section was to build analytical models with the ability to describe the damping levels that can be obtained from diagonal multi-strand beams (DMSB) during a flexural loading where the DMSB would be rotated through angles of rotation ranging from 0°–45°. The first purpose of these analytical models was to estimate the DMSB stiffness and the second was to describe the damping behaviour for these systems.

100

5.3.1 Effect of angle of rotation φ on system damping levels

The diagonal multi-strand beams (DMSB) discussed in this chapter were positioned at 45° with the horizontal axis during the experiments, unlike the setup used for the multi-strand beams (MSB) in Chapter 3 where the strands were placed horizontally. Given that both the numerical and the analytical models in this work are designed to cover the range of angles 0°–45°, it was crucial to investigate the effect of the angle of rotation on the damping characteristics of the DMSB. Investigation of these characteristics was conducted numerically and involved studying the effect of φ on both the strain energy (stiffness) levels and the energy dissipation (frictional forces) levels.

5.3.1.1 Effect of φ on the strain energy (system stiffness)

The second moment of area was adopted to represent the stiffness in this work as the other parameters that could have an effect on the stiffness during rotating the DMSB, such as the length and the modulus of elasticity, were unchanged. The strands used in this work were formed into square key steel beams and the overall dimensions of the DMSB were kept square (the width equals the height) during the entire configurations. The strain energy can be represented as

$$U = \frac{1}{2}Kx^2 \qquad\qquad 5.1$$

where U is the strain energy, K is the system stiffness and x is the system displacement.

The rotating the DMSB with angle of rotation in the range of 0°–45° is expected to have no effect on the behaviour of the second moment of area [104].

5.3.1.2 Effect of φ on the strain dissipation levels (frictional forces)

In a system where there is dry frictional contact, the frictional forces induced between the mating surfaces play an important role in determining the level of energy that can dissipate per cycle. The relation between the energy dissipation and the frictional forces is shown in Equation 5.2 [53, 102].

$$dW = 4F_d \Delta u \qquad\qquad 5.2$$

where dW is the energy dissipation per cycle, F_d is the frictional force and Δu is the relative displacement between the surfaces in contact.

The frictional forces depend primarily on both the normal forces applied perpendicular in the thickness direction of the surfaces of contact and the coefficient of friction between the mating surfaces. The normal forces in this work were the clamping forces and the flexural loading applied to the system. The clamping forces were maintained perpendicular to the surfaces of contact; however, the flexural loading was no longer perpendicular to the thickness direction of the contacted strands because the surfaces of contact between the mating strands for the diagonal multi-strand beams (DMSB) were inclined with an angle of φ, while the flexural load was kept vertical during the entire loading process (see Figure 5.3).

In order to count for the vertical flexural load effect on the inclined contact surface, the component of the flexural load that was normal to the contact surface was considered as a normal force acting to generate the frictional forces in addition to the clamping forces that were already normal to the contact surface. Figure 5.7 shows the distribution of the flexural load in the DMSB. This distribution assumes that all contact surfaces reach sliding stage during the rotation of the DMSB in a range of angles of 0°–45°.
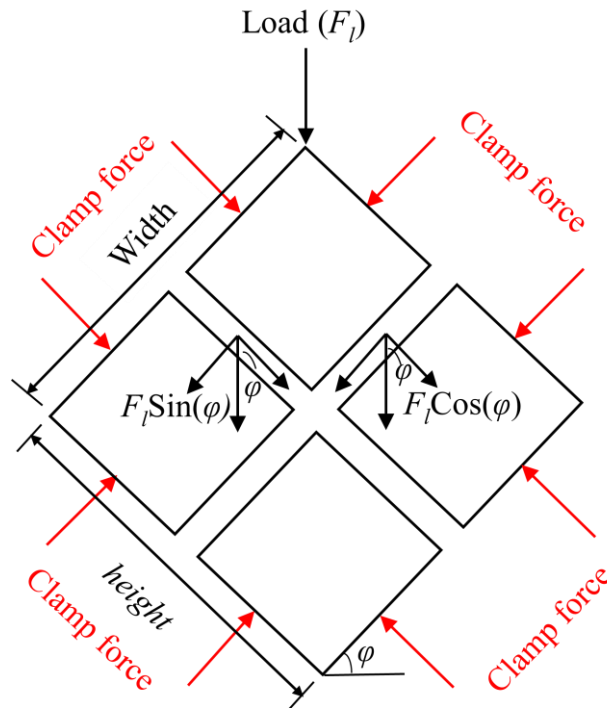
Figure 5.7 Load distribution on inclined contact surfaces – diagonal four-strand beam is shown

According to Figure 5.7, the frictional forces (F_d) acting on the surfaces that were in contact could be expressed as

$$F_d = F_c \mu + F_l \cos(\phi) \mu + F_l \sin(\phi) \mu \qquad 5.3$$

where F_d is the frictional force, F_c is the clamp force, F_l is the flexural load and μ is the coefficient of friction.

The analytically obtained profile for the frictional force within the range of the angles of rotation of 0°–45° is shown in Figure 5.8 and Figure 5.9 for Configurations db03 and db06. The general behaviour tended toward a slight increase in the values of the frictional forces with increasing the angle of rotation. This could cause an increase in the amount of the energy that might dissipate per cycle from the DMSB due to friction.
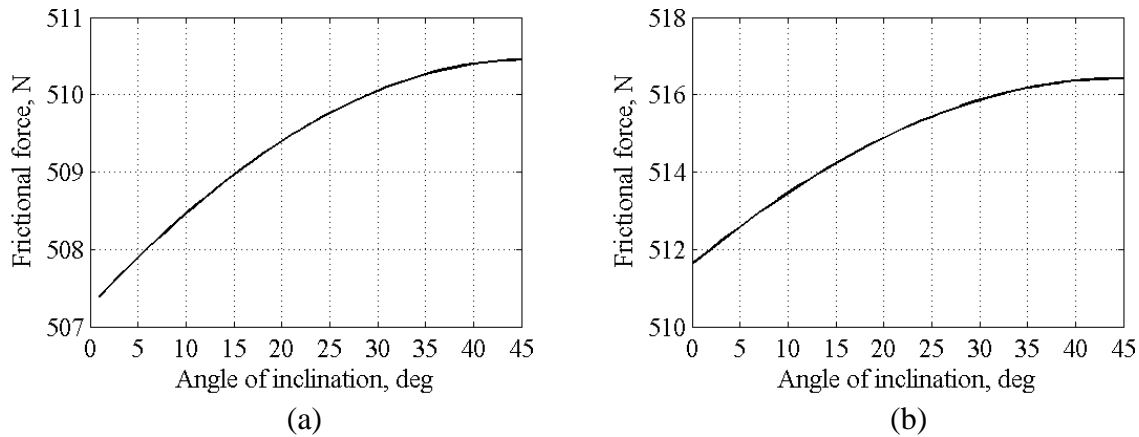
Figure 5.8 The frictional force versus the angle of rotation for Configuration db03 at PK-PK displacement of (a) 1.0 mm and (b) 1.7 mm
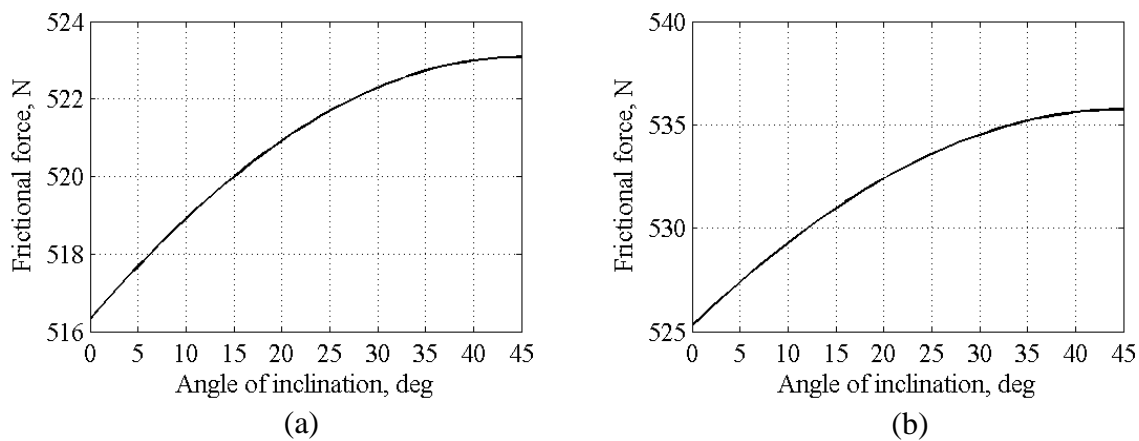
Figure 5.9 The frictional force versus the angle of rotation for Configuration db06 at PK-PK displacement of (a) 1.0 mm and (b) 1.7 mm

5.3.2 Analytical hysteresis loops

The DMSB stiffness was predicted through estimating the value of the frictional second moment of area (I_f) analytically in a technique similar to that explained earlier in Section 3.6.1where the upper and lower bounds (Equation 3.11 and Equation 3.13) for the linear relationship of the displacement-coefficient of friction were calculated and then the amount of the coefficient of friction that could bond the contact status was found through Equation 3.19. Next, depending on the values of the displacement at each specific coefficient of

friction values, the frictional second moment of area was estimated. Figure 5.10 shows the linear relationship between the displacements and the coefficient of friction values for Configurations db03 and db06 at an angle of rotation of 45° and a peak amplitude displacement of 0.5 mm.
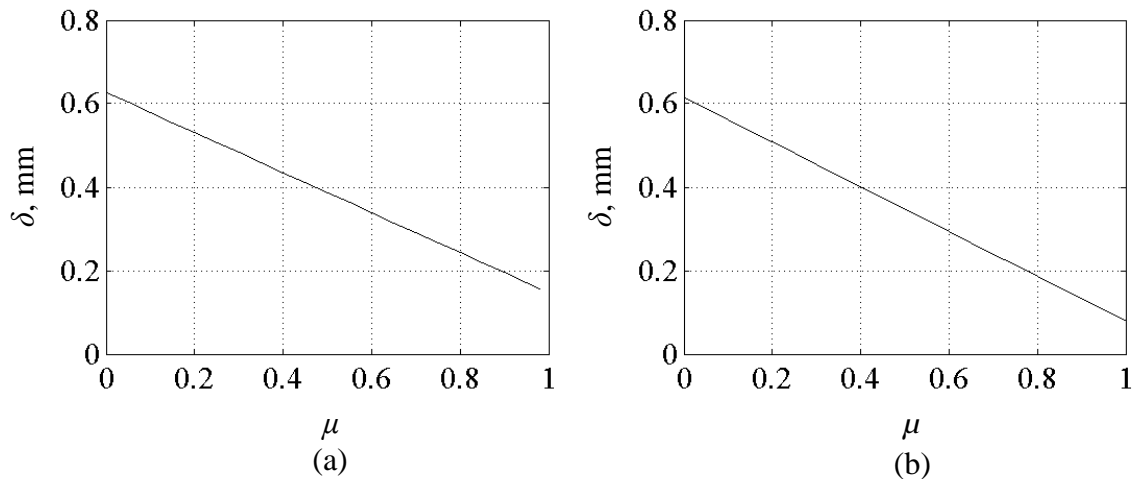
Figure 5.10 Displacement versus coefficient of friction at a peak amplitude displacement
loading of 0.5 mm for Configurations (a) db03 and (b) db06

The linearity of the relation between the displacement and the coefficient of friction was validated through building FE models and exposing them to ramp loading with different coefficient of friction values at the contact regions each time, as shown in Figure 5.11.
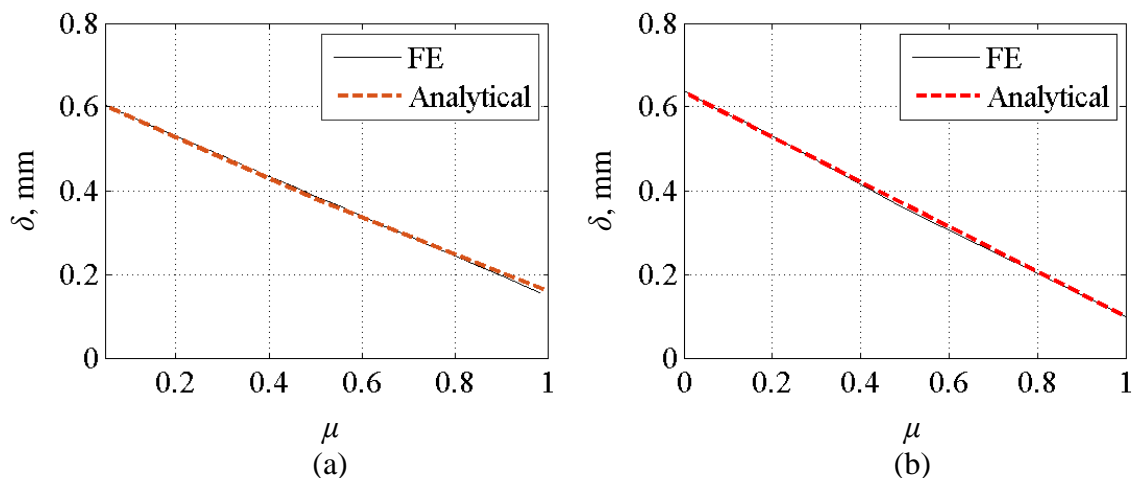
Figure 5.11 Peak displacement versus coefficient of friction for the DMSB comparing the
FE and analytical model for Configurations (a) db03 and (b) db06

The analytically obtained frictional second moment of area (I_f) is presented in Figure 5.12 for Configurations db03 and db06. The relation between the frictional coefficient of friction and the coefficient of friction values was nonlinear.
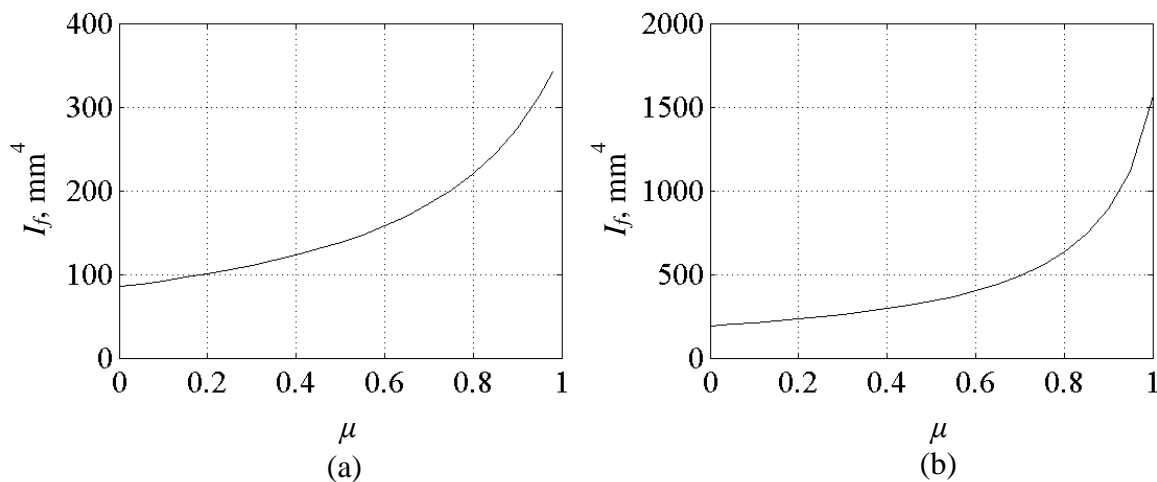
Figure 5.12 The frictional second moment of area versus the coefficient of friction obtained analytically for Configurations (a) db03 and (b) db06

The author at this stage preferred not to include all the sensitivity studies performed on the DMSB to investigate the effect of coefficient of friction and loadings on the frictional second moment of area as it might have been considered repetitive even though the DMSB system described in this chapter differed from the MSB system used in Chapter 3 but similar behaviour of the sensitivity was observed (for more information, read Section 3.6.1).

The same pathway as was used to calculate the analytical hysteresis loop in Section 3.6.3 was followed here, however the models here included the effect of the angle of rotation (φ). The model counts for the friction effect between the mating strands by introducing the term I_f which presents the stiffness of the DMSB experiencing dry frictional contact. The model produces a force-displacement response. This was extended into a force-displacement hysteresis loop to estimate the loss factor value (damping levels) that the DMSB could provide for the specific configurations, Table 5.1, at the range of the angles of rotation (φ).

Figure 3.21 shows the various loading and unloading stages for the hysteresis loop. The starting point for the hysteresis loop begins from the origin point (0) in the Cartesian

coordinate system. Point (1) represents the sliding stage during the loading phase, second stage, ending at point (2).

To estimate the force-displacement hysteresis loop, the shear stress between the mating strands and the frictional stresses at the contact regions can be used to determine the force required to start the slipping in diagonal multi-strand beams. At the moment when the contacted strands begin to slide, the frictional force equals the shear force that tries to initiate the slipping. This force is described by Equation 3.21. The deformation that results from the slip force can be calculated through Equation 3.22. The third stage is the damping stage and this represents the transition from the sticking region into the sliding region. The damping stage starts from point (2) and represents the maximum force and displacement applied on the system, ending at point (3). This stage determines the damping amount in the produced hysteresis loop.

Depending on the applied force F_2 the maximum resulting displacement δ_2 is calculated by Equation 3.23. The force F_3 and displacement δ_3 at the end of the damping stage are calculated through Equations 3.24 and 3.25 respectively.

 The fourth stage is the sliding stage during the unloading phase. The fourth stage starts from point (3) and travels all the way to the position of the maximum force and loading on the other side of the hysteresis loop, the bottom left side, ending up at point (4).
The force F_4 and the displacement δ_4 of point (4) are found through Equations 3.26 and 3.27 respectively.

The sliding stage during the loading phase starts from point (5) and ends at point (2). The force F_5 and the displacement δ_5 at the start of the sliding stage are calculated through Equations 3.28 and 3.29 respectively.

The analytically obtained hysteresis loops are presented in Figure 5.13 through Figure 5.16 for the DMSB with Configurations db03, db06, db09 and db12 at peak-to-peak displacement loading of 1.0 mm and 1.7 mm. These configurations had an angle of rotation (φ) of 45° with the horizontal axis.

(a)   (b)
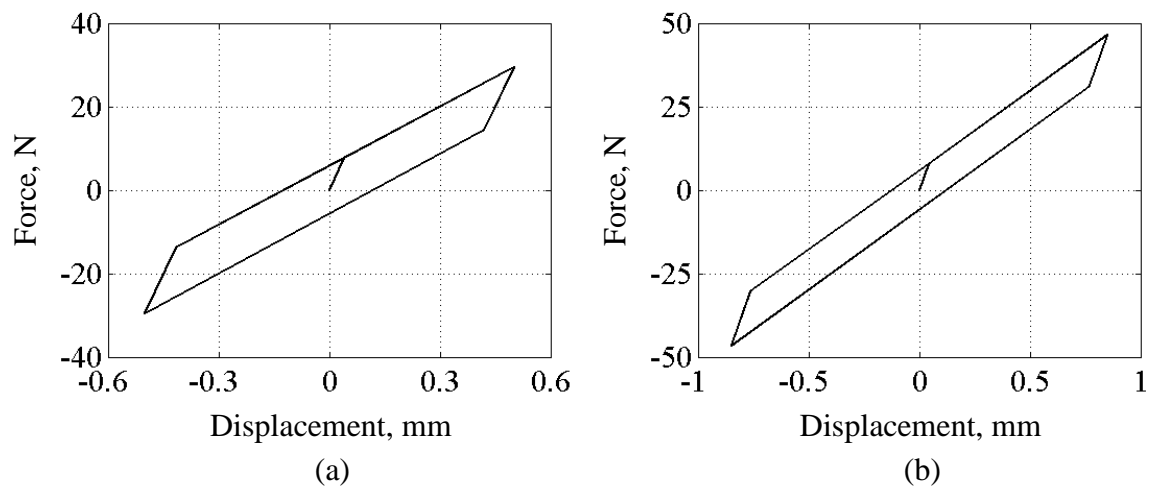
Figure 5.13 Analytical hysteresis loop for Configuration db03 at PK-PK displacement of (a) 1.0 mm and (b) 1.7 mm

(a)   (b)
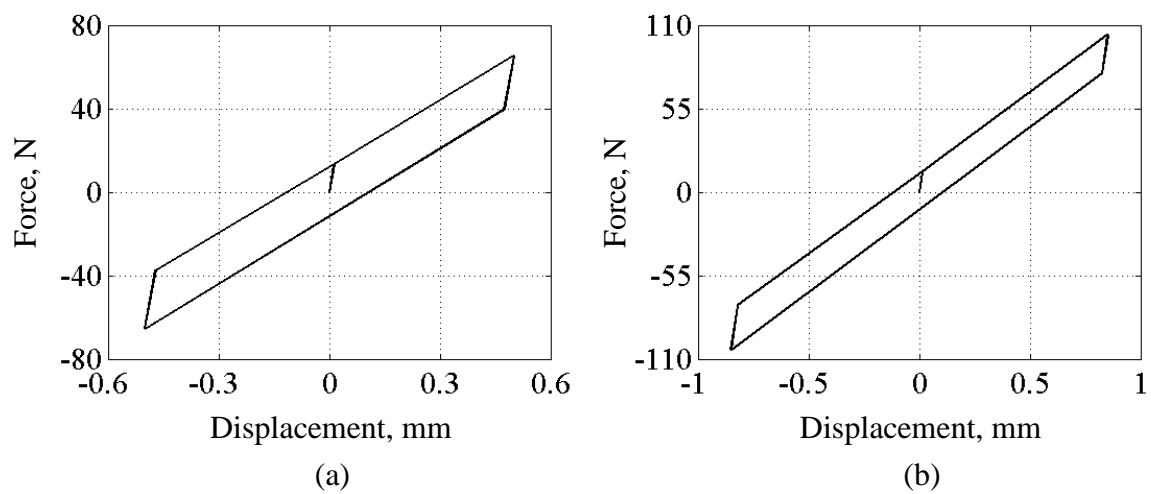
Figure 5.14 Analytical hysteresis loop for Configuration db06 at PK-PK displacement of (a) 1.0 mm and (b) 1.7 mm
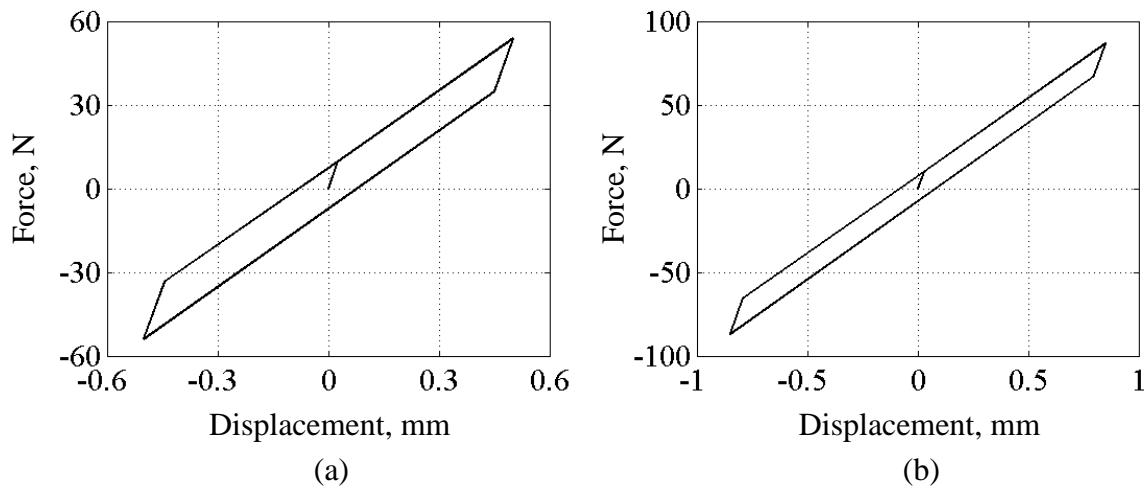
Figure 5.15 Analytical hysteresis loop for Configuration db09 at PK-PK displacement of (a) 1.0 mm and (b) 1.7 mm
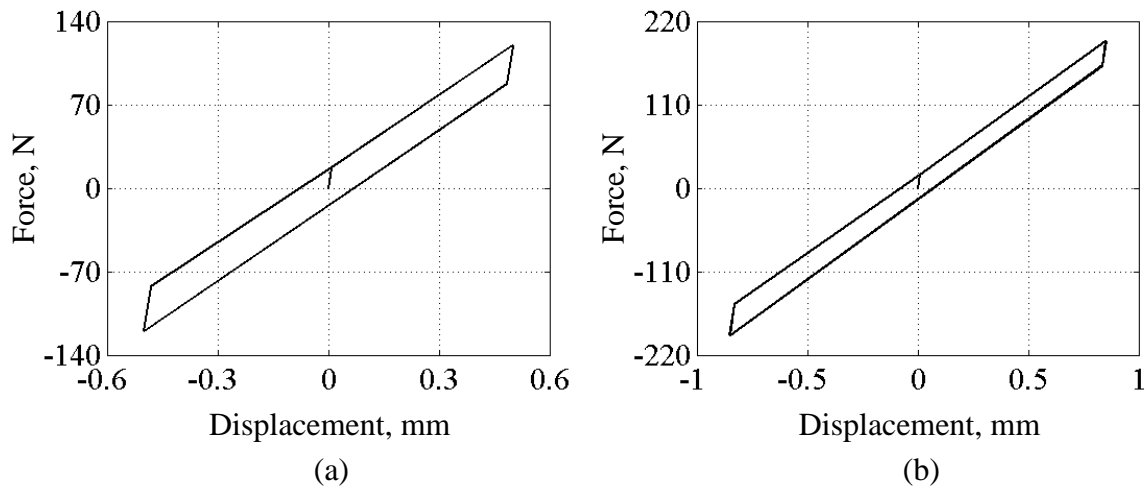
Figure 5.16 Analytical hysteresis loop for Configuration db012 at PK-PK displacement of (a) 1.0 mm and (b) 1.7 mm

5.4 Quasi-static numerical simulation of the DMSB

Numerical models of the DMSB for Configuration db01 through db12, Table 5.1, at an angle of rotation of 45° were built to simulate the experimental (Section 5.2) and the analytical quasi-static flexural behaviour (Section 5.3).

The three point bend was adopted for the entire configurations during the quasi-static sinusoidal displacement loading and the clamping forces were applied as an equivalent

distributed pressure on the outer surfaces. The clamp pressure was maintained normal to the contact surfaces between the mating surfaces during rotating the DMSB with angle of rotation 0° through 45°. Finite element commercial package, ANSYS, was used to construct the DMSB. Mesh and contact details were as defined previously in Section 3.5.

The numerical models for the DMSB were positioned at an angle of rotation of 45° and comprised four-strand and nine-strand arrangements that were clamped and exposed to flexural loading, as shown in Figure 5.17a and b respectively. The numerical models were constructed of square sectioned strands gathered through a frictional contact between the mating surfaces and held together by a clamp force to form the DMSB.

Configurations db03 and db06 were rotated at a range of angle of rotation (φ) of 0°–45° with the horizontal axis to investigate the effect of φ on the generated damping levels. DMSB models comprising four strands and nine strands are shown in Figure 5.18 and Figure 5.19 respectively, where the DMSB were rotated at angles of rotation of 15°, 25°, 35° and 45°. The individual strands used in the DMSB had a cross-section of 4×4 mm. The effects of parameters such as the span distance, the number of strands in the system and the clamp force level on the damping levels during the flexural loading were investigated. The modulus of elasticity was 190 GPa, deriving from the experimental work to evaluate the material properties as was presented in Section 3.3. The coefficient of friction was 0.25 and based on the experimental results to investigate the coefficient of friction values discussed in Section 3.4.

(a)

(b)
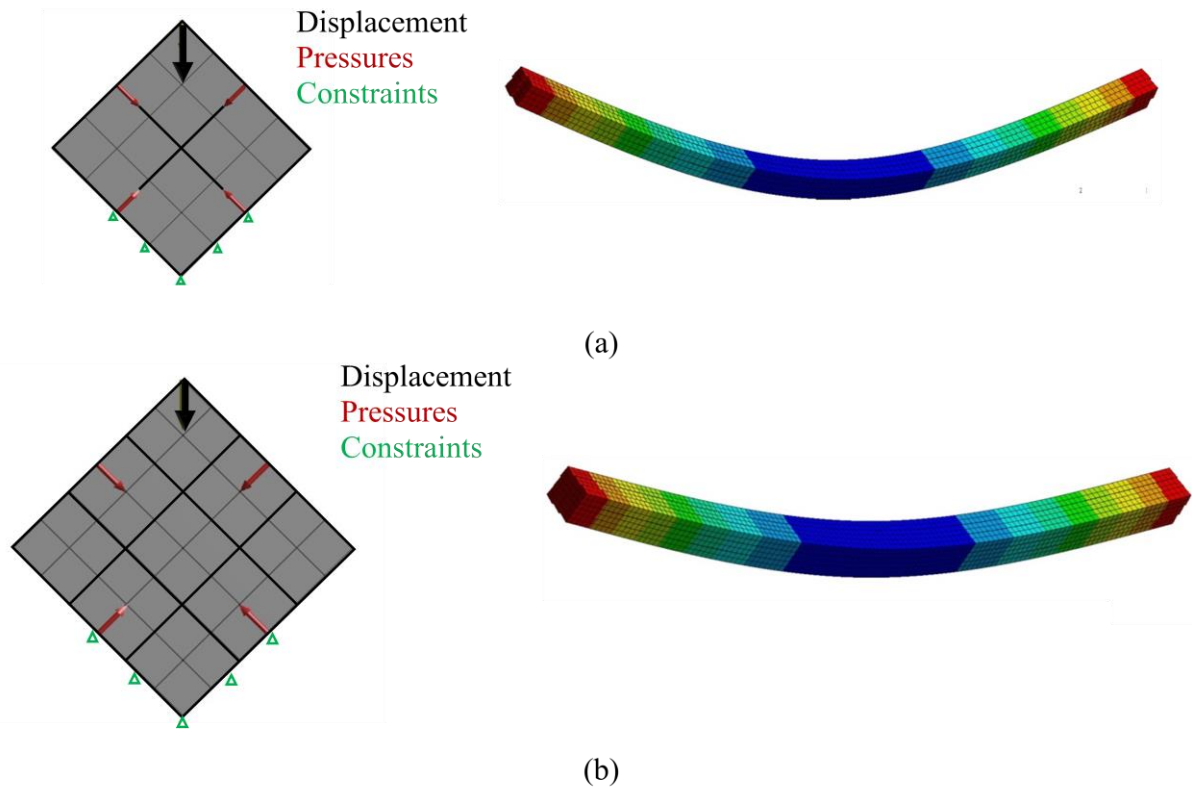
Figure 5.17 Numerical modelling of the DMSB positioned at angle of rotation of 45° and comprised of (a) four strands, and (b) nine strands – elemental arrangements as shown in the cross-sectioned view

The frictional behaviour was seen as a small phase difference in the force signal. A typical pair of force-displacement signals obtained numerically is shown in Figure 5.20.

Numerically obtained force-displacement relationships (hysteresis loops) for Configurations db03, db06, db09 and db12 at peak-to-peak quasi-static sinusoidal displacement loadings of 1.0 mm and 1.7 mm are shown in Figure 5.21. The average effective stiffness was estimated by applying a polynomial fit to the numerically obtained hysteresis loop. The energy dissipation amount per cycle was measured by numerical integration of the force-displacement curve. The loss factor was calculated from the hysteresis loop through counting the energy dissipation and the stored strain energy [99, 100].

(a)   (b)

(c)   (d)
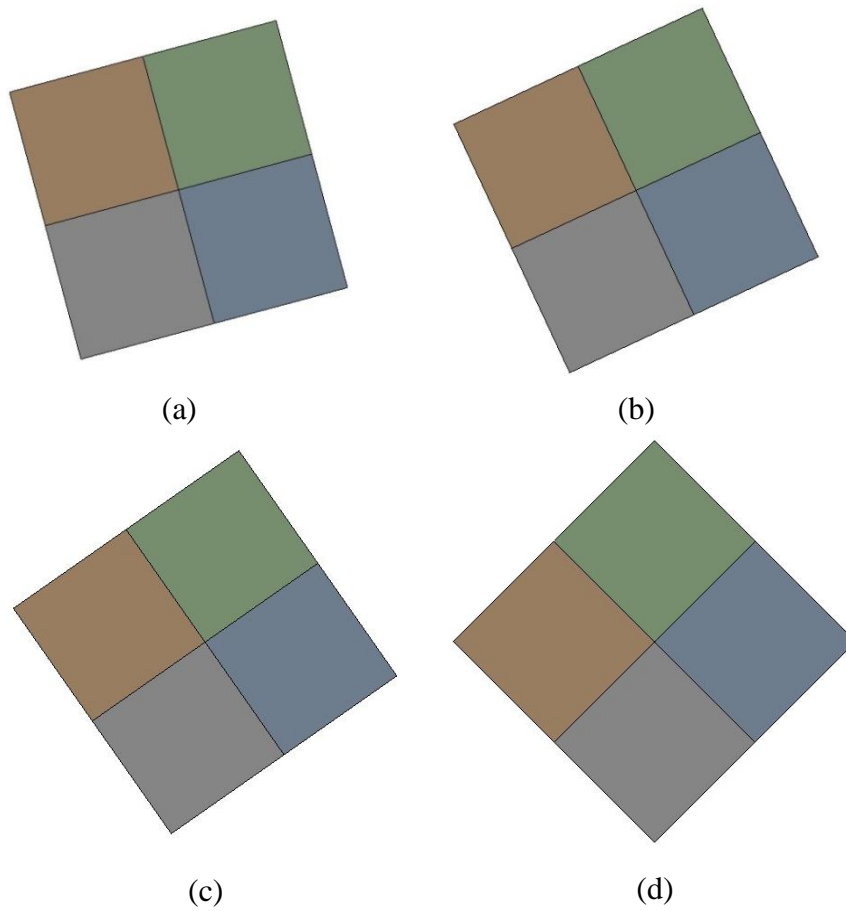
Figure 5.18 DMSB comprised of four strands (db03) with the system positioned at angles of rotation of (a) 15°, (b) 25°, (c) 35° and (d) 45° – individual strands are coloured separately

(a)   (b)

(c)   (d)
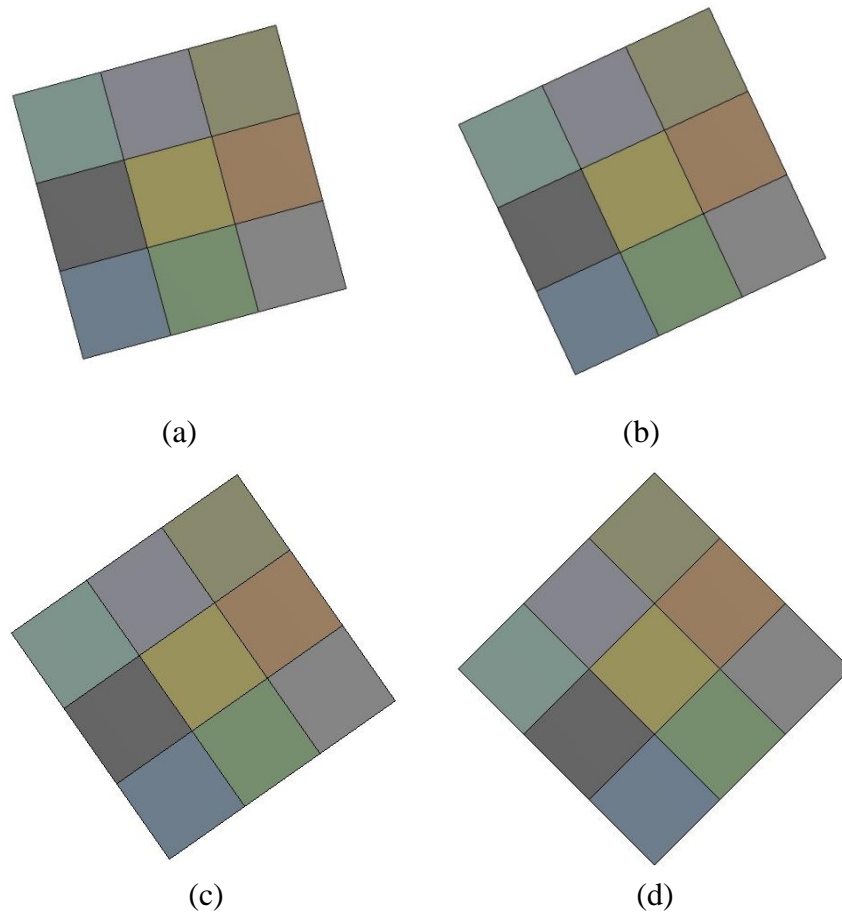
Figure 5.19 DMSB comprised of nine strands (db06) with the system positioned at angles of rotation of (a) 15°, (b) 25°, (c) 35° and (d) 45° – individual strands are coloured separately
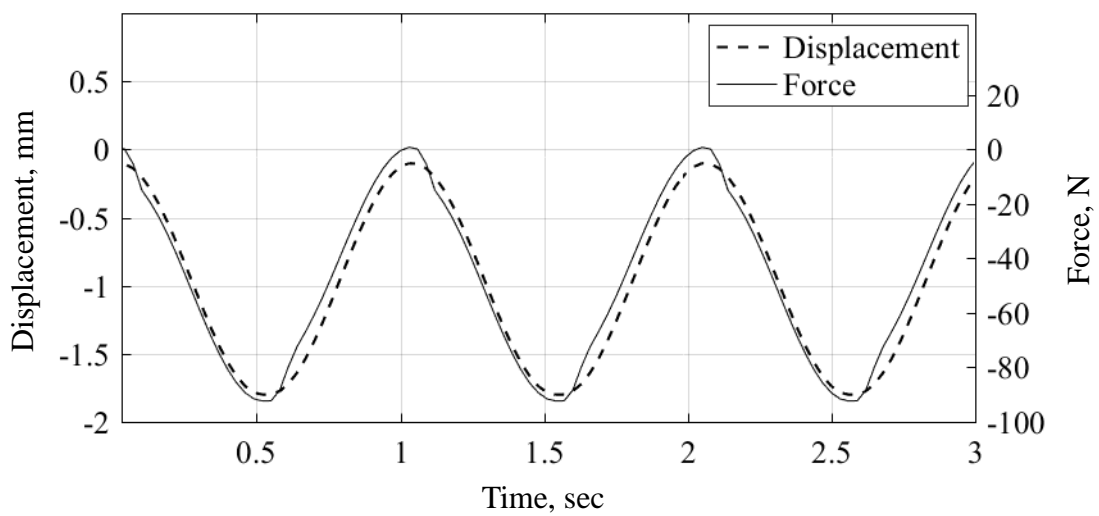
Figure 5.20 Numerical force-displacement time histories for Configuration db03 at displacement loading of 1.7 mm

(a)

(b)

(c)

(d)
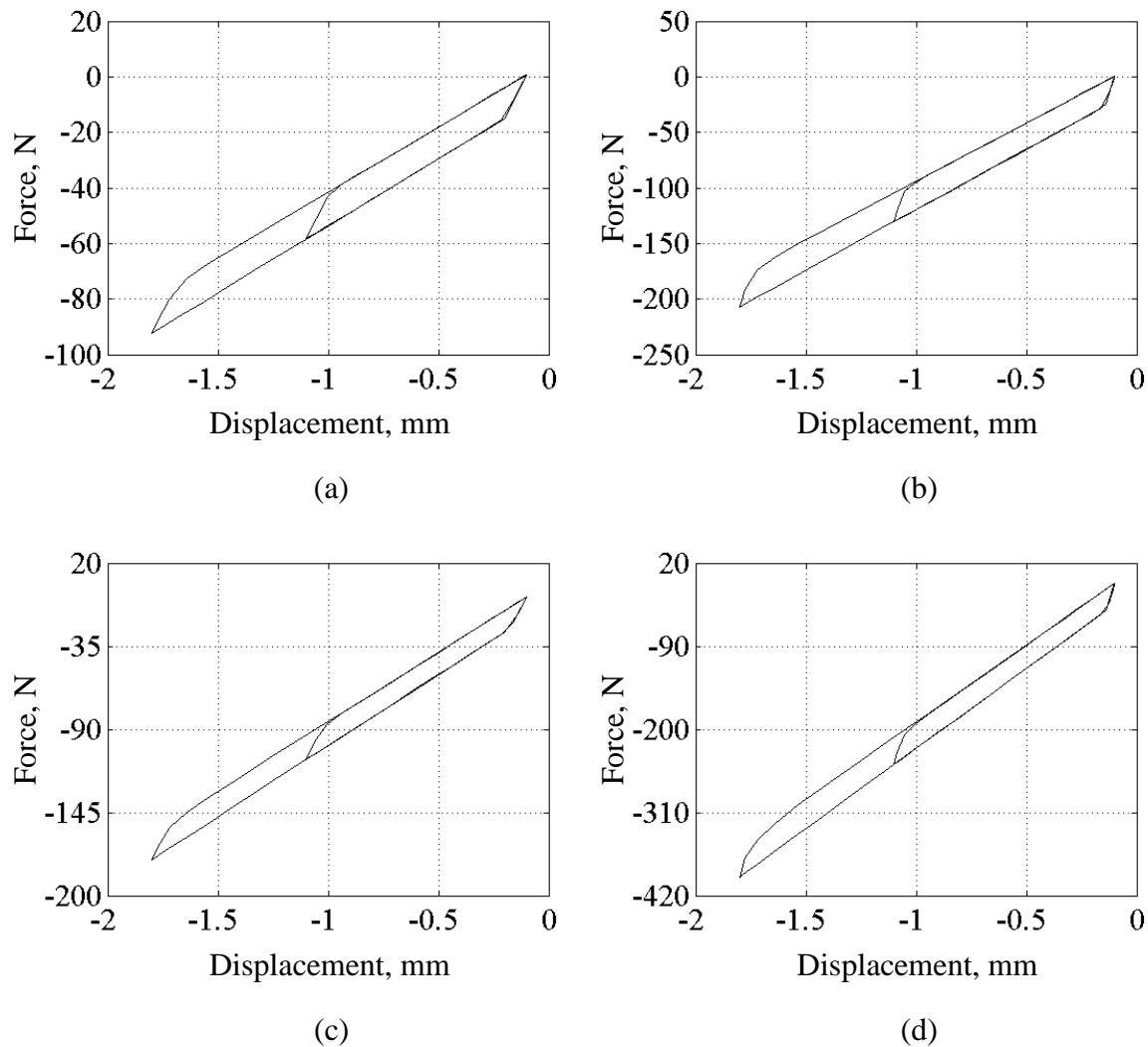
Figure 5.21 Numerical hysteresis loop of the DMSB at PK-PK displacement loading of 1.0 mm and 1.7 mm for Configurations (a) db03, (b) db06, (c) db09 and (d) db12

5.5   Results and discussion

The section is devoted to discussion of the results of the diagonal multi-strand beams (DMSB) that were obtained during the flexural behaviour investigations. The force-displacement curves (hysteresis loops) were used to describe the damping behaviour of the DMSB and the loss factor was considered to determine the damping levels in the system. The results for the comparison between the hysteresis loops that were obtained experimentally and numerically and analytically are shown in Figure 5.22 and Appendix H

for the entire configurations shown in Table 5.1 at peak-to-peak displacement of 1.0 mm and 1.7 mm. The analytical and numerical and experimental damping parameters for the entire configurations presented in Table 5.1 are listed in Appendix I. Comparison of the damping characteristics that were obtained analytically, numerically and experimentally is presented in Table 5.2.

The numerical and analytical hysteresis loops were in good agreement and they followed most of the experimental force-displacement curves at the end of the loading phase; however, non-symmetric sliding was observed during the experiments between the opposite mating surfaces. This would be due to local surface condition and imperfection clamping which caused the experimental hysteresis loops to differ from the analytical and numerical hysteresis loops where the sliding was assumed to be perfect. Non-symmetric sliding appeared to be most significant in low applied load levels.

Similar levels of loss factor were obtained for DMSB that did not have the same number of strands but where the individual strands had the same cross-section, for example, db01 and db4, db3 and db06, db07 and db12 (Table 5.2). The energy dissipation levels per cycle and the stored strain energy increased by increasing the strands number and this could be related to the overall cross-section of the DMSB increasing, which increased the stiffness; also, the number of contact surfaces was increased by increasing the strands number, which resulted in increasing the energy dissipation.

The loading level had inverse correlation with the loss factor and direct correlation with the energy dissipation and the stored strain energy, whereas the stiffness was not affected. The relation between the stiffness and the strain energy (Equation 5.1) explains why the lack of change in the stiffness with increasing the loading level could have caused the strain energy to increase. The clamp force had a direct correlation with the loss factor and the energy dissipation as the normal force on the contact regions increased, whereas the strain energy and the stiffness were not affected. The span distance had inverse correlation with each of energy dissipation, strain energy and stiffness as, for the same amount of loading, the sliding distance would be larger in shorter structures, which would lead to an increase in energy dissipation (Equation 5.2). In addition, shorter structures are stiffer than long structures, which explains why the strain energy increased with reduction of the span distance. The loss factor had a direct correlation with the loss factor.

(a)

(b)

(c)

(d)

(e)

(f)
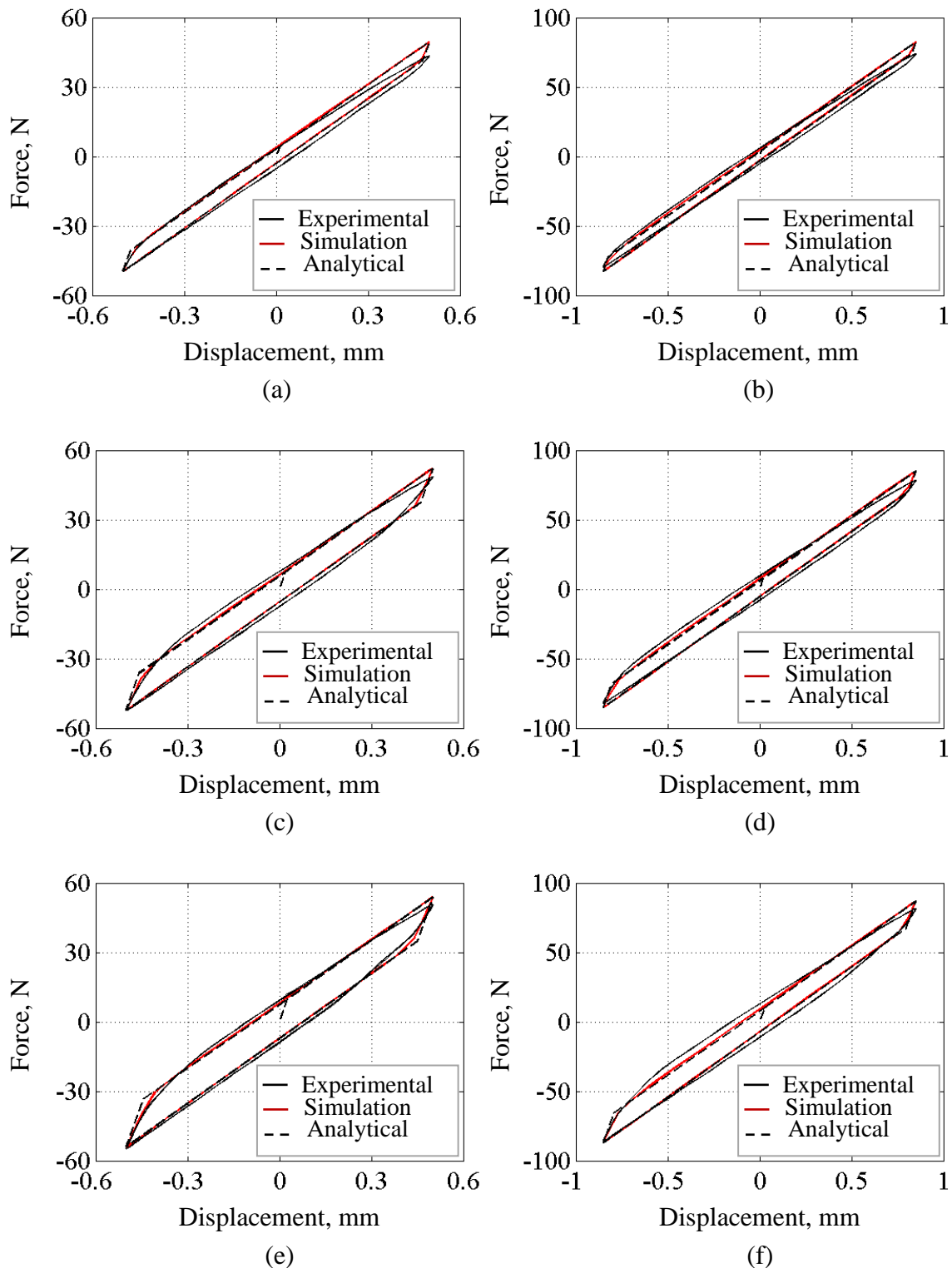
Figure 5.22 Comparison of experimental and numerical and analytical hysteresis loops for Configuration db07 at PK-PK displacement of (a) 1.0 mm and (b) 1.7 mm and for Configuration db08 at PK-PK displacement of (c) 1.0 mm and (d) 1.7 mm and for Configuration db09 at PK-PK displacement of (e) 1.0 mm and (f) 1.7 mm

Table 5.2 Comparison of analytically, numerically and experimentally obtained damping characteristics for Configurations db01–db12

Configuration	Loading, mm	Analytical		Numerical		Experimental	
		Loss factor	Stiffness, N/mm	Loss factor	Stiffness, N/mm	Loss factor	Stiffness, N/mm
db01	1.000	0.126	52.19	0.121	47.42	0.090	46.19
	1.700	0.079	50.46	0.078	48.30	0.069	47.27
db02	1.000	0.219	56.36	0.208	45.98	0.140	52.36
	1.700	0.138	52.97	0.134	47.23	0.118	45.53
db03	1.000	0.275	59.15	0.258	45.26	0.192	58.15
	1.700	0.175	54.64	0.169	46.50	0.175	45.02
db04	1.000	0.126	116.5	0.118	110.3	0.107	93.42
	1.700	0.082	113.0	0.077	108.6	0.093	92.19
db05	1.000	0.223	122.3	0.205	110.8	0.150	95.31
	1.700	0.137	118.2	0.131	111.0	0.111	97.66
db06	1.000	0.276	130.5	0.260	106.5	0.214	100.7
	1.700	0.172	121.6	0.168	111.8	0.156	98.51
db07	1.000	0.088	98.75	0.083	93.48	0.100	85.40
	1.700	0.057	96.71	0.055	93.76	0.076	87.47
db08	1.000	0.151	104.0	0.143	90.89	0.175	90.44
	1.700	0.096	99.88	0.092	93.40	0.122	87.39
db09	1.000	0.191	107.5	0.179	89.44	0.194	92.58
	1.700	0.121	102.0	0.115	92.45	0.161	86.81
db10	1.000	0.093	221.1	0.083	211.8	0.102	172.7
	1.700	0.065	218.1	0.057	209.5	0.094	173.3
db11	1.000	0.152	232.2	0.141	215.4	0.153	180.8
	1.700	0.100	223.6	0.092	210.6	0.123	176.6
db12	1.000	0.191	239.2	0.177	214.3	0.220	184.7
	1.700	0.124	227.9	0.115	214.9	0.173	181.5

Numerical and analytical hysteresis loop results of rotating the DMSB in a range of angles of 0°–45° were obtained. Figure 5.23 and Figure 5.24 show hysteresis loops for Configurations db03 and db06 at peak-to-peak displacement loading of 1.0 mm and 1.7 mm respectively where the DMSB were rotated at 15°, 30° and 45°. The energy dissipation amounts per cycle and the loss factor were increased with increasing the angle of rotation, while the stored strain energy stayed at similar levels during the rotation and these findings agree with the results obtained from the investigation of the effect of angle of rotation on the stored energy and energy dissipation in Section 5.3.1. Table 5.3 through Table 5.6 present the damping parameters that were obtained analytically and numerically for the DMSB rotated in a range of angles from 0°–45° at PK-PK displacement loading of 1.0 mm and 1.7 mm.
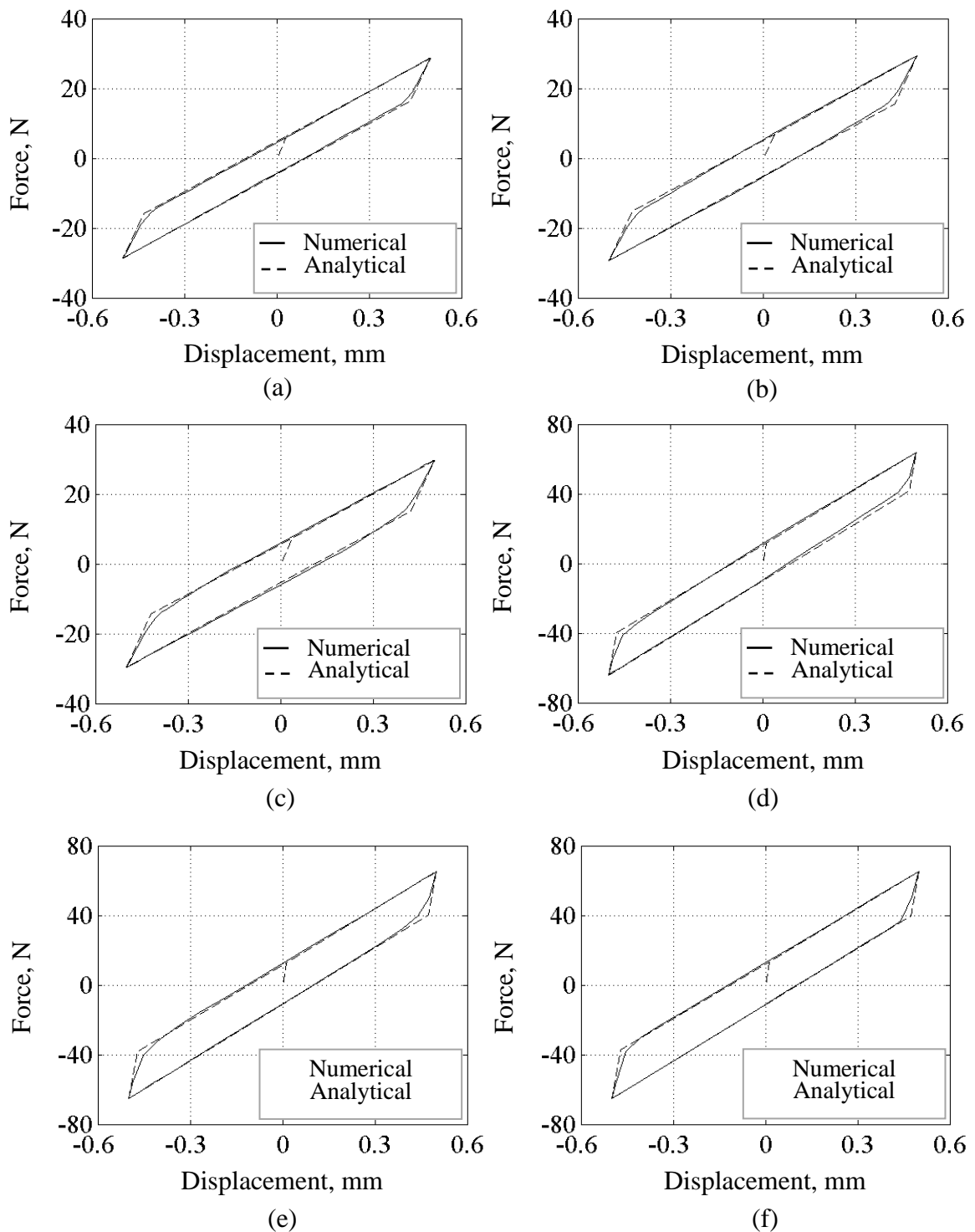
Figure 5.23 Numerical and analytical hysteresis loops at peak displacement loading of 1.0 mm for Configuration db03 at angle of rotation of (a) 15°, (b) 30° and (c) 45° and for Configuration db06 at angle of rotation of (d) 15°, (e) 30° and (f) 45°
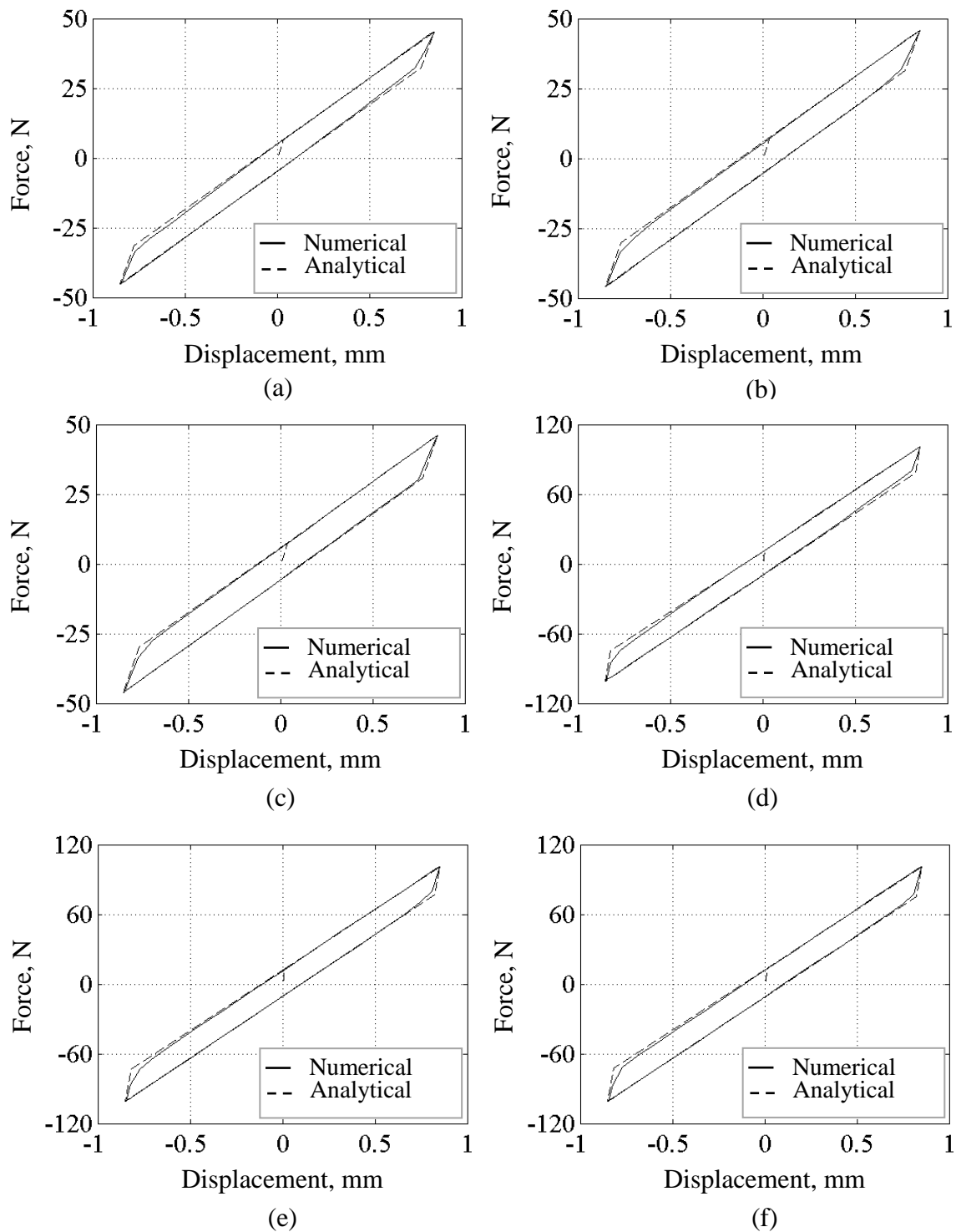
Figure 5.24 Numerical and analytical hysteresis loops at peak displacement loading of 1.7 mm for Configuration db03 at angle of rotation of (a) 15°, (b) 30° and (c) 45° and for Configuration db06 at angle of rotation of (d) 15°, (e) 30° and (f) 45°

120

Table 5.3 Analytical damping characteristics of the DMSB for Configurations db03 and db06 at PK-PK displacement loading of 1.0 mm during rotation in range of angles 0°–45°

Angle of rotation	Analytical			
	Loss factor	Energy dissipation / cycle, mJ	Strain energy, mJ	Stiffness, N/mm
db03				
0	0.174	7.154	13.09	58.36
5	0.222	8.532	12.22	56.23
10	0.234	9.045	12.32	57.04
15	0.244	9.492	12.40	57.75
20	0.253	9.886	12.43	58.18
25	0.261	10.20	12.46	58.56
30	0.267	10.45	12.48	58.87
35	0.273	10.59	12.32	59.07
40	0.273	10.74	12.50	59.21
45	0.275	10.78	12.48	59.15
db06				
0	0.175	16.16	29.38	129.9
5	0.219	18.90	27.52	125.2
10	0.231	20.06	27.68	126.9
15	0.242	21.08	27.69	128.0
20	0.253	21.96	27.65	128.6
25	0.261	22.69	27.70	129.5
30	0.267	23.25	27.70	130.1
35	0.272	23.66	27.70	130.5
40	0.275	23.91	27.70	130.7
45	0.276	24.00	27.63	130.5

Table 5.4 Numerical damping characteristics of the DMSB for Configurations db03 and db06 at PK-PK displacement loading of 1.0 mm during rotation in range of angles 0°–45°

Angle of rotation	Numerical			
	Loss factor	Energy dissipation / cycle, mJ	Strain energy, mJ	Stiffness, N/mm
db03				
0	0.184	7.473	12.91	48.29
5	0.191	7.366	12.28	46.44
10	0.196	7.697	12.49	46.95
15	0.202	8.087	12.75	48.41
20	0.217	8.694	12.77	47.42
25	0.231	9.214	12.69	44.99
30	0.243	9.630	12.63	45.62
35	0.251	9.938	12.58	46.57
40	0.256	10.12	12.55	45.81
45	0.259	10.19	12.54	45.51
db06				
0	0.182	16.41	28.64	113.6
5	0.193	16.57	27.35	110.6
10	0.195	17.03	27.83	112.5
15	0.209	18.37	27.97	112.5
20	0.224	19.55	27.80	109.0
25	0.236	20.54	27.66	108.5
30	0.246	21.32	27.55	109.4
35	0.254	21.89	27.46	107.4
40	0.258	22.24	27.40	106.6
45	0.260	22.35	27.38	106.5

Table 5.5 Analytical damping characteristics of the DMSB for Configurations db03 and
db06 at PK-PK displacement loading of 1.7 mm during rotation in range of angles 0°–45°

Angle of rotation	Analytical			
	Loss factor	Energy dissipation / cycle, mJ	Strain energy, mJ	Stiffness, N/mm
db03				
0	0.111	12.98	37.15	55.04
5	0.138	15.29	35.21	53.10
10	0.146	16.22	35.35	53.59
15	0.153	17.05	35.37	53.89
20	0.160	17.76	35.39	54.15
25	0.165	18.34	35.42	54.37
30	0.169	18.74	35.21	54.54
35	0.172	19.13	35.45	54.67
40	0.174	19.33	35.46	54.73
45	0.175	19.41	35.38	54.64
db06				
0	0.113	29.80	84.18	123.3
5	0.137	34.44	80.09	119.1
10	0.145	36.45	80.11	119.8
15	0.152	38.22	80.10	120.4
20	0.158	39.75	79.98	120.8
25	0.163	41.01	80.02	121.2
30	0.167	42.00	80.03	121.6
35	0.170	42.71	79.94	121.7
40	0.171	43.14	80.01	122.0
45	0.172	43.28	80.06	122.1

Table 5.6 Numerical damping characteristics of the DMSB for Configurations db03 and db06 at PK-PK displacement loading of 1.7 mm during rotation in range of angles 0°–45°

Angle of rotation	Numerical			
	Loss factor	Energy dissipation / cycle, mJ	Strain energy, mJ	Stiffness, N/mm
db03				
0	0.117	13.52	36.65	49.68
5	0.125	13.81	35.11	47.68
10	0.130	14.50	35.54	48.37
15	0.139	15.55	35.54	47.53
20	0.148	16.48	35.44	47.22
25	0.155	17.27	35.36	47.40
30	0.161	17.88	35.29	47.29
35	0.166	18.33	35.23	46.77
40	0.168	18.59	35.21	46.55
45	0.169	18.70	35.19	46.50
db06				
0	0.116	29.87	82.14	116.3
5	0.125	30.87	78.44	110.9
10	0.132	32.85	79.15	111.7
15	0.141	34.90	78.95	110.6
20	0.148	36.67	78.76	111.1
25	0.154	38.11	78.59	110.7
30	0.159	39.22	78.47	110.3
35	0.163	40.05	78.36	110.4
40	0.167	41.03	78.22	111.4
45	0.168	41.18	78.13	111.8

The configurations of the diagonal multi-strand beams (DMSB) presented in Table 5.1 had counterparts among the multi-strand beams (MSB) presented in Table 3.1 that shared common physical properties except that the DMSB were rotated at 45°, while the MSB were at 0° with the horizontal axis (see Table 5.7). Figure 5.25 compares the loss factor between the MSB and the DMSB that were obtained analytically at PK-PK displacement loadings of 1.0 mm and 1.7 mm. The configurations of the DMSB achieved higher loss factor values than the configurations of the MSB. This could be related to the increase in the energy dissipation amounts when the DMSB system rotated at 45° due to the increased surfaces of contact in these systems, as shown in Figure 5.26. The stored strain energy (stiffness) was at similar levels for both the MSB and the DMSB as shown in Figure 5.28, the reason being

that the same number of strands and the same cross-section were used when comparing between the configurations of the MSB and the DMSB and therefore the stiffness would remain stable whether the system was flat or rotated by an angle (the reader can refer to Section 5.3.1).

Table 5.7 Physically matched configurations of MSB and DMSB

MSB	DMSB
sb04	db01
sb05	db02
sb06	db03
sb10	db04
sb11	b05
sb12	db06
sb16	db07
sb17	db08
sb18	db09
sb22	db10
sb23	db11
sb24	db12
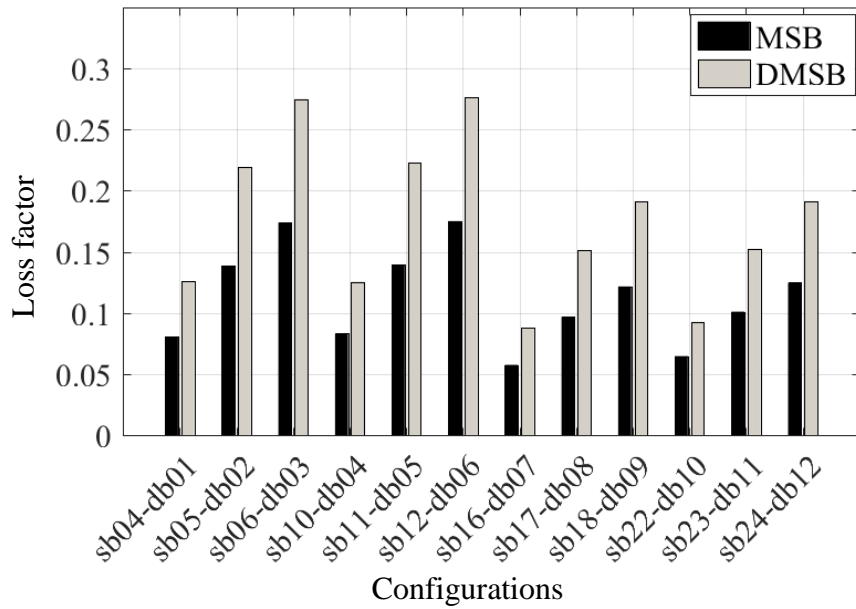
(a)
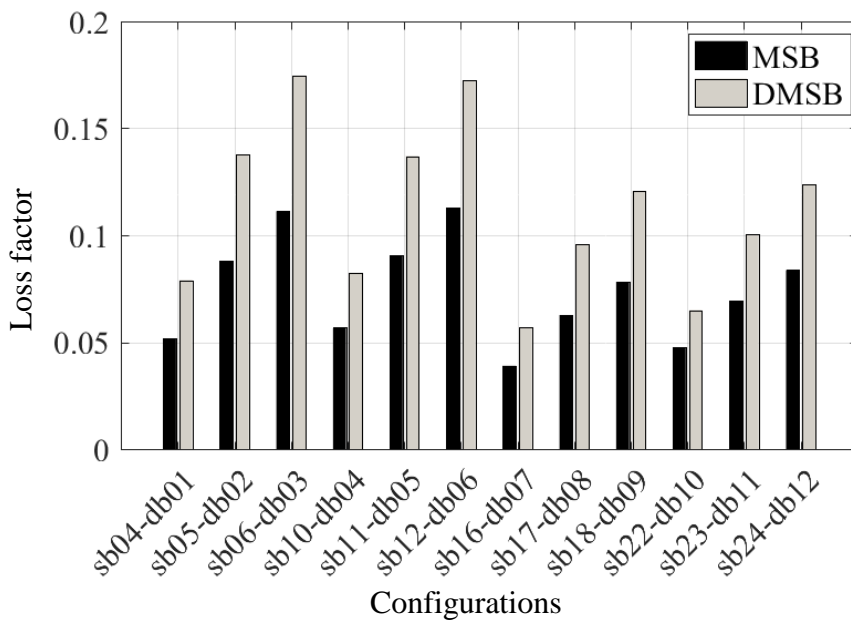
(b)

Figure 5.25 Comparison of the loss factor between multi-strand beams (MSB) and diagonal multi-strand beams (DMSB) rotated at 45° and exposed to a PK-PK displacement loading of (a) 1.0 mm and (b) 1.7 mm

(a)

(b)
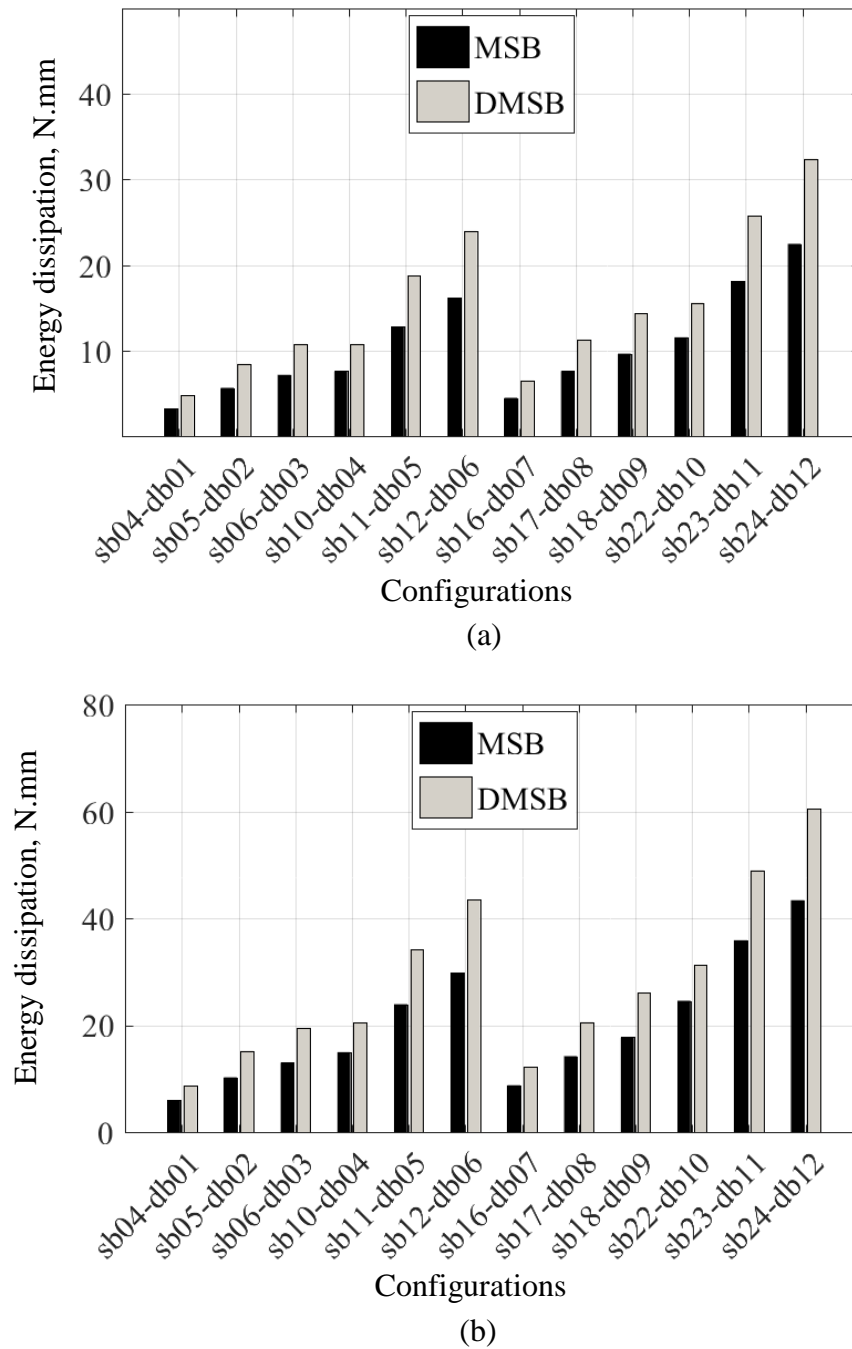
Figure 5.26 Comparison of the energy dissipation between multi-strand beams (MSB) and diagonal multi-strand beams (DMSB) rotated at 45° and exposed to a PK-PK displacement loading of (a) 1.0 mm and (b) 1.7 mm

(a)

(b)
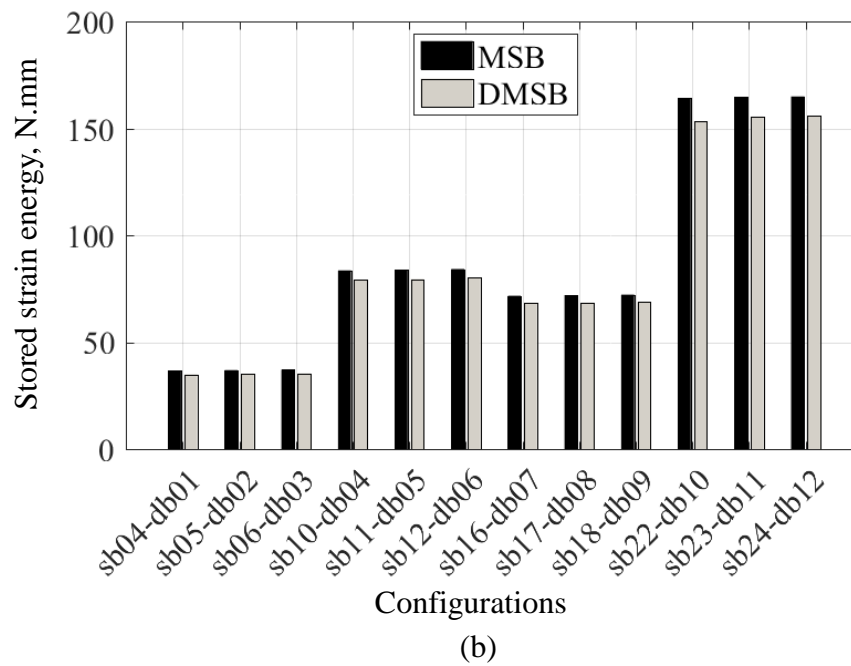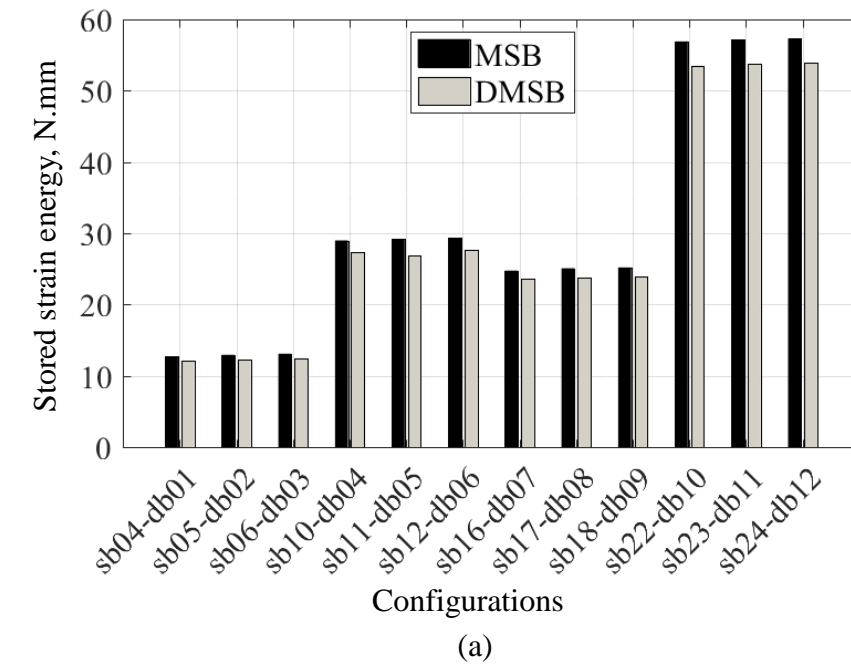
Figure 5.27 Comparison of the stored strain energy between multi-strand beams (MSB) and diagonal multi-strand beams (DMSB) rotated at 45° and exposed to a PK-PK displacement loading of (a) 1.0 mm and (b) 1.7 mm
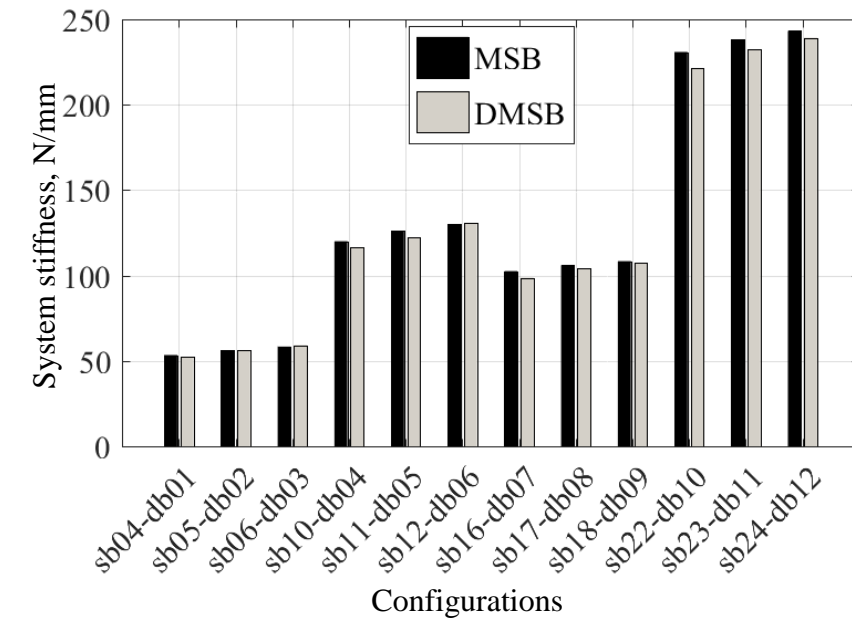
(a)
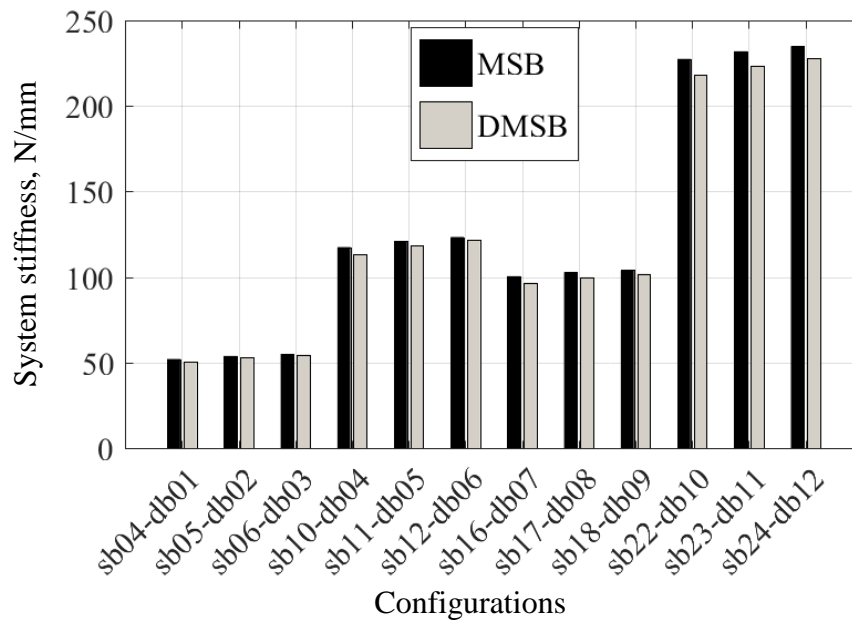
(b)

Figure 5.28 Comparison of the system stiffness between multi-strand beams (MSB) and diagonal multi-strand beams (DMSB) rotated at 45° and exposed to a PK-PK displacement loading of (a) 1.0 mm and (b) 1.7 mm

5.6 Conclusions

The diagonal multi-strand beams (DMSB) were modelled analytically and numerically and were investigated experimentally in this chapter. Configurations of the DMSB that were rotated at 45° were compared with some configurations of Chapter 3 that physically matched them but were not rotated. Rotation of the DMSB in a range of angles of 0°–45° was investigated analytically and numerically. The work done in this chapter revealed findings which can be summarised as follows:

- In relation to damping

    ✓ The number of strands in the DMSB had no effect on the loss factor value when using individual strands of the same cross-section size, while energy dissipation level, strain energy and stiffness each had a direct correlation with the number of strands.

    ✓ The clamp force level had a direct correlation with the loss factor level and the energy dissipation per cycle, while the stiffness and the strain energy were not affected by the clamp force level.

    ✓ The displacement loading level had inverse correlation with the loss factor and direct correlation with both the energy dissipation and the strain energy, while the stiffness was not affected by the loading levels.

    ✓ The span distance had direct correlation with the loss factor, while energy dissipation, strain energy and stiffness each had inverse correlation with the span distance.

    ✓ The DMSB (rotated at 45°) had higher loss factor and energy dissipation levels when compared with the MSB (flat at 0°) because friction on each strand is higher, while the strain energy and the stiffness were not affected.

    ✓ The loss factor and energy dissipation increased when the DMSB were rotated in a range of angles of 0°–45°, while the strain energy and the stiffness were not affected.

- In relation to modelling

    ✓ The analytical and numerical models followed the experimental force-displacement curve for the DMSB rotated at 45°.

    ✓ The analytical and numerical models were able to describe the damping behaviour of the DMSB that were rotated in a range of angles of 0°–45°.

Chapter 6
Quasi-static damping behaviour of multi-strand bars and wires

6.1 Introduction

Systems comprising dry friction contacts can provide considerable levels of damping over large operating temperature ranges. When temperature insensitive materials, such as metallic or carbon fibres, are considered, this damping can occur over a significantly wider temperature range than what is typical for common damping materials such as viscoelastic polymers. Energy dissipation from friction interfaces involving a small number of relatively large contact surfaces, such as turbine blade roots, has received significant research interest [53, 54]. On the other hand, damping from a large number of relatively small contacts, such as found in a multi-strand bars and wires, is not nearly as well understood. There is therefore a need for efficient and accurate models to allow optimisation of this kind of damping mechanism in order to improve vibration attenuation in mechanical systems. Practical examples of these systems include fibre bundles, woven fabrics, multi-strand wire dampers and isolators, composite materials with dry frictional contact from poor wetting and damaged/delaminated fibre composites.

In Chapters 3, 4 and 5, the damping behaviour in multi-strand beams, where the strands had square cross-section, were investigated through building analytical models, numerical analyses and experimental tests. This chapter focuses on studying the damping behaviour in multi-strand bars and wires where the strands have circular cross-section.

The knowledge gained from the previous chapters regarding the damping behaviour of these systems and the ability to predict analytically the stiffness of systems experiencing dry frictional behaviour between the mating surfaces, made it possible to transit the work geometrically to another level where strands of circular cross-section with meso and micro dimensions were used in.

This chapter proposes an analytical model that describes the stiffness behaviour for frictionally constrained multi-strand bars (MSR) and wires (MSW) constructed from circular cross-section strands followed by numerical analyses and experimental tests. The analytical model predicts the frictional system stiffness, for simply supported boundary conditions, which is then used to determine the damping from the force-displacement hysteresis under harmonic loading. The analytical model developed includes the frictional effects by introducing them directly into the system stiffness. This does not depend on any empirical parameters other than material properties and the coefficient of friction. The interfaces of the un-bonded strands are allowed to slide against each other reducing the system stiffness as these structures, when sliding, have several neutral axes. The results from the model were capable of defining the stick and sliding regions. Validation of the analytical model was carried out through numerical simulations using finite elements and quasi-static tests on a Universal Test System (UTS). The experimental and numerical works were performed on meso and micro levels. The force-displacement hysteresis behaviour from both the numerical simulations and quasi-static tests were compared with the analytical model demonstrating good agreement for a variety of conditions.

6.2 Multi-strand bars and wires description

The multi-strand bars (MSR) and the multi-strand wires (MSW) in this chapter were composed of individual strands. These strands were steel bars and wires with circular cross-section and each strand had frictional contact with its neighbours. The arrangement allowed for the outer strands to be placed radially around a core strand. It was prerequisite that the individual strands had the same diameter and that the total number of strands involved in the system was set according to Equations 6.1 and 6.2 in order to ensure that each strand had a contact with its adjacent strands. Depending on the total number of strands in the system, there will be several orbits containing radially placed strands around the core strand with a

minimum number of strands of six to create, first, orbit. The sequence of adding strands to a new orbit was achieved through adding the minimum number of strands required to create an orbit (six) to the number of strands in the last orbit that the system has.

For instance, a system that has seven strands will has one core strand and six strands placed radially around a core strand, which is sufficient to create the first orbit, with a pitch angle of 360° divided by the number of outer strands in the outer orbit (in case there was more than one orbit). Figure 6.1a shows a seven-strand bar. To create the second orbit, the minimum number of strands required to create an orbit (six) is added to the number of strands in the last orbit that the system has, first orbit in this case which had six strands, to conclude that the second orbit will has twelve strands. The total number of strands will be, in this case, the sum of the number of strands in the previous system (seven strands) and the number of strands in the second orbit (twelve), which is nineteen. Nineteen-strand bar is shown in Figure 6.1b. Table 6.1 lists numbers of strands that create multi-strand bars and wires where all the involved strands have contact with their neighbours.

$$N_{next\,orbit} = N_{previous\,orbit} + 6, \qquad\qquad 6.1$$

$$N_{new\,system} = N_{previous\,system} + N_{next\,orbit}. \qquad\qquad 6.2$$

where, N is the number of strands.

The pitch angle between the strands centre at any orbit was found by

$$\alpha_{ob} = \frac{360}{N_{ob}} \qquad\qquad 6.3$$

where, α_{ob} is the pitch angle between the strands centres at orbit ob (see Figure 6.1a) and N_{ob} is the number of strands at that specific orbit. The radius of orbit ob can be defined as

$$R_{ob} = \frac{r}{\sin\left(\dfrac{\alpha_{ob}}{2}\right)} \qquad\qquad 6.4$$

where, r the radius of the individual strands.

Table 6.1 Number of strands in multi-strand bars and wires where all strands have contact with their neighbours

Number of strands in multi-strand bar and wire	Core strand	Number of strands in last orbit	Pitch angle in last orbit
7	1	6	60.0°
19	1	6+6=12	30.0°
37	1	12+6=18	20.0°
61	1	18+6=24	15.0°
91	1	24+6=30	12.0°
127	1	30+6=36	10.0°
169	1	36+6=42	8.57°
217	1	42+6=48	7.50°

The height of the seven-strand system (Figure 6.1a) can be expressed as

$$h_7 = 6r$$

6.5

while the height of the nineteen-strand system (Figure 6.1b) is expressed as

$$h_{19} = 9.4641\,r$$

6.6

(a)

(b)
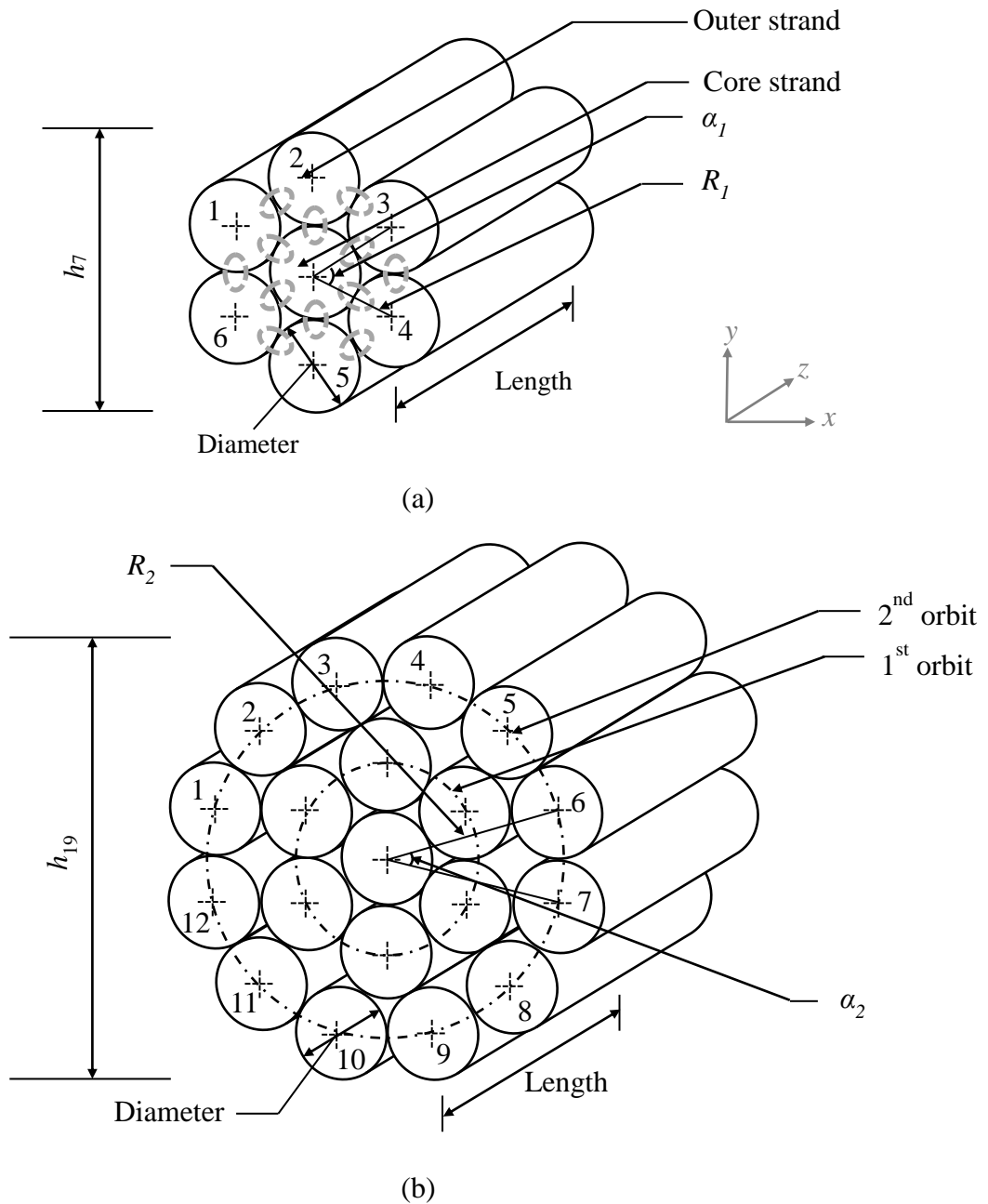
Figure 6.1 Arrangement of strands in multi-strand bar system comprising (a) seven strands –
contact regions are indicated by the 'dashed ovals'– and (b) nineteen strands

The estimated height of any multi-strand bar or wire can be expressed as

$$h_{any} = 2r\left(1 + \frac{\cos\left(\frac{360}{2N_{last}}\right)}{\sin\left(\frac{360}{2N_{last}}\right)}\right)$$ 6.7

where, h_{any} is the height of any multi-strand bar or wire and N_{last} is the number of strands in the last orbit for that system.

Several configurations are considered in this chapter as shown in Table 6.2. The reader should take note that the analytical model described in this paper only pertains to the configurations listed in Table 6.2. Mild steel strands and spring steel strands are assigned to the MSR and MSW respectively and a three point bend configuration is adopted to load the system.

Table 6.2 Multi-strand bar and wire configurations

Configuration	No of strands	Diameter of individual strand, mm	Length, mm	Displacement amplitude, mm
msr1	7	3.00	250	0.50, 1.00, 1.50
msr2	7	4.00	250	0.50, 1.00, 1.50
msw1	7	0.50	45.0	0.10, 0.15
msw2	19	0.50	45.0	0.10, 0.15
msw3	37	0.50	45.0	0.10, 0.15
msw4	61	0.50	45.0	0.10, 0.15

Radial clamping forces are required to hold the individual strands together. These forces are also essential to create the frictional forces between the mating surfaces. The clamping effect was applied as discrete forces in the analytical models but for convenience, as distributed pressure during the numerical analyses [97].

The MSR and MSW are exposed to flexural deformations and as the bars and wires flex, if the load is large enough, slip between individual strands occurs along the length. This is shown in Figure 6.2.

Figure 6.2 Typical multi-strand bar undergoing flexure (seven-strand bar shown)

6.3 Material properties

The modulus of elasticity and the density of the strands can affect the damping levels in a frictional system. Insufficient information about these material properties for the circular cross-sectioned strands (bars and wires) was available therefore it was essential to estimate these properties experimentally. Identification of the material properties was required for analytical modelling and numerical analysis therefore it was important to obtain these properties. Free vibration tests were performed on the circular cross-sectioned bar and wire strands to determine the material modulus of elasticity.

6.3.1 Beam free vibration

Natural frequencies of the circular cross-sectioned bars and wires were found through the obtained free decay responses from free vibration tests. The modulus of elasticity was then calculated through the natural frequency formula for the first mode.

6.3.2 Experimental work

Free vibration tests were performed in order to obtain the natural frequencies for circular cross-sectioned bars with diameters of 3.0 mm and 4.0 mm and circular cross-sectioned spring steel wires with a diameter of 0.5 mm. Free lengths of 250 mm and 40 mm were used for the tested bar and wire strands respectively. The experiments were repeated five times for each case to provide consistency and repeatability. A special vice was designed and manufactured to hold the bars and wires during the free vibration test. This is shown in Figure 6.3. To ensure a firm grip, 15% (50 mm) of the total bar length (300 mm) was

embedded in the vice during the test. The design of the vice allowed it to be used for bars with diameters of 3.0 mm and 4.0 mm and wires with 0.5 mm diameter.

(a)   (b)
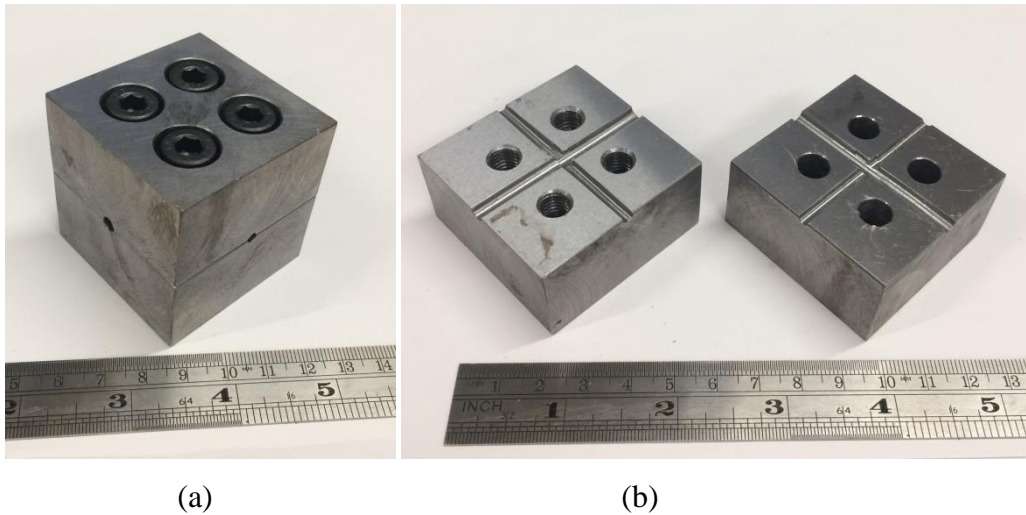
Figure 6.3 The vice used for the free vibration test (a) as one part and (b) dismantled

A Laser Optical Displacement Sensor with a sensitivity of 2 V/mm was used to obtain the displacement signals of the bars and wires under free vibration. The resulting voltage signals were acquired digitally using a sample rate of 50000 sample/sec for the bars and 19980 sample/sec for the wires. The total duration of the signal was 2.0 sec (see Figure 6.4).

The natural frequency was estimated from average time period during the resulting free vibration. In order to estimate the modulus of elasticity of the tested bars and wires, the formula for the natural frequency for the first mode was used (through calculating Equation 3.2) in terms of the modulus of elasticity [96].
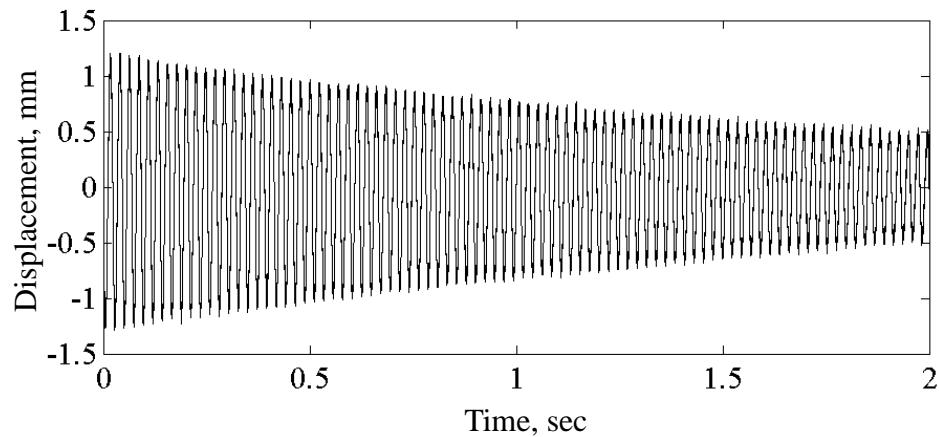
(a)
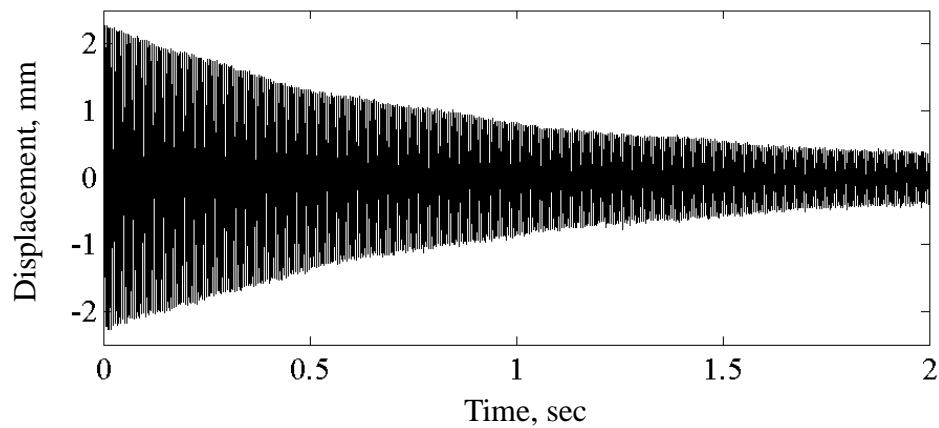
(b)

Figure 6.4 Time domain free decay signal of a (a) 4.0×250 mm circular bar and (b) 0.5×40 mm circular wire

At this stage, an estimate of the density of the bars and wires was needed. Ten bars (five bars with diameter of 3.0 mm and five bars with diameter of 4.0 mm) and five wires with diameter of 0.5 mm were weighed on electronic scales and accurate dimensional measurements were made to calculate the volume and by the use of Equation 3.1, the average density was found to be approximately 7852 kg/m^3 for bars with diameter 3.0 mm and 7843 kg/m^3 for bars with diameter of 4.0 mm and 7850 kg/m^3 for wires with diameter of 0.5 mm. For simplicity, a common value of 7850 kg/m^3 was used in the subsequent work of this chapter.

The natural frequencies (ω_n) measured from the free vibration test and their corresponding modulus of elasticity values (E) for bars with diameter of 3.0 mm and 4.0 mm and wires with diameter of 0.5 mm are shown in Table 6.3.

Table 6.3 Material properties obtained experimentally for circular bars of dimensions of
3.0×250 mm and 4.0×250 mm and circular wires of dimensions of 0.5×40 mm

Circular bar of dimensions 3.0×250 mm		Circular bar of dimensions 4.0×250 mm		Circular wire of dimensions 0.5×40 mm	
f, Hz	E, GPa	f, Hz	E, GPa	f, Hz	E, GPa
33.51	195.4	43.91	188.5	217.3	203.7
33.45	194.7	43.85	188.0	217.2	203.5
33.63	196.7	43.91	188.5	217.4	203.9
33.56	196.0	43.86	188.1	217.1	203.3
33.56	195.9	43.80	187.6	217.3	203.7
Average					
33.54	195.7	43.86	188.1	217.3	203.6

6.4 Analytical modelling

The damping behaviour of multi-strand bars and wires, where the individual strands have circular cross-section, experiencing frictional contact is studied and modelled in this section. The contact condition between the mating surfaces has a direct effect on the overall system stiffness and its response. Therefore, it is essential to estimate the stiffness of the multi-strand bar in order to describe the damping behaviour accurately. The prediction of the frictional second moment of area for the multi-strand bars and wires is the prerequisite to estimate the system stiffness in the current study. As in Chapter 3, the term "frictional second moment of area" refers to the effective second moment of area that account for effects of friction.

The multi-strand bars (MSR) and wires (MSW) contain strands of the same length that are in a simply supported configuration with a load applied in the centre normal to the uppermost strand.

The analytical model developed included the frictional effects by introducing them directly into the system stiffness with no dependence on any empirical parameters other than material properties and the coefficient of friction. The damping level was estimated through describe the force-displacement relationship, hysteresis loop, obtained analytically and then evaluate the loss factor.

6.4.1 Frictional second moment of area

The stiffness of the system is represented by the frictional second moment of area. When these systems are either bonded or frictionless, the second moment of area can be calculated using the parallel axis theorem as shown in Equation 3.9.

For a bonded case, all the strands in the system are counted as one body, therefore the transfer distance of each strand (d) is the distance from the centroid of the individual strand to the geometric centre of the whole system as shown in Figure 6.5a. For a frictionless case, the transfer distance (d) is equal to zero (as shown in Figure 6.5b) as each strand has its own neutral axis and there is no transfer distance between the strand's neutral axis and the geometric centre of the system. For instance, in Figure 6.5b there are two separate systems. In a frictional case, the transfer distance (d) should increase with increasing the coefficient of friction, μ, and the direction of this increment is towards the contact regions as shown in Figure 6.5c.

For a case that the friction is involved between the mating strands, the analytical method predicts the frictional second moment of area at any magnitude of μ up to a limit of the equivalent of the strands being bonded. This is achieved firstly by estimating the displacement relationship with a range of magnitudes for μ from frictionless contact through fully bonded contact. The estimated displacements are then used to predict the frictional second moment of area as a function of μ.
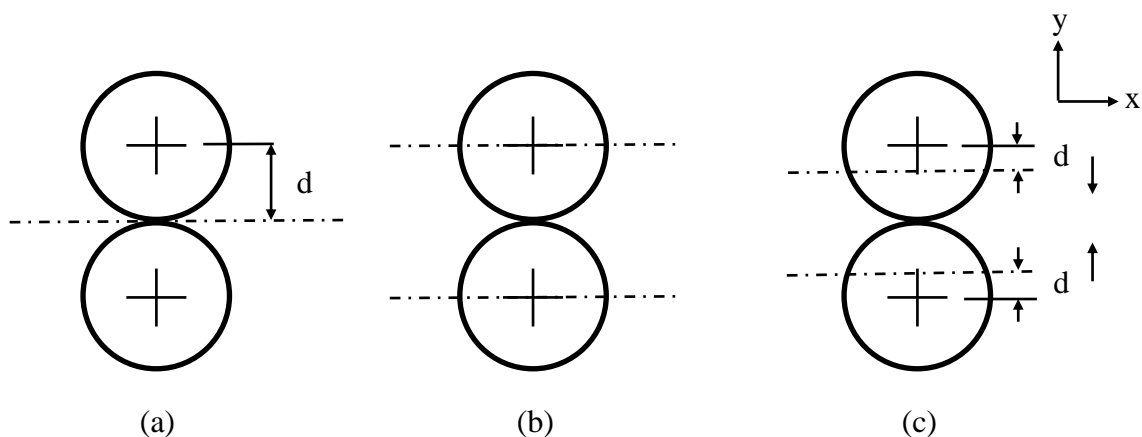
Figure 6.5 Second moment of area, I_{xx}, and transfer distance (d) for strands that are (a) bonded, (b) frictionless and (c) frictional – dashed lines represent the neutral axes

Two cases are considered in order to provide the upper and lower bounds for the frictional second moment of area: strands with perfectly bonded contact and strands with a frictionless contact. Equation 6.8 is used to calculate the second moment of area for a multi-strand bar with frictionless contact.

$$I_{frictionless} = \frac{N\pi r^4}{4}$$ 6.8

where, N is the number of strands involved in the system, r is the radius of the individual strands in the multi-strand bar. The peak displacement in a frictionless system is as was shown previously in Equation 3.11.

The second moment of area of a seven-strand bar, where it has one orbit of outer strands and a core strand, in a bonded contact can be calculated as

$$I_{bond7} = \frac{(N_1+1)}{4}\pi r^4 + \pi r^2 \left[\sum_{nn=1}^{N_1} R_1 \sin\left(\frac{\alpha_1}{2} + (nn-1)\alpha_1\right) \right]^2$$ 6.9

where, N_1 is the number of strands in the first orbit and α_1 is the pitch angle between the strands centres in the first orbit.

$$R_1 = \frac{r}{\sin\left(\dfrac{\alpha_1}{2}\right)}$$ 6.10

Equation 6.9 can be re-written as

$$I_{bond7} = \frac{55}{4}\pi r^4$$ 6.11

The second moment of area for a nineteen-strand bar, where it has two orbits of strands and a core strand (see Table 6.1), in a bonded case can be calculated as

$$I_{bond19} = I_{bond7} + \frac{N_2}{4}\pi r^4 + \pi r^2 \left[\sum_{mm=1}^{N_2} R_2 \sin\left(\frac{\alpha_2}{2} + (mm-1)\alpha_2\right) \right]^2$$ 6.12

where, N_2 is the number of strands in the second orbit and α_2 is the pitch angle between strands centres at that orbit (see Figure 6.1) and

$$R_2 = \frac{r}{\sin\left(\dfrac{\alpha_2}{2}\right)} \qquad\qquad 6.13$$

Equation 6.12 can be re-written as

$$I_{bond19} = \frac{425.2768}{4}\pi r^4 \qquad\qquad 6.14$$

The peak displacement in a bonded is calculated through Equation 3.13.

To calculate the equivalent coefficient of friction, μ, during the bonding case (sticking), a correlation at the contact between the strands was required for the shear stress and the frictional stress from the frictional forces.

The contact status should remain stuck as long as the frictional stress is greater than or equal to the maximum shear stress. Therefore the last moment that the system is considered stuck is when the frictional stress equals the shear stress as was presented in Equation 3.14.

The frictional stress can be expressed as

$$\sigma_{fri} = \frac{F_c \mu_w}{b_w l} = \frac{F_{friction}}{A_{interface}} \qquad\qquad 6.15$$

where, F_c is the clamping force, μ_w is the coefficient of friction at the interface layer, b_w and l are the width and the length of the interface.

The shear stress can be expressed as [99]

$$\tau_w = \frac{FQ}{Ib_w} \qquad\qquad 6.16$$

where, τ_w is the shear stress at the required interface layer, F is the force applied to the system and Q is the first moment of area for the sheared area.

At this stage, the position where the maximum shear stress expected to take place should be identified. The multi-strand bar was divided into multiple layers (see Figure 6.6) in order to integrate the first moment of area and the shear stress through each layer.
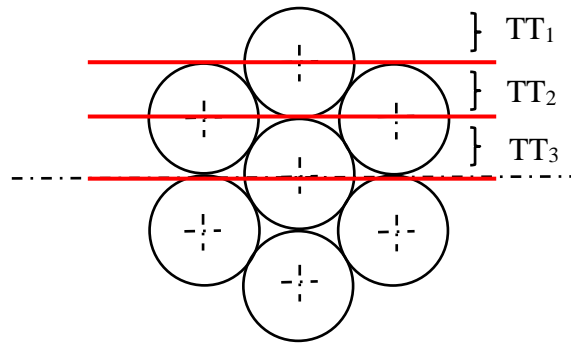
Figure 6.6 Dividing the multi-strand bar into layers in order to describe the profile of Q and τ

The first moment of area, Q, in circular cross-sections (see Figure 6.7) can be expressed as

$$Q = \int y'dA$$ 6.17

where, y' is the distance between the edge of the sheared area and the neutral axis and dA is the segment area which is expressed as

$$dA = 2sdy$$ 6.18

where,

$$s = \sqrt{r^2 - y^2} \, ,$$ 6.19

$$y = r\sin(\theta),$$ 6.20

Substituting Equations 6.18 and 6.19 into Equation 6.17 leads to

$$Q = \int_y^r 2y'\sqrt{r^2 - y^2}dy$$ 6.21
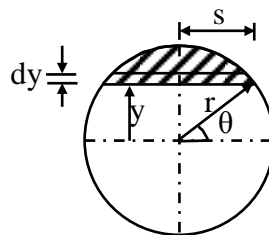
Figure 6.7 Sheared section in a circular cross-section

The first moment of area and the shear stress at the different layers (Figure 6.6) were found as follows:

- For Layer TT$_1$ (see Figure 6.8):

The first moment of area is expressed as

$$Q_1 = \int_{y_1}^{r} 2(2r + y)\sqrt{r^2 - y^2}\,dy$$
6.22

and the shear stress is expressed as

$$\tau_1 = \frac{FQ_1}{I_{bond7}\,2s_1}$$
6.23
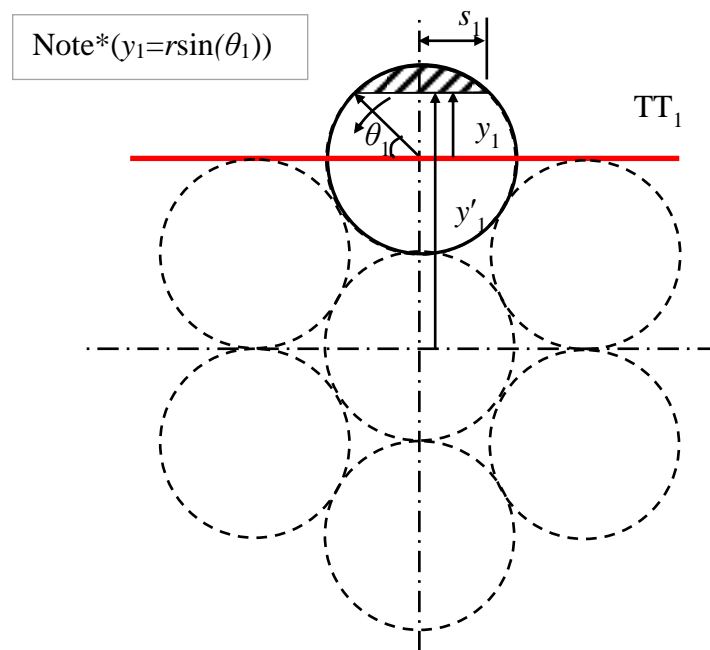
Figure 6.8 The shear stress at layer TT$_1$ where $90 > \theta_1 > 0$

- For layer TT$_2$ (see Figure 6.9):

The first moments of area are expressed as

$$Q_{21} = \int_{0}^{y_{21}} 2(2r - y)\sqrt{r^2 - y^2}\,dy$$
6.24

$$Q_{22} = \int_{y_{22}}^{r} 2(r+y)\sqrt{r^2 - y^2}\, dy \qquad\qquad 6.25$$

$$Q_2 = Q_{21} + 2Q_{22} \qquad\qquad 6.26$$

and the shear stress is expressed as

$$\tau_2 = \frac{F(Q_2 + Q_1)}{I_{bond7}\, 2(s_{21} + 2s_{22})} \qquad\qquad 6.27$$
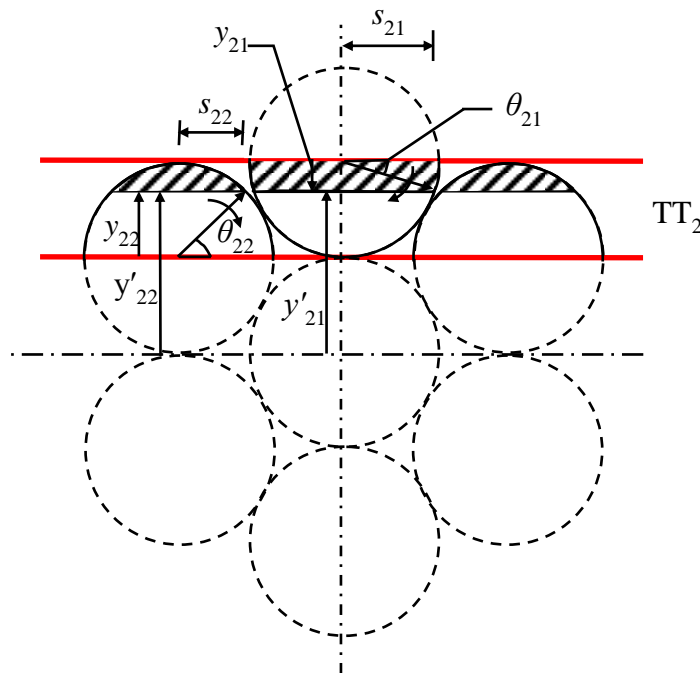
Figure 6.9 The shear stress at layer TT$_2$ where $0 < \theta_{21} < 90$ and $90 > \theta_{22} > 0$

-   For layer TT$_3$ (see Figure 6.10):

The first moments of area are expressed as

$$Q_{31} = \int_{y_{31}}^{r} 2y\sqrt{r^2 - y^2}\, dy \qquad\qquad 6.28$$

$$Q_{32} = \int_{0}^{y_{32}} 2(r-y)\sqrt{r^2 - y^2}\, dy \qquad\qquad 6.29$$

$$Q_3 = Q_{31} + 2Q_{32} \qquad\qquad 6.30$$

and the shear stress as

$$\tau_3 = \frac{F(Q_3 + Q_2 + Q_1)}{I_{bond7}\, 2(s_{31} + 2s_{32})} \qquad\qquad 6.31$$
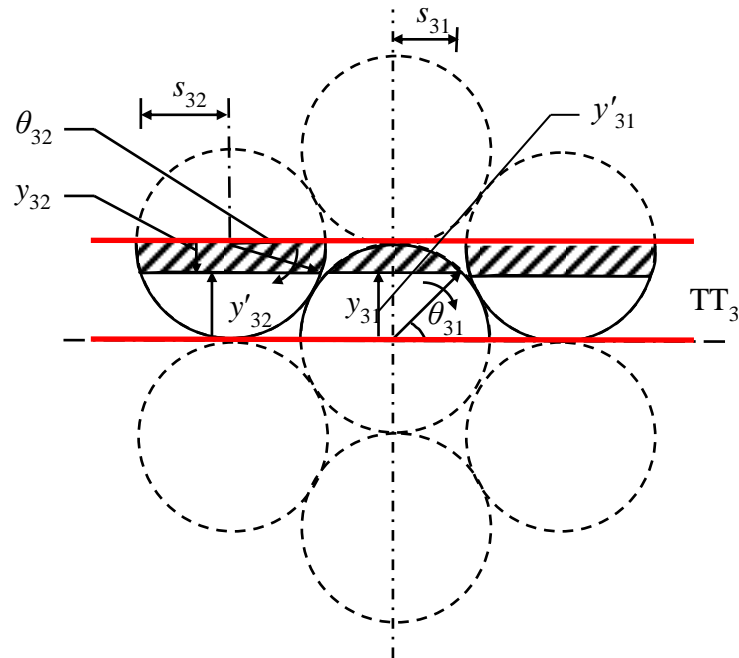
Figure 6.10 The shear stress at layer TT$_3$ where $90 > \theta_{31} > 0$ and $0 < \theta_{32} < 90$

Figure 6.11 and Figure 6.12 show the profile of the first moment of area and the profile of the shear stress respectively along the height of the seven-strand bars.
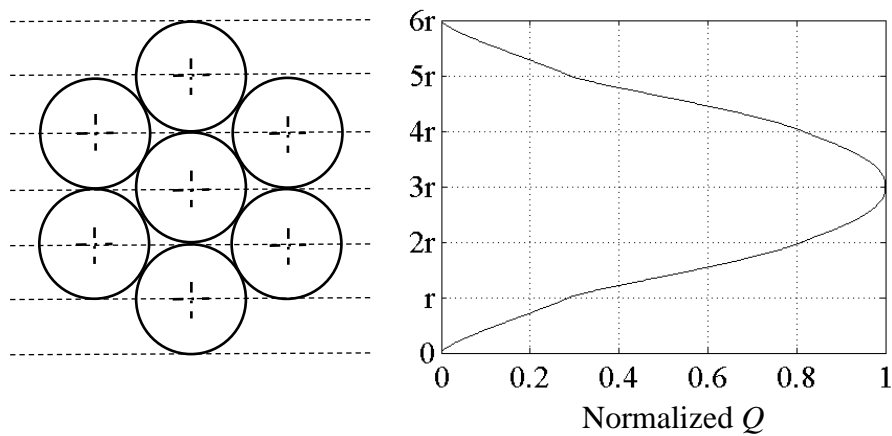
Figure 6.11 The profile of the first moment of area, Q, around the neutral axis of the seven-strand bar
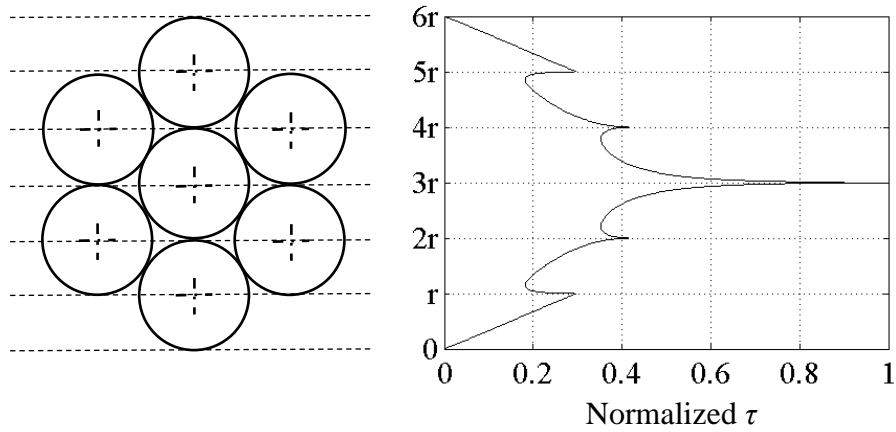
Figure 6.12 The profile of the shear stress, τ , around the neutral axis of the seven-strand bar

The technique that was used to generate both the first moment of area and the shear stress profiles for the seven-strand bars was used to generate the first moment of area profile and the shear stress profile for nineteen-strand bars.

Figure 6.13 and Figure 6.14 show the profile of both the first moment of area and the shear stress of a nineteen-strand bar.
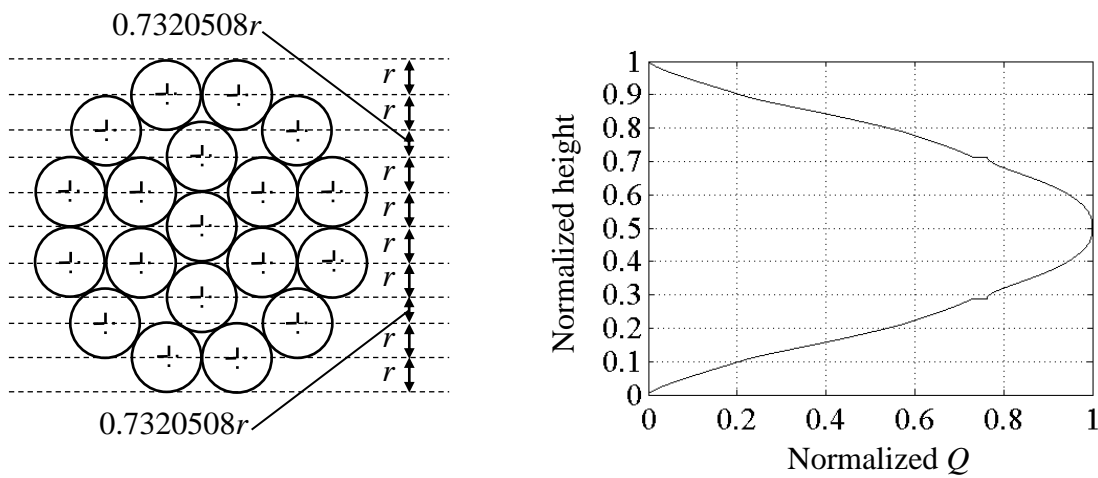
Figure 6.13 The profile of the first moment of area, Q, around the neutral axis of the nineteen-strand bar
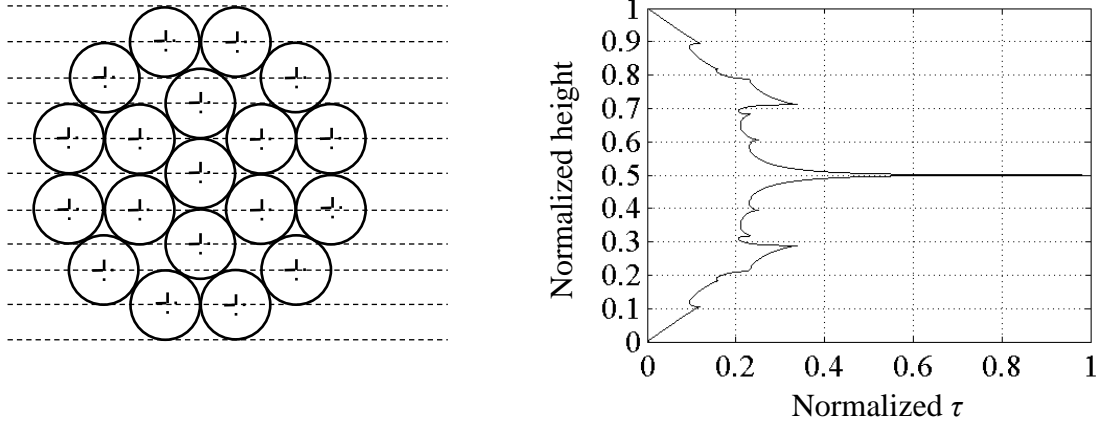
Figure 6.14 The profile of the shear stress, τ, around the neutral axis of the nineteen-strand bar

Examination of Figure 6.12 and Figure 6.14 show the trend of the shear stresses which lead to the conclusion that the position where slip is initiated occurs where the shear stress is maximised. For seven-strand bars and wires and depending on this conclusion, the first slip should start at the middle of the multi-strand system however the core strand is a solid body and cannot be separated into two bodies therefore; the first three strands at the top will start the slip in the system.

Through calculating Equation 6.16 for the interface where the maximum shear stress occurs, the maximum shear stress in a seven-strand system can be described as

$$\tau_{7\max} = \frac{FQ_{7\max}}{I_{bond7}b_w}$$

6.32

where, $\tau_{7\max}$ is the maximum shear stress in the seven-strand bar or wire and b_w is the width of the interface and $Q_{7\max}$ is the maximum first moment of area in the seven-strand system and is described as

$$Q_{7\max} = \pi r^2 \left[\sum_{aa=1}^{(N_1/2)} R_1 \sin\left(\frac{\alpha_1}{2} + (aa-1)\alpha_1 \right) \right]$$

6.33

which can be re-written as

149

$$Q_{7\max} = 4\pi r^3$$

6.34

Substituting Equations 6.15 and 6.32 into Equation 3.14 and solving in term of the coefficient of friction, the equivalent coefficient of friction of the seven-strand system was then described as

$$\mu_7 = \frac{4F\pi r^3 l}{I_{bond7}F_c}$$

6.35

The maximum shear stress in a nineteen-strand bar or wire can be expressed as

$$\tau_{19\max} = \frac{FQ_{19\max}}{I_{bond19}b_w}$$

6.36

where, $\tau_{19\max}$ is the maximum shear stress in the nineteen-strand system and $Q_{19\max}$ is the maximum first moment of area in the nineteen-strand bar or wire and was expressed analytically as

$$Q_{19\max} = \pi r^2 \left[\sum_{ab=1}^{(N_1/2)} R_1 \sin\left(\frac{\alpha_1}{2} + (ab-1)\alpha_1 \right) \right] + \cdots$$
$$\cdots \pi r^2 \left[\sum_{ac=1}^{(N_2/2)} R_2 \sin\left(\frac{\alpha_2}{2} + (ac-1)\alpha_2 \right) \right]$$

6.37

which can be re-written as

$$Q_{19\max} = 18.9282\pi r^3$$

6.38

Substituting Equations 6.15 and 6.36 into Equation 3.14 and solve in terms of the coefficient of friction produces the equivalent coefficient of friction of the nineteen-strand system which can be described as

$$\mu_{19} = \frac{Q_{19\max}Fl}{I_{bond19}F_c}$$

6.39

The previous technique can be followed to estimate the equivalent-to-bond coefficient of friction in the case of using larger number of strands in the multi-strand system depending on Table 6.1 in selecting the strands number.

By knowing that the coefficient of friction in frictionless contact was zero, a relationship was plotted between the displacement (δ) and the coefficient of friction (μ). This relationship provides the magnitudes of the displacement at any specific coefficient of friction between the frictionless and the bonded states. The corresponding displacements for each coefficient of friction were used to calculate the related frictional second moment of area through Equation 3.20.

Configurations in Table 6.2 were used in order to analytically describe the relationship between the displacement and the coefficient of friction with different loading conditions and different strand parameters.

Figure 6.15 shows the analytically obtained relationship between the displacement (δ) and the coefficient of friction (μ) during different loading conditions and different geometric parameters for Configurations msr1 and msr2 shown in Table 6.2. The linear relationship between the displacement and the coefficient of friction was verified earlier through building numerical models and compares the obtained numerical results with the analytical models in Section 3.6.1.

The effect of the friction on the system stiffness was illustrated through depicting the nonlinear relationship of the frictional second moment of area with the coefficient of friction in Figure 6.16 which highlights the importance of determining the frictional system stiffness to describe the system response accurately during a frictional contact.

The relationship of the system displacement and the frictional second moment of area with the coefficient of friction were in similar trends for the other configurations and therefore the author preferred to limit the presentation of these relations to Configuration msr1 and msr2.
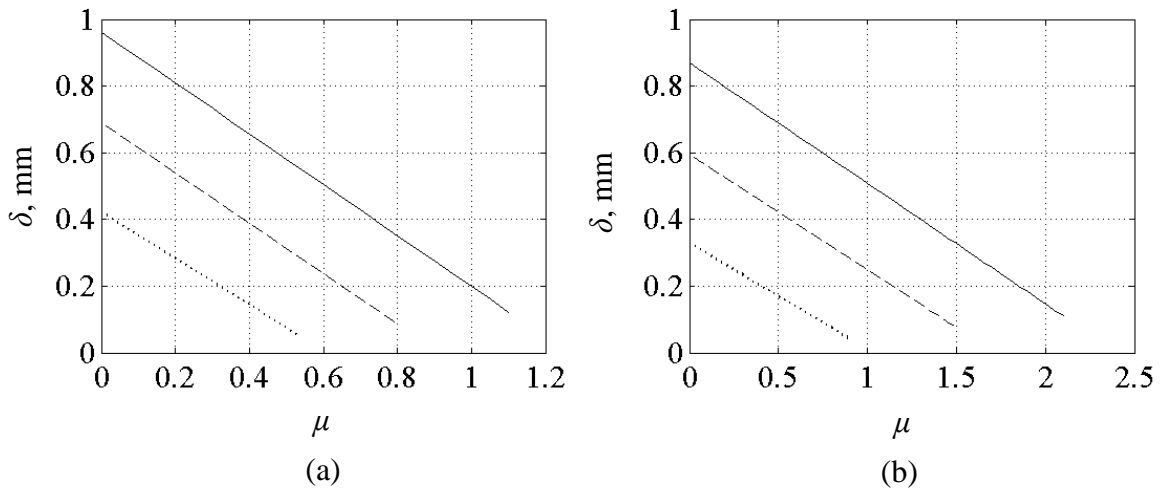
Figure 6.15 The relationship of the displacement, δ, and the coefficient of friction, μ, for Configurations (a) msr1 and (b) msr2 – solid, dashed and dotted lines are for maximum forcing peak displacements of 0.5 mm, 1.0 mm and 1.5 mm respectively
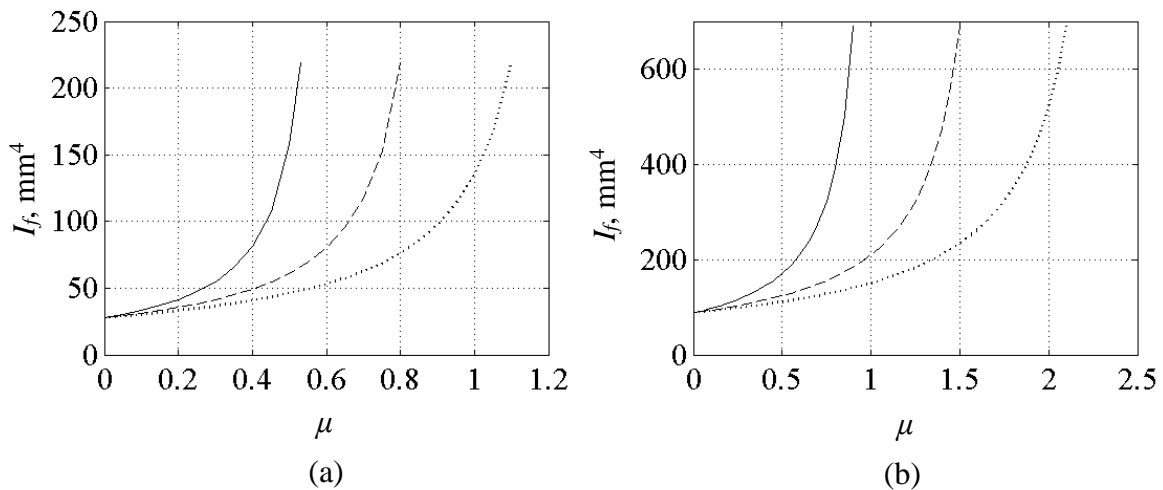
Figure 6.16 The relationship of the frictional second moment of area, I_f, and the coefficient of friction, μ, for Configurations (a) msr1 and (b) msr2 – solid, dashed and dotted lines are for maximum forcing peak displacements of 1.5 mm, 1.0 mm and 0.5 mm

6.4.2 Sensitivity of the frictional second moment of area

The frictional contact between the individual strands in the multi-strand bars and wires caused the general stiffness of the system to change during the transition of the contact status from sticking phase and microslip phase and then through the slide phase. In this section,

finite element models for Configurations msr1 and msr2 are built to investigate the transition of the frictional second moment of area through contact phases. Details about the finite element models are provided in Section 6.6. The numerical results for the applied ramp displacement of 1.5 mm and the reaction force resulting from the applied displacement were used to plot the force-displacement relationship. The transition phases are evident in Figure 6.17 for Configurations msr1 and msr2. The transition of the frictional second moment of area through the contact phases is depicted in Figure 6.18 for Configurations msr1 and msr2 through the use of Equation 3.20. The behaviour of both the transition distance and the frictional second moment of area through sticking, microslip and sliding phases shed the light to the importance of the ability to describe the system stiffness during frictional behaviour analytically.

It should be noted that although after the microslip region is completed, that the frictional second moment of area, I_f, approaches the second moment of area for a frictionless contact condition but will not ever fully converge because the frictional second moment of area will still contain amount of friction as the level of sliding to the level of sticking increases.

(a)

(b)

153
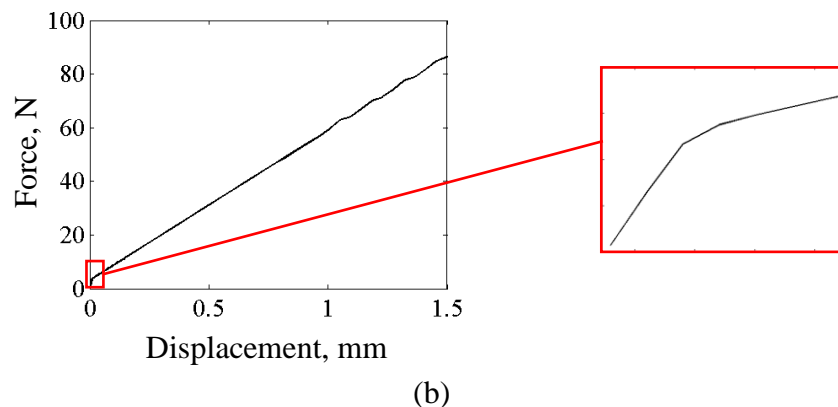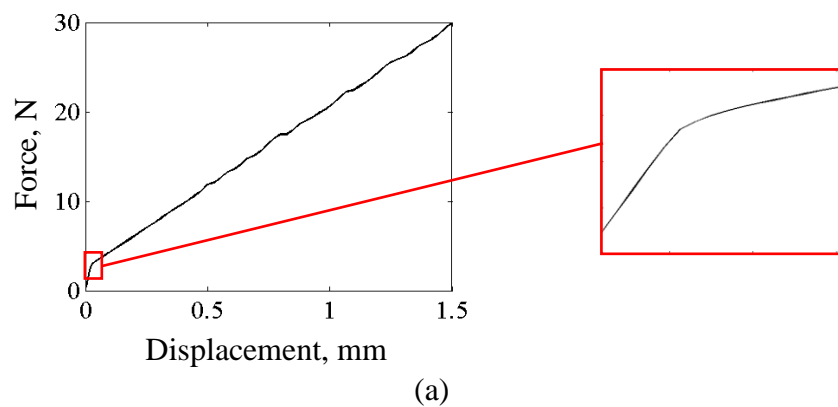
Figure 6.17 Force-displacement relationship obtained numerically were the contact transition regions are shown for Configurations (a) msr1 and (b) msr2

(a)

(b)
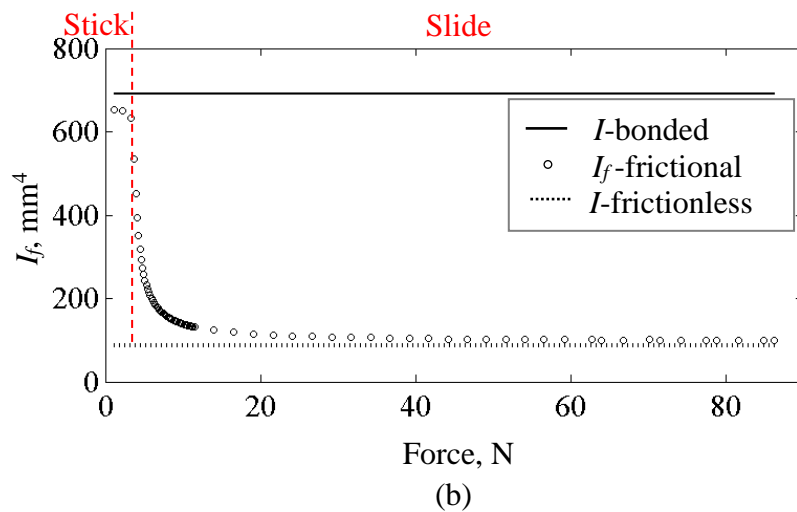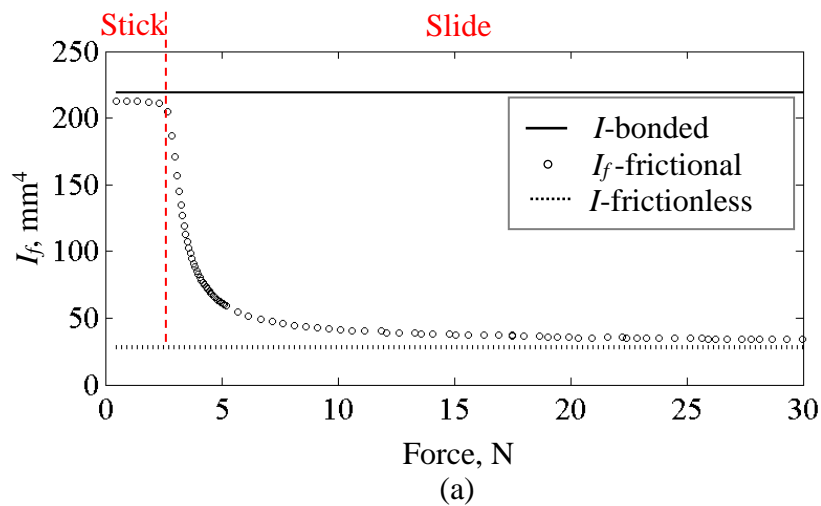
Figure 6.18 The transition of the frictional second moment of area through the contact phases for Configurations (a) msr1 and (b) msr2

6.4.3 Analytical hysteresis loop

The analytical model was built to present the damping behaviour of the multi-strand bars (MSR) and wires (MSW) experiencing flexural loading with the presence of friction. The model is able to produce force-displacement relationship which is used to describe the hysteresis loops for the configurations listed in Table 6.2.

The multi-strand bars and wires presented in this chapter comprised circular individual strands and due to the arrangement of these strands (see Figure 6.1) in the system, strands with neutral axes that are not at the same vertical level will start to bend together when sliding phase take place.

The analytical model in this chapter considers that the individual strands in the multi-strand system start sliding at several stages. The system that has the entire strands in stick status will split into two systems at the moment when the first group of strands start sliding as shown in Figure 6.19b. The contact phase between the new two systems is a slide phase while the strands within each system are in a stick phase. The position where the first group start to slide is defined through knowing where the maximum shear stress occurs. The strands in the new system which are in stick status will also start to slide as the force resulted from the applied displacement increase enough to cause sliding. Figure 6.19a shows the loading and unloading stages.

The procedure of describing the analytical hysteresis loops for the seven-strand bar or wire and nineteen-strand bar or wire is explained in this section and similar technique can be used for larger number of strands in the system.

    –   **For a seven-strand bar (7sr) and seven-strand wire (7sw):**

The slip initiation is expected to occur through two levels. The first, happens where the maximum shear stress occurs, depending on the analytical work in Section 6.4.1 to describe the profile of the shear stress in a seven-strand bar, at the neutral axis of the whole system as shown in Figure 6.12. Section 1A in Figure 6.19b represents the first slip level, the three strands at the top, in the system and the force needed to start the slip is expressed as

$$Fsl_{1A7} = \frac{2\left(F_c + 2F_c\sin(\alpha_1/2) + F/2\right)\mu I_{3top}}{Q_{3top}l} \qquad\qquad 6.40$$

where I_{3top} and Q_{3top} are the second moment of area and the first moment of area for stuck strands at first level of slip respectively and they can be expressed as

$$I_{3top} = \frac{27}{4}\pi r^4 \qquad\qquad 6.41$$

$$Q_{3top} = Q_{7\max} \qquad\qquad 6.42$$

The displacement resulted from the force that initiated the slip is calculated through

$$dsl_{1A7} = \frac{Fsl_{1A7}l^3}{48EI_{3top}}$$ 6.43

The second slip level happens after the first slip took place and caused the original system to separate into two new systems that each one of them has stick contact condition between the individual strands. The force needed to start the slip in the new resulted system, the strand at the top of the system depending on the profile of the shear stress shown in Figure 6.12, is the force needed to start the slip in the first level in addition to the force needed to start the slip in the resulted new system.

$$Fsl_{1B7} = Fsl_{1A7} + \frac{2(F_c + F/2)\mu I_{1top}}{Q_{1top}l}$$ 6.44

where, I_{1top} and Q_{1top} are the second moment of area and the first moment of area for the stuck strand at the second slip level respectively and they can be expressed as

$$I_{1top} = \frac{17}{4}\pi r^4$$ 6.45

$$Q_{1top} = 2\pi r^3$$ 6.46

The displacement at the end of the slip stage is described as

$$dsl_{1B7} = dsl_{1A7} + \frac{Fsl_{1B7}l^3}{48EI_{1top}}$$ 6.47

By the end of the slip stage, the system starts to slide. The end of the slide phase during the unloading stage, Point 2 in Figure 6.19, presents the peak force and displacement in the frictional system. Depending on the peak force F, the peak displacement is calculated through Equation 3.23.

The microslip phase starts from Point 2 to Point 3, Figure 6.19, passing through the original system position. This stage determines the amount of damping that the system could produce. The force and displacement at the first slip level are calculated as

$$F_{3A7} = F - 2\left[\frac{2(F_c + 2F_c \sin(\alpha_1/2))\mu I_{3top}}{Q_{3top}l}\right]$$ 6.48

$$d_{3A7} = \delta_2 - 2\left[\frac{2(F_c + 2F_c\sin(\alpha_1/2))\mu l^2}{48Q_{3top}E}\right]$$ 6.49

The force and displacement of the second slip level during the microslip phase, Point 3B in Figure 6.19, are expressed as

$$F_{3B7} = F_{3A7} - 2\left[\frac{2F_c\mu l_{1top}}{Q_{1top}l}\right]$$ 6.50

$$d_{3B7} = d_{3A7} - 2\left[\frac{2F_c\mu l^2}{48Q_{1top}E}\right]$$ 6.51

The microslip phase is followed by the slip phase during the loading stage which ends in Point 4, Figure 6.19, the force F_4 and the displacement δ_4 at this point presents the peak values. They are calculated through the use of Equations 3.26 and 3.27.

The transition from the loading stage to the unloading stage crosses through the microslip phase. Similarly, this phase has two levels to initiate the slip. The first slip level ends at Point 5A as shown in Figure 6.19. The force F_{5A7} and the displacement d_{5A7} are calculated as

$$F_{5A7} = F_4 + 2\left[\frac{2(F_c + 2F_c\sin(\alpha_1/2) + F)\mu l_{3top}}{Q_{3top}l}\right]$$ 6.52

$$d_{5A7} = \delta_4 + 2\left[\frac{2(F_c + 2F_c\sin(\alpha_1/2) + F)\mu l^2}{48Q_{3top}E}\right]$$ 6.53

The force F_{5B7} and the displacement d_{5B7} of the second slip level which ends at Point 5B are calculated as

$$F_{5B7} = F_{5A7} + 2\left[\frac{2(F_c + F)\mu l_{1top}}{Q_{1top}l}\right]$$ 6.54

$$d_{5B7} = d_{5A7} + 2\left[\frac{2(F_c + F)\mu l^2}{48Q_{1top}E}\right]$$ 6.55
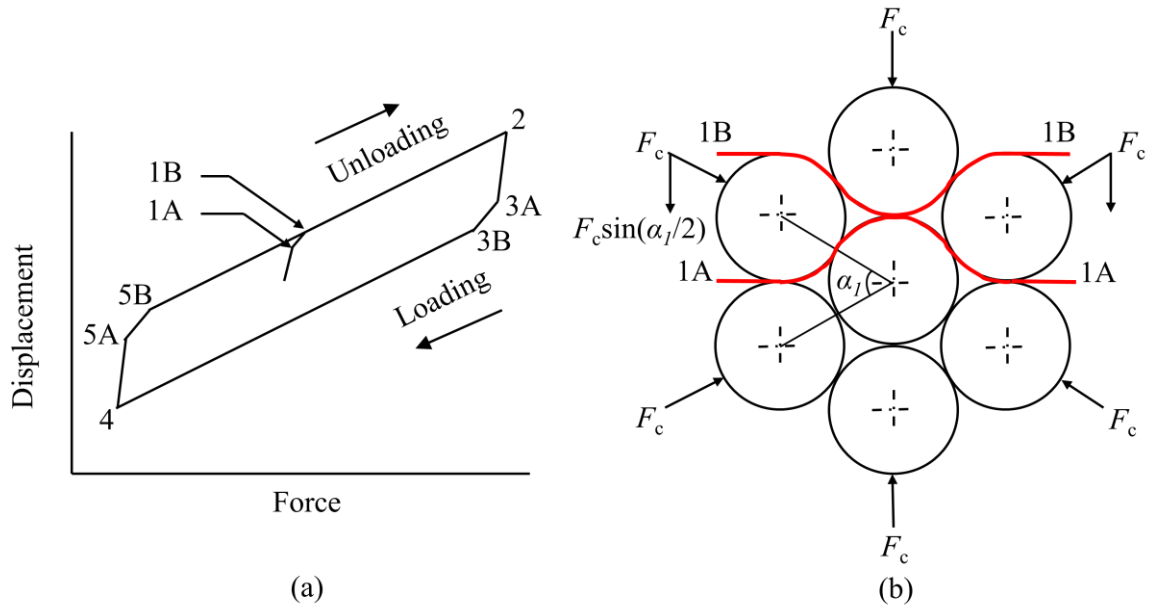
Figure 6.19 Analytical hysteresis loop for seven-strand system where (a) the loading and unloading stages and (b) the predicted strands to start slip are shown

    –   **For a nineteen-strand bar (19sr) and nineteen-strand wire (19sw):**

Depending on the shear profile of the nineteen-strand bar or wire (Figure 6.14), there are three slip levels contained in the microslip phase. The first slip level initiates at the position of the maximum shear stress which is on the neutral axis of the multi-strand system. Similar to the seven-strand system, new systems created due to the first slip where the individual strands have still stuck contact condition between each other.

The clamp forces are varied during the three slip levels and they are expressed as

$$F_{c1} = 2F_c \sin\left(\frac{5\alpha_2}{2}\right) + 2F_c \sin\left(\frac{3\alpha_2}{2}\right) + 2F_c \sin\left(\frac{1\alpha_2}{2}\right) \qquad 6.56$$

$$F_{c2} = 2F_c \sin\left(\frac{5\alpha_2}{2}\right) + 2F_c \sin\left(\frac{3\alpha_2}{2}\right) \qquad 6.57$$

$$F_{c3} = 2F_c \sin\left(\frac{5\alpha_2}{2}\right) \qquad 6.58$$

where, α_2 is the pitch angle between the stands in the second orbit and can be calculated using Equation 6.3, F_{c1}, F_{c2} and F_{c3} are the clamp forces at the first, second and third slip level respectively.

The first slip level ends at Point 1A as shown in Figure 6.20a. The force F_{1A19} for the first slip level (Section 1A in Figure 6.20b) are expressed as

$$F_{1A19} = \frac{2(F_{c1} + F/2)\mu I_{9top}}{Q_{9top}l}$$
<div align="right">6.59</div>

where, I_{9top} and Q_{9top} are the second and the first moments of area respectively for the strands that stuck in the first slip level and they are expressed as

$$I_{9top} = \frac{423.2768}{8}\pi r^4$$
<div align="right">6.60</div>

$$Q_{9top} = Q_{19max}$$
<div align="right">6.61</div>

The displacement d_{1A19} in the first slip level is expressed as

$$d_{1A19} = \frac{F_{1A19}l^3}{48EI_{9top}}$$
<div align="right">6.62</div>

The second slip level ends in Point 1B as shown in Figure 6.20a. The force F_{1B19} of the second slip level are expressed as

$$F_{1B19} = F_{1A19} + \frac{2(F_{c2} + F/2)\mu I_{5top}}{Q_{5top}l}$$
<div align="right">6.63</div>

where, I_{5top} and Q_{5top} are the second and the first moment of areas respectively for the strands that are stuck in the second slip level and they can be expressed as

$$I_{5top} = \frac{192.1384}{4}\pi r^4$$
<div align="right">6.64</div>

$$Q_{5top} = 14.9282\pi r^3$$
<div align="right">6.65</div>

The displacement d_{1B19} of the second slip level can be expressed as

$$d_{1B19} = d_{1A19} + \frac{F_{1B19}l^3}{48EI_{5top}}$$
<div align="right">6.66</div>

The third slip level ends at Point 1C as shown in Figure 6.20a and the force F_{1C19} is calculated by

$$F_{1C19} = F_{1B19} + \frac{2(F_{c3} + F/2)\mu I_{2top}}{Q_{2top}l}$$

6.67

where, I_{2top} and Q_{2top} are the second and the first moments of area for the strands that are stuck in the third slip level and they are expressed as

$$I_{2top} = \frac{113.4256}{4} \pi r^4$$

6.68

$$Q_{2top} = 7.4641 \pi r^3$$

6.69

The displacement d_{1C19} of the third slip level is expressed as

$$d_{1C19} = d_{1B19} + \frac{F_{1C19}l^3}{48EI_{2top}}$$

6.70

At this stage, the strands in the system start the slide phase during the unloading stage which ends at the peak force and peak displacement position, point 2 as shown in Figure 6.20a, The peak force F is used to calculate the peak displacement δ_2 of the system taking into account the frictional effect using Equation 3.23.

The microslip phase as explained earlier had three slip levels and ends. The first slip level ends at Point 3A (depicted in Figure 6.20a). The force F_{3A19} and the displacement d_{3A19} for the first slip level is expressed as

$$F_{3A19} = F - 2\left[\frac{2F_{c1}\mu I_{9top}}{Q_{9top}l}\right]$$

6.71

$$d_{3A19} = \delta_2 - 2\left[\frac{2F_{c1}\mu l^2}{48Q_{9top}E}\right]$$

6.72

The second slip level ends at Point 3B as shown in Figure 6.20a. The force F_{3B19} and the displacement d_{3B19} of the second slip level are calculated as

$$F_{3B19} = F_{3A19} - 2\left[\frac{2F_{c2}\mu I_{5top}}{Q_{5top}l}\right]$$

6.73

$$d_{3B19} = d_{3A19} - 2\left[\frac{2F_{c2}\mu l^2}{48Q_{5top}E}\right]$$

6.74

The microslip phase ends at the end of the third slip level (Point 3C in Figure 6.20a) and the force F_{3C19} and the displacement d_{3C19} are expressed as

$$F_{3C19} = F_{3B19} - 2\left[\frac{2F_{c3}\mu l_{2top}}{Q_{2top}l}\right] \qquad 6.75$$

$$d_{3C19} = d_{3B19} - 2\left[\frac{2F_{c3}\mu l^2}{48Q_{2top}E}\right] \qquad 6.76$$

The loading stage (sliding phase) starts at Point 3C and ends at Point 4 as shown in Figure 6.20a. The force F_4 and the displacement δ_4 present the peak values and they are calculated through Equations 3.26 and 3.27 respectively.

The transition from loading to unloading stages crosses through the microslip phase which comprises three slip levels. The first slip level ends at Point 5A as shown in Figure 6.20a. the force F_{5A19} and the displacement d_{5A19} for the first slip level are calculated as

$$F_{5A19} = F_4 + 2\left[\frac{2(F_{c1} + F)\mu l_{9top}}{Q_{9top}l}\right] \qquad 6.77$$

$$d_{5A19} = \delta_4 + 2\left[\frac{2(F_{c1} + F)\mu l^2}{48Q_{9top}E}\right] \qquad 6.78$$

The second slip level ends at Point 5B as shown in Figure 6.20a and the force F_{5B19} and the displacement d_{5B19} for this slip level are calculated as

$$F_{5B19} = F_{5A19} + 2\left[\frac{2(F_{c2} + F)\mu l_{5top}}{Q_{5top}l}\right] \qquad 6.79$$

$$d_{5B19} = d_{5A19} + 2\left[\frac{2(F_{c2} + F)\mu l^2}{48Q_{5top}E}\right] \qquad 6.80$$

The microslip phase ends by the end of the third slip level at Point 5C as depicted in Figure 6.20a. The force F_{5C19} and the displacement d_{5C19} for this level are expressed as

$$F_{5C19} = F_{5B19} + 2\left[\frac{2(F_{c3} + F)\mu l_{2top}}{Q_{2top}l}\right] \qquad 6.81$$

$$d_{5C19} = d_{5B19} + 2\left[\frac{2(F_{c3} + F)\mu l^2}{48Q_{2top}E}\right] \qquad 6.82$$
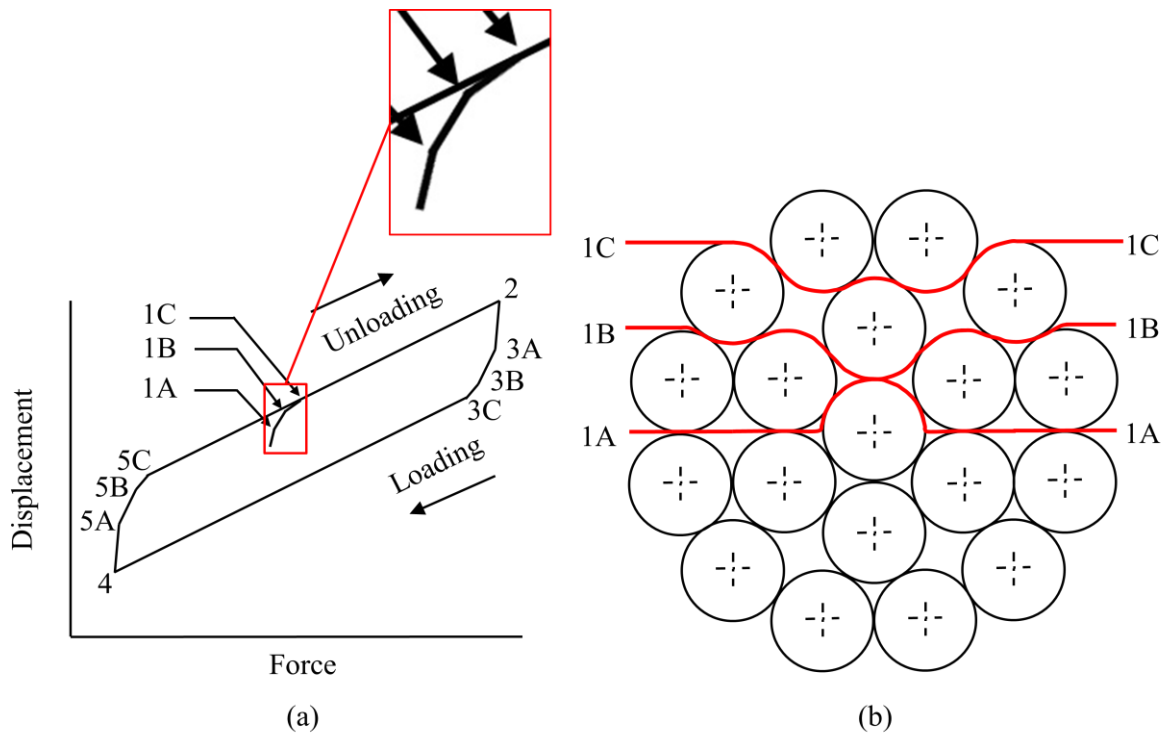
Figure 6.20 Analytical hysteresis loop for nineteen-strand system where (a) the loading and unloading stages and (b) the predicted strands to start slip are shown

Similar technique can be used to describe the hysteresis loops analytically for multi-strand system with larger number of strands. Figure 6.21 shows analytically obtained hysteresis loops for Configurations msr1, msr2, msw1, msw2, msw3 and msw4 (Table 6.2) at different peak displacement loadings. The different clamp forces that are used in the different models are obtained from the clamp force calculations in later Sections 6.5.1.1 and 6.5.2.1.
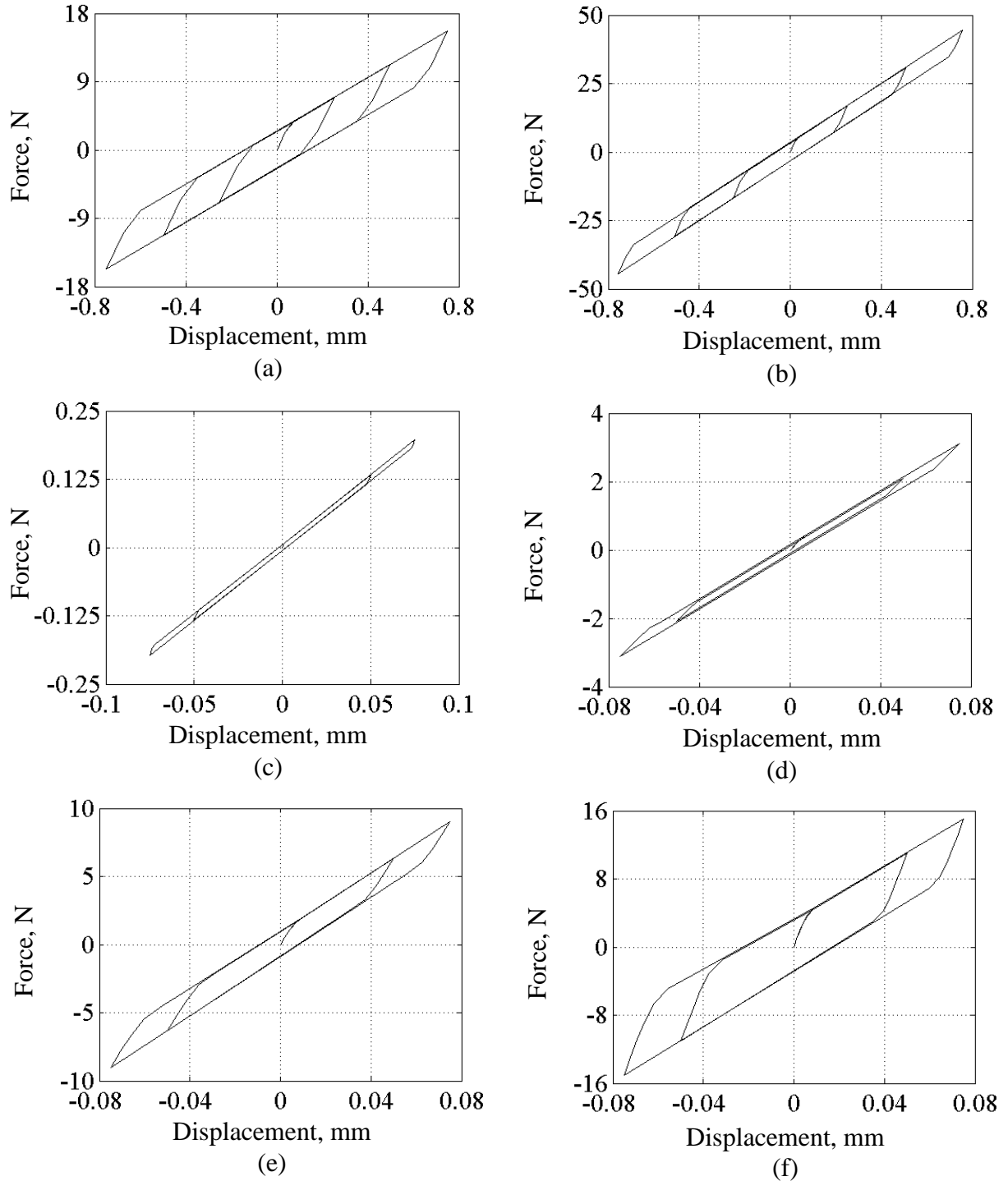
Figure 6.21 Analytical hysteresis loops at different peak displacement loadings for
Configurations (a) msr1, (b) msr2, (c) msw1, (d) msw2, (e) msw3 and (f) msw4

The average effective stiffness is defined as the average stiffness between the loading and unloading stages. The energy dissipated per cycle is measured as the area inside the analytical hysteresis loop. The stored strain energy is calculated as the area contained between the average effective stiffness and the displacement axis and Equation 3.31used to calculate the loss factor.

6.5 Quasi-static experiments on multi-strand bars and wires

This section is devoted to the experiments performed at the meso-scale and the micro-scale levels on the multi-strand bars and wires where these systems comprise individual strands with circular cross-section.

Mechanical clamps were used to hold the strands together for the seven-strand bar while heat shrink rings were used for the seven and nineteen strand wires. The geometric nomenclature is shown in Figure 6.1. The term quasi-static as stated earlier in Chapter 4 refers to a test in which the inertial forces have a negligible effect on the system response.

6.5.1 Experiments on seven-strand bars

Seven-strand bars comprising circular cross-sectional strands were used in the tests. The material used was 303 Grade Stainless Steel. The identification of the material properties was performed experimentally earlier in Section 6.3.

6.5.1.1 Clamp mechanism and its calibration

Two clamps were designed and manufactured. Each clamp unit was designed to apply a clamping effect on the six radially placed strands at the same time with the same clamp force. The clamps were located approximately 80 mm from each end of the bar. Figure 6.22a shows the multi-strand bar with the clamps attached.

(a)   (b)
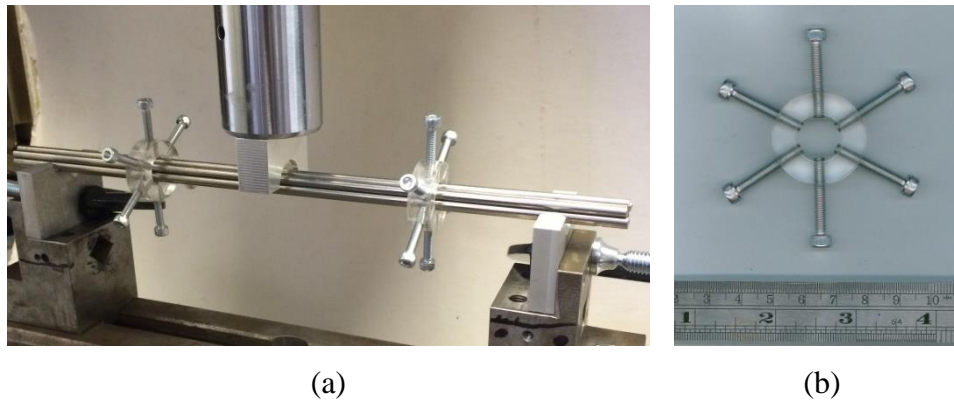
Figure 6.22 Three point flexure test configuration of the multi-strand bar (a) with clamps
and bearings, (b) the clamp unit

The clamp force was applied as a torque to the fasteners bolted in the clamp unit (shown in Figure 6.22b). As before, testing was carried out to relate the torque on the bolts to the compressive force applied. The data from the tests is provided in Figure 6.23.
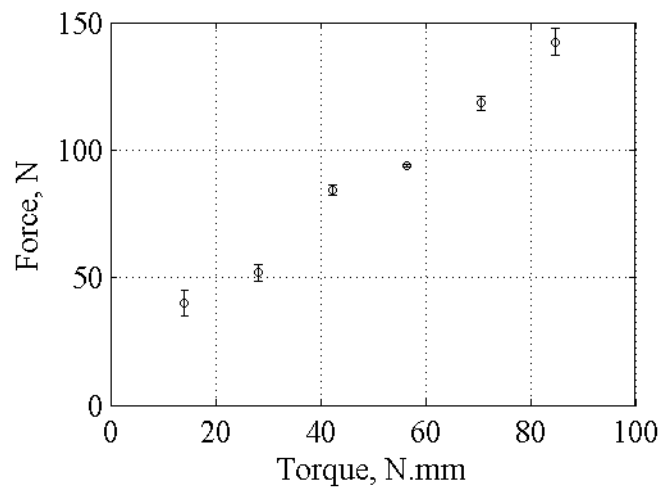
Figure 6.23 Equivalent clamp force values

6.5.1.2 Experimental set-up and methodology

The three point flexure tests consisted of the seven-strand bar (Configurations msr1 and msr2 detailed in Table 6.2) being placed between two stationary support bearings at each end and a uniaxial motion loading support bearing applied equidistance from the stationary supports. These support bearings were specially designed and manufactured (shown in Figure 6.24) in order to fit the multi-strand bar due to its circular shape, in the length direction. Careful consideration taken into account in the design process of these supports to

minimize the boundary conditions effect through the sharp contact edge between the supports and the multi-strand bars. Each multi-strand system had its own bearings as there were two sets of bars with different individual strands diameters (3 mm and 4 mm). Each of the support bearings was located 125 mm from the centre of the bar while the loading bearing was positioned centrally along the length of the bar.

Figure 6.24 Support bearing

The loading was applied in the thickness direction through the loading bearing using the same MTS 858 Table Top servo-hydraulic test machine(see Figure 6.22a). The applied displacement was altered during the tests. The setup for the test is shown in Figure 6.25.

At the start of each experiment, the loading bearing was lowered until an initial contact was made with the bar. From this point, the loading bearing was lowered an additional 0.1 mm to apply a light compressive load to avoid flatting of the peak in the obtained force signal. A sinusoidal displacement at 1.0 Hz was then applied to the bar starting from the 0.1 mm initial displacement to additional peak-to-peak (PK-PK) displacement of 0.5 mm, 1.0 mm and 1.5 mm. Each of the PK-PK displacements used level of clamping force of 142 N. The amounts of the sinusoidal displacements were chosen to ensure operation within the elastic region.
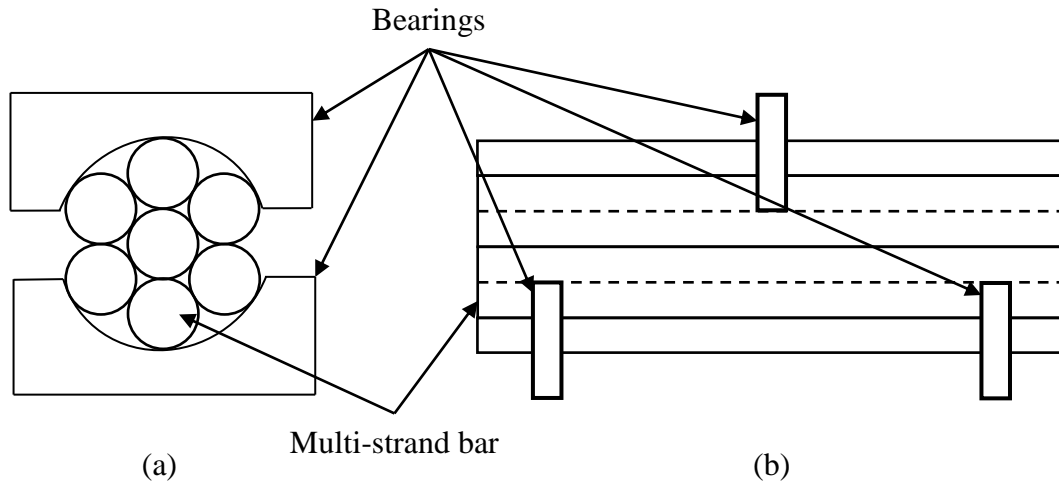
Figure 6.25 Setup of the three point bend test (a) side view, (b) front view

6.5.1.3 Experimental results

The force and displacement signals obtained from the tests were used to estimate the damping generated. The sampling frequency for each recorded signal was 1000 Hz. Figure 6.26 shows typical force and the displacement time histories where the effect of the friction was apparent as a lag between the two signals.

The experimental data contained some electrical noise as shown in Figure 6.27. As before, a Fast Fourier Transform filter was used to remove this noise as shown in Figure 6.28 (see Section 4.3.1).

Polynomial fit was applied to the experimental hysteresis loops in order to estimate the average effective stiffness. The energy dissipation amount per cycle was measured by numerical integration of the force-displacement curve. Equation 3.31 was then used to calculate the loss factor from the energy dissipation and the stored strain energy.

(a)

(b)
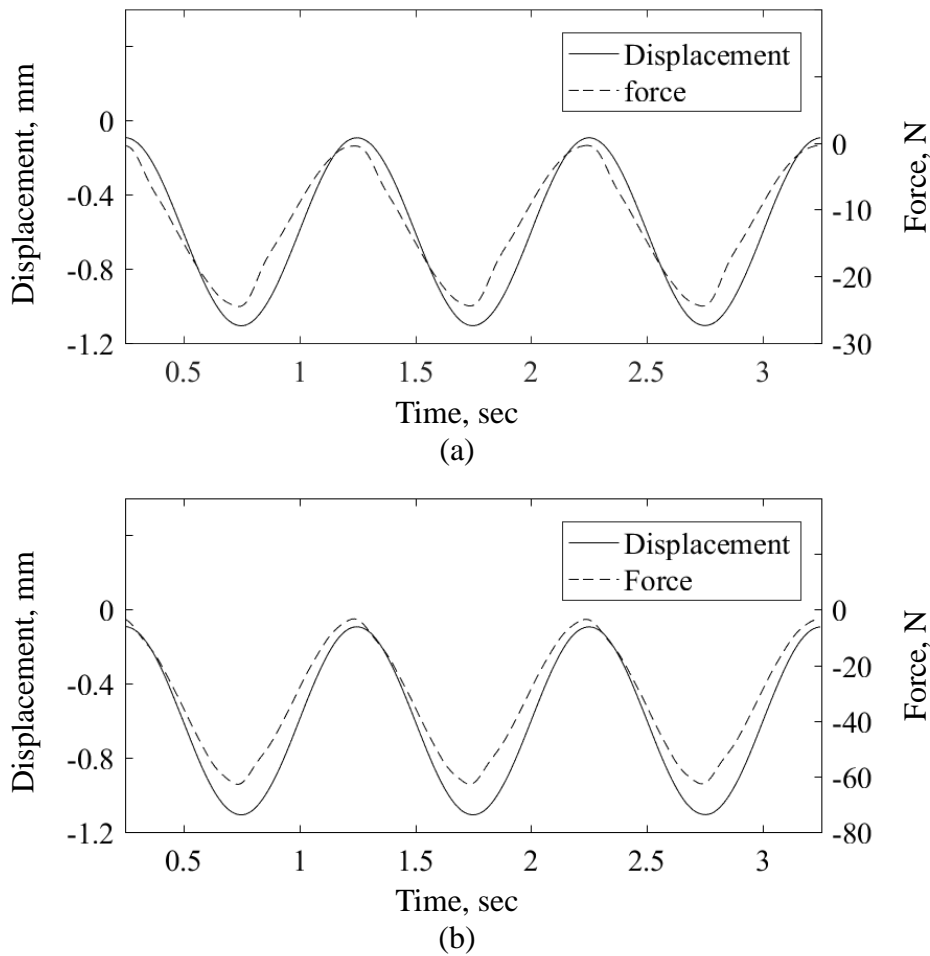
Figure 6.26 The force and displacement time history at peak displacement of 1.0 mm for Configurations (a) msr1 and (b) msr2

(a)   (b)
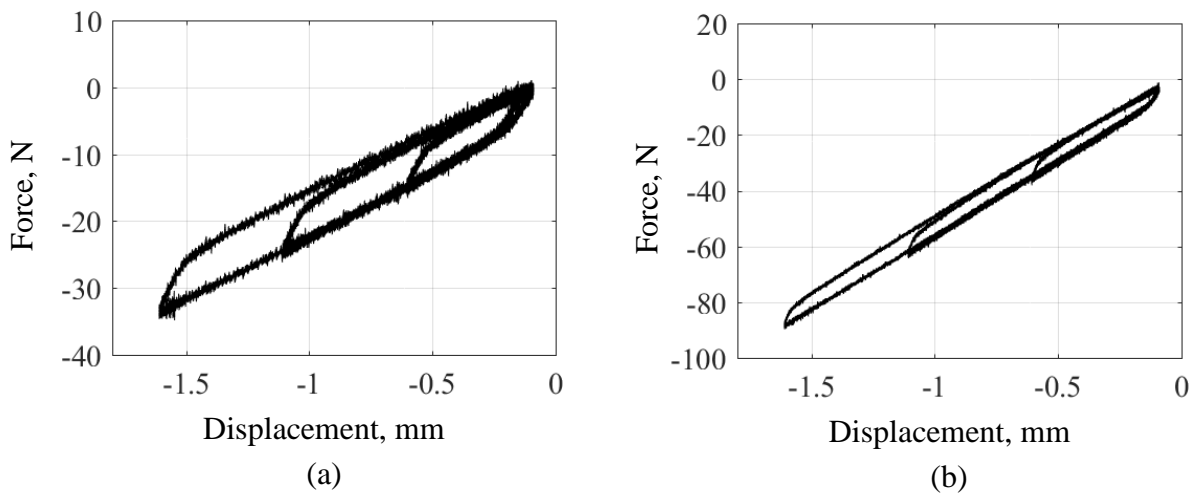
Figure 6.27 Unfiltered force-displacement (hysteresis loops) relationships at 0.5 mm, 1.0 mm and 1.5 mm peak displacements for Configurations (a) msr1 and (b) msr2
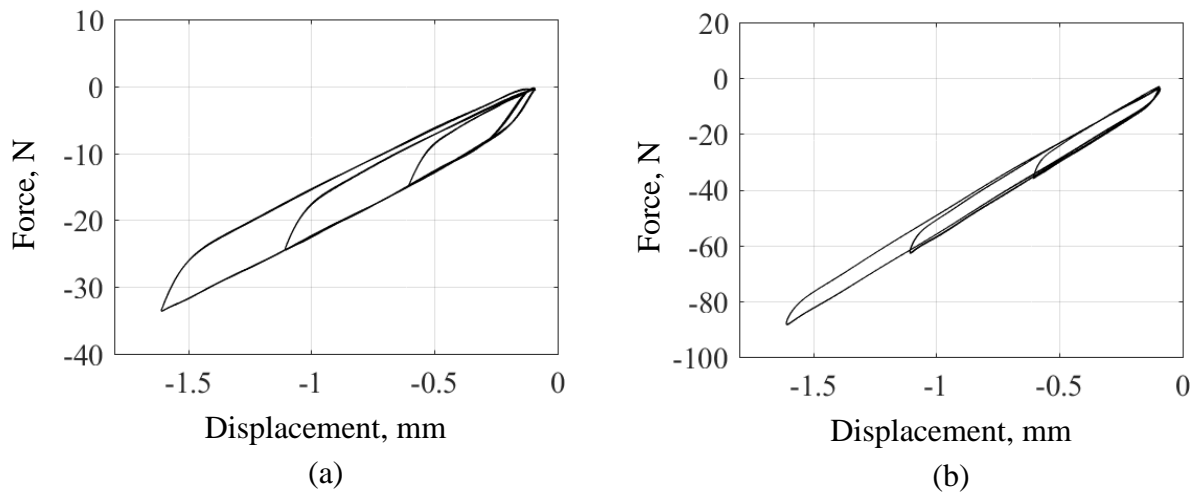
Figure 6.28 Filtered force-displacement (hysteresis loops) relationships at 0.5 mm, 1.0 mm and 1.5 mm peak displacements for Configurations (a) msr1 and (b) msr2

6.5.2 Experiments on seven-strand wires and nineteen-strand wires

Multi-strand wires comprising seven strands (Configuration msw1) and nineteen strands (Configuration msw2) were used in the tests. The individual strands were made of spring steel and the material properties that were identified earlier in Section 6.3. Heat shrink rings were used to provide the clamping effect required to hold the individual steel strands together. These systems were subjected to three point flexure tests.

6.5.2.1 Clamping with heat shrink rings

Heat shrink rings were used to clamp the individual strands together as it was impractical to use metal rings with tiny bolts and also because of the additional mass of such clamps. On the other hand, heat shrink rings provided inexpensive, light weight clamps with no need for the bolts.

The heat shrink material was polypropylene , a thermoplastic polyolefin polymer. Polyolefin polymers consist of carbon and hydrogen atoms and are non-porous. They are used as heat-shrink wraps in consumer merchandise and wire protection. Polyolefin can shrink when subjected to heat and in some places they are called shrink wraps. Nevertheless, this material can melt if exposed to very high temperature (the minimum temperature to trigger the heat shrink action was 90C°) and can break when exposed to very cold temperature. The material

used had a shrink ratio of 2:1 of its original diameter when exposed to a heat source over 150 C° [106,107].

- **Pressure applied by heat shrink rings**

Press-fit theory for thick-walled cylinders was used to estimate the clamping pressure that the heat shrink rings applied to the multi-stand wire. These rings were considered thick as their average radius was less than 20 times their thickness [108].

In order to estimate the pressure that the heat shrink ring applies, the radial interference displacement was required. This is the difference between the radial displacement of the ring and the radial displacement of the multi-strand wire as shown in Figure 6.29 and expressed as,

$$\delta_r = \delta_{rr} - \delta_{rm} \qquad\qquad 6.83$$

where, δ_r is the radial interference displacement, δ_{rr} is the radial displacement of the heat shrink ring and δ_{rm} is the radial displacement of the multi-strand wire.

Multi-strand wire   Heat shrink ring
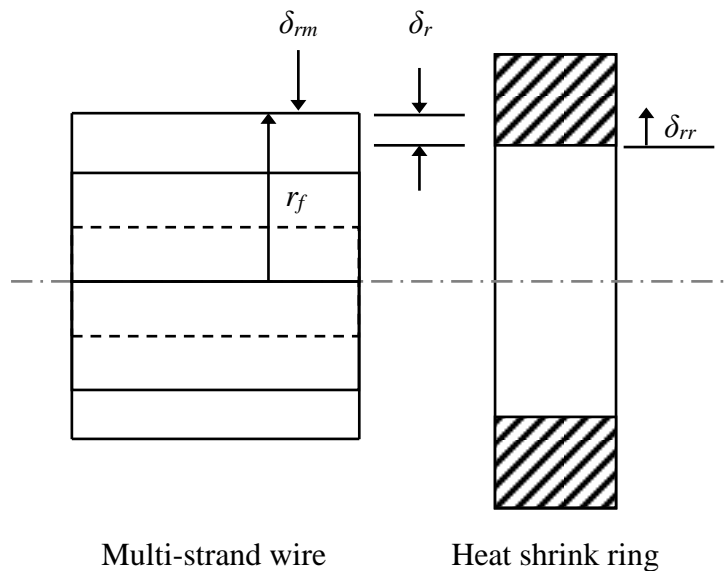
Figure 6.29 Press-fit theory applied to the multi-strand wire and the heat shrink ring

As the heat shrink ends are free, the condition was considered plane stress (zero longitudinal stress) and from standard elasticity theory [109]:

$$\varepsilon_r = \frac{d\delta}{dr} = \frac{1}{E}(\sigma_r - \upsilon\sigma_\theta)$$
<div align="right">6.84</div>

$$\varepsilon_\theta = \frac{\delta}{r} = \frac{1}{E}(\sigma_\theta - \upsilon\sigma_r)$$
<div align="right">6.85</div>

where, σ_r and σ_θ are the radial and the circumferential stresses respectively and υ is Poisson's ratio.

Re-arranging Equation 6.85 in term of the radial interference leads to

$$\delta = \frac{r}{E}(\sigma_\theta - \upsilon\sigma_r)$$
<div align="right">6.86</div>

At this stage, the radial displacement for both the heat shrink ring and the multi-strand wire are calculated and substituted in Equation 6.83.

- **For the heat shrink ring radial displacement:**

Reusing Equation 6.86 in terms of heat shrink ring gives:

$$\delta_{rr} = \frac{r_f}{E_r}(\sigma_{\theta r} - \upsilon_r\sigma_{rr})$$
<div align="right">6.87</div>

where, r_f is the nominal radius, E_r and υ_r are the modulus of elasticity and Poisson's ratio for the heat shrink ring respectively.

The radial and the circumferential stresses for internally pressurized thick-walled cylinders (heat shrink ring) were described as

$$\sigma_{rr} = \frac{P_f\, r_f{}^2\left(1 - \dfrac{r_o{}^2}{r_f{}^2}\right)}{r_o{}^2 - r_f{}^2}$$
<div align="right">6.88</div>

$$\sigma_{\theta r} = \frac{P_f\, r_f{}^2\left(1 + \dfrac{r_o{}^2}{r_f{}^2}\right)}{r_o{}^2 - r_f{}^2}$$
<div align="right">6.89</div>

where, σ_{rr} and $\sigma_{\theta r}$ are the radial and the circumferential stresses for internally pressurized thick-walled cylinder, P_f is the interference pressure, r_o is the over-all heat shrink ring radius.

Substituting Equations 6.88 and 6.89 into Equation 6.87 gives

$$\delta_{rr} = \frac{r_f \, P_f}{E_r} \left(\frac{r_o^2 + r_f^2}{r_o^2 - r_f^2} + \upsilon_r \right)$$

$$6.90$$

- **For the multi-strand wire radial displacement:**

Reusing Equation 6.86 in term of multi-strand wire system gives

$$\delta_{rm} = \frac{r_f}{E_m} (\sigma_{\theta m} - \upsilon_m \sigma_{rm})$$

$$6.91$$

where, E_m and υ_m are the modulus of elasticity and Poisson's ratio for the multi-strand steel wires respectively.

The radial and circumferential stresses for externally pressurized thick-walled cylinders (multi-strand wire system) were described as

$$\sigma_{rm} = \frac{P_f \, r_f^2}{r_f^2 - r_i^2} \left(\frac{r_i^2}{r_f^2} - 1 \right)$$

$$6.92$$

$$\sigma_{\theta m} = -\frac{P_f \, r_f^2}{r_f^2 - r_i^2} \left(\frac{r_i^2}{r_f^2} + 1 \right)$$

$$6.93$$

where, σ_{rm} and $\sigma_{\theta m}$ are the radial and the circumferential stresses for externally pressurized thick-walled cylinder and r_i is inner radius of the multi-strand wire system (zero for solid cylinders).

Substituting Equations 6.92 and 6.93 into Equation 6.91 gives

$$\delta_{rm} = -\frac{r_f \, P_f}{E_m} \left(\frac{r_f^2 + r_i^2}{r_f^2 - r_i^2} - \upsilon_m \right)$$

$$6.94$$

- **For the radial displacement at interference fit:**

The radial interference was then calculated through substituting Equations 6.90 and 6.94 into Equation 6.83 gives

$$\delta_r = r_f \, P_f \left[\frac{r_o^2 + r_f^2}{E_r (r_o^2 - r_f^2)} + \frac{\upsilon_r}{E_r} + \frac{r_f^2 + r_i^2}{E_m (r_f^2 - r_i^2)} - \frac{\upsilon_m}{E_m} \right]$$

$$6.95$$

Re-writing Equation 6.95 in term of the interference pressure, as the interference radial displacement is known already, gives

$$P_f = \frac{\delta_r}{\frac{r_f}{E_r}\left(\frac{r_o^2 + r_f^2}{r_o^2 - r_f^2} + \upsilon_r\right) + \frac{r_f}{E_m}\left(\frac{r_f^2 + r_i^2}{r_f^2 - r_i^2} - \upsilon_m\right)} \qquad 6.96$$

The interference pressure P_f represents the pressure applied by the heat shrink ring on the multi-strand wire. The equivalent pressure applied from the entire heat shrink rings, used to hold the strands in the system, on each strand's body was expressed as

$$P_{eq} = P_f \frac{N_r l_r}{l} \qquad 6.97$$

where, P_{eq} is the equivalent pressure applied to the individual strands, N_r is the number of heat shrink rings used to clamp the individual strands, l_r is the length of each heat shrink ring and l is the length of the multi-strand wire.

The equivalent clamp force affecting on the individual strands was calculated through

$$F_{ceq} = P_{eq}\pi r l \qquad 6.98$$

The mechanical material properties, modulus of elasticity, of the heat shrink were required as these properties were one of the parameters that determine the amount of pressure that the heat shrink ring applied to the multi-strand wire. Experiments were performed on heat shrink strips using the Visco-analyser machine (see Figure 6.30). The Visco-analyser machine is a dynamic mechanical analysis (DMA) machine. It provides sinusoidal loading with a maximum load capacity of 100 N. The software estimates modulus and loss factor from the load and deflection time history and the specimen geometry. Two specimens were tested: the first was the material in its original form while the second was material after being exposed to heat (90°C) and allowed to cool for 30 minutes. Measurements were made to the cross-section of the heat shrink strip in order to provide these measurements to the machine program. Each test was repeated eleven times. Table 6.4 shows the moduli of elasticity for both, unheated and heated, specimens. The average value of the modulus of elasticity for the heated specimen (85 MPa) was used for subsequent calculations.
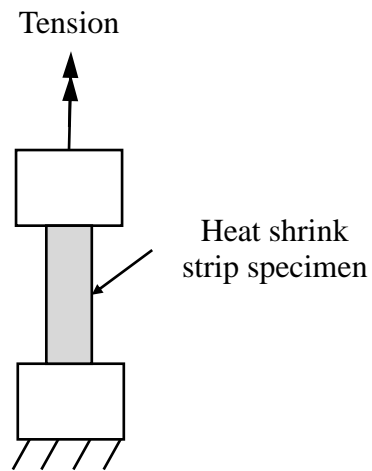
Figure 6.30 Setup for the heat shrink test

Table 6.4 The modulus of elasticity of the unheated and heated heat shrinks

Test Number	Unheated heat shrink E, MPa	Heated heat shrink E, MPa
1	84.7	94.7
2	98.9	89.7
3	97.9	89.4
4	96.6	88.3
5	95.2	87.0
6	93.7	85.7
7	92.3	84.4
8	91.1	83.2
9	89.7	81.9
10	88.4	80.7
11	87.0	79.4
Average	92.3	85.9

Some parametric values that were used in Equation 6.96 to calculate the clamp pressure and subsequently the clamp forces are listed in Table 6.5.

Table 6.5 Parametric data of the heat shrink ring and the multi-strand wire

Parameter	msw1	msw2
δ_r, mm	0.050	0.300
r_f, mm	0.750	1.200
r_o, mm	0.700	1.500
r_i, mm	0.000	0.000
υ_r	0.420	0.420
E_r, GPa	0.850	0.850
υ_m	0.300	0.300
E_m, GPa	203.6	203.6

From the previous calculations, the clamp force applied on the strands by the heat shrink rings was 0.94 N and 10 N for Configurations msw1 and msw2 respectively.

6.5.2.2 Experimental set-up and methodology

The DMA machine used for material characterisation was also used to conduct quasi-static tests on Configurations msw1 and msw2 (Table 6.2). Configuration msw1 comprised seven steel strands whereas Configuration msw2 comprised nineteen steel strands. The individual circular cross-sectioned strands in both configurations were 0.5 mm in diameter and a total length of 60 mm. The span distance was 45 mm. The length and span distance dimensions were chosen according to the chamber size of the DMA machine.

Four heat shrink rings were used to clamp Configurations msw1 and msw2. The pre-shrunk diameter of the seven and nineteen strand wires were 1.6 mm and 4.8 mm respectively. On heating the shrink ratio was 2:1. Each ring was 1.0 mm in length and had a wall thickness of 0.3 mm. Figure 6.31 shows both multi-strand wires clamped with heat shrink rings.

Cyclic sinusoidal peak-to-peak displacement loading of 0.15 mm and 0.10 mm at a frequency of 2.5 Hz were applied to the seven-strand wire and the nineteen-strand wire respectively. A static compressive pre-displacement of 0.1 mm was set as the minimum displacement during the subsequent sinusoidal displacement. The experimental force and the displacement results were recorded at sampling frequencies of 5100 Hz and 20000 Hz for Configurations msw1 and msw2 respectively. The seven-strand wire experiencing flexural loading is shown in Figure 6.32.

<table>
<tr><td>(a)</td><td>(b)</td></tr>
</table>
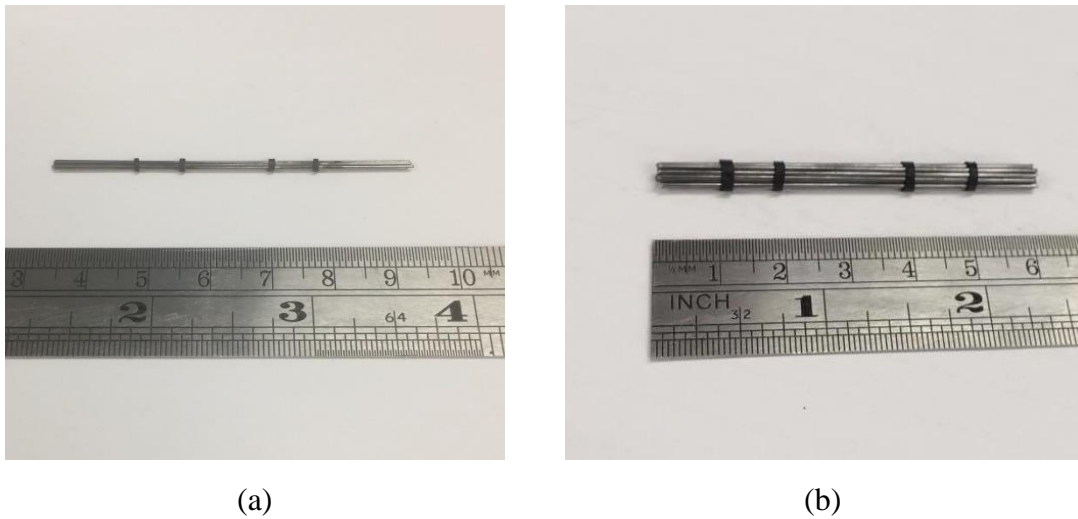
Figure 6.31 Heat shrink rings clamping (a) seven-strand wire and (b) nineteen-strand wire

Figure 6.32 Seven-strand wire during the three point flexure loading

6.5.2.3 Experimental results

Three point flexure tests performed on seven-strand wire and nineteen-strand wire using the DMA machine. The force and the displacement signals were obtained experimentally and used to plot the force-displacement relationships (hysteresis loops) in order to estimate the damping amounts in these wire systems. The unfiltered hysteresis loops are shown in Figure 6.33 for Configuration msw1 and msw2. Fast Fourier transform filter was adopted to filter

the force and the displacement signals. The reason for choosing this technique was explained earlier in Section 4.3.1. The filtered data are shown in Figure 6.34 for Configurations msw1 and msw2.

The force and the displacement time histories for Configurations msw1 and msw2 are depicted in Figure 6.35. The effect of friction appears in the force signal as a phase difference and a distortion caused by the nonlinearity.

The experimental hysteresis loops were exposed to polynomial fit in order to estimate the average effective stiffness. The energy dissipation amount per cycle was calculated through a numerical integration of the force-displacement curve. Equation 3.31 was then used to count the loss factor through calculating the energy dissipation and the stored strain energy that were obtained from the experimental hysteresis loops.

(a)   (b)
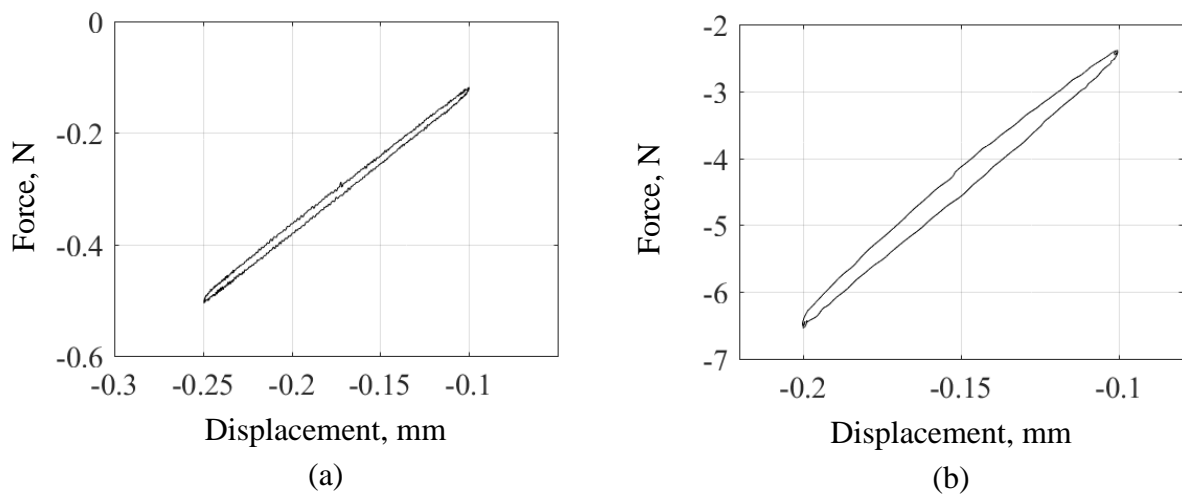
Figure 6.33 Unfiltered hysteresis loops for (a) seven-strand wire (msw1) and (b) nineteen-strand wire (msw2)

(a)   (b)
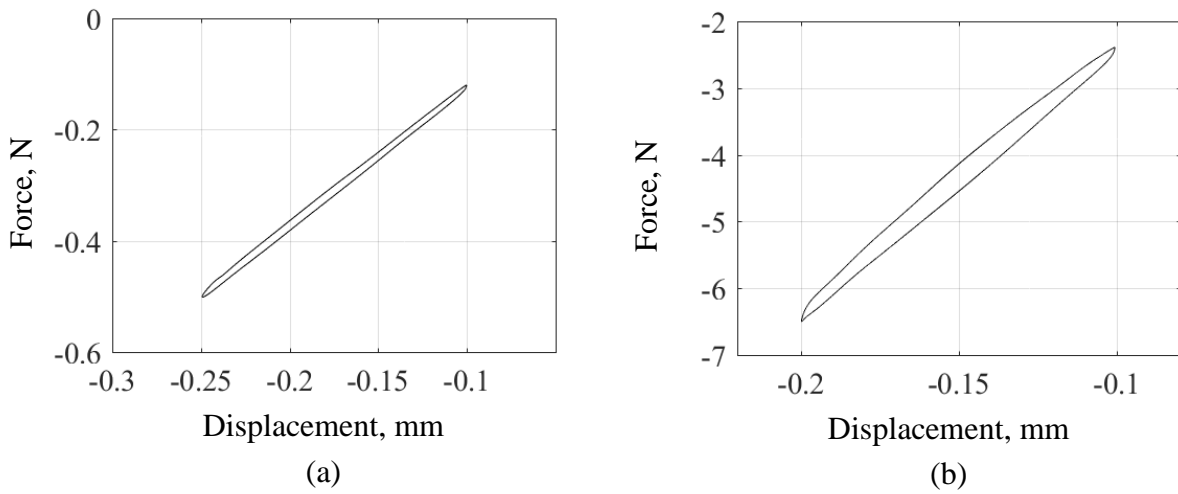
Figure 6.34 Filtered hysteresis loops for (a) seven-strand wire (msw1) and (b) nineteen-strand wire (msw2)

(a)

(b)
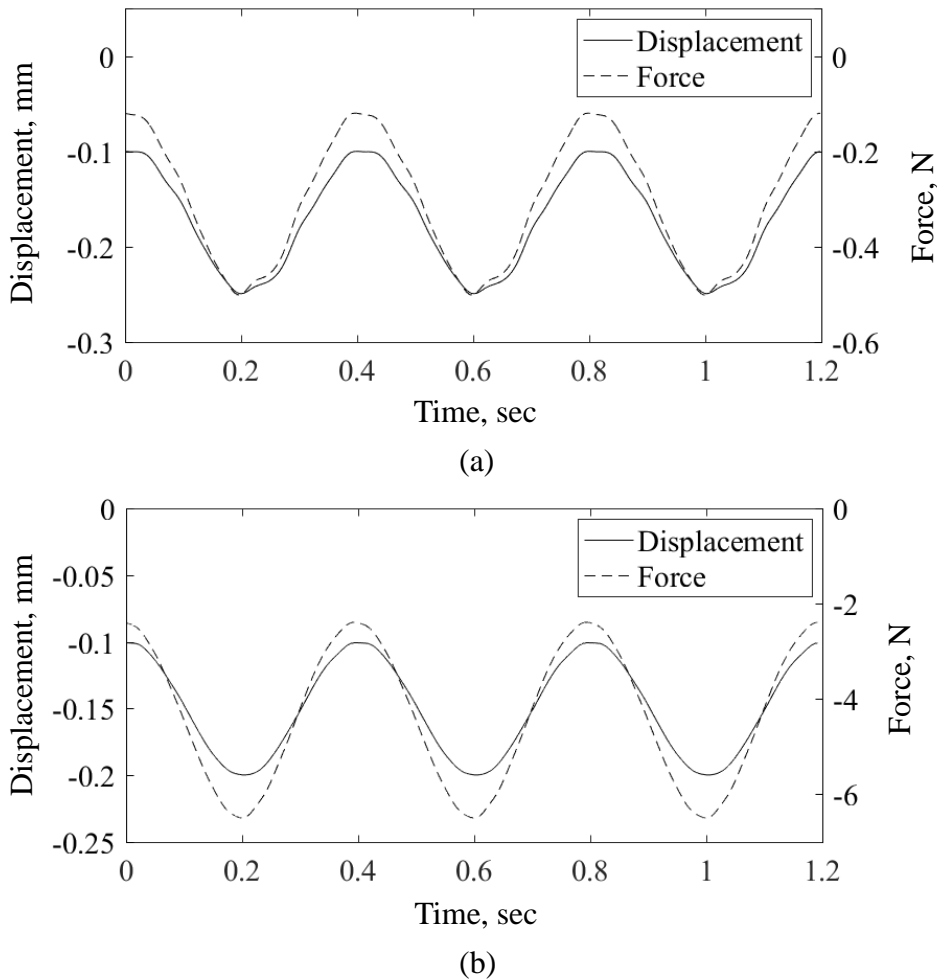
Figure 6.35 Time history of the force and the displacement signals for (a) seven-strand wire (msw1) and (b) nineteen-strand wire (msw2)

6.6 Quasi-static numerical analysis

Finite element (FE) models were built for Configurations msr1, msr2, msw1 and msw2 (Table 6.2) to simulate the frictional behaviour of the multi-strand bars and wires.

The numerical modelling process was identical to that carried out for the square sectioned bars studied previously. FE models were constructed using ANSYS and comprised Solid 3-D 20-node quadratic hexahedral (SOLID186) elements for the body representation of each strand while 8-node surface-surface contact (CONTA174) and target segment (TARGE170) were used to represent the contact pairs. Each strand was represented as a linear elastic material with Poisson's ratio of 0.3 and the mechanical properties of the strands are listed in Table 6.6. The selection of the material properties for the strands was based on the experimental results obtained from Section 6.3. A Coulomb friction model was used for each contact pair with $\mu=0.25$ estimated by using the analytical model described in Section 6.4.1 along with experimental results.

Mesh properties for the multi-strand bars and the multi-strand wires are presented in Table 6.6. Statistical data of the number of nodes and elements and element lengths used to build the FE models for different configurations were provided in Table 6.6. The element sizes were chosen depending on the validation study performed on Configurations msr1 and msw1. Two criteria were taken into consideration when choosing the element size. The first was the consistency of the resulting numeric forcing values and the second was the computational expense due to the increased number of the nodes and elements that represent the strands bodies when using smaller element sizes. The effect of body element size on the number of nodes and elements and the validation study are presented in Table 6.7 and it was clear that the selected element sizes should not affect the accuracy of the numerical analyses and maintain sensible analysis time cost.

Table 6.6 Statistical data of the numerical models

Configurations	Number of nodes	Number of elements	Body element size, mm	End side element size, mm	Modulus of elasticity, GPa
msr1	70969	14364	2.000	0.750	195.7
msr2	110509	21924	2.000	1.000	188.1
msw1	70969	14364	0.360	0.125	203.6
msw2	232171	46872	0.360	0.125	203.6

Table 6.7 Validation of the effect of body element size on the number of nodes, the number of elements and the reaction force for Configuration msr1

Element size, mm	No. of nodes	No. of elements	Force, N
2.750	53049	10716	136.6
2.500	56409	11400	136.7
2.250	63129	12768	136.7
2.000	70969	14364	136.7
1.750	81049	16416	136.7
1.500	94489	19152	136.7
1.250	112409	22800	136.8
1.000	140409	28500	136.8

6.6.1 Boundary conditions and loadings

Each configuration was constrained and loaded as a three-point flexure with a sinusoidal displacement loading. The boundary conditions and loadings were applied to the FE models to match those applied in the analytical models and the experimental tests. The clamping force was presented in the simulation as a radially distributed pressure [95, 100] on the strands, directed toward the centre of the wire system as depicted in Figure 6.36.
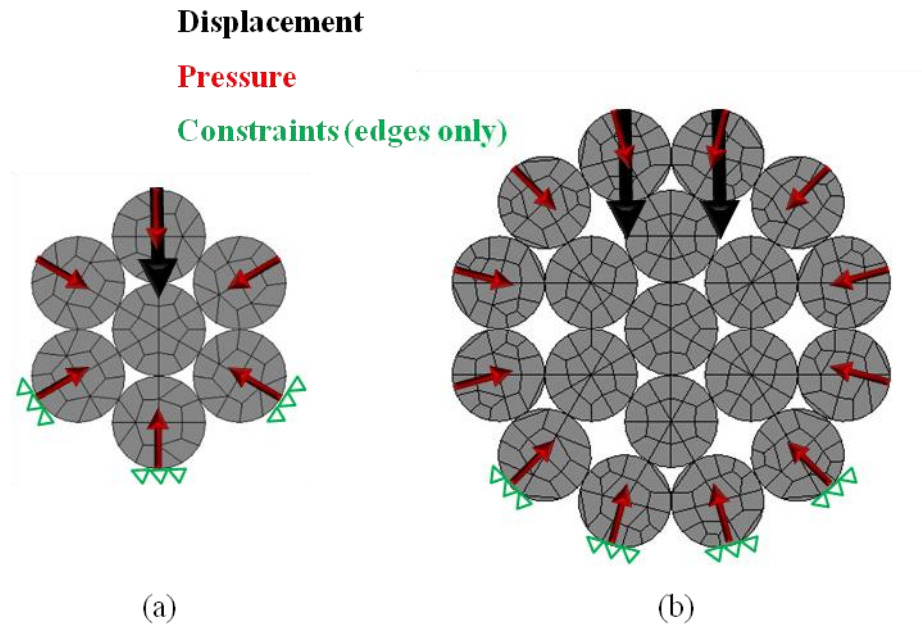
Figure 6.36 Boundary conditions and loads of FE models for (a) msw1 and (b) msw2

Peak-to-peak (PK-PK) displacements of 0.5 mm, 1.0 mm and 1.5 mm were considered for Configurations msr1 and msr2 while PK-PK displacements of 0.1 mm and 0.15 mm were applied to Configuration msw1 and only 0.1 mm PK-PK displacement was applied to Configuration msw2. A seven-strand bar (msr1) experiencing flexural loading and a nineteen-strand wire (msw2) are shown in Figure 6.37. The clamp pressure was the ratio of the clamping forces to the area where the clamping forces was applied. A quasi-static sinusoidal displacement (ignoring transient effects) was used to obtain force-displacement hysteresis loops that were used to determine the system loss factor.
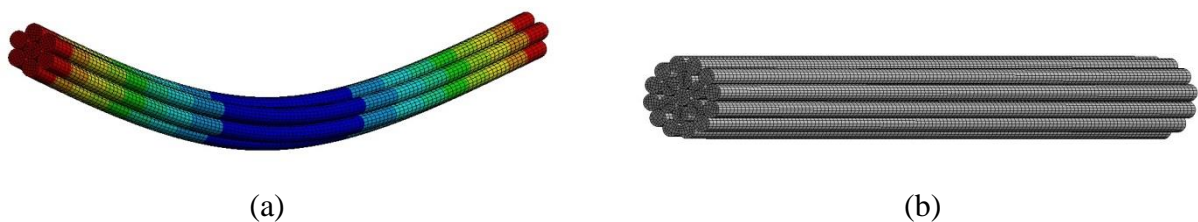
Figure 6.37 FE models showing (a) typical deformation depicted for a seven-strand bar (msr1) under bending and (b) A nineteen-strand wire (msw2)

6.6.2 Numerical results

The simulated force-displacement data were obtained from the numerical models for Configurations msr1, msr2 and msw1. The solver was unable to reach convergence for Configurations msw2, msw3 and msw4 although finer mesh was used – for Configuration msw2, the solver required six days computation time on a high performance PC. Peak-to-peak (PK-PK) displacements of 0.5 mm, 1.0 mm and 1.5 mm were applied to the FE models of Configurations msr1 and msr2 and the force-displacement relationships (hysteresis loops) obtained during the simulation are shown in Figure 6.37a and b. The numerical force-displacement relationships obtained from applying PK-PK displacements of 0.1 mm and 0.15 mm to Configuration msw1 are depicted in Figure 6.37c.

For all obtained numerical hysteresis loops, dry friction behaviour was observed visually in the hysteresis loops – see Figure 6.38 as an example.

(a)

(b)

(c)
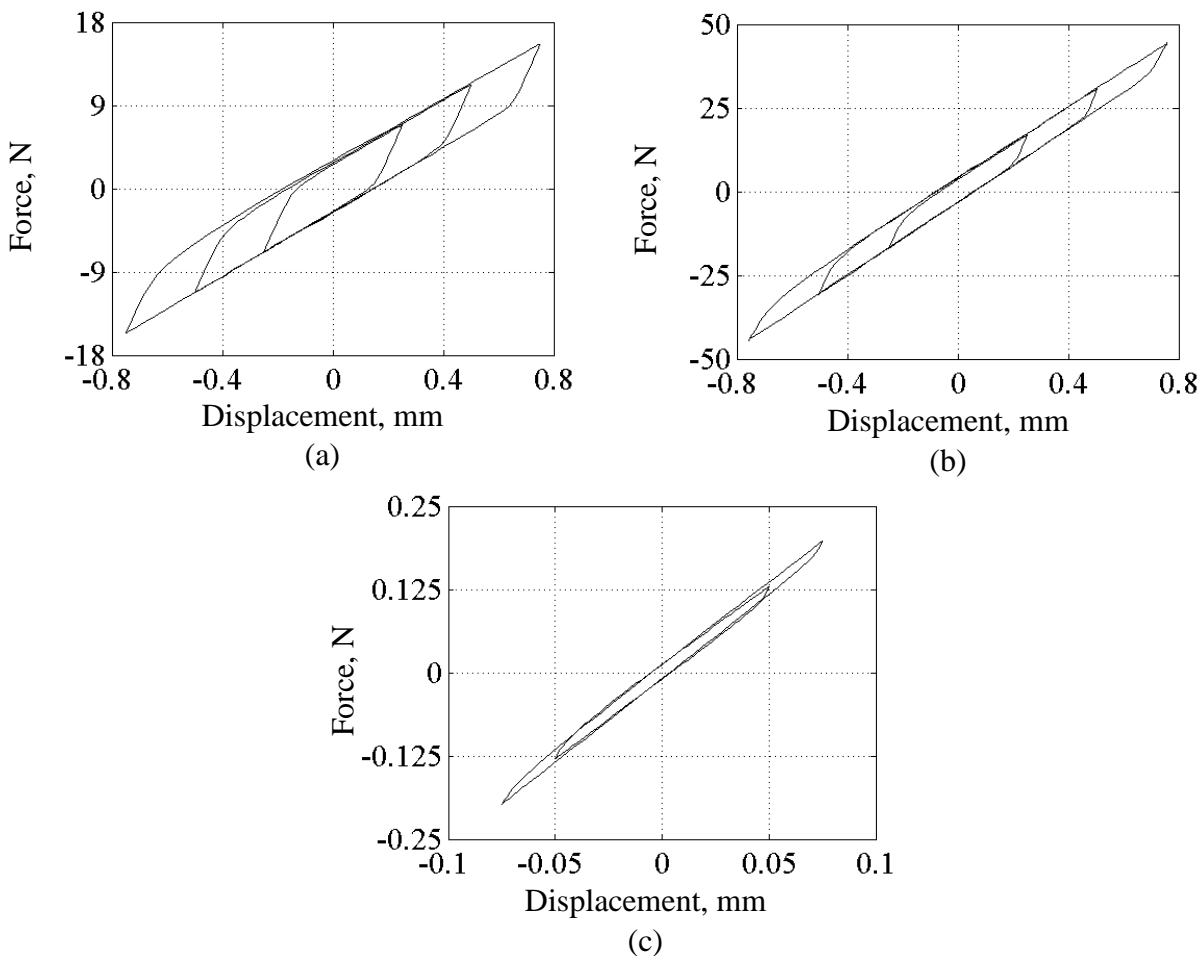
Figure 6.38 Numerical hysteresis loops at different peak displacement loadings for Configurations (a) msr1, (b) msr2 and (c) msw1

6.7 Results and discussion

In this section, the hysteresis loops obtained from analytical models, experimental tests and numerical analysis are compared together for the configurations listed in Table 6.2 at different loading displacement. Generally, there was an agreement in the damping behaviour described by the three techniques.

Table 6.8, Table 6.9 and Table 6.10 list the analytical and the experimental and the numerical damping characteristics respectively.

Comparison of analytically, experimentally and numerically obtained hysteresis loops is shown in Figure 6.38 for Configurations msr1 (seven-strand bar with each strand diameter of 3.0 mm) and msr2 (seven-strand bar with each strand diameter of 4.0 mm) at peak-to-peak (PK-PK) displacement loadings of 0.5 mm, 1.0 mm and 1.5 mm. The effect of increasing the diameter of the individual strands in the system was to cause a reduction in the loss factor whereas the energy dissipation per cycle, the peak strain energy and the stiffness were increased. The stiffness increased as it is directly proportional to the second moment of area while the increase of the energy dissipation and the peak strain energy was due to that increased force required to displace the system for the same amount.

The effect of increasing the peak displacement was noticed as a reduction in the loss factor values for all configurations which agrees with the conclusions obtained from the previous chapters. The stiffness behaviour showed no significant change for different levels of loading for the same configuration (Table 6.9).

Comparison of the analytically and numerically obtained hysteresis loops for Configuration msw1 (seven-strand wire) at PK-PK displacement of 0.1 mm was shown in Figure 6.39a while a comparison of analytical, experimental and numerical hysteresis loops for Configuration msw1 at PK-PK displacement of 0.15 mm was shown in Figure 6.39b. Experimental and analytical hysteresis loops were compared and depicted in Figure 6.39c for Configuration msw2 (nineteen-strand wire) at PK-PK displacement of 0.1 mm.
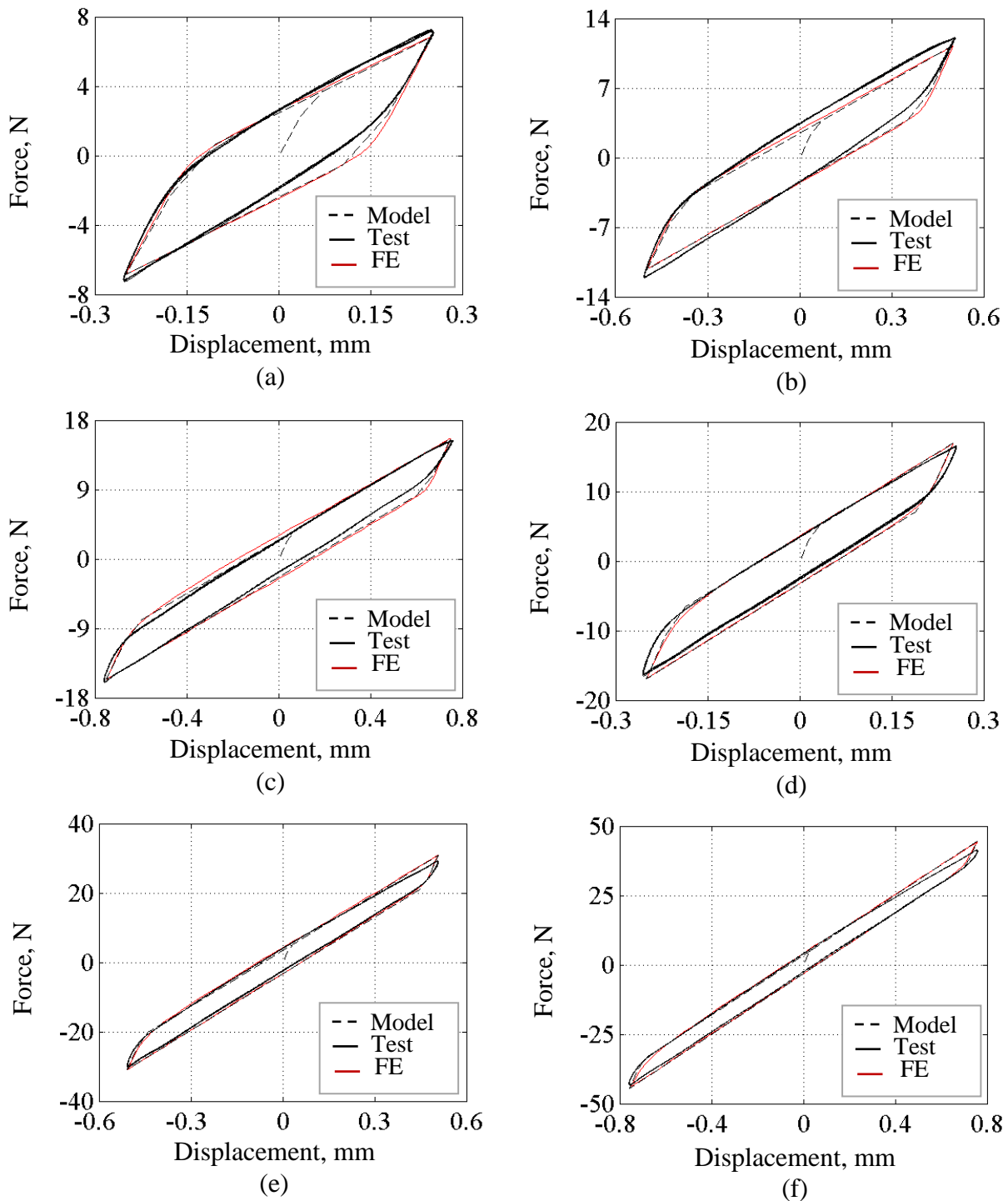
Figure 6.39 Comparing Analytical, experimental and numerical hysteresis loops for both Configuration msr1 at PK-PK displacement loading of (a) 0.5 mm, (b) 1.0 mm and (c) 1.5 mm and for Configuration msr2 at PK-PK displacement loading of (d) 0.5 mm, (e) 1.0 mm and (f) 1.5 mm

Analytical hysteresis loops for Configurations msw2, msw3 (thirty-seven-strand wire) and msw4 (sixty-one-strand wire) at PK-PK displacement loadings of 0.1 mm and 0.15 mm were shown in Figure 6.21d, e and f.
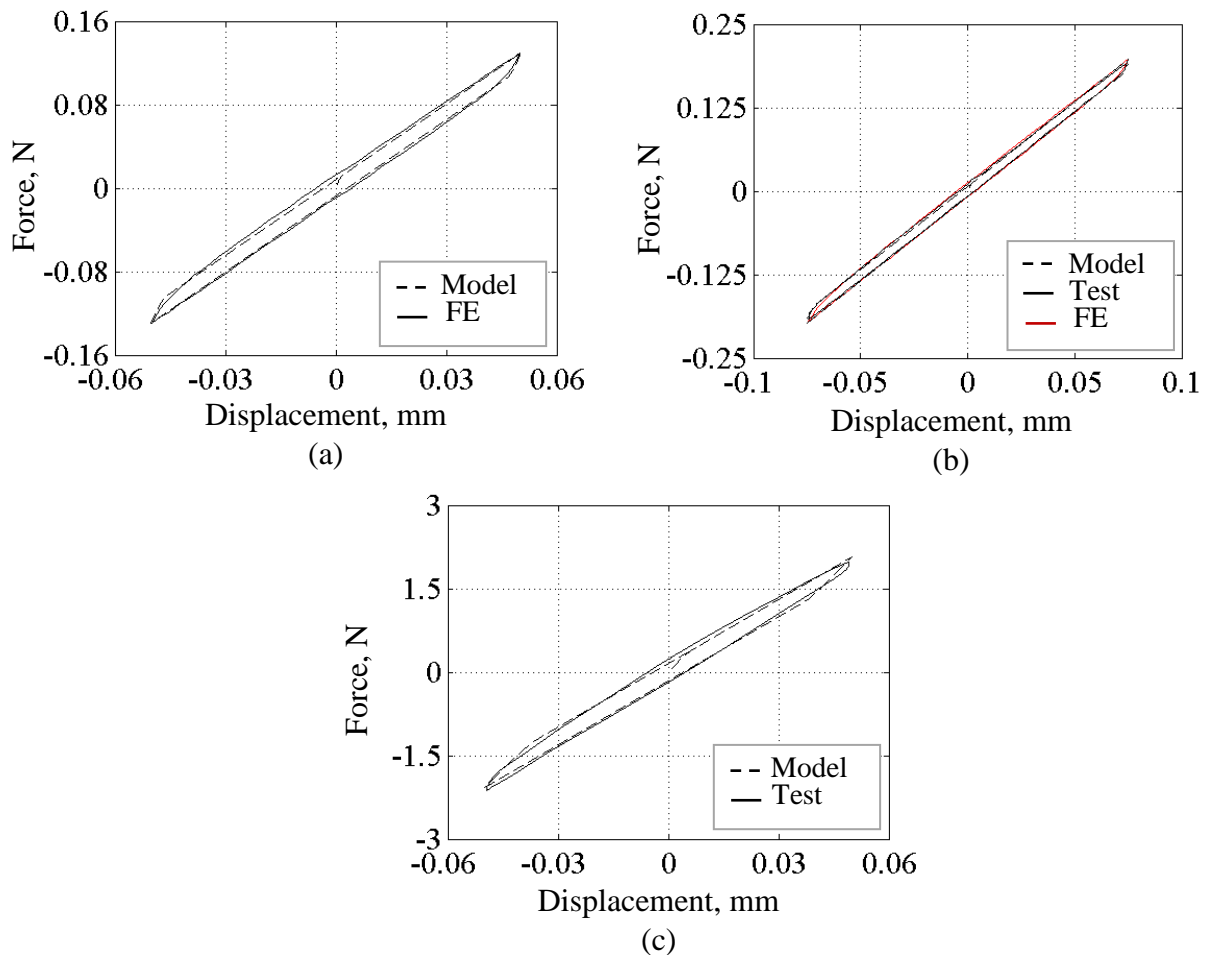
Figure 6.40 Comparing (a) analytical and numerical hysteresis loops for Configuration msw1at PK-PK displacement of 0.1 mm and (b) analytical, experimental and numerical hysteresis loops for Configuration msw1 at PK-PK displacement of 0.15 mm and (c) analytical and experimental hysteresis loops for Configuration msrw2 at PK-PK displacement of 0.1 mm

Table 6.8 Analytical damping characteristics for Configuration msr1 through Configuration msw4

Configurations	PK-PK displacement, mm	Analytical			
		Stiffness, N/mm	Strain energy, mJ	Energy dissipation /cycle, mJ	Loss factor
msr1	0.500	17.67	1.489	1.829	0.391
msr1	1.000	17.64	4.734	4.219	0.283
msr1	1.500	17.59	10.53	6.654	0.201
msr2	0.500	54.28	3.673	2.926	0.253
msr2	1.000	54.00	14.67	6.305	0.136
msr2	1.500	54.40	32.49	9.537	0.093
msw1	0.100	2.422	0.006	0.001	0.082
msw1	0.150	2.517	0.014	0.002	0.055
msw2	0.100	38.45	0.098	0.027	0.088
msw2	0.150	39.61	0.224	0.041	0.058
msw3	0.100	108.2	0.292	0.154	0.168
msw3	0.150	107.4	0.634	0.264	0.132
msw4	0.100	159.8	0.465	0.552	0.378
msw4	0.150	157.6	0.984	0.933	0.301

Table 6.9 Experimental damping characteristics for Configuration msr1 through Configuration msw2

Configurations	PK-PK displacement, mm	Experimental			
		Stiffness, N/mm	Strain energy, mJ	Energy dissipation /cycle, mJ	Loss factor
msr1	0.500	21.27	1.525	1.802	0.376
msr1	1.000	17.87	5.240	4.953	0.300
msr1	1.500	18.25	10.82	5.740	0.168
msr2	0.500	54.49	3.627	2.691	0.236
msr2	1.000	53.53	13.90	5.777	0.132
msr2	1.500	55.11	30.77	8.661	0.089
msw1	0.150	2.520	0.014	0.002	0.050
msw2	0.100	39.47	0.098	0.030	0.098

Table 6.10 Numerical damping characteristics for Configurations msr1 through Configuration msw1

Configurations	PK-PK displacement, mm	Numerical			
		Stiffness, N/mm	Strain energy, mJ	Energy dissipation /cycle, mJ	Loss factor
msr1	0.500	17.36	1.370	1.946	0.452
msr1	1.000	15.12	4.657	4.577	0.312
msr1	1.500	16.37	10.04	7.373	0.233
msr2	0.500	49.06	3.609	2.910	0.256
msr2	1.000	53.66	13.98	6.739	0.153
msr2	1.500	53.46	31.40	9.858	0.099
msw1	0.100	2.388	0.006	0.001	0.099
msw1	0.150	2.543	0.014	0.002	0.061

6.8 Conclusions

The conclusions that can be derived from the work described in this chapter are detailed below.

- Analytical models:

  ✓ The analytical models described the damping behaviour in the multi-strand bars and multi-strand wires accurately. The analytical models followed the slip phases that occur when several strands start slipping at different times.

  ✓ The analytical models were able to estimate the frictional stiffness of the multi-strand systems using the frictional second moment of area.

  ✓ The importance of the analytical models developed in this chapter is evident as they provided prediction for all configurations.

  ✓ The analytical models save the cost and the time that would be spent on the experimental tests and numerical analyses.

  ✓ The technique used in this chapter to describe the shear stress profile along the vertical axis of the multi-strand system can predict the positions of which specific strands start the slip phase.

  ✓ The relationship of the frictional second moment of area to the coefficient of friction is nonlinear.

  ✓ The analytical models followed the damping behaviours that were produced experimentally and numerically for the same test configurations.

- The experiments:

    ✓ The different clamp techniques used in the experiments used to clamp the multi-strand bars (circular clamp units) and the multi-strand wires (heat shrink rings) were proper clamp methods as the experimental results being verified through a comparison with the analytical and numerical results.

    ✓ The modulus of elasticity of the heat shrinks tend to reduce slightly when exposed to heat as shown in the experimental work in Section 6.5.2.1 (Table 6.4).

- Numerical modelling:

    ✓ The numerically obtained hysteresis loops agreed with the analytical and experimental results and followed similar frictional behaviours.

    ✓ The clamp force can be applied as an equivalent distributed pressure on the outer surfaces of the strands as this case makes easier for the FE package to come with a convergence for the solution.

    ✓ The FE package (ANSYS) was not able to obtain solutions for Configurations msw2 (nineteen-strand wire), msw3 (thirty-seven-strand wire) and msw4 (sixty-one-strand wire).

- Damping:

    ✓ The loss factor can increase dramatically when the multi-strand system comprises higher number of strands.

    ✓ The loss factor decreases with increasing the level of loadings.

    ✓ The loss factor decreases when increasing the diameter of the individual strands for the same strands lengths.

    ✓ The frictional second moment of area (frictional system stiffness) values change as the multi-strand system transits from stick and microslip and slide phases.

    ✓ The energy dissipation and the peak strain energy increase with increasing loadings.

    ✓ The energy dissipation and the peak strain energy increase with increasing the diameter of the individual strand for the same strands lengths.

    ✓ The loading levels had no significant effect of the frictional systems stiffness.

    ✓ Increasing the individual strand diameters increases the frictional stiffness for the same strands lengths.

Chapter 7

Dynamic characteristics of multi-strand systems

7.1 Introduction

In the previous chapters, the damping behaviour in multi-strand systems subjected to flexural loading was studied. The change of the loading with time was small enough, relative to the system natural frequency, so that the inertial forces had negligible effect on the system response. In practical applications, damping is only required in dynamic conditions, usually around system resonances. While Coulomb friction damping is theoretically insensitive to excitation frequency, it was considered essential to evaluate the performance of the multi-strand systems under dynamic loading and to explain any changes seen.

In this chapter, the responses of the multi-strand beams (MSB) and the multi-strand wires (MSW) to vibrational excitations over a range of frequencies were examined. Consequently, the resulting damping amounts from the frictional contacts between the individual strands were calculated over the excitation frequency range.

7.2 Dynamic experiments on multi-strand beams

Dynamic experiments were conducted to investigate the sensitivity of the loss factor to vibration frequency. These tests were performed on the same square-section beams that were studied under quasi-static conditions in Chapter 4. A shaker was used to excite the multi-strand beam in a range of frequencies at different levels of amplitude. The pinned-pinned

configuration was adopted for the tests. Frequency response function was obtained for the MSB at each of the excitation amplitudes.

7.2.1 Experimental set-up and methodology

Configuration sb12 (Table 3.1) was selected for the tests, being made up of nine square cross-sectioned steel strands. Each of these strands had a free length of 300 mm and cross-section size of 4×4 mm. The peak-to-peak (PK-PK) amplitude levels for the dynamic tests were 0.5 mm, 1.0 mm and 2.0 mm. While the same configuration as for quasi-static tests (Chapter 4) was used, some changes to the test arrangements were required to allow the use of an electrodynamic shaker (Ling Dynamic Systems V455 500 N peak sine force) rather than the hydraulic test machine used previously in Chapters 4 and 5.

A test rig was designed and manufactured for the dynamic test. The fundamental natural frequency of the manufactured test rig was examined by performing an impulse hammer test on the test rig. An accelerometer (PCB Model 352C68) with a sensitivity of 95.82 mV/g was used to measure the response of the test rig. Both the impulse signal of the hammer and the free decay signal of the test rig were recorded with a frequency of 2000 sample/sec for each signal. Figure 7.1 shows the time history of the hammer signal and test rig signal. A frequency response function ratio of the acceleration to the forcing was then plotted as shown in Figure 7.2. This indicated that the fundamental natural frequency of the test rig was approximately 250 Hz.
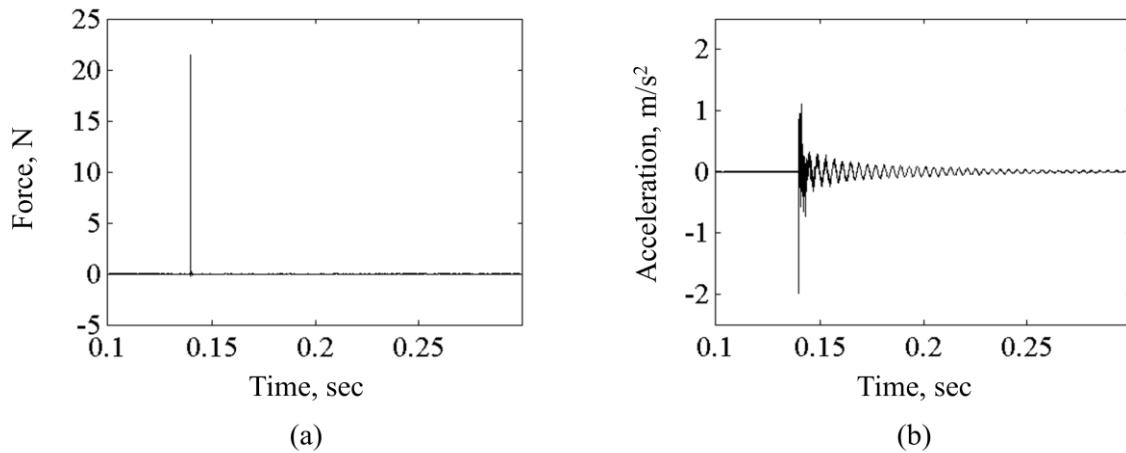
Figure 7.1 Time histories of the (a) impulse signal of the hammer and (b) free decay test rig signal
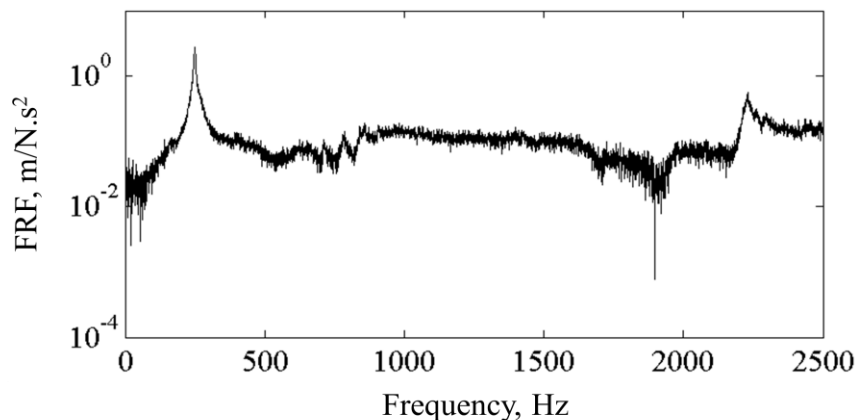
Figure 7.2 The frequency response function (FRF) of the manufactured test rig

The test fixture is shown in Figure 7.3. The strands comprising the beam were compressed and constrained (in the direction of excitation) using two clamps placed 55 mm from each end of the beam. The torque on the bolts was set so that the clamping force applied by each clamp was 250 N (i.e. a total of 500 N over the beam). A third clamp, attached at the midpoint of the beam, was connected to the shaker via a transversely flexible "stinger" and a force sensor. This clamp was only used to connect the shaker to the beam; hence, bolts were tightened enough to avoid relative motion between the beam midpoint and the shaker but not enough to have a significant effect on the overall clamp force.

The beam was placed between two pairs of support rollers in order to mimic a simply supported boundary. Each roller pair held the beam with sufficient pressure to stop the beam from dropping onto the roller holders during testing. Again, this pressure was kept to a minimum to avoid significant changes to the overall clamp force. The distance between the roller pairs, i.e. the span of the beam, was set at 250 mm.

The system was excited using sinusoidal wave forms with frequencies in the range 10 Hz to 200 Hz. The motion of the central clamp, and hence the midpoint of the beam, was measured using a laser displacement sensor. A closed-loop controller was used to maintain constant displacement amplitude at each frequency. The layout of the instrumentation and signals is provided in Figure 7.4.

(a)   (b)
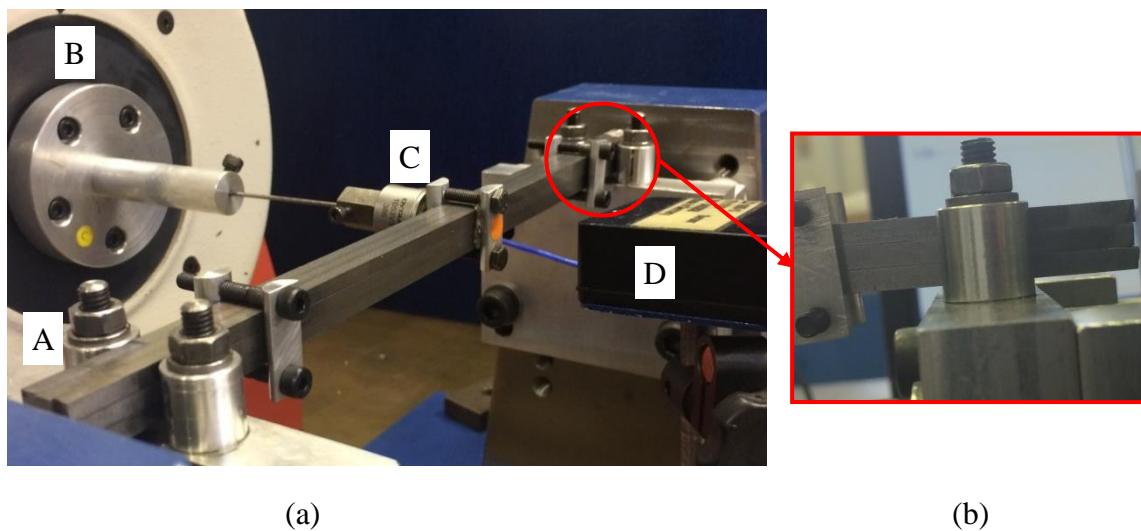
Figure 7.3 Set-up for the dynamic experiment with: (A) support rollers, (B) electrodynamic shaker (LDS V455), (C) force sensor (Dytran 1053V3), (D) laser displacement sensor (MicroEpsilon LD1605-10)
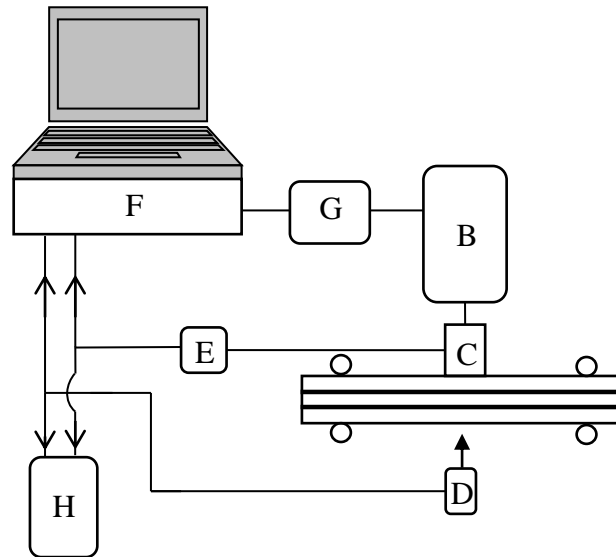
Figure 7.4 Instrumentation layout for the dynamic experiment with (B) – (D) as Figure 7.3, (E) signal conditioning unit (F) controller (SigLab 20-22A), (G) 1 kW power amplifier (H) oscilloscope (Picoscope 4424)

At each frequency of interest, force and displacement signals were acquired at a sampling rate of 50 kHz over a period of 2 seconds. During testing, some high frequency noise was noticeable, particularly on the displacement reading. This was attributed primarily to the surface roughness at the laser measurement point and, at higher amplitudes, possible slip at the support rollers and in the clamp used to connect the shaker. To remove these effects, the force and displacement signals were isolated using a fast Fourier transform based filter that rejected spectral components with frequencies greater than 25 times the test frequency or below 5 Hz. This relatively large pass-band was employed to ensure that important harmonics arising from the nonlinear response were not excluded: it was observed that the excluded spectral components had magnitudes that were three orders of magnitude lower than the fundamental.

A plot showing the receptance frequency response function (FRFs) at different amplitude levels is provided in Figure 7.5. The figure also shows best-fit curves obtained using equivalent linear single degree-of-freedom (SDOF) system models. The parameters of these models are provided in Table 7.1. From these results, it can be seen that the system stiffness

and damping reduced as the dynamic amplitude increased. This softening behaviour for a friction system is in line with observations made by others [6, 16].
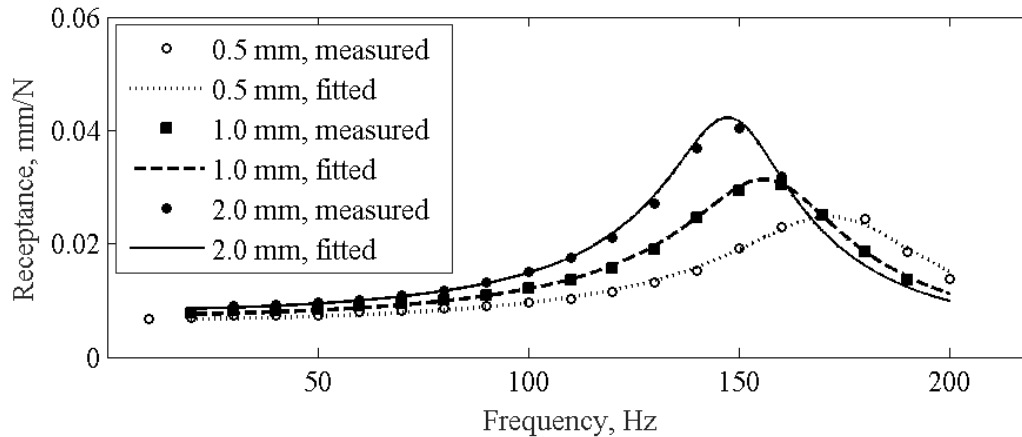
Figure 7.5 Receptance for a clamp force of 250 N per clamp for PK-PK displacement amplitudes of 0.5 mm, 1 mm and 2 mm

Table 7.1 System properties of beam Configuration 2 under various loading and clamping conditions

PK-PK amplitude, mm	Natural frequency, Hz	Damping ratio	Effective mass, kg
0.500	174.7	0.130	0.125
1.000	158.2	0.120	0.136
2.000	148.8	0.100	0.136

The nonlinear behaviour was also investigated by examining the hysteresis loops at each frequency. In order to do this, inertia effects first had to be removed from the measured force signal f_{meas} using,

$$f = f_{meas} + \omega^2 x m_{eff}$$
7.1

where x is the measured displacement, ω the frequency of excitation in rad/s and m_{eff} the effective mass (from the SDOF curve fits). Figure 7.6 shows examples of the hysteresis loops obtained from the experiments for different PK-PK excitation displacements and frequencies.
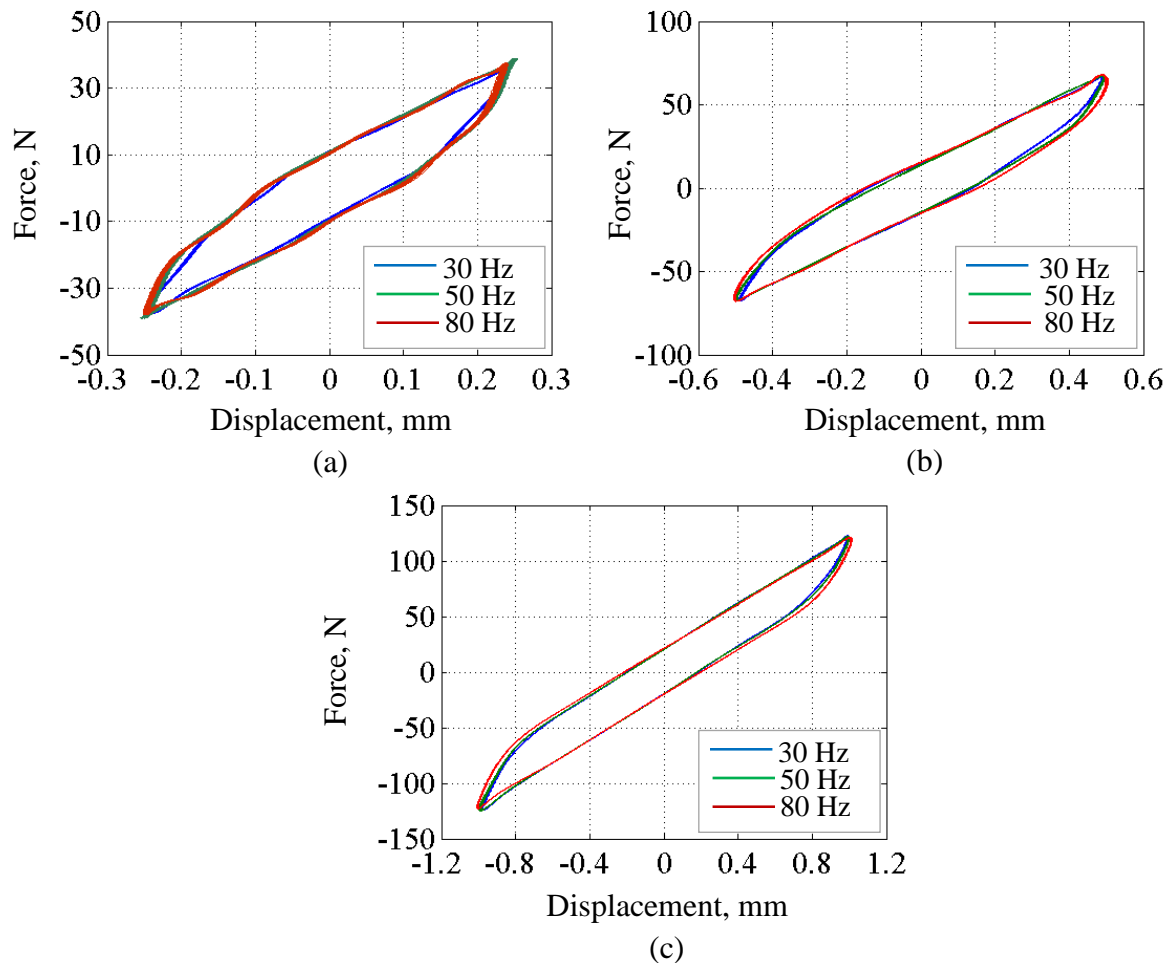
Figure 7.6 Experimental hysteresis loops for Configuration sb12 at different frequencies with PK-PK excitation displacements of (a) 0.5 mm, (b) 1 mm and (c) 2 mm

It can be seen, for the parameters considered, that all of the excitation levels achieve macroslip. As the excitation amplitude is increased, the beam extends into the macroslip region increasing the energy dissipated along with the peak strain energy. Importantly these increase at different rates therefore making the loss factor nonlinear with respect to the amplitude.

Figure 7.7 shows the loss factors(obtained from the SDOF fit to the receptance curve) for the full range of frequencies considered at PK-PK displacements of 0.5 mm, 1 mm, and 2 mm respectively. The vertical line in each plot shows the system natural frequency. It can be seen that for all displacements, the loss factor remains relatively constant and close to the value

indicated by the receptance curve fit (note that the curve fit used a viscous damping model but at resonance, the equivalent system loss factor is twice the damping ratio).
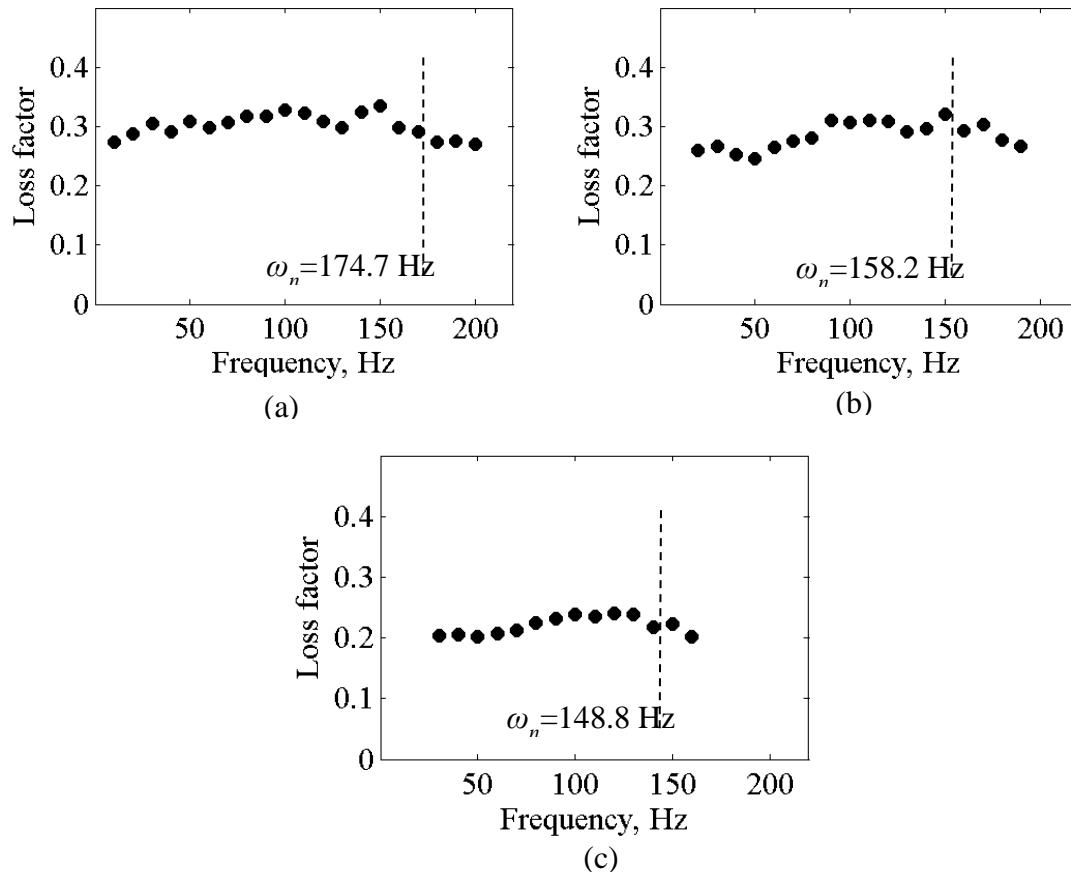
Figure 7.7 Loss factor values for Configuration sb12 over a range of excitation frequencies with PK-PK displacement of (a) 0.5 mm, (b) 1 mm and (c) 2 mm

Figure 7.8 presents the energy dissipation per cycle over the range of excitation frequencies for PK-PK displacements of 0.5 mm, 1 mm, and 2 mm respectively. While the values remain reasonably close, there is some fluctuation caused by differences in actual amplitude of vibration (the controller achieved amplitude accuracy to within 10%) and possibly distortion caused by higher harmonics that were evident at higher frequencies.

(a)

(b)

(c)
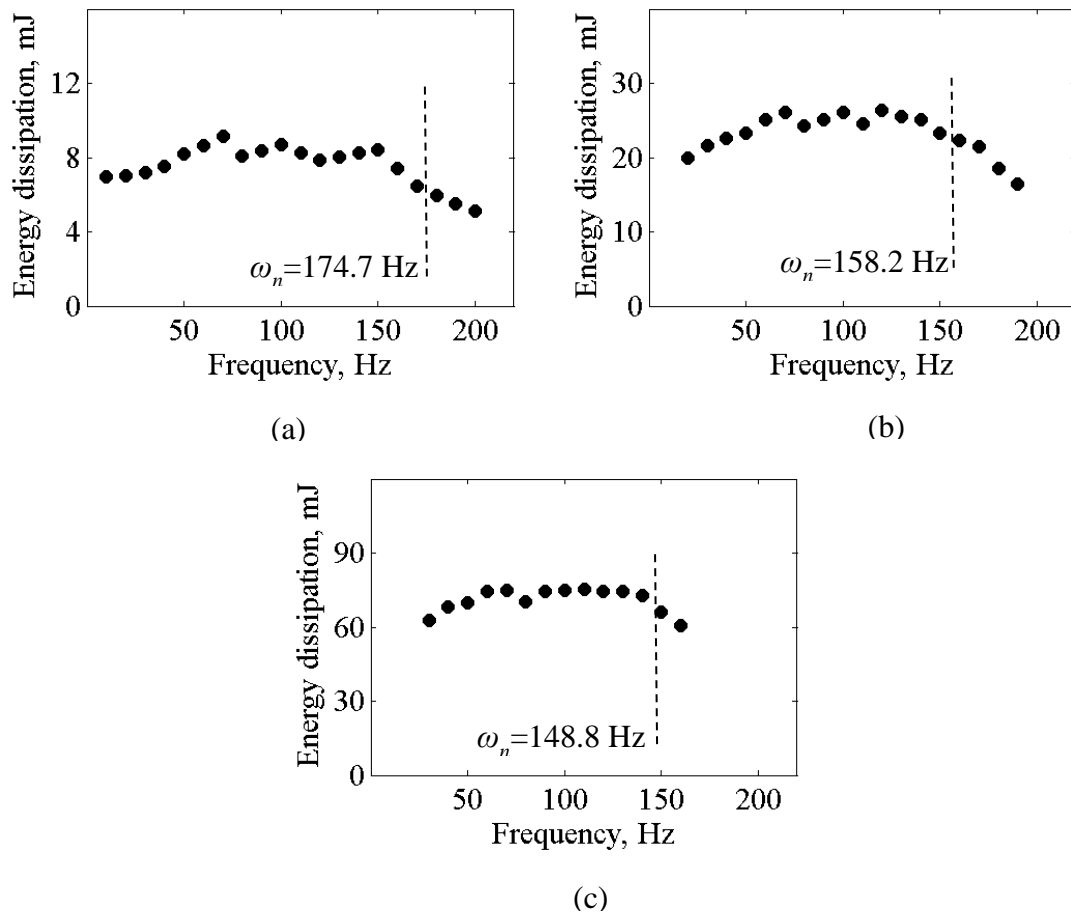
Figure 7.8 Energy dissipation per cycle for Configuration sb12 at PK-PK displacement amplitudes of (a) 0.5 mm, (b) 1.0 mm and (c) 2.0 mm

The effect of the applied (shaker) load on the contact pressure may also have been significant here. This is because this applied load would have been in-phase with the displacement at low frequencies, retarding the onset of slip (and thereby increasing energy loss) but at resonance, this force would be 90 degrees out of phase with the displacement, and therefore would not affect the onset of macroslip significantly.

Figure 7.9 shows the PK-PK stored strain energy amounts at for Configuration sb12 at each tested frequency and at different levels of excitation amplitudes. The strain energy

was calculated through measuring the area under the average effective stiffness where the average effective stiffness was found by a polynomial fit to the experimentally obtained hysteresis loops.

(a)

(b)

(c)
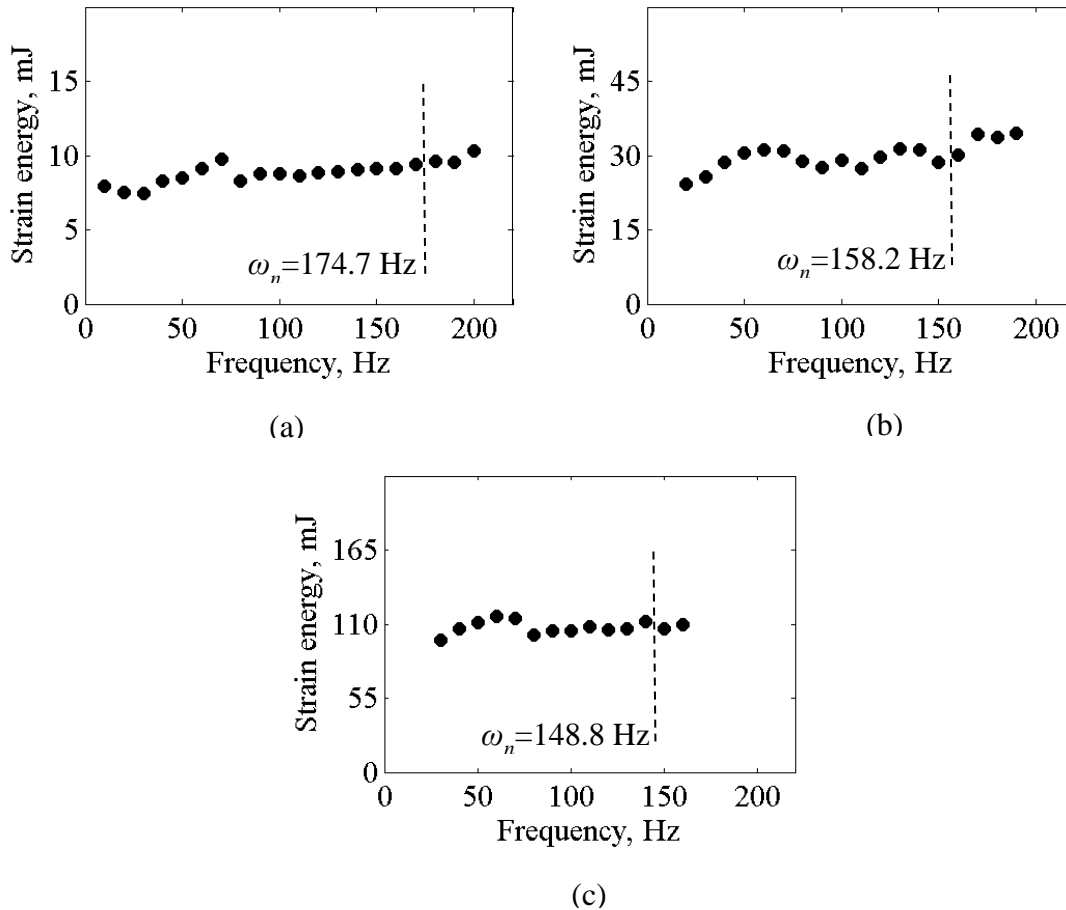
Figure 7.9 Stored strain energy for Configuration sb12 at PK-PK displacement amplitudes of (a) 0.5 mm, (b) 1.0 mm and (c) 2.0 mm

7.3 Dynamic experiments on multi-strand wires

Dynamic tests were performed to investigate the damping characteristics of the seven-strand wire. Free and forced vibration tests were conducted to identify the natural frequencies of the system. The arrangement of the seven-strand wire is similar to Configuration msw1 shown in Table 6.2 but with longer strands (196 mm instead of 45 mm). The strands experienced dry friction contact between each other. Heat shrink rings were used to keep the strands together during the tests. More information about the use of the heat shrink rings with the multi-strand wires can be found in Section 6.5.2.1.

7.3.1 Free vibration tests

Free vibration tests were performed on a seven-strand wire where each strand had a diameter of 0.5 mm and a free length of 196 mm. The individual strands were kept in contact with each other by using seven heat shrink rings. The heat shrinks were separated between each other by a distance of 25 mm along the length of the strands. Cantilever configuration was adopted for the test and the decay signal was recorded and analysed to estimate the natural frequency and the damping level. Results were compared with free decay signal of a solid wire with free length of 196 mm and diameter of 1.5 mm which was the same as the multi-strand wire's overall diameter. Signals were sampled at frequency of 100000 sample/sec and the duration of each signal was 2 sec. A clamp, made of aluminium, was manufactured in order to provide the fixed end for the cantilever configuration where strain gauge cement was used to stick the strands into the clamper.

Figure 7.10 shows the layout for the seven-strand wire and the solid wire in cantilever configuration. The tests were repeated five times for the consistency purposes.

Figure 7.11 shows the free decay time history signals of both the seven-strand wire and the solid wire for one of the tests. The time history signals were converted into frequency domain signals by the means of the fast Fourier transform in order to estimate the natural frequencies.

The frequency domain signals of both the seven-strand wire and the solid wire for one of the tests were shown in Figure 7.12. The friction effect between the individual strands in the multi-strand wire can be seen in the behaviour of the frequency response function shown in Figure 7.13 where a comparison is depicted between the frequency response function of the multi-strand wire and the solid wire. The fundamental natural frequency of both the seven-strand wire and the solid wire obtained from the free vibration tests are shown in Figure 7.14. The average fundamental natural frequency was 9.58 Hz for the seven-strand wire and was 28 Hz for the solid wire.

(a)   (b)
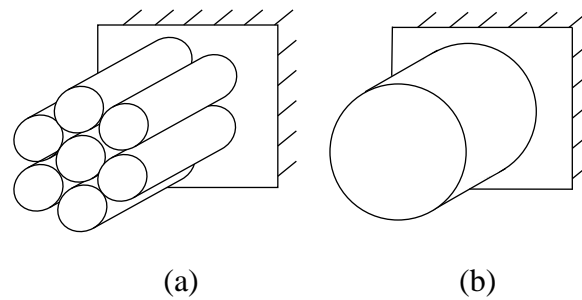
Figure 7.10 The free vibration test layout in cantilever configuration for (a) seven-strand wire and (b) solid wire

(a)   (b)
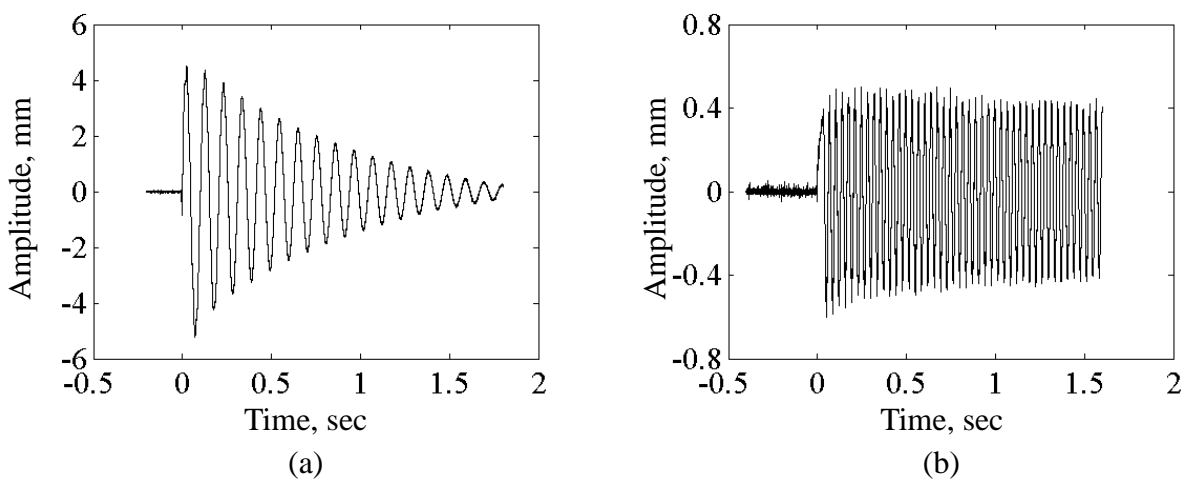
Figure 7.11 The free decay history signal of (a) seven-strand wire and (b) solid single wire

In this section, the damping characteristics are evaluated from the free vibration. The frictional behaviour of the multi-strand wire is nonlinear. To provide accurate description of the damping ratio (ζ), it was decided to measure the damping ratio between every two adjacent peaks separately through the logarithmic decrement in the decay signal. The logarithmic decrement was expressed as

$$\delta = \frac{2\pi\zeta}{\sqrt{1-\zeta^2}}$$

7.1

where, δ is the logarithmic decrement. Solving Equation 7.1 in terms of the damping ratio gives

$$\zeta = \sqrt{\frac{\delta^2}{4\pi^2 + \delta^2}}$$

7.2
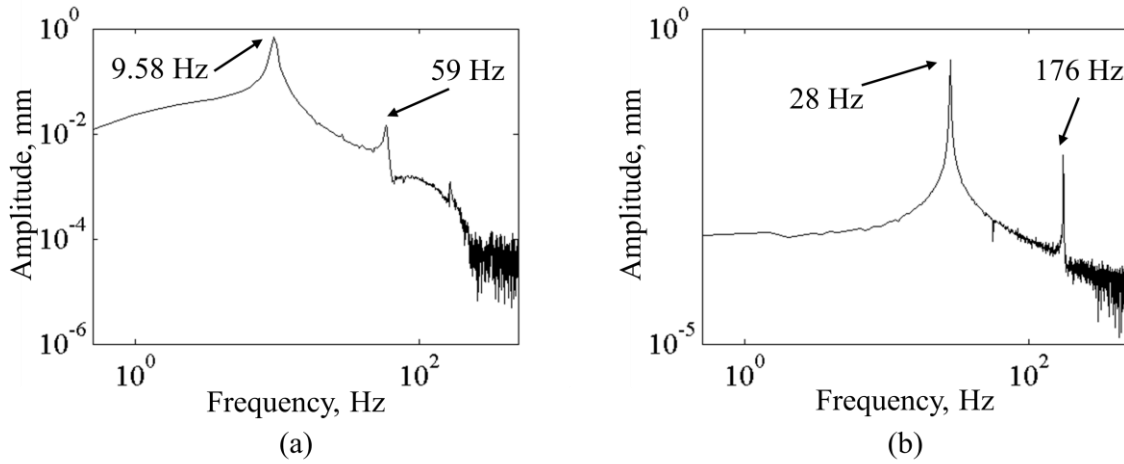
Figure 7.12 Frequency domain signal of (a) seven-strand wire and (b) solid wire
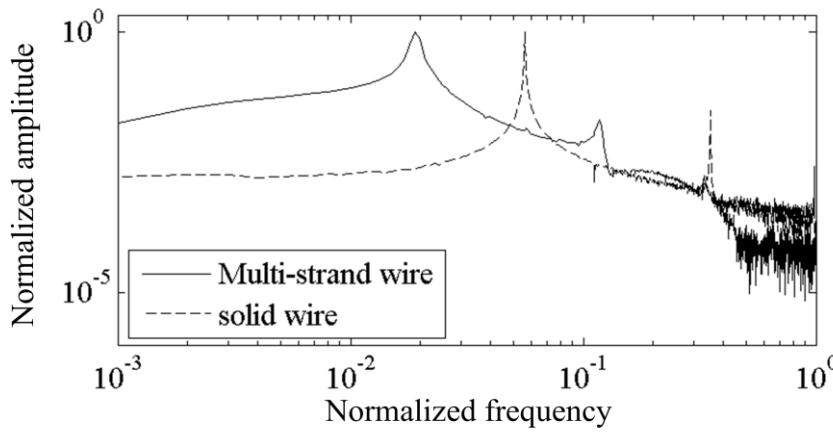
Figure 7.13 Comparison of the frequency response function between the multi-strand wire and the solid wire
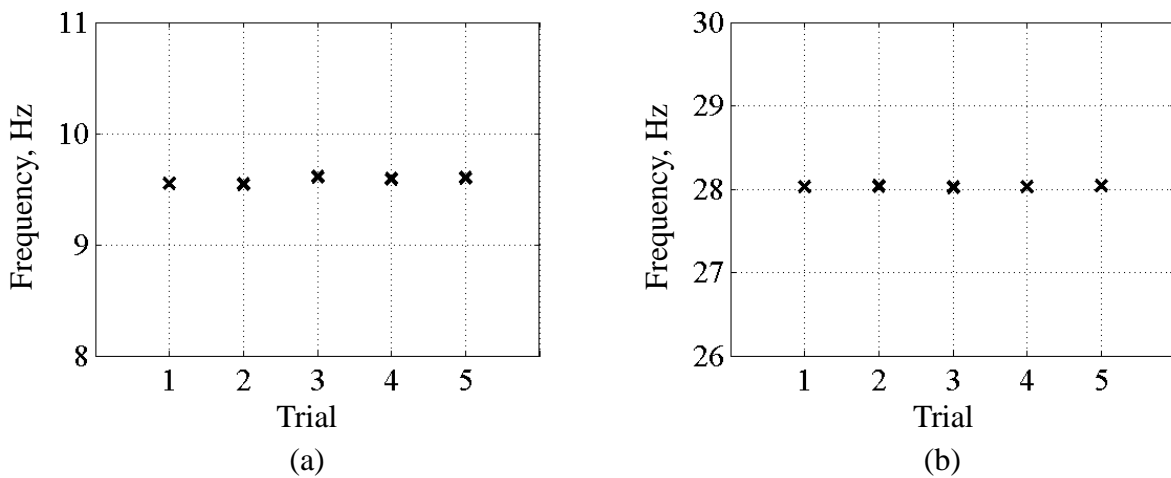
Figure 7.14 The fundamental natural frequency obtained from free vibration tests performed on (a) seven-strand wire and (b) solid wire

The damping ratio values versus the amplitudes contained in the decay signal of the free vibration tests conducted on the seven-strand wire are shown in Figure 7.15. Examining the results reveal that the damping tends to be less when measured at higher amplitudes compared to damping levels measured at lower amplitudes. This conclusion, displacement dependent damping, was observed in the previous chapters and was referred to as the ratio of the energy dissipation levels to the stored strain energy are higher in low amplitude displacements compared to those obtained from higher amplitudes. As expected, the damping ratio obtained from the free vibration tests performed on the solid wire were very low therefore the decay in the time domain signal was unnoticeable for the selected caption time (2 sec). The damping ratio values obtained from the solid wire versus the amplitude are shown in Figure 7.16.
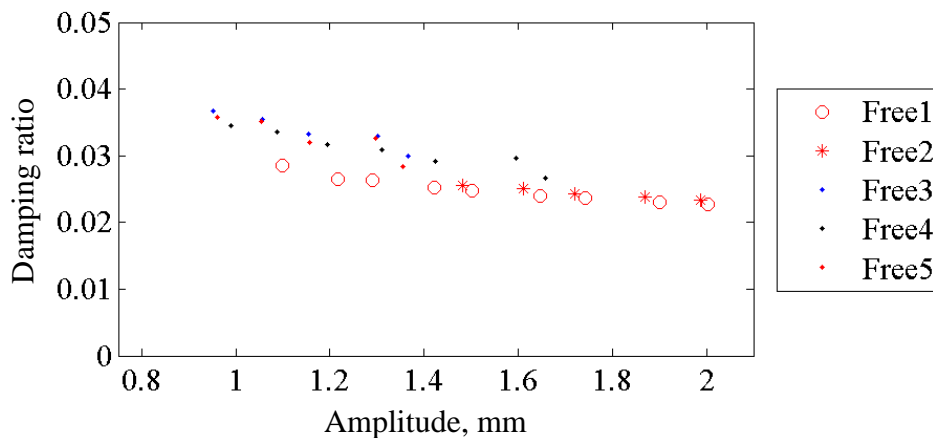
Figure 7.15 The damping ratio versus the amplitude of the free decay signal for seven-strand wire obtained from five free vibration trials
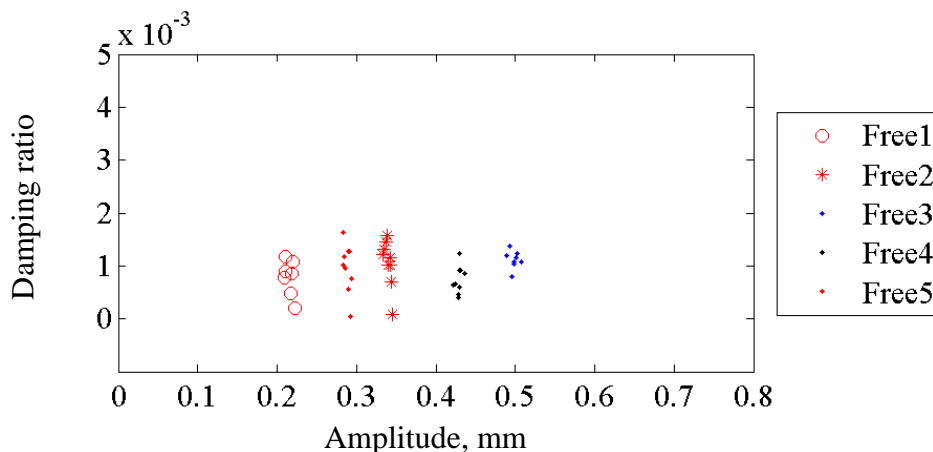
Figure 7.16 The damping ratio versus the amplitude of the free decay signal for solid wire obtained from five free vibration trials

7.3.2 Forced vibration tests

Forced vibration tests were performed on a seven-strand wire. Each strand has circular cross-section with a diameter of 0.5 mm and free length of 196 mm. The strands where kept together using seven heat shrink rings. The purpose of the forced vibration tests was to describe the frequency response function in order to compare the obtained fundamental natural frequency with the one obtained from the free vibration test (Section 7.3.1).

Testing was first carried out using a white noise signal. The frequencies were in the range of 1–100 Hz. A 100 N capacity electrodynamic shaker (Data Physics V20) was used to excite the seven-strand wire. Force sensor (DYTRAN instruments 1053V3) was used to measure the forcing during the test. The force sensor was attached to the shaker. The clamp which represented the fixed end of the seven-strand wire was attached to the force sensor. A laser displacement sensor (MicroEpsilon LD1605-10) was used to measure the displacements during the test. The laser displacement sensor was positioned at 30 mm from the fixed end of the seven-strand wire. The excited seven-strand wire and test layout are shown in Figure 7.17 and Figure 7.18 respectively. The obtained frequency response function shown in Figure 7.19 and indicates that the value of the natural frequency (9.6 Hz) agrees with the one estimated from the free vibration test (9.58 Hz).
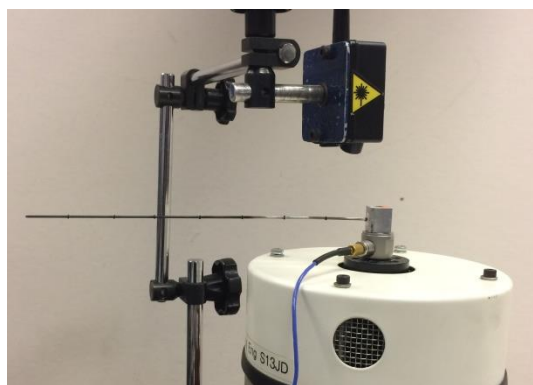
Figure 7.17 The seven-strand wire exposed to based excitation

a. Controller(SigLab Dynamic Signal Analysis System 20-22A)

b. Power amplifier (Data Physics 100W)
c. Electrodynamic Shaker
d. Force Sensor
e. Laser displacement sensor
f. Signal conditioner unit
g. Clamper
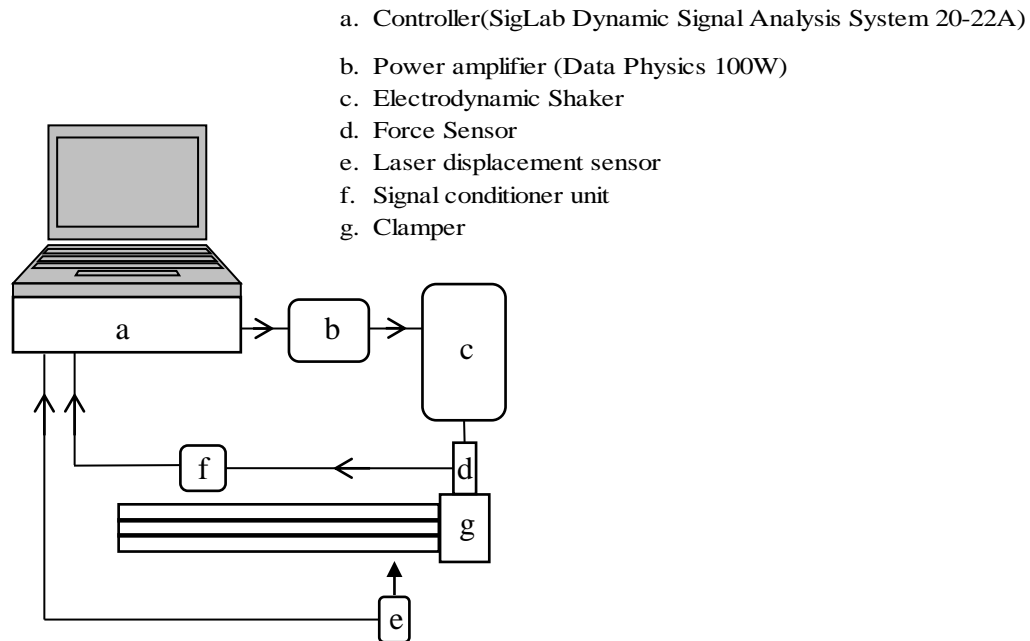
Figure 7.18 Setup for the forced vibration tests
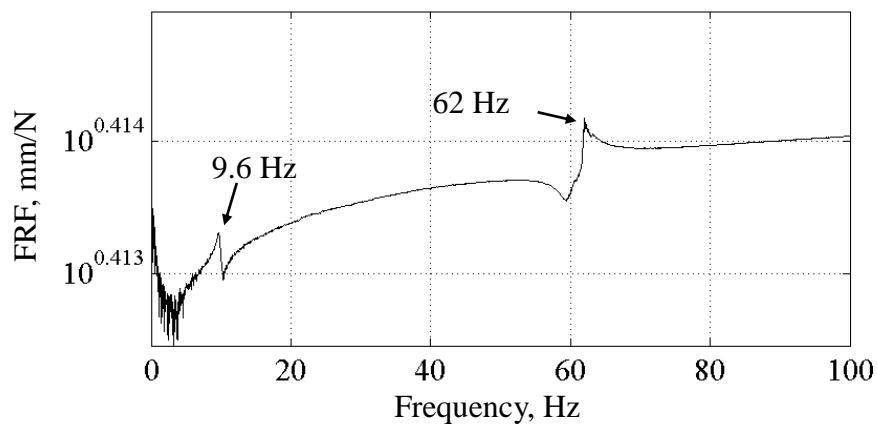
Figure 7.19 The frequency response function of the seven-strand wire

7.3.3 Prediction

The analytical model described in Section 6.4.3 was used to predict the damping ratios obtained from exciting the seven-strand wire in a cantilever configuration. These results were compared with the damping ratios estimated from the free vibration tests described in Section 7.3.1. Figure 7.20 compares the damping ratios obtained using different techniques.
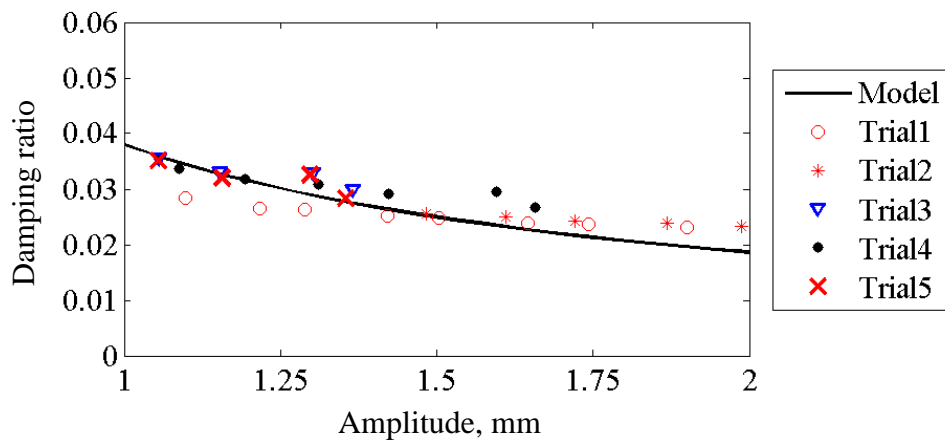
Figure 7.20 Analytical model prediction of the damping ratio compared to the results of the free vibration tests

7.4 Conclusions

The dynamic behaviour of the loss factor in a multi-strand beam was addressed. The main conclusion that can be drawn from the data presented in this chapter is that the loss factor can be considered frequency independent. It was verified that the multi-strand beam and the multi-strand wire were highly nonlinear and that the natural frequencies depended on the level of excitation. For the parameters considered in this chapter, the damping level decreased with increasing displacement amplitude and this behaviour was clear in the free vibration experiments performed in this chapter.

Chapter 8

Summary and Conclusions

8.1 Summary

The aim of the study was to describe, understand and optimise the frictional damping behaviour in multi-strand structures. This was achieved through developing analytical models which were verified using systematic experiments and numerical models. The study provided a necessary insight into the physics for multi-strand structures that are largely prevalent in mechanical (e.g. cables) and electrical (e.g. wires) elements.

Preliminary studies on multi-strand beams (MSB) as described in Chapters 3 and 4 and diagonal multi-strand beams (DMSB) as described in Chapter 5 provided the required understanding and explanations for the frictional damping behaviour in these systems. Then in Chapter 6 the study was extended to explain and optimise the damping behaviour in multi-strand bars (MSR) and multi-strand wires (MSW) where the strands had circular cross-sections. Important contributions of this study are the prediction of the frictional system stiffness and full description of the frictional damping behaviour as presented by the analytical models developed in this study and verified through extensive experimental and numerical work.

The numerical models showed limitations in simulating complex multi-strand wires (nineteen-strand wire and more) where the contact configurations caused solution problems in addition to computational expense. On the other hand, the preparation of complex multi-strand wires for experimental set-up is considered difficult as well as time consuming. Therefore, the analytical models presented in this study provide a convenient and accurate alternative as the required damping parameters can be obtained in a significantly shorter period of time.

8.2 Conclusions

In Chapter 2, it was shown that existing studies of multi-strand systems ignore the friction effect between the individual strands during flexural loading, whereas in the current study this effect has been given careful consideration and its consequences on the general stiffness of the system (termed frictional stiffness in this study) have been addressed.

The analytical models presented in Chapters 3, 5 and 6 to represent the multi-strand beams (MSB), the diagonal multi-strand beams (DMSB) and the multi-strand bars and wires (MSR and MSW) respectively were able to predict the frictional damping behaviour of these systems for all the configurations studied and followed the numerical and experimental flexural behaviour accurately. It was expected with the multi-strand bars and wires that several strands with different neutral axes would start to slip at the same time. Therefore, the technique presented in Chapter 6 to approximate the shear stress profile along the height of the system predicted the positions of the strands that started to slip first.

In Chapter 7, the dynamic behaviour of the MSB and the MSW was addressed. The loss factor was found to be independent of the excitation frequency. The natural frequency was inversely proportional to the level of excitation. The independence of the damping parameters from the excitation vibration validates that static or quasi-static excitations can present actual behaviour of the system.

As described in Chapter 5, the beam rotation angle was directly proportional to both the loss factor and the energy dissipation per cycle, while both the system stiffness and the stored energy were found to be independent of the angle of rotation.

Examining the results from Chapters 3–5, several general conclusions can be drawn.

- The relation of the coefficient of friction to the applied load was linear, while it was nonlinear with the frictional second moment of area.
- The loss factor was independent of the number of individual strands involved in the system if the cross-section size of the individual strands remained the same.
- The loss factor was inversely proportional to the cross-section size of the strands whereas it was directly proportional to the length of strands.

- Interestingly, the energy dissipation level per cycle was independent of the number of individual strands if the overall cross-section of the system was kept unchanged.

- There was direct proportion between the normal force and both the loss factor and the energy dissipation per cycle, whereas the relation between the loading amplitude and the loss factor was inversely proportional.

- The system stiffness was approximately independent of both the normal force and the loading amplitude.

In all the techniques used (analytical, numerical and experimental), similar behaviours for the damping parameters were observed. Visual observation for the comparison between the numerically, analytically and experimentally obtained hysteresis loops validated the experimental work to estimate the coefficient of friction and the material properties.

Multi-strand bars (MSR) and multi-strand wires (MSW) were considered in Chapter 6. The FE models showed limitations in simulating multi-strand bars and wires comprising more than seven strands.

In the multi-strand bars and wires, the loss factor was directly proportional to the number of strands and inversely proportional to the diameter of the individual strands. Both the energy dissipation per cycle and the stored energy were directly proportional to the applied loading and the diameter of the individual strands. The frictional second moment of area showed independence of the applied loading, while it was in direct relation to the diameter of the individual strands.

The work in this thesis had some limitations which can be summarised as follows:

- The analytical models ignore stretching of the strands. Thus all parts move together. This is reasonable at low compression loads.

- The loading regime was limited to a flexural behaviour for all the work of this thesis. Other loading patterns can be of interest to apply on the multi-strand systems.

for instance, extending the analytical models that describe the multi-strand wires into analytical models that describe spiral multi-strand wires might require to investigate the torsion loading effect. This is covered in the future work (Section 8.3).

- The boundary conditions adopted for the work in this thesis were three point bend and cantilever configurations.

- The shear stress that initiate's the slippage between the individual strands during the flexural behaviour was assumed to be constant which means that, theoretically, the slip occur simultaneously along the length of the multi-strand systems.

The clamping techniques used during the experiments to keep the individual strands together in the MSR (clamp rings) and MSW (heat shrink rings) are thought to be proper clamping methods as the results have been verified through the analytical and numerical results.

The good agreement between the experimental and the numerical results indicates that the representation of clamp force as a distributed pressure in the numerical solution was appropriate .

8.3 Recommendations for future work

The work in this thesis was devoted to understanding and optimising the frictional damping gained from flexing multi-strand wires comprised of steel strands. Analytical models were introduced to describe and evaluate the damping levels in these systems. Listed below are recommendations for future work.

1- The analytical model introduced in this work depends on the applied load being large enough to start the slip phase and the bulk system stiffness exceeding the system stiffness in the sticking phase. Developing the analytical model to include the case where the applied load is not sufficient to start slip and causing a microslip contact in the system could be useful.

2- The loading in this study was flexural. Extending the study in the future to include torsional loading in addition to flexural can be of interest to investigate the effect of this type of loading on the damping behaviour.

3- The multi-strand bars and wires comprised straight strands. This study can be extended to braided strands positioned around a straight core strand.

4- A real-life application of the frictional damping system presented in this study would be possible and inexpensive to apply. This damping system could be implemented successfully as follows:

    a. In the form of special types of composite where some strands are artificially implanted with dry friction contact. In this way, significant damping levels will be produced from the system with no additional mass added to the mechanical system due to the damping system. However, the effect of reducing the composite stiffness should be taken into consideration.

    b. As damping mechanisms attached to vibrational systems such as those of turbine blade structures. This can be implemented as a frictional damper at the base of the blade.

    c. In civil structures as a damping system where very low temperatures can restrict the use of conventional damping systems (viscoelastic damper).

5- The study used one-piece strands to construct the beams, bars and wires. Instead, segmented strands could be used to construct the multi-strand system in order to investigate the resulting damping levels. This situation could change the system response which in turn would result in different damping levels.

6- In the case of multi-strand beams where the individual strands were square cross-sectioned, the coefficient of friction (static and dynamic) was found experimentally. For multi-strand bars and wires, approximately similar coefficients of friction were given to the strands. Even the chosen values are believed to represent the real coefficient of friction values as the values of the study's numerical and analytical models showed good agreement in comparison with the experimental results. It would be interesting to introduce systematic experiments to investigate the coefficient of friction in circular cross-sectioned strands where the interfacial area is a line contact.

7- A study of the effect of friction on the wear level at the interface between the mating surfaces would be of importance at higher loading amplitudes.

8- The coefficient of friction was assumed to have a constant value over the whole surface of the contact. Thinking about the surface finishing of the used strands and the friction at the micro-scale level introduces doubts about whether this is true and

suggests that there should be a way to assume different values of the coefficient of friction along the surface of contact.

Bibliography

[1] E. Rabinowicz, The nature of the static and kinetic coefficients of friction, J. Appl. Phys. 22 (1951) 1373–1379.

[2] D. Karnopp, Computer simulation of Stick-Slip Friction in mechanical dynamic systems, J. Dyn. Syst. Meas. Control. 107 (1985) 100–103.

[3] F.P. Bowden, L. Leben, The nature of sliding and the analysis of friction, in: Proceddings R. Socity London, 1938: pp. 371–391.

[4] S.S. Antoniou, A. Cameron, C.R. Gentle, The friction-speed relation from stick-slip data, Wear. 36 (1976) 235–254.

[5] E. Rabinowicz, The Intrinsic Variables affecting the Stick-Slip Process, Proc. Phys. Soc. 71 (1958) 668–675.

[6] P.L. Ko, C.A. Brockley, The Measurement of Friction and Friction- Induced Vibration, J. Lubr. Technol. (1970) 543–549.

[7] T. Sakamoto, J. Tanii, T. Tsukizoe, A Friction Apparatus for Measuring the Normal Displacement of a Sliding Body, J. Phys. E-Scientific Instruments. 13 (1980) 1017–1020.

[8] E. Marui, S. Kato, Forced Vibration of a Base-Excited Single-Degree-of-Freedom System With Coulomb Friction, J. Dyn. Syst. Meas. Control. 106 (1984) 280–285.

[9] P. Stelter, Nonlinear vibrations of structures induced by dry friction, Nonlinear Dyn. Eng. Syst. (1990) 329–345.

[10] P.R. Dahl, Solid Friction Model, Natl. Tech. Inf. Serv. 158 (1968) 1–24.

[11] S. Andersson, A. Söderberg, S. Björklund, Friction models for sliding dry, boundary and mixed lubricated contacts, Tribol. Int. 40 (2007) 580–587.

[12] D.A. Haessig, B. Friedland, On the modeling and simulation of friction, J. Dyn. Syst. Meas. Control. 113 (1991) 354–362.

[13] C. Canudas de Wit, H. Olsson, K.J. Astrôm, P. Lischinsky, Dynamic Friction Models and Control Design, Am. Control Conf. (1993) 1–6.

[14] C. Canudas de Wit, H. Olsson, K.J. Astrom, P. Lischinsky, A new model for control of systems with friction, IEEE Trans. Automat. Contr. 40 (1995) 419–425.

[15] D.A. Saravanos, D.A. Hopkins, Effects of delaminations on the damped dynamic characteristics of composite laminates : Analysis and experiments, J. Sound Vib. 192 (1996) 977–993.

[16] M.H. Kargarnovin, M.T. Ahmadian, R.-A. Jafari-Talookolaei, Analytical solution for the dynamic analysis of a delaminated composite beam traversed by a moving constant force, J. Vib. Control. 19 (2012) 1524–1537.

[17] Z. Li, M.J. Crocker, Effects of thickness and delamination on the damping in honeycomb–foam sandwich beams, J. Sound Vib. 294 (2006) 473–485.

[18] C.N. Della, D. Shu, Vibration of beams with double delaminations, J. Sound Vib. 282 (2005) 919–935.

[19] C.N. Della, D. Shu, P. MSRao, Vibrations of beams with two overlapping delaminations, Compos. S. 66 (2004) 101–108.

[20] M.G. Andrews, R. Massabo, B.N. Cox, Multiple Delamination of Laminated Structures, in: ICF11, Italy 2005, 2013.

[21] U.A. Girhammar, D. Pan, Dynamic analysis of composite members with interlayer slip, Int. J. Solids Struct. 30 (1993) 797–823.

[22] U.A. Girhammar, A simplified analysis method for composite beams with interlayer slip, Int. J. Mech. Sci. 51 (2009) 515–530.

[23] P. Ansourian, Behaviour of stiffened composite beams with partial shear interaction accounting for time effects, Procedia Eng. 14 (2011) 402–409.

[24] M.A. Uddin, A.H. Sheikh, T. Bennett, B. Uy, Large deformation analysis of two layered composite beams with partial shear interaction using a higher order beam theory, Int. J. Mech. Sci. 122 (2017) 331–340.

[25] M. a. Osipenko, Y.I. Nyashin, R.N. Rudakov, A contact problem in the theory of leaf spring bending, Int. J. Solids Struct. 40 (2003) 3129–3136.

[26] Y. Yum, Frictional behavior of automotive leaf spring, Proc. 4th Korea-Russia Int. Symp. Sci. Technol. Ulsan, South Korea,. 3 (2000) 5–10.

[27] C. Blok, Dry friction energy dissipation, University of Technology, 2007.

[28] J. Lindberg, N. Gralen, Measurement of friction between single fibers* II. frictional properties of wool fibers measured by the fiber-twist method, Text. Res. J. 18 (1948) 287–301.

[29] H.G. Howell, The friction of a fibre round a cylinder and its dependence upon

cylinder radius, J. Text. Inst. 45 (1954) 575–579.

[30] B.S. Gupta, Y.E. El Mogahzy, Friction in fibrous materials: Part I: structural model, Text. Res. J. 61 (1991) 547–555.

[31] Y.E. El Mogahzy, B.S. Gupta, Friction in fibrous materials: part II: experimental study of the effects of structural and morphological factors, Text. Res. J. 63 (1993) 219–230.

[32] N. Ngoc, P. Brumiaux, J.M. Castelain, Modeling friction for yarn / fabric simulation Application to bending hysteresis, in: 14th Eur. Simul. Symp., 2002.

[33] E. Syerko, S. Comas-cardona, C. Binetruy, Models of mechanical properties/behavior of dry fibrous materials at various scales in bending and tension: A review, Compos. Part A Appl. Sci. Manuf. 43 (2012) 1365–1388.

[34] M. Raoof, R. Hobbs, Analysis of multilayered structural strands, J. Egineeering Mech. 114 (1988) 1166–1182.

[35] M. Raoof, T.J. Davies, Simple determination of the maximum axial and torsional energy dissipation in large diameter spiral strands, Comput. Struct. 84 (2006) 676–689.

[36] L.E. Goodman;, C.B. Brown, Cyclic Tangential Loading, J. Appl. Mech. 29 (1962) 17–22.

[37] D. Dini, D.A. Hills, Frictional Energy Dissipation in a Rough Hertzian Contact, J. Tribol. 131 (2009) 214011–214018.

[38] E.B. Pires;, J.T. Oden, Analysis of contact problems with friction under oscillating loads, Comput. Methods Appl. Mech. Eng. 39 (1983) 337–362.

[39] D. Nowell;, D.A. Hills;, A. Sackfield, Contact of dissimilar elastic under normal cylinders loading, J. Mechnaics Phys. Solids. 36 (1988) 59–75.

[40] J.J. Kalker, A Minimum principle for the law of dry friction, with application to elastic cylinders in rolling contact, part 1: fundamentals-application to steady rolling, J. Appl. Mech. 38 (1971) 875–880.

[41] J.J. Kalker, On elastic line contact, J. Appl. Mech. 39 (1972) 1125–1132.

[42] N. Ahmadi, L.M. Keer, T. Mura, Non-Hertzian contact stress analysis for an elastic half space-normal and sliding contact, 19 (1982) 357–373.

[43] J. Shi, X. Cao, H. Zhu, Tangential contact stiffness of rough cylindrical faying surfaces based on the fractal theory, J. Tribol. 136 (2014) 0414011–0414018.

[44]   D.M. Mulvihill, O. Smerdova, M.P.F. Sutcliffe, Friction of carbon fibre tows, Compos. Part A Appl. Sci. Manuf. 93 (2016) 185–198.

[45]   L.E. Goodman, Contact stress analysis of nominally loaded rough spheres, Trans. ASME J. Appl. Mech. 29 (1962) 515–522.

[46]   V.I. Mossakovskii, Compression of elastic bodies under conditions of adhesion (Axisymmetric case), J. Appl. Math. Mech. 27 (1963) 630–643.

[47]   O.I. Zhupanska, A.F. Ulitko, Contact with friction of a rigid cylinder with an elastic half-space, J. Mech. Phys. Solids. 53 (2005) 975–999.

[48]   D.A. Spence, Self similar solution to adhesive contact problems with incremental loading, Proceddings R. Socity. A (1968) 55–80.

[49]   D.A. Spence, The hertz contact problem with finite friction, J. Elast. 5 (1975) 297–319.

[50]   D.J. Haines, E. Ollerton, Contact stress distributions on elliptical contact surfaces subjected to radial and tangential forces, Proc. Inst. Mech. Eng. 177 (1963) 95–114.

[51]   D.J. Haines, Contact stresses in flat elliptical contact surfaces which support radial and shearing forces during rolling, Proc. Inst. Mech. Eng. Conf. Proc. 179 (1964) 154–168.

[52]   L. Vu-Quoc, X. Zhang, L. Lesburg, Normal and tangential force-displacement relations for frictional elasto-plastic contact of spheres, Int. J. Solids Struct. 38 (2001) 6455–6489.

[53]   V. Brizmer, Y. Kligerman, I. Etsion, The effect of contact conditions and material properties on the elasticity terminus of a spherical contact, Int. J. Solids Struct. 43 (2006) 5736–5749.

[54]   W. Liu, Y. Zhang, Z. Feng, J. Zhao, Effects of stick-slip on stress intensity factors for subsurface short cracks in rolling contact, Sci. China Technol. Sci. 56 (2013) 2413–2421.

[55]   L.E. Goodman, J.H. Klumpp, Analysis of slip damping with reference to turbine blade vibration, J. Appl. Mech. 23 (1956) 421–429.

[56]   J.H. Griffin, A review of friction damping of turbine blade vibration, Int. J. Turbo Jet Engines. 307 (1990) 297–307.

[57]   A. Rizvi, C.W. Smith, R. Rajasekaran, K.E. Evans, Dynamics of dry friction damping in gas turbines: literature survey, J. Vib. Control. 22 (2016) 296–305.

[58] C.H. Menq, P. Chidamparam, J.H. Griffin, Friction damping of two-dimensional motion and its application in vibration control, J. Sound Vib. 144 (1991) 421–447.

[59] W.E. Whiteman, A.A. Ferri, Displacement-dependent dry friction damping of a beam-like structure, J. Sound Vib. 198 (1996) 313–329.

[60] B. Singh, B.K. Nanda, Dynamic analysis of damping in layered and welded beams, Eng. Struct. 48 (2013) 10–20.

[61] D.J. Nelson, J.W. Hancock, Interfacial slip and damping in fibre reinforced composites, J. Mater. Sci. 13 (1978) 2429–2440.

[62] R. Chandra, S.P. Singh, K. Gupta, Damping studies in fiber-reinforced composites /a review, Compos. Struct. 46 (1999) 41–51.

[63] J.-M. Berthelot, M. Assarar, Y. Sefrani, A. El Mahi, Damping analysis of composite materials and structures, Compos. Struct. 85 (2008) 189–204.

[64] A. El Mahi, M. Assarar, Y. Sefrani, J.-M. Berthelot, Damping analysis of orthotropic composite materials and laminates, Compos. Part B Eng. 39 (2008) 1069–1076.

[65] E.H. Dowell, The behavior of a linear, damped modal system with a non-linear spring-mass-dry friction damper system attached, J. Sound Vib. 89 (1983) 65–84.

[66] E.H. Dowell, H.B. Schwartz, Forced response of a cantilever beam with a dry friction damper attached, Part II: experiment, J. Sound Vib. 91 (1983) 269–291.

[67] E.H. Dowell, H.B. Schwartz, Forced response of a cantilever beam with a dry friction damper attached, Part I: theory, J. Sound Vib. 91 (1983) 255–267.

[68] M. Carfagni, E. Lenzi, M. Pierini, The loss factor as a measure of mechanical damping, in: 16th Int. Modal Anal. Conf., 1998: pp. 580–584.

[69] M. Carfagni, M. Pierini, Determining the loss factor by the power input method (PIM), Part 1 : Numerical investigation, J. Vib. Acoust. 121 (1999) 417–421.

[70] M. Carfagni, M. Pierini, Determining the loss factor by the power input method (PIM), Part 2 : Experimental investigation with impact hammer excitation, J. Vib. Acoust. 121 (1999) 422–428.

[71] K. Koo, I. Lee, Dynamic behavior of thick composite beams, J. Reinf. Plast. Compos. 14 (1995) 196–210.

[72] A. V Srinivasan, D.G. Cutts, Dry friction damping mechanisms in engine blades, J. Eng. Power. 105 (1983) 332–341.

[73] H.A. Sherif, T.M. Abu Omar, Mechanism of energy dissipation in mechanical system

with dry friction, Tribol. Int. 37 (2004) 235–244.

[74] J. Wang, T. Chen, X. Wang, Y. Xi, The study on friction damping technology with constraint friction layer, 23rd Int. Congr. Sound Vib. (2016) 1–8.

[75] R. Yuan, Q. Zhou, Q. Zhang, Y. Xie, Fractal theory and contact dynamics modeling vibration characteristics of damping blade, Adv. Math. Phys. 2014 (2014) 1–7.

[76] W. Pan, X. Li, N. Guo, Z. Yang, Z. Sun, Three-dimensional fractal model of normal contact damping of dry-friction rough surface, Adv. Mech. Eng. 9 (2017) 1–11.

[77] X. Zhou, E. Shin, K.W. Wang, C.E. Bakis, Interfacial damping characteristics of carbon nanotube-based composites, Compos. Sci. Technol. 64 (2004) 2425–2437.

[78] R.M. Lin, C. Lu, Modeling of interfacial friction damping of carbon nanotube-based nanocomposites, Mech. Syst. Signal Process. 24 (2010) 2996–3012.

[79] G. Formica, W. Lacarbonara, Three-dimensional modeling of interfacial stick-slip in carbon nanotube nanocomposites, Int. J. Plast. 88 (2017) 204–217.

[80] K. Asadi, H. Ahmadian, H. Jalali, Micro/macro-slip damping in beams with frictional contact interface, J. Sound Vib. 331 (2012) 4704–4712.

[81] P. Boisse, A. Gasser, B. Hagege, J.-L. Billoet, Analysis of the mechanical behavior of woven fibrous material using virtual tests at the unit cell level, J. Mater. Sci. 40 (2005) 5955–5962.

[82] W. Chen, X. Deng, Structural damping caused by micro-slip along frictional interfaces, Int. J. Mech. Sci. 47 (2005) 1191–1211.

[83] A.F. Metherell, S. V Diller, Instantaneous energy dissipation rate in a lap joint — uniform clamping pressure, ASME J. Appl. Mech. 35 (1968) 123–128.

[84] V.N. Burlayenko, T. Sadowski, Nonlinear dynamic analysis of harmonically excited debonded sandwich plates using finite element modelling, Compos. Struct. 108 (2014) 354–366.

[85] S.R. Ghoreishi, P. Davies, P. Cartraud, T. Messager, Analytical modeling of synthetic fiber ropes. Part II: A linear elastic model for multilayered fibrous structures, Int. J. Solids Struct. 44 (2007) 2943–2960.

[86] S.R. Ghoreishi, T. Messager, P. Cartraud, P. Davies, Validity and limitations of linear analytical models for steel wire strands under axial loading, using a 3D FE model, Int. J. Mech. Sci. 49 (2007) 1251–1261.

[87] G.S. Ramteke, L. Yenarkar, Analysis of wire rope, Int. J. Eng. Res. Technol. 3 (2014)

14–18.

[88] G. Kastratovic, N. Vidanovic, The analysis of frictionless contact effects in wire rope strand using the finite element method, Int. J. Transp. Logist. (2010) 33–40.

[89] G. Shibu, K. V Mohankumar, S. Devendiran, Analysis of a three layered straight wire rope strand using finite element method, Proc. World Congr. Eng. 2011, WCE 2011. 3 (2011) 2588–2593.

[90] I. Gerdemeli, S. Kurt, A.S. Anil, Fatigue life analysis of wire rope strands with finite element method, Key Eng. Mater. 572 (2014) 513–516.

[91] F. Foti, A. De Luca, Analytical and finite element modelling of the elastic − plastic behaviour of metallic strands under axial − torsional loads, Int. J. Mech. Sci. 115–116 (2016) 202–214.

[92] G. Kastratovic, N. Vidanovic, Some aspects of 3D finite element modeling of independent wire rope, FME Trans. 39 (2011) 37–40.

[93] E. Imrak, C. Erdonmez, On the problem of wire rope model generation, Math. Comput. Appl. 15 (2010) 259–268.

[94] C. Erdonmez, C.E. Imrak, Modeling and numerical analysis of the strand, J. Nav. Sci. Eng. 5 (2009) 30–38.

[95] X. Shi, Y. Pan, X. Ma, Modeling and analysis of the rope–sheave interaction at traction interface, J. Appl. Mech. 84 (2017) 0310051–0310059.

[96] R. Blevins, Formula For Natural Frequency and Mode shape, Krieger Publishing Company, 1979.

[97] C. Lord, Damping Effects of Debonded Composites, The University of Sheffield, 2012.

[98] W. Thomson, Theory of vibration and applications, 5th ed., CRC Press, 1996.

[99] S.P. Goodier, J.N. Timoshenko, Theory of elasticity, Third edit, McGraw-Hill classic textbook reissue series. McGraw-Hill, 1970.

[100] C. Lord, J. Rongong, A single layer constitutive model for the dynamics and vibration damping of layered built-up structures using microslip and macroslip models, in: 54TH AIAA/ASME/ASCE/AHS/ASC Struct. Struct. Dyn. Mater. Conf., American Institute of Aeronautics and Astronautics, 2013: pp. 7374–7387.

[101] K. Chandrasekhar, J.A. Rongong, E.J. Cross, Frequency and amplitude dependent behaviour of tangled metal wire dampers, Int. Conf. Noise Vib. Eng. (2014) 559–572.

[102] H.K. Asker, J.A. Rongong, C.E. Lord, Stiffness and loss factor of unbonded , multi-strand beams under flexural deformation, in: Int. Conf. Eng. Vib., Ljubljana, Slovenia, 2015: pp. 1518–1529.

[103] N. Zhou, T.K. Ghosh, On-line measurement of fabric-bending behaviour: background, need and potential solutions, Int. J. Cloth. Sci. Technol. 10 (1998) 143–156.

[104] J.. Meriam, L.. Kraige, Engineering mechanics: statics, 7th ed., John Wiley and Sons, 2003.

[105] C.F. Beards, Structural Vibration: Analysis and Damping, Arnold, 1996.

[106] Minimum recommended heat shrink temperature, (n.d.). http://www.insultab.com/technical-info/shrink-temp.html (accessed May 30, 2017).

[107] Tubing and heat shrink, (n.d.). http://www.texloc.com/closet/cl_propertycomparison.html (accessed May 30, 2017).

[108] E.J. Hearn, Mechanics of materials, vols. 1 and 2 Edited by E. J. Hearn. Pp. 643. Pergamon Press, Oxford. 1978, 1978.

[109] J.K. Nisbett, R.G. Budynas, Mechanical engineering design, 2011.

[110] E. Chatelet, G. Michon, L. Manin, G. Jacquet, Stick/slip phenomena in dynamics: Choice of contact model. Numerical predictions & experiments, Mech. Mach. Theory. 43 (2008) 1211–1224.

[111] B.A.S.W.H. Bernard, Work and heat transfer in the presence of sliding friction, Am. Assoc. PhysicsTeachers. 52 (1984) 1001–1007.

Appendix A

A.1 Torque values and the equivalent reaction force

Table A.1 Torque vales on each fastener and the equivalent reaction force

Torque, N.mm	Trial 1	Trial 2	Trial 3	Trial 4	Trial 5	Force, N
14.12	55.30	49.20	50.70	53.40	55.80	52.88
28.24	78.20	74.60	76.60	84.20	82.60	79.24
42.36	97.58	107.6	96.34	104.8	94.59	100.2
56.49	130.0	146.0	130.0	126.0	122.0	130.8
70.61	167.0	156.0	141.0	152.0	158.0	154.8
84.73	198.0	193.5	188.0	184.0	186.0	189.9
98.86	200.0	235.0	224.0	213.0	198.0	214.0
112.9	236.0	243.0	254.0	270.0	248.0	250.2

Appendix B

B.1 Relationship between the displacement and the coefficient of friction

The analytically build relationship between the displacement and the coefficient of friction through using Equation 3.19 during different loading conditions and different geometric parameters for Configuration sb07 through Configuration sb24.
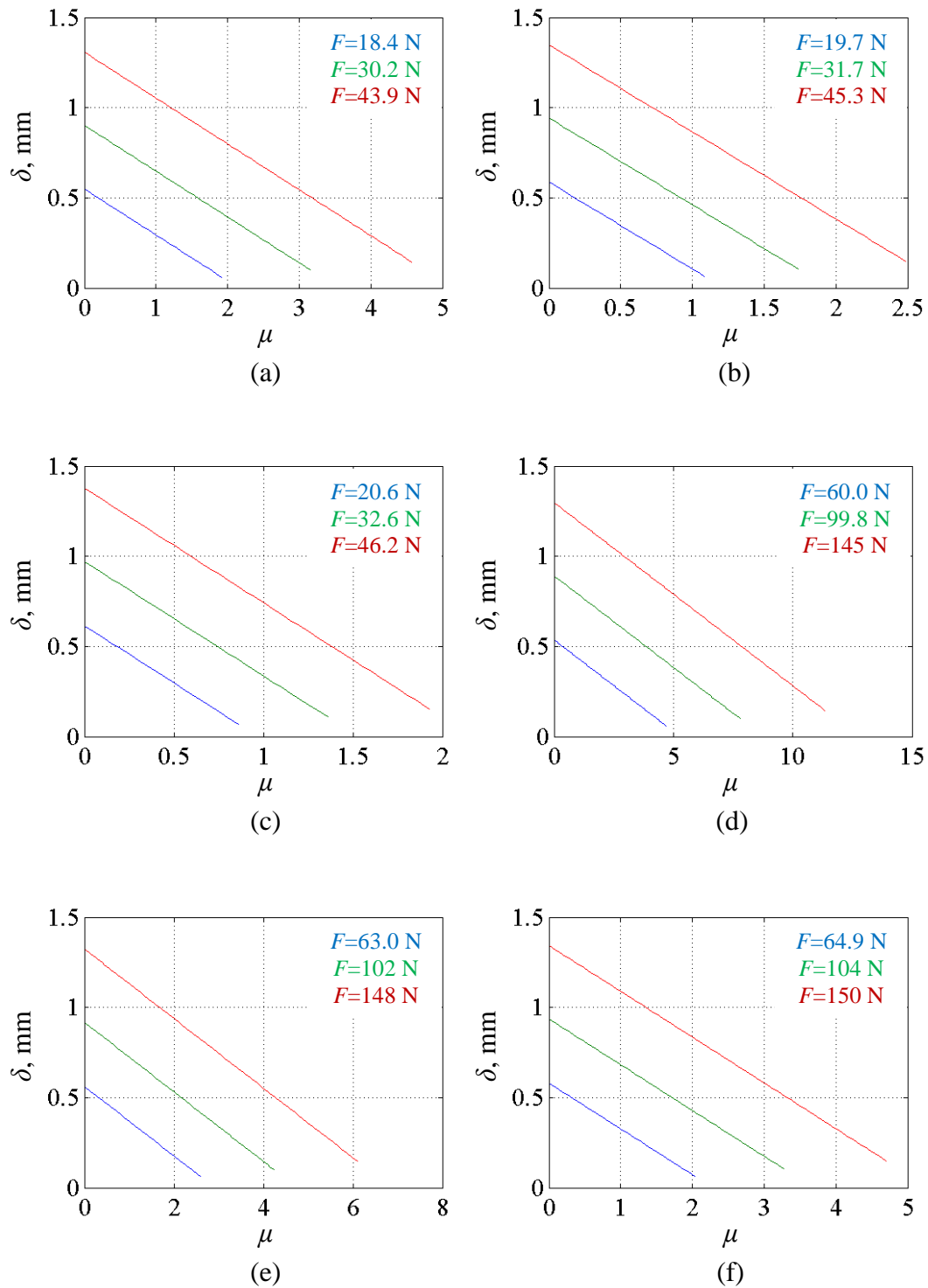
Figure B.1 Deformations versus coefficient of friction for Configurations (a) sb07 through (f) sb12 respectively
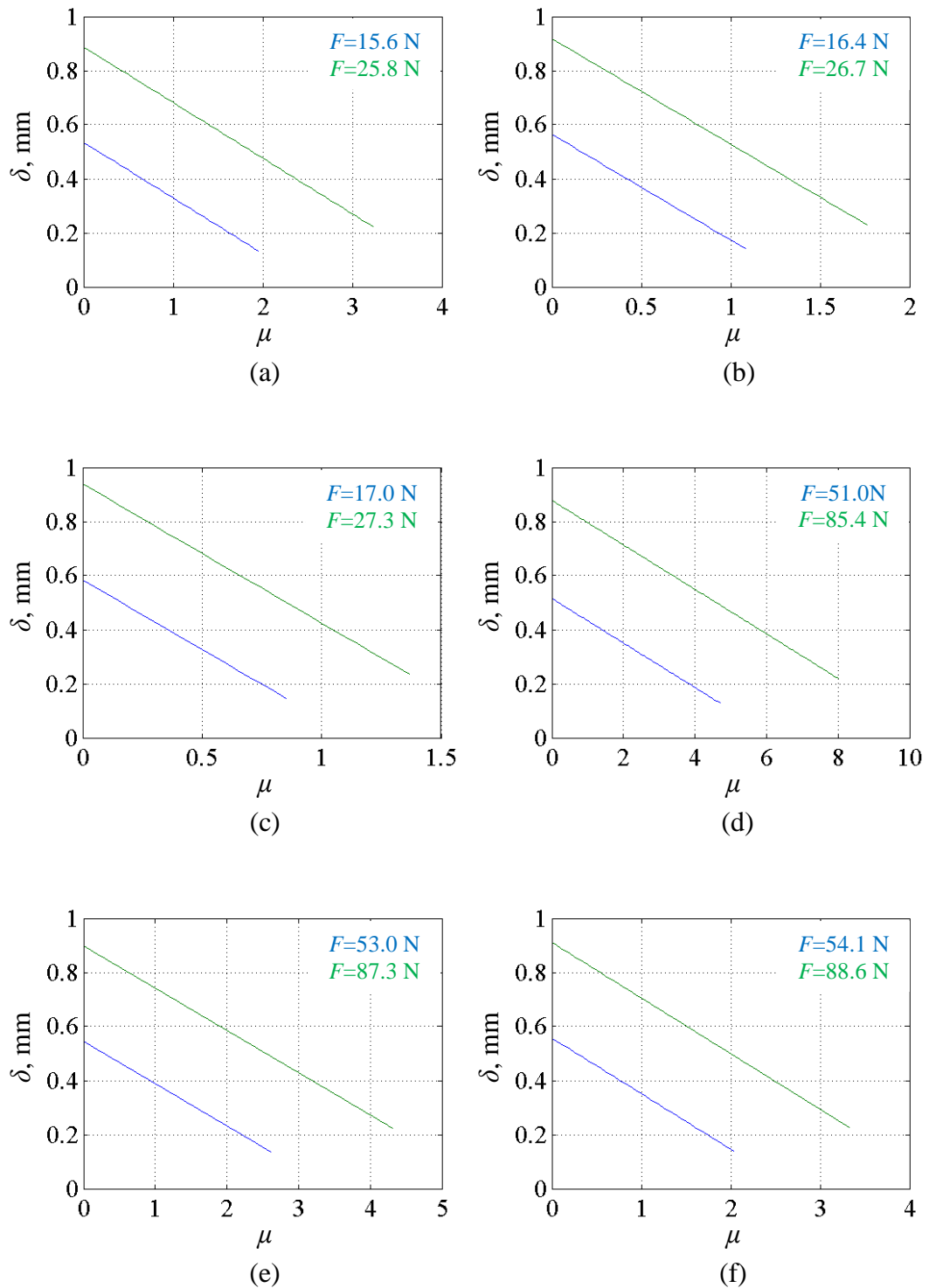
Figure B.2 Deformations versus coefficient of friction for Configurations (a) sb13 through (f) sb18 respectively
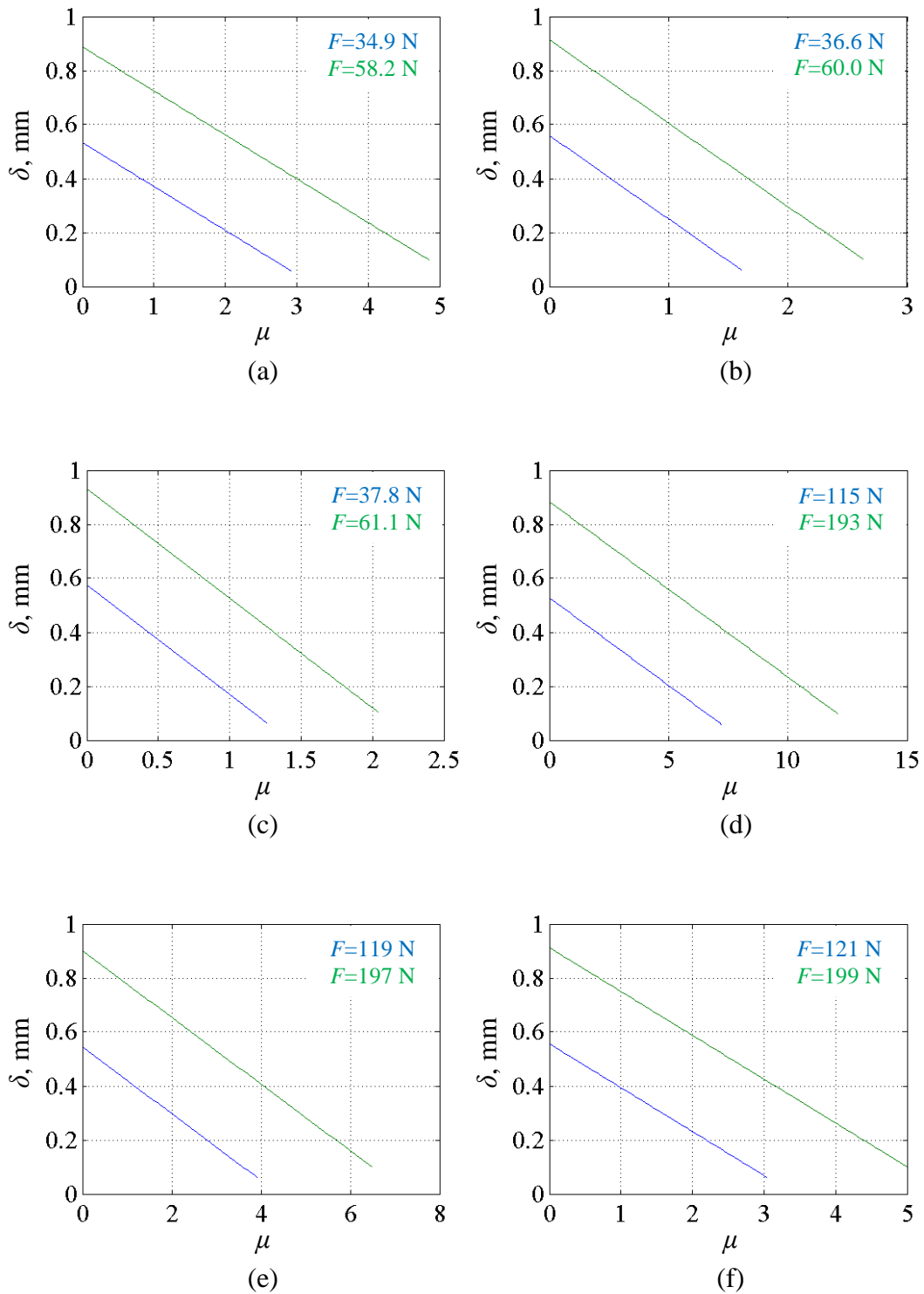
Figure B.3 Deformations versus coefficient of friction for Configurations (a) sb19 through (f) sb24 respectively

Appendix C

C.1 Relationship between the frictional second moment of area and the coefficient of friction

The relationships of the frictional second moment of area against the coefficient of friction are built using Equation 3.20 and described in Figure C.1 through Figure C.3 for Configuration sb07 through sb24.
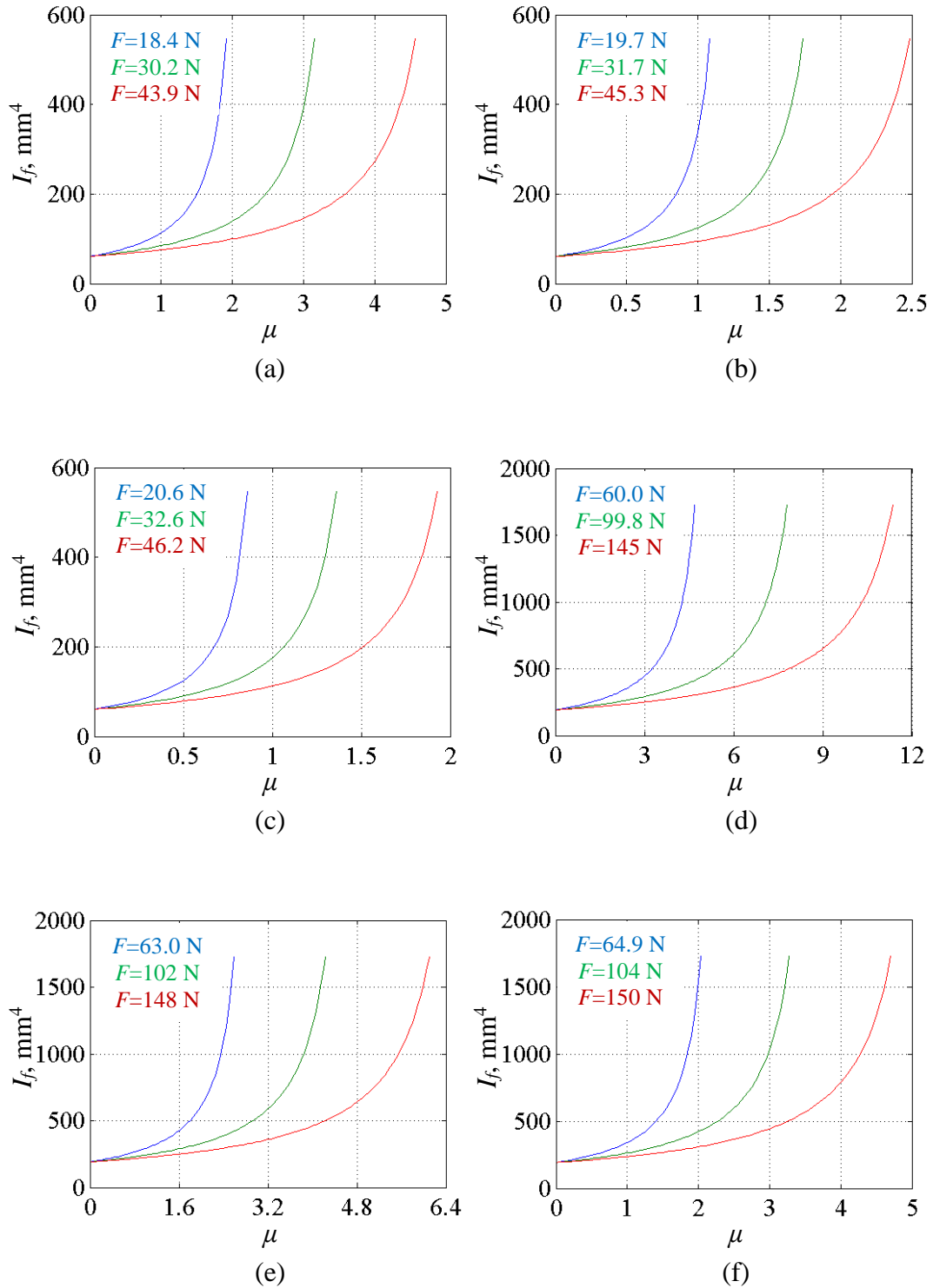
Figure C.1 Second moment of area versus coefficient of friction for Configurations (a) sb07 through (f) sb12 respectively
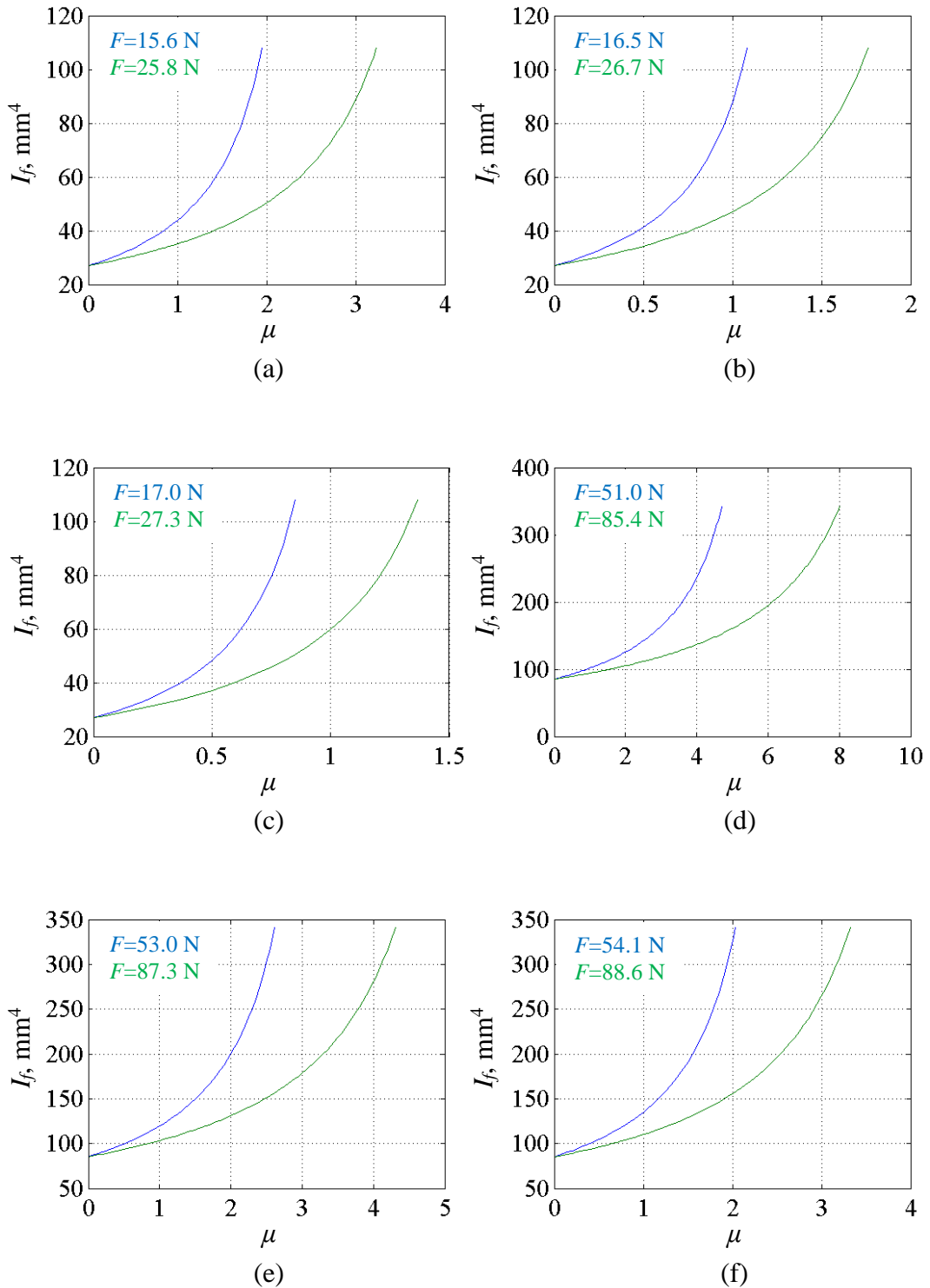
Figure C.2 Second moment of area versus coefficient of friction for Configurations (a) sb13 through (f) sb18 respectively
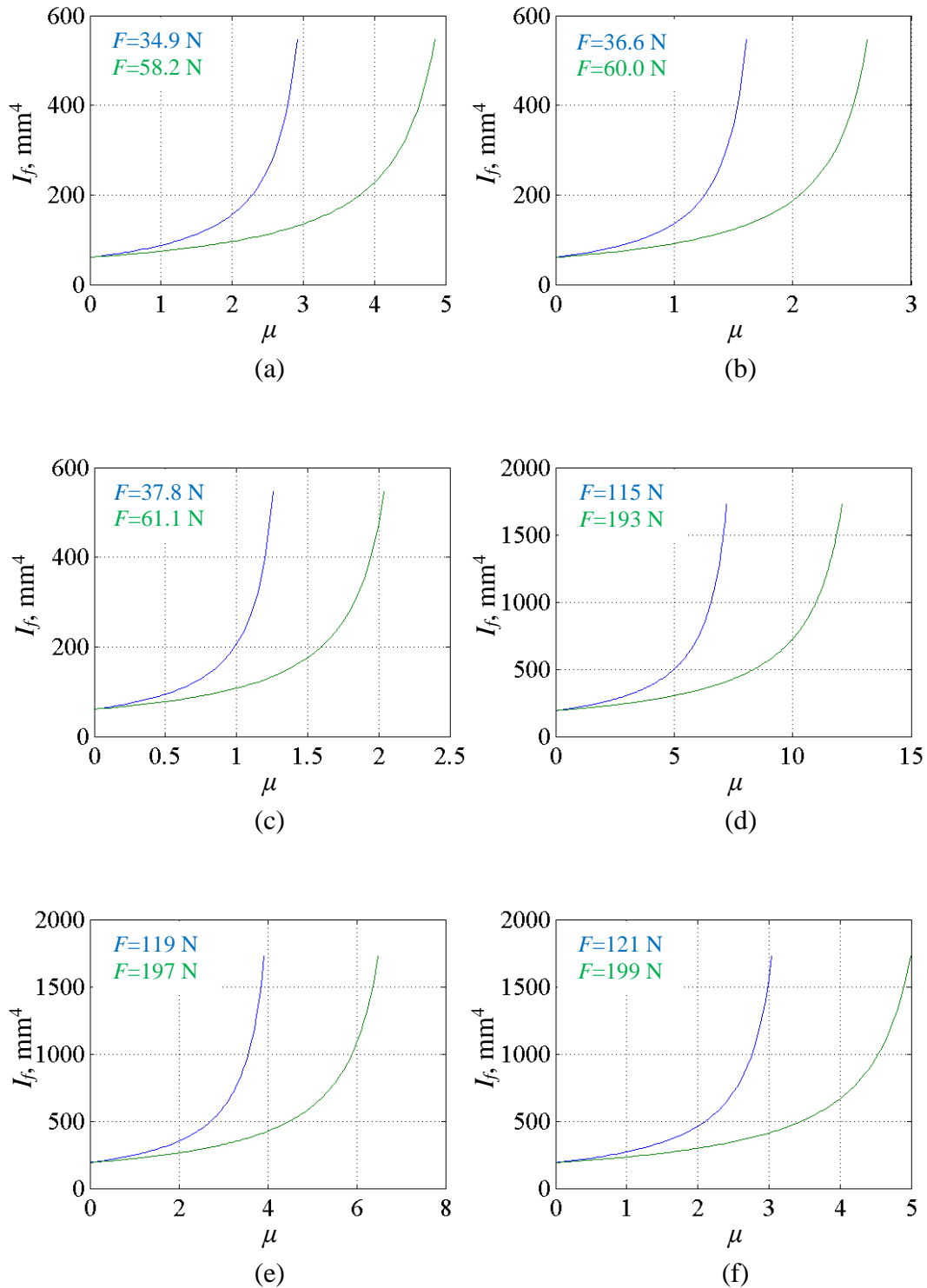
Figure C.3 Second moment of area versus coefficient of friction for Configurations (a) sb19 through (f) sb24 respectively

Appendix D

D.1 Comparison of hysteresis loops of multi-strand beams – analytical and numerical

Figure D.1 through Figure D.9 show comparison between the analytical hysteresis loops and the numerically obtained hysteresis loops for Configuration sb01 through sb21.
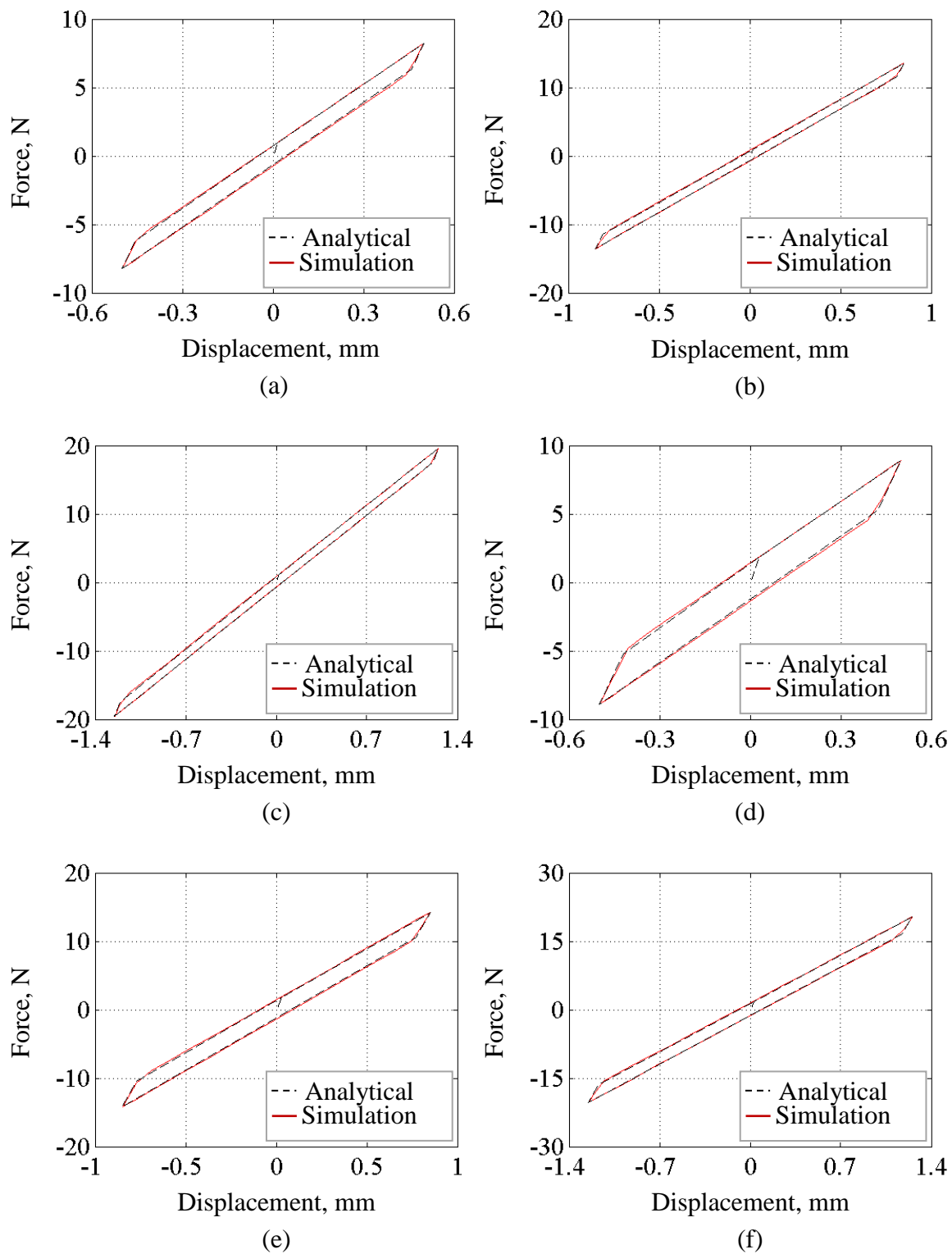
Figure D.1 Comparison of analytical and numerical hysteresis loops for Configuration sb01 at PK-PK loading of (a) 1.0 mm, (b) 1.7 mm, (c) 2.5 mm and for Configuration sb02 at PK-PK loading of (d) 1.0 mm, (e) 1.7 mm and (f) 2.5 mm
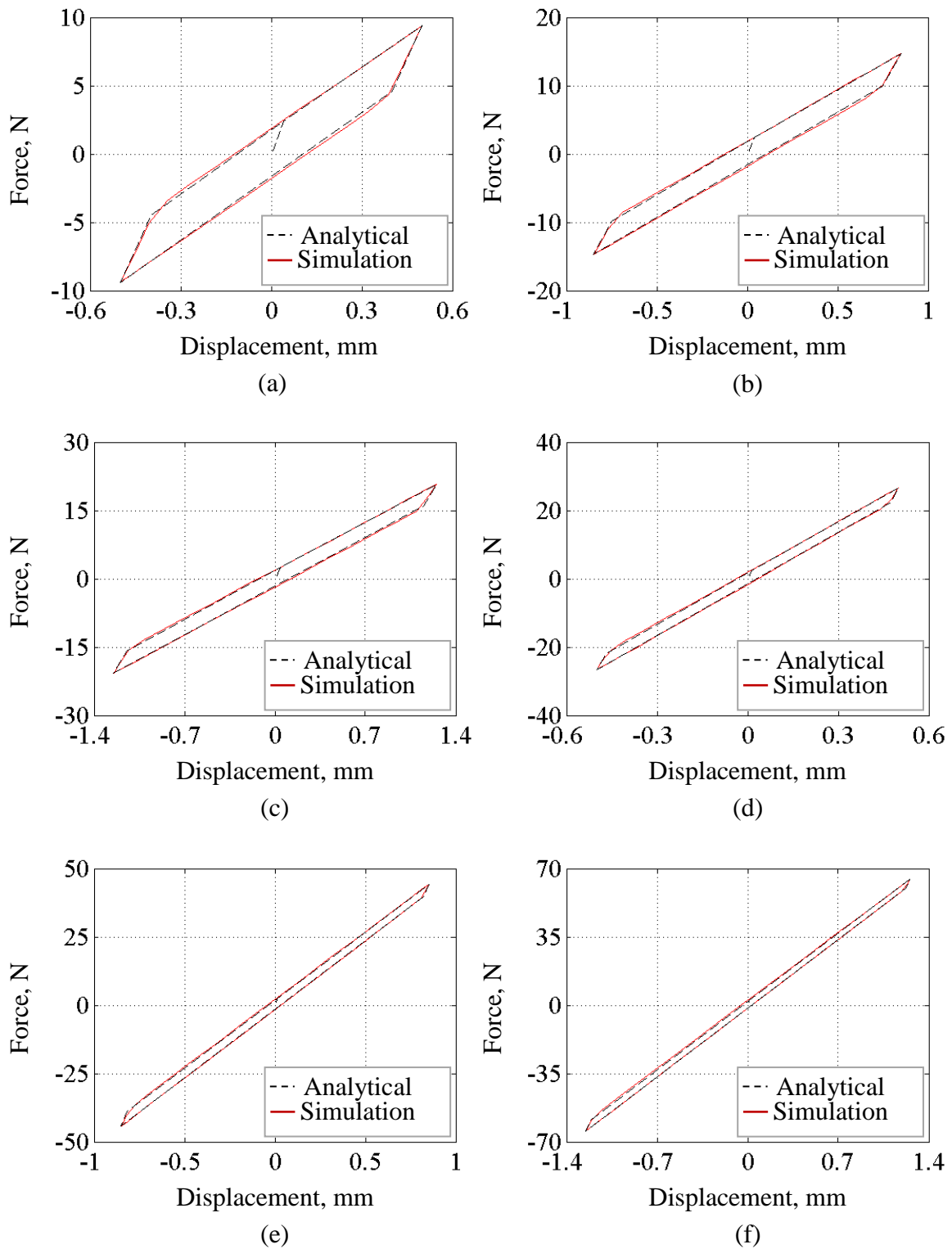
Figure D.2 Comparison of analytical and numerical hysteresis loops for Configuration sb03 at PK-PK loading of (a) 1.0 mm, (b) 1.7 mm, (c) 2.5 mm and for Configuration sb04 at PK-PK loading of (d) 1.0 mm, (e) 1.7 mm and (f) 2.5 mm
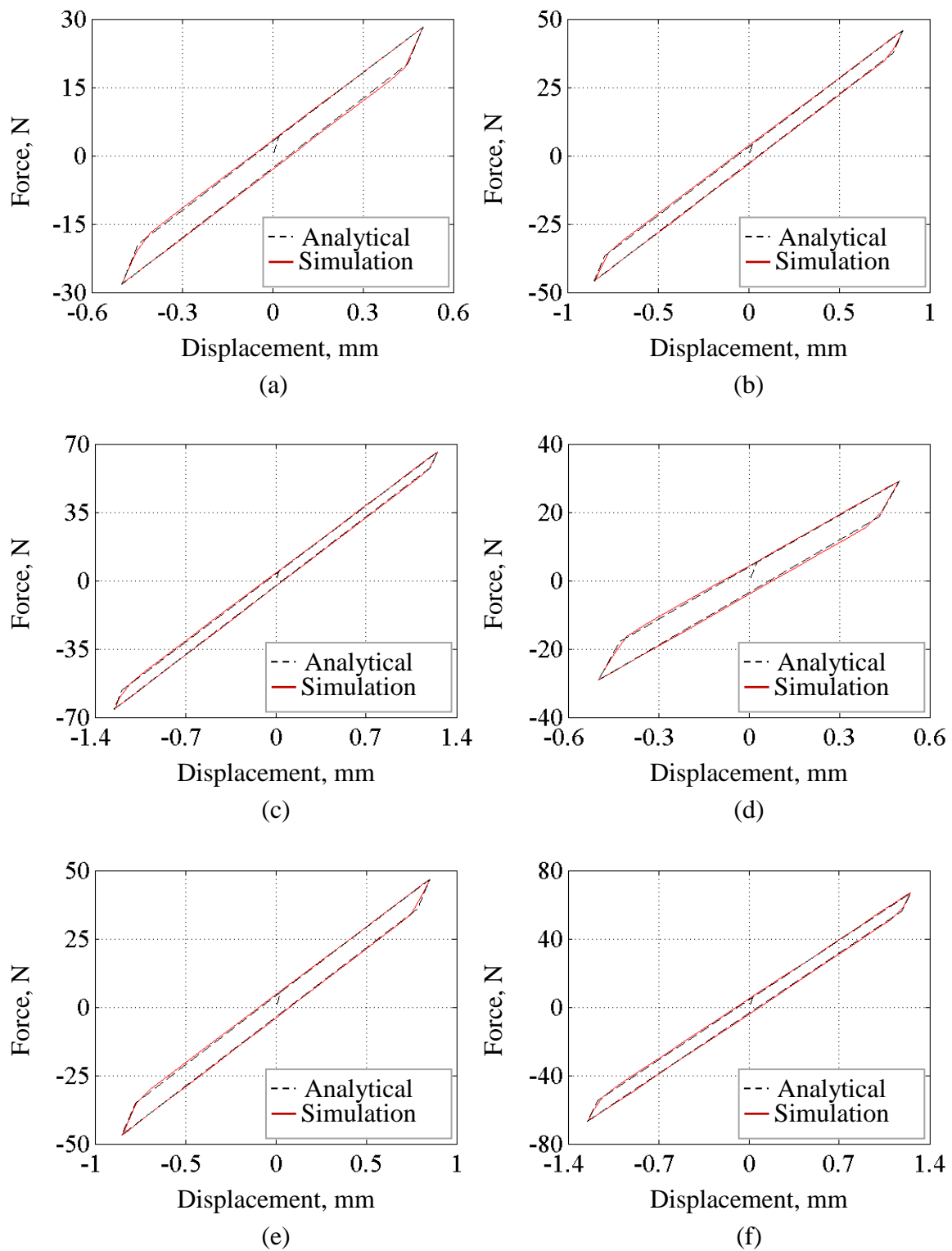
Figure D.3 Comparison of analytical and numerical hysteresis loops for Configuration sb05 at PK-PK loading of (a) 1.0 mm, (b) 1.7 mm, (c) 2.5 mm and for Configuration sb06 at PK-PK loading of (d) 1.0 mm, (e) 1.7 mm and (f) 2.5 mm
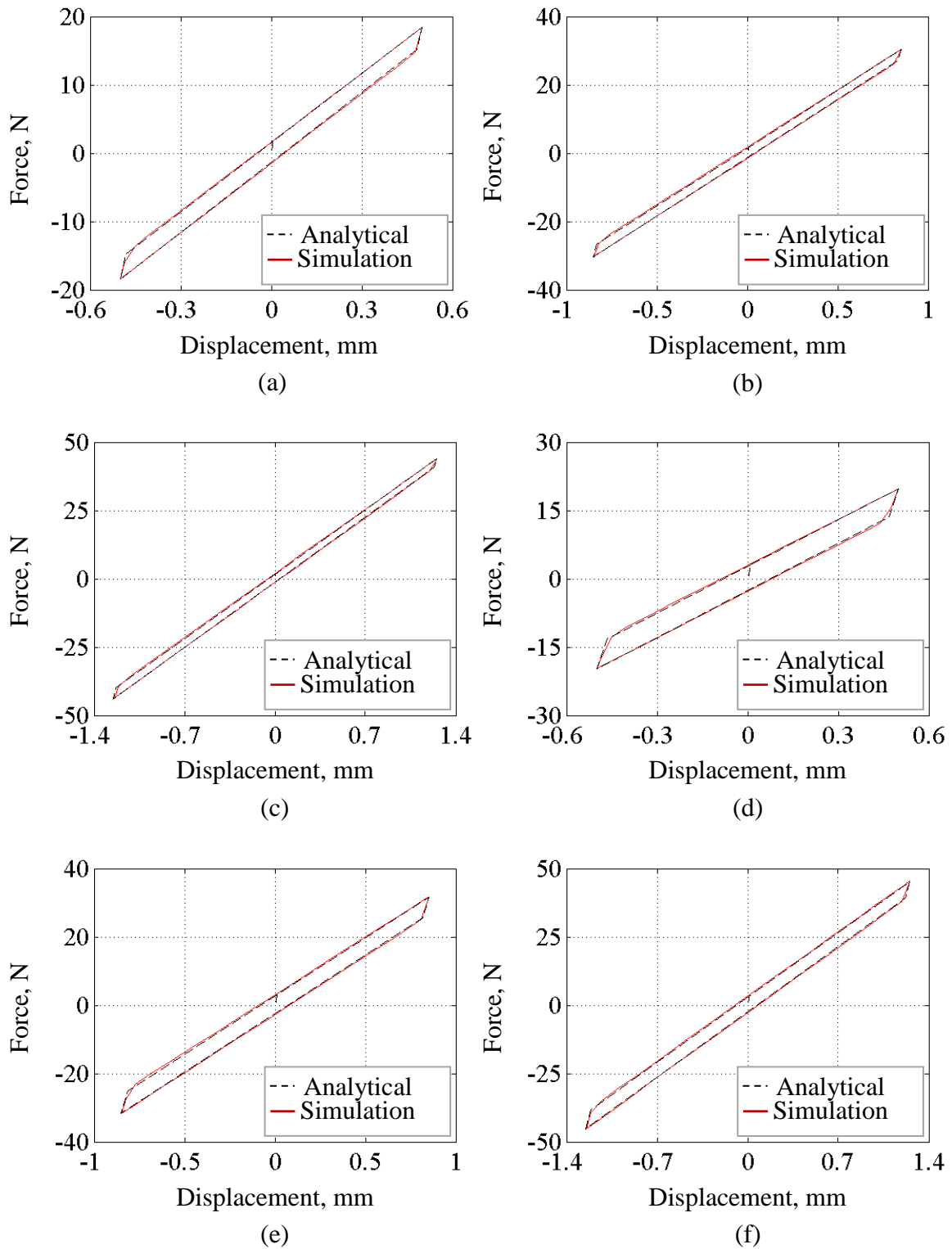
Figure D.4 Comparison of analytical and numerical hysteresis loops for Configuration sb07 at PK-PK loading of (a) 1.0 mm, (b) 1.7 mm, (c) 2.5 mm and for Configuration sb08 at PK-PK loading of (d) 1.0 mm, (e) 1.7 mm and (f) 2.5 mm
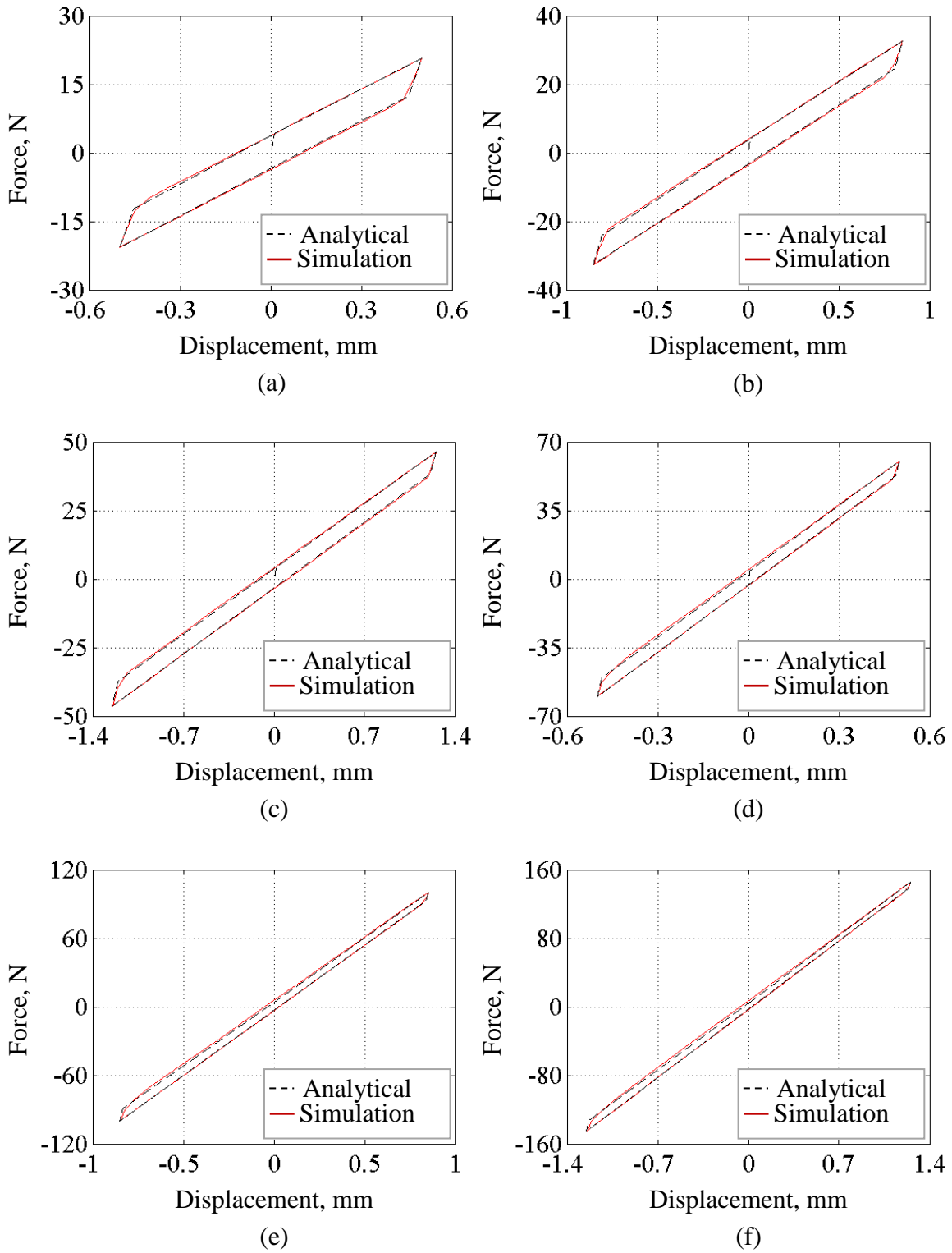
Figure D.5 Comparison of analytical and numerical hysteresis loops for Configuration sb09 at PK-PK loading of (a) 1.0 mm, (b) 1.7 mm, (c) 2.5 mm and for Configuration sb10 at PK-PK loading of (d) 1.0 mm, (e) 1.7 mm and (f) 2.5 mm
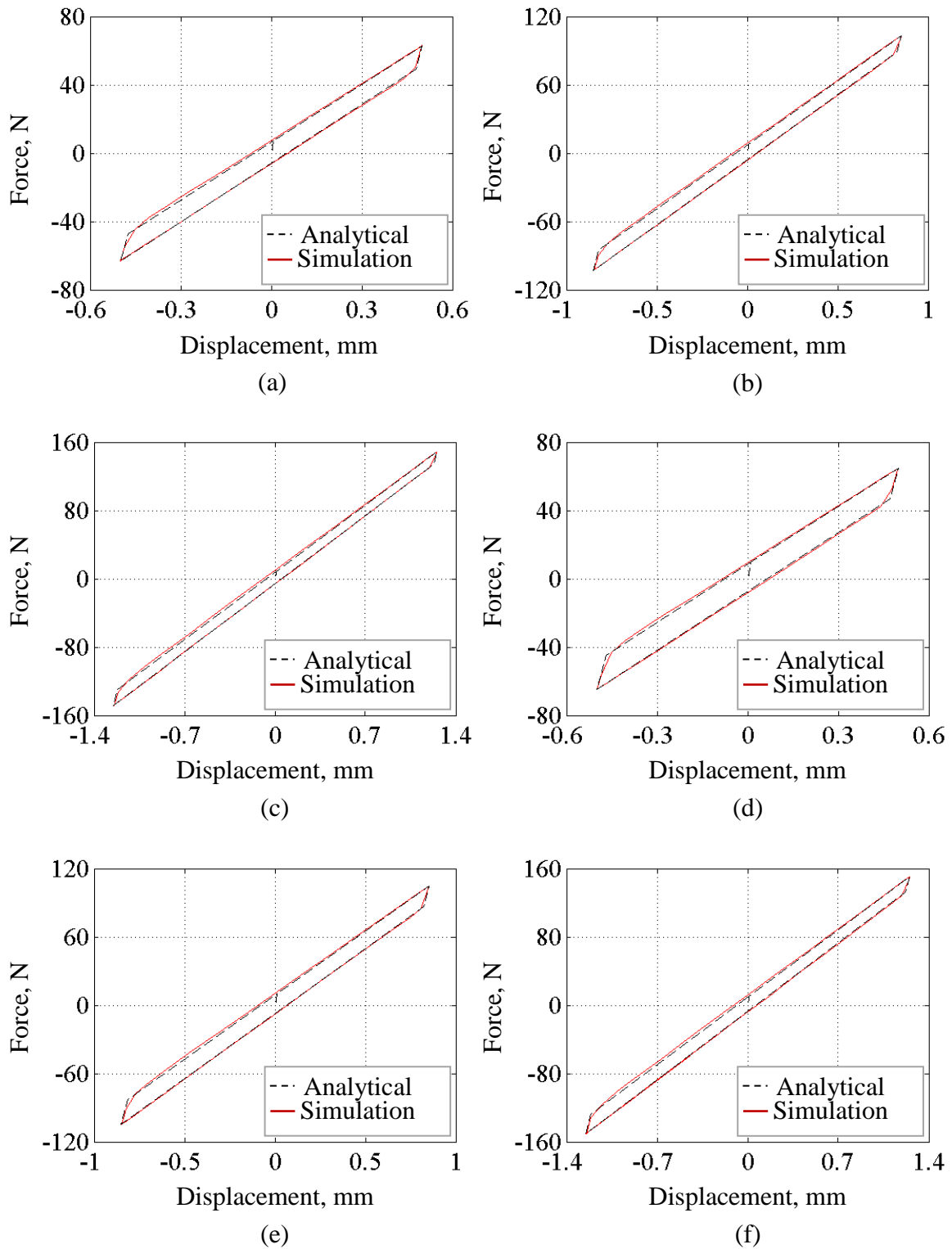
Figure D.6 Comparison of analytical and numerical hysteresis loops for Configuration sb11 at PK-PK loading of (a) 1.0 mm, (b) 1.7 mm, (c) 2.5 mm and for Configuration sb12 at PK-PK loading of (d) 1.0 mm, (e) 1.7 mm and (f) 2.5 mm
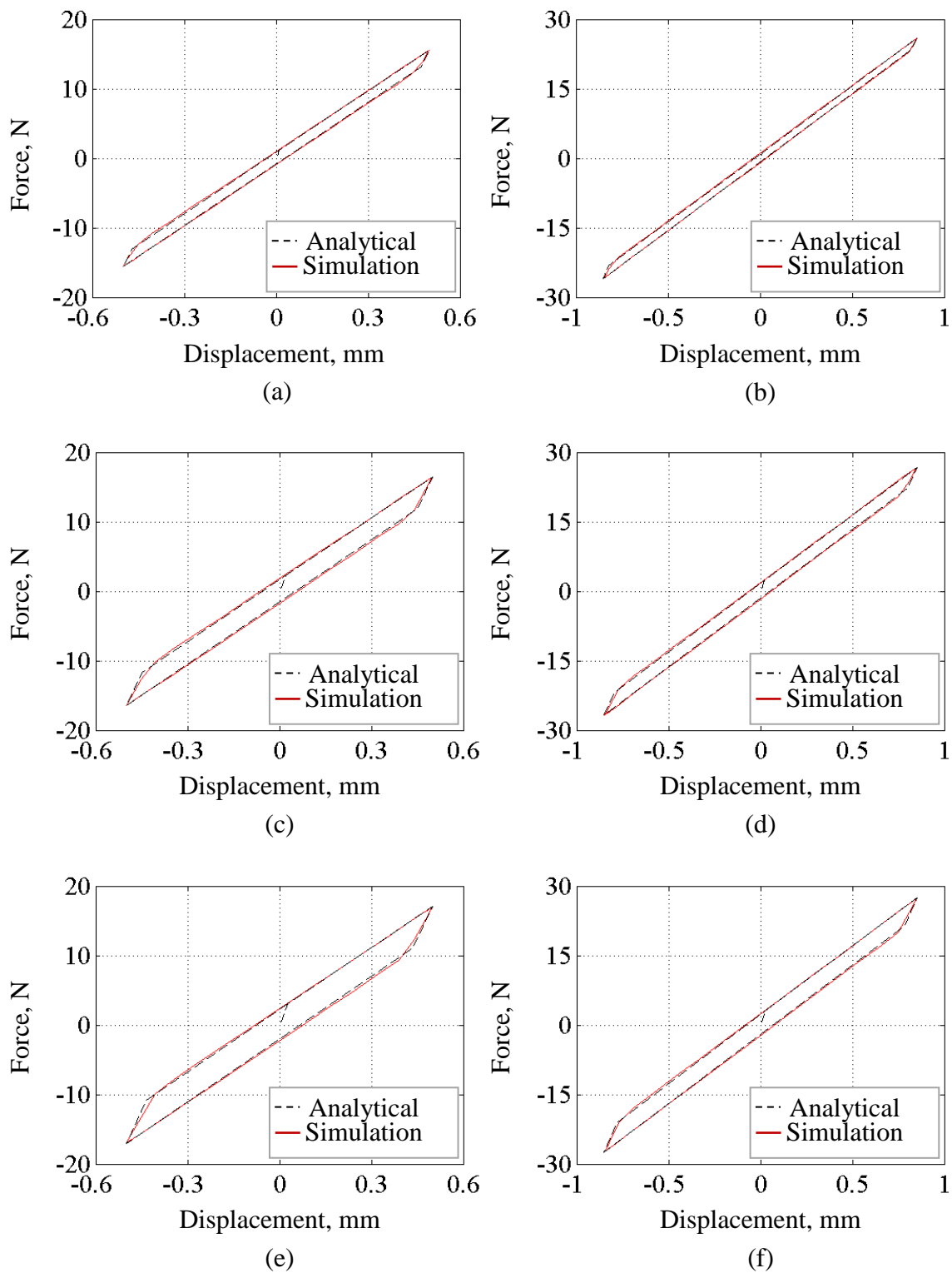
Figure D.7 Comparison of analytical and numerical hysteresis loops for Configuration sb13 at PK-PK loading of (a) 1.0 mm, (b) 1.7 mm and for Configuration sb14 at PK-PK loading of (c) 1.0 mm, (d) 1.7 mm and for Configuration sb15 at PK-PK loading of (e) 1.0 mm and (f) 1.7 mm
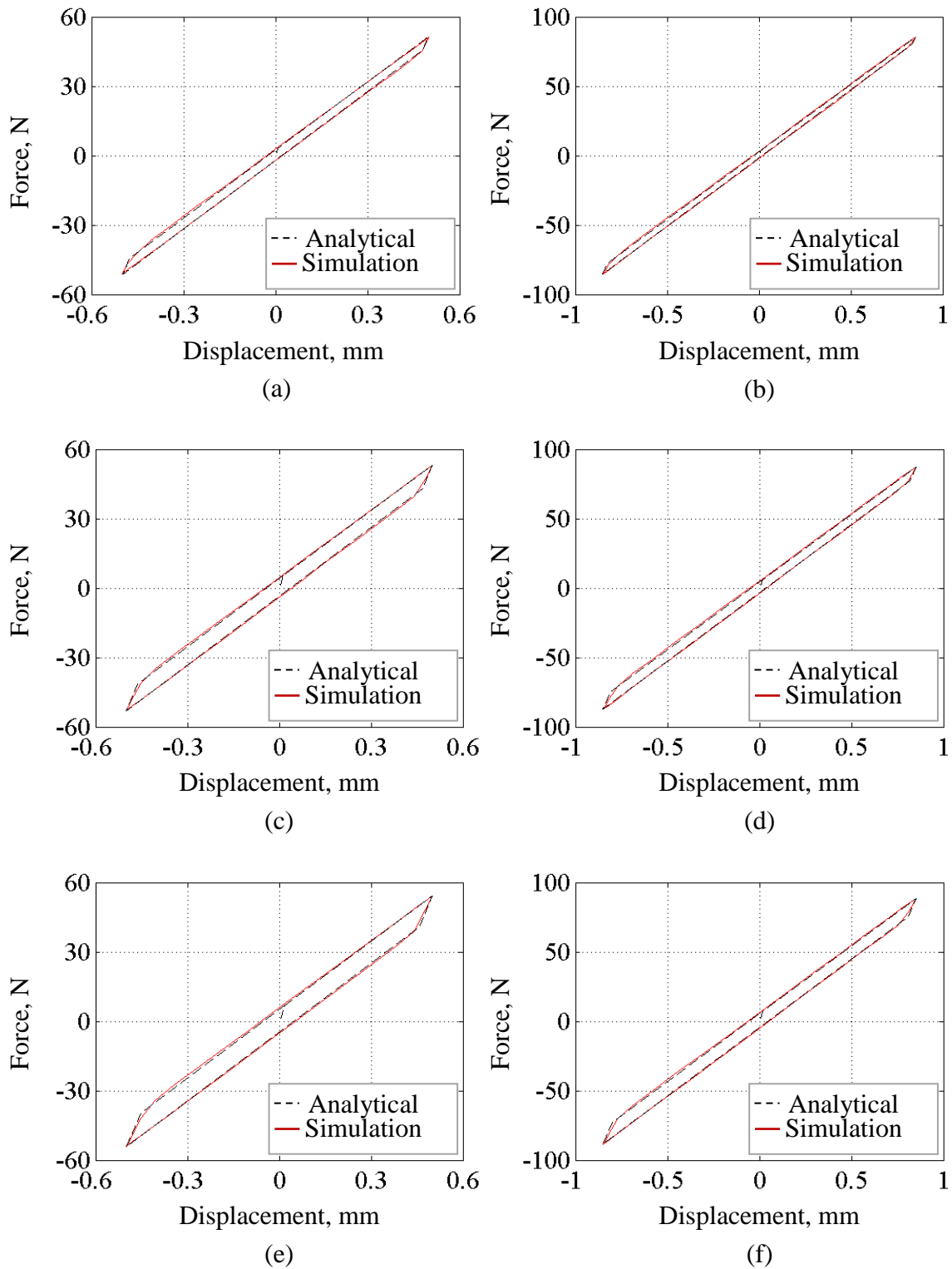
Figure D.8 Comparison of analytical and numerical hysteresis loops for Configuration sb16 at PK-PK loading of (a) 1.0 mm, (b) 1.7 mm and for Configuration sb17 at PK-PK loading of (c) 1.0 mm, (d) 1.7 mm and for Configuration sb18 at PK-PK loading of (e) 1.0 mm and (f) 1.7 mm
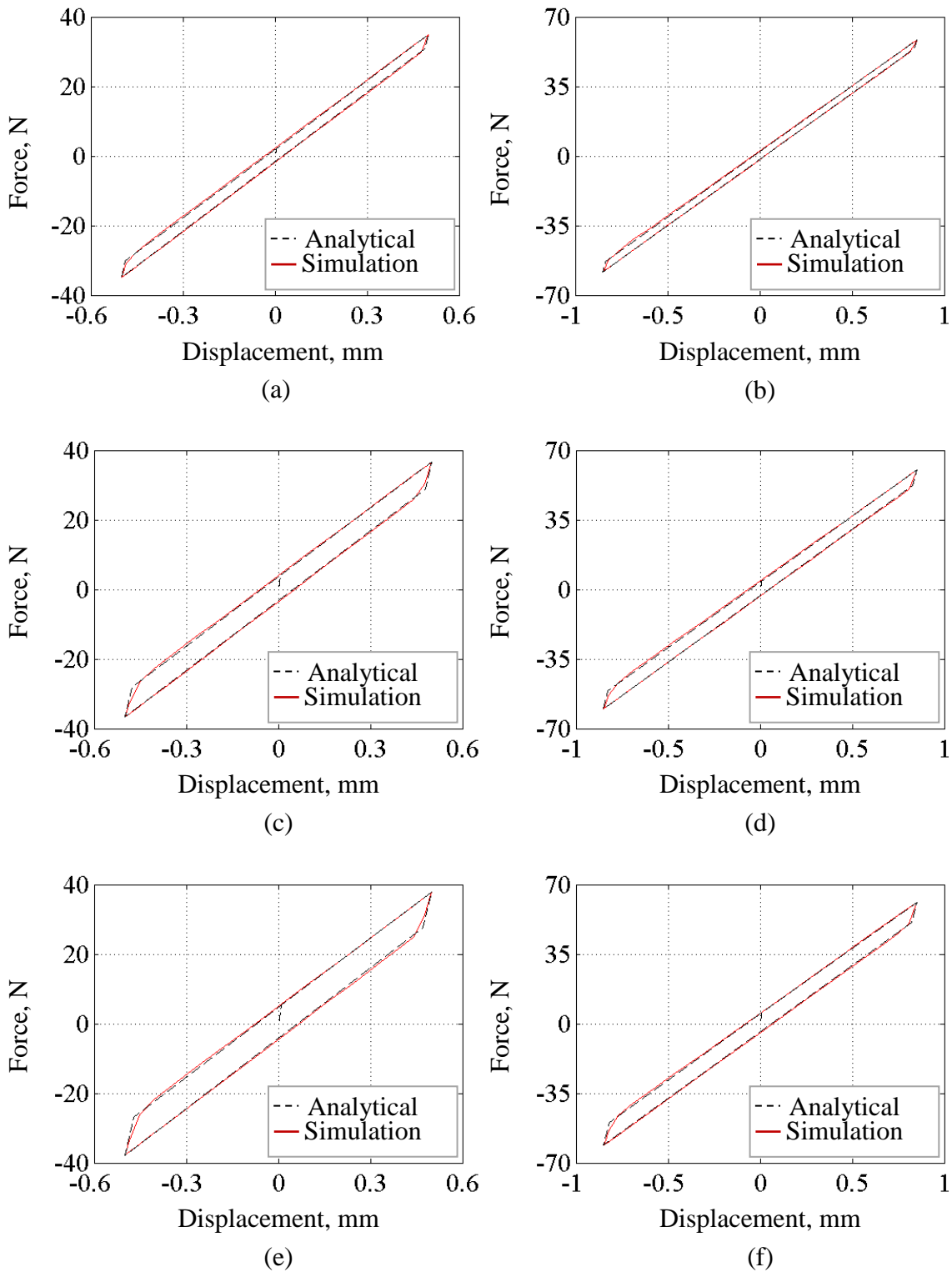
Figure D.9 Comparison of analytical and numerical hysteresis loops for Configuration sb19 at PK-PK loading of (a) 1.0 mm, (b) 1.7 mm and for Configuration sb20 at PK-PK loading of (c) 1.0 mm, (d) 1.7 mm and for Configuration sb21 at PK-PK loading of (e) 1.0 mm and (f) 1.7 mm

Appendix E

E.1 Analytical, numerical and experimental Damping characteristics of multi-strand beams (MSB)

Table E.1 Analytical damping characteristics for Configuration sb01 through Configuration sb12

Configuration	Loading, mm	Analytical			
		Loss factor	Energy dissipation / cycle, mJ	Strain energy, mJ	Stiffness, N/mm
sb01	1.000	0.109	1.309	3.830	16.48
	1.700	0.067	2.325	10.99	15.90
	2.500	0.048	3.545	23.70	15.63
sb02	1.000	0.188	2.336	3.947	17.86
	1.700	0.119	4.178	11.16	16.74
	2.500	0.084	6.344	23.96	16.22
sb03	1.000	0.233	2.965	4.050	18.78
	1.700	0.151	5.355	11.29	17.30
	2.500	0.107	8.151	24.15	16.61
sb04	1.000	0.080	3.216	12.74	53.40
	1.700	0.052	5.965	36.67	52.07
	2.500	0.038	9.546	79.18	51.46
sb05	1.000	0.139	5.627	12.93	56.38
	1.700	0.088	10.22	36.94	53.85
	2.500	0.064	15.91	79.58	52.71
sb06	1.000	0.174	7.154	13.09	58.36
	1.700	0.111	12.98	37.15	55.04
	2.500	0.080	20.08	79.88	53.54
sb07	1.000	0.105	2.852	8.611	36.79
	1.700	0.066	5.152	24.78	35.62
	2.500	0.048	8.052	53.57	35.10
sb08	1.000	0.187	5.125	8.741	39.52
	1.700	0.116	9.112	25.02	37.28
	2.500	0.082	13.92	53.84	36.25
sb09	1.000	0.237	6.591	8.854	41.35
	1.700	0.148	11.70	25.20	38.39
	2.500	0.105	17.81	54.15	37.00
sb10	1.000	0.083	7.587	28.98	120.0
	1.700	0.057	14.94	83.55	117.4
	2.500	0.045	25.37	180.5	116.2
sb11	1.000	0.139	12.77	29.19	126.0
	1.700	0.091	23.90	83.91	120.9
	2.500	0.068	38.64	181.1	118.7
sb12	1.000	0.175	16.16	29.38	129.9
	1.700	0.113	29.80	84.18	123.3
	2.500	0.083	47.41	181.5	120.3

Table E.2 Analytical damping characteristics for Configuration sb13 through Configuration sb24

Configuration	Loading, mm	Analytical			
		Loss factor	Energy dissipation / cycle, mJ	Strain energy, mJ	Stiffness, N/mm
sb13	1.000	0.074	1.723	7.434	31.18
	1.700	0.046	3.105	21.40	30.44
sb14	1.000	0.130	3.079	7.549	32.90
	1.700	0.081	5.489	21.57	31.53
sb15	1.000	0.164	3.939	7.644	34.05
	1.700	0.103	7.043	21.74	32.21
sb16	1.000	0.057	4.468	24.75	102.6
	1.700	0.039	8.763	71.69	100.4
sb17	1.000	0.097	7.616	25.08	105.9
	1.700	0.063	14.19	72.04	102.7
sb18	1.000	0.122	9.633	25.20	108.3
	1.700	0.078	17.75	72.23	104.2
sb19	1.000	0.073	3.861	16.79	69.91
	1.700	0.048	7.247	48.45	68.46
sb20	1.000	0.127	6.768	16.94	73.34
	1.700	0.080	12.26	48.75	70.57
sb21	1.000	0.162	8.667	17.05	75.62
	1.700	0.101	15.57	48.94	71.93
sb22	1.000	0.065	11.54	56.90	230.8
	1.700	0.048	24.55	164.1	227.4
sb23	1.000	0.101	18.13	57.14	238.3
	1.700	0.069	35.87	164.6	231.9
sb24	1.000	0.125	22.47	57.32	243.2
	1.700	0.084	43.36	164.9	234.9

Table E.3 Numerical damping characteristics for Configuration sb01 through Configuration sb12

| Configuration | Loading, mm | Numerical | | | |
		Loss factor	Energy dissipation / cycle, mJ	Strain energy, mJ	Stiffness, N/mm
sb01	1.000	0.116	1.390	3.801	14.86
	1.700	0.072	2.460	10.92	15.20
	2.500	0.051	3.746	23.57	15.28
sb02	1.000	0.201	2.468	3.913	14.50
	1.700	0.128	4.434	11.06	14.86
	2.500	0.090	6.728	23.79	15.15
sb03	1.000	0.248	3.133	4.020	14.84
	1.700	0.162	5.680	11.19	14.71
	2.500	0.115	8.678	23.95	15.01
sb04	1.000	0.085	3.347	12.58	50.57
	1.700	0.054	6.112	36.25	50.70
	2.500	0.039	9.602	78.33	50.53
sb05	1.000	0.147	5.895	12.74	48.99
	1.700	0.092	10.59	36.47	50.20
	2.500	0.066	16.35	78.65	50.87
sb06	1.000	0.184	7.473	12.91	48.29
	1.700	0.117	13.52	36.65	49.68
	2.500	0.084	20.73	78.92	50.57
sb07	1.000	0.110	2.944	8.503	35.02
	1.700	0.068	5.269	24.51	34.59
	2.500	0.049	8.119	52.99	34.31
sb08	1.000	0.196	5.314	8.621	34.09
	1.700	0.122	9.436	24.69	35.08
	2.500	0.086	14.33	53.26	34.91
sb09	1.000	0.251	6.86	8.722	33.78
	1.700	0.156	12.15	24.84	34.63
	2.500	0.110	18.45	53.48	35.11
sb10	1.000	0.085	7.577	28.28	114.7
	1.700	0.056	14.42	81.63	113.9
	2.500	0.043	23.77	176.51	113.3
sb11	1.000	0.145	12.93	28.47	115.7
	1.700	0.092	23.75	81.91	115.5
	2.500	0.068	37.57	176.9	114.7
sb12	1.000	0.182	16.41	28.64	113.6
	1.700	0.116	29.87	82.14	116.3
	2.500	0.084	46.72	177.3	115.6

Table E.4 Numerical damping characteristics for Configuration sb13 through Configuration sb24

Configuration	Loading, mm	Numerical			
		Loss factor	Energy dissipation / cycle, mJ	Strain energy, mJ	Stiffness, N/mm
sb13	1.000	0.078	1.798	7.381	29.46
	1.700	0.048	3.237	21.26	29.71
sb14	1.000	0.136	3.209	7.497	28.75
	1.700	0.085	5.746	21.43	29.37
sb15	1.000	0.171	4.081	7.608	28.36
	1.700	0.109	7.370	21.57	29.15
sb16	1.000	0.060	4.590	24.51	98.43
	1.700	0.039	8.682	70.72	98.43
sb17	1.000	0.102	7.898	24.69	96.61
	1.700	0.065	14.47	71.00	98.66
sb18	1.000	0.127	9.891	24.85	95.94
	1.700	0.081	18.01	71.22	98.12
sb19	1.000	0.076	3.954	16.56	67.58
	1.700	0.048	7.280	47.81	66.85
sb20	1.000	0.132	6.948	16.71	66.85
	1.700	0.083	12.527	48.05	67.74
sb21	1.000	0.168	8.874	16.82	66.09
	1.700	0.105	15.917	48.24	67.99
sb22	1.000	0.064	11.16	55.25	222.4
	1.700	0.045	22.60	159.5	221.4
sb23	1.000	0.103	17.91	55.49	225.9
	1.700	0.068	34.22	159.9	223.9
sb24	1.000	0.127	22.29	55.68	222.9
	1.700	0.083	41.93	160.2	224.9

Appendix F

F.1 Comparison of hysteresis loops of multi-strand beams – analytical, numerical and experimental

Figures F.1 through F.9 show comparison of analytical, numerical and experimental hysteresis loops.
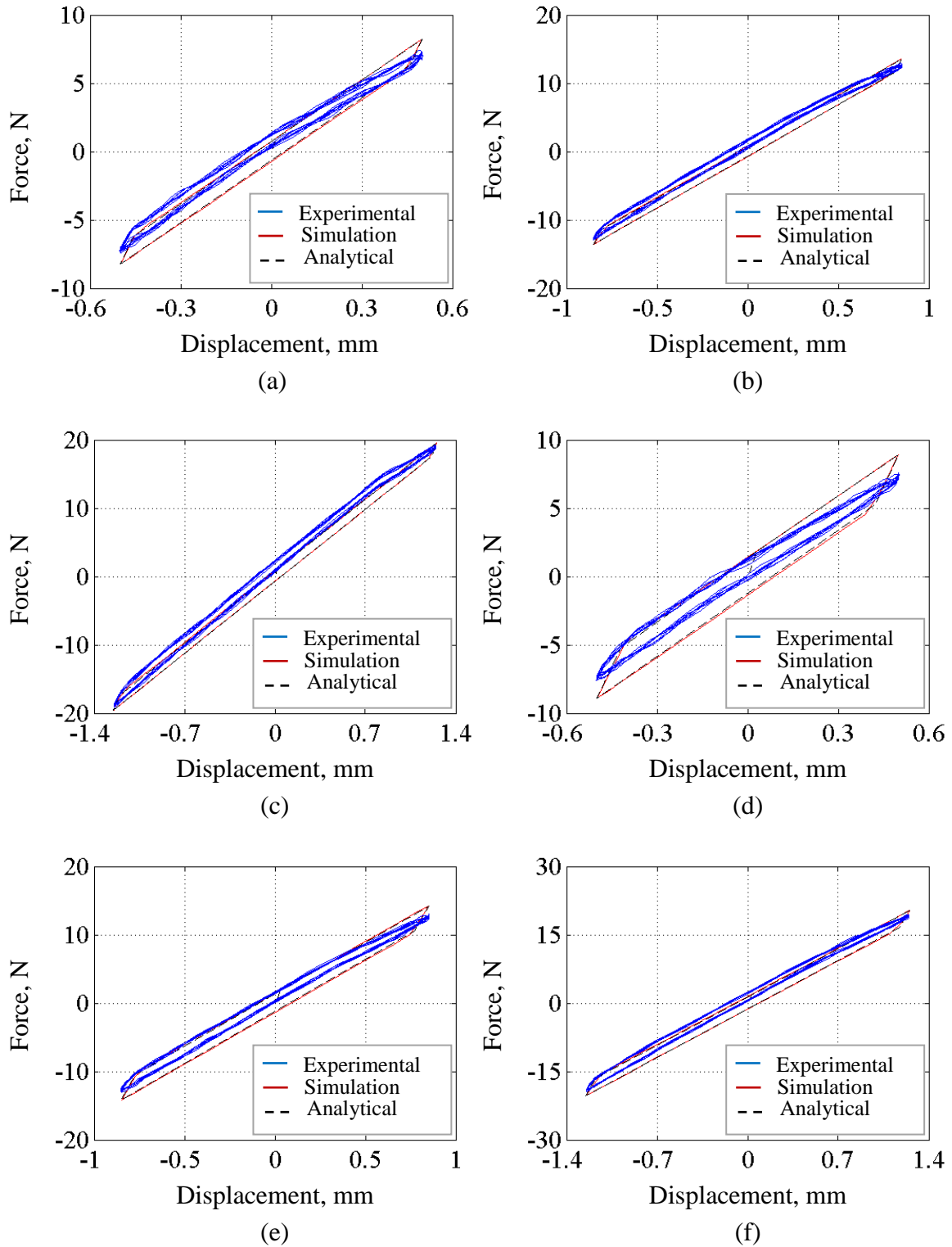
Figure F.1 Comparison of experimental, numerical and analytical hysteresis loops for Configuration sb01 at PK-PK loading of (a) 1.0 mm, (b) 1.7 mm, (c) 2.5 mm and for Configuration sb02 at PK-PK loading of (d) 1.0 mm, (e) 1.7 mm and (f) 2.5 mm
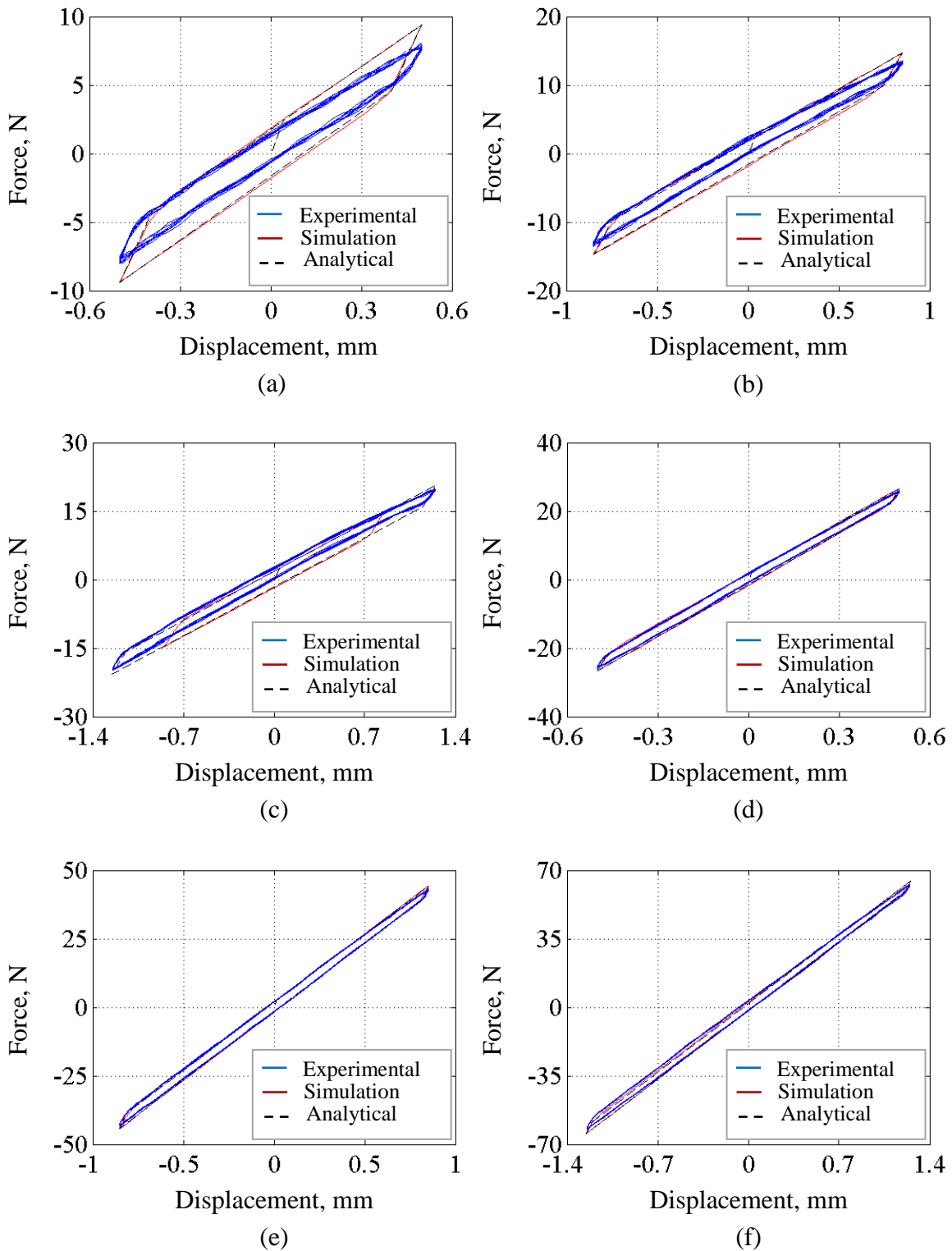
Figure F.2 Comparison of experimental, numerical and analytical hysteresis loops for Configuration sb03 at PK-PK loading of (a) 1.0 mm, (b) 1.7 mm, (c) 2.5 mm and for Configuration sb04 at PK-PK loading of (d) 1.0 mm, (e) 1.7 mm and (f) 2.5 mm
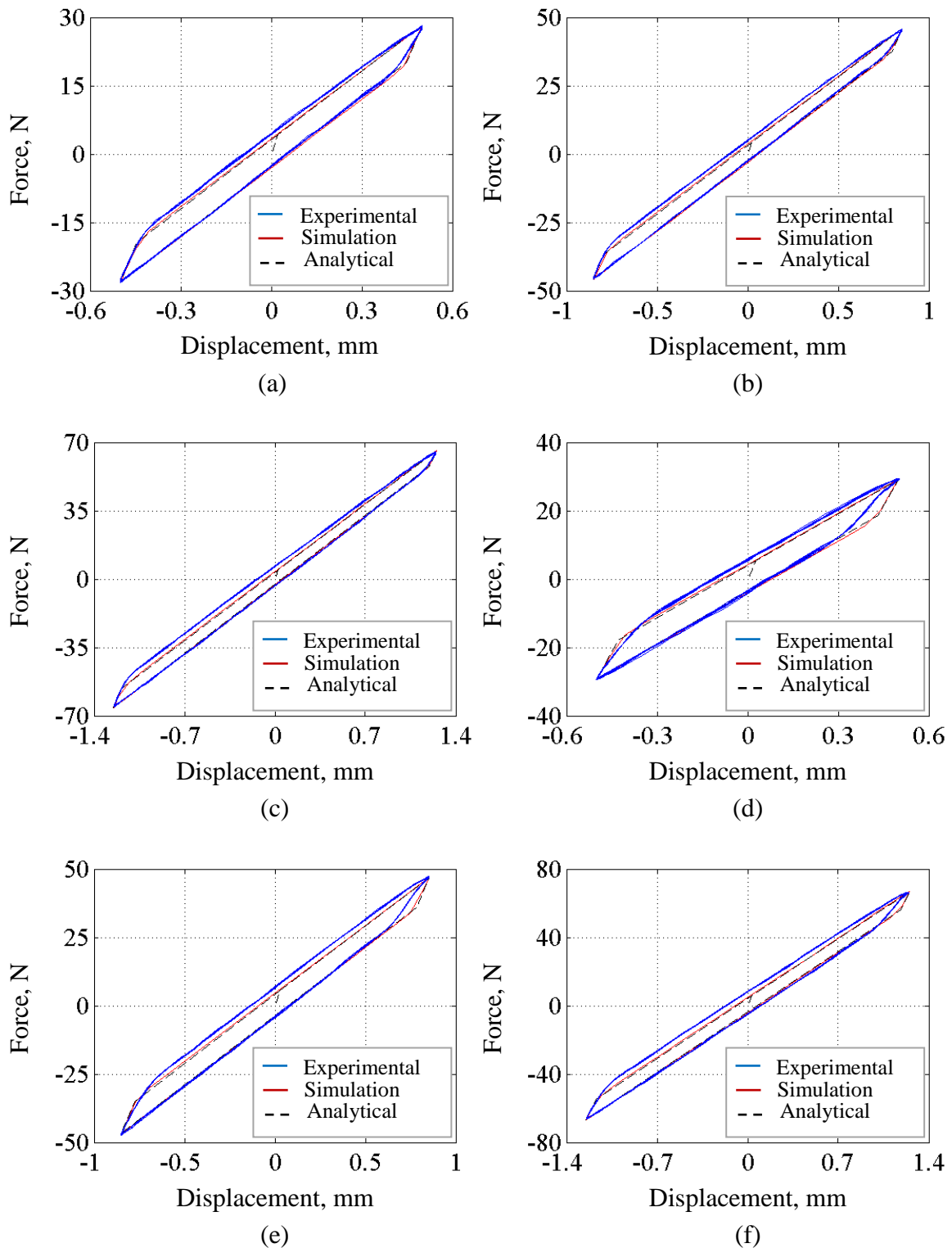
Figure F.3 Comparison of experimental, numerical and analytical hysteresis loops for Configuration sb05 at PK-PK loading of (a) 1.0 mm, (b) 1.7 mm, (c) 2.5 mm and for Configuration sb06 at PK-PK loading of (d) 1.0 mm, (e) 1.7 mm and (f) 2.5 mm
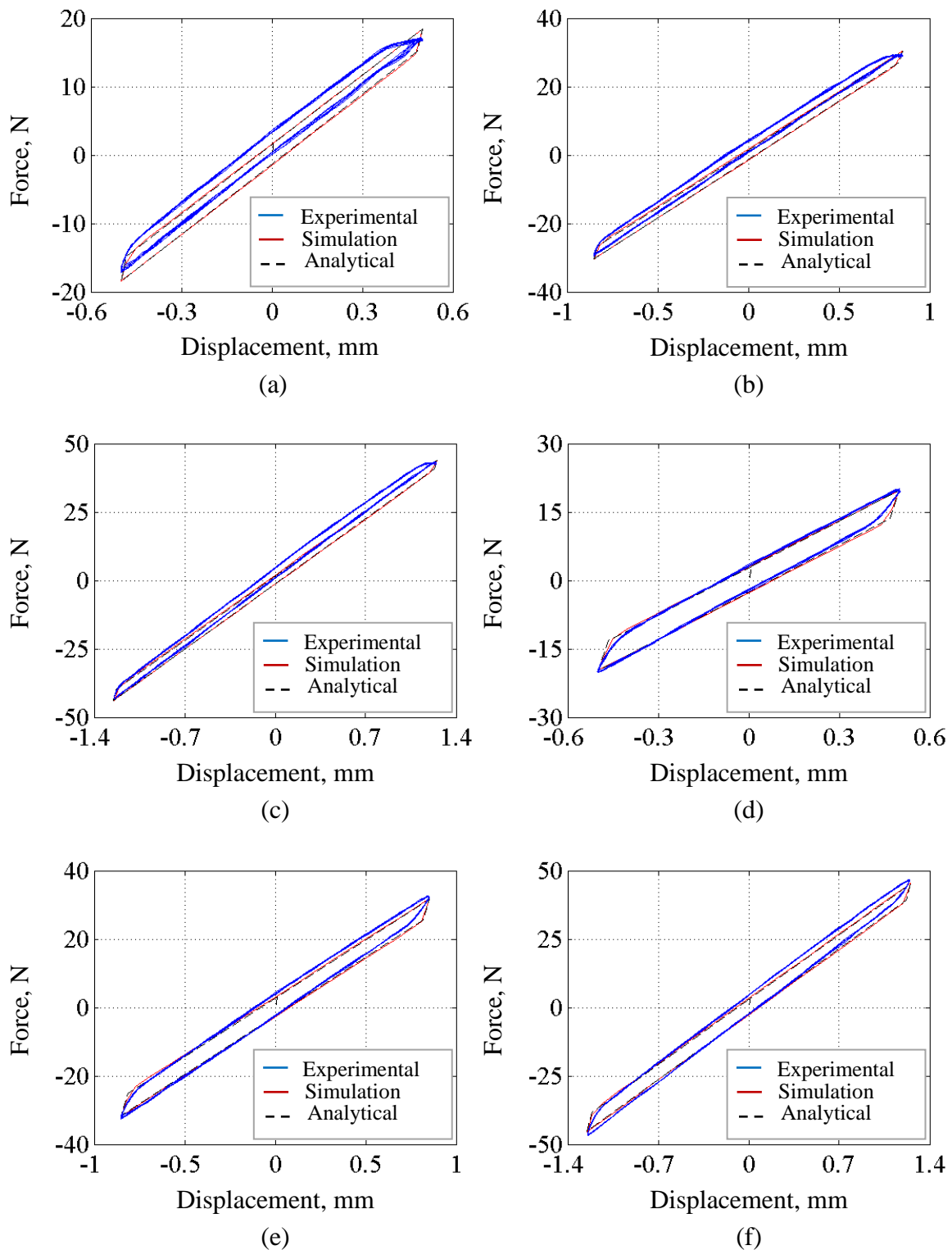
Figure F.4 Comparison of experimental, numerical and analytical hysteresis loops for Configuration sb07 at PK-PK loading of (a) 1.0 mm, (b) 1.7 mm, (c) 2.5 mm and for Configuration sb08 at PK-PK loading of (d) 1.0 mm, (e) 1.7 mm and (f) 2.5 mm
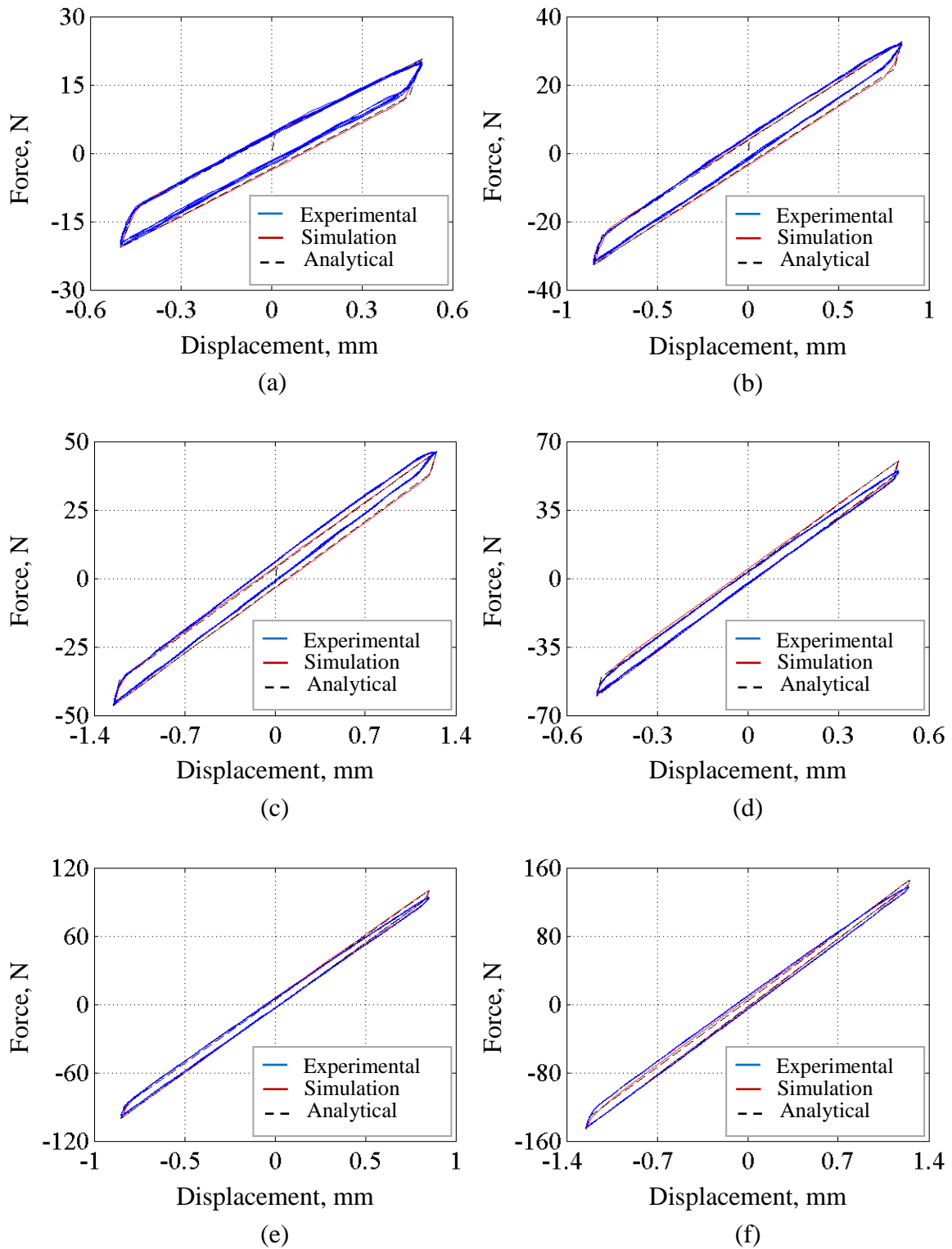
Figure F.5 Comparison of experimental, numerical and analytical hysteresis loops for Configuration sb09 at PK-PK loading of (a) 1.0 mm, (b) 1.7 mm, (c) 2.5 mm and for Configuration sb10 at PK-PK loading of (d) 1.0 mm, (e) 1.7 mm and (f) 2.5 mm
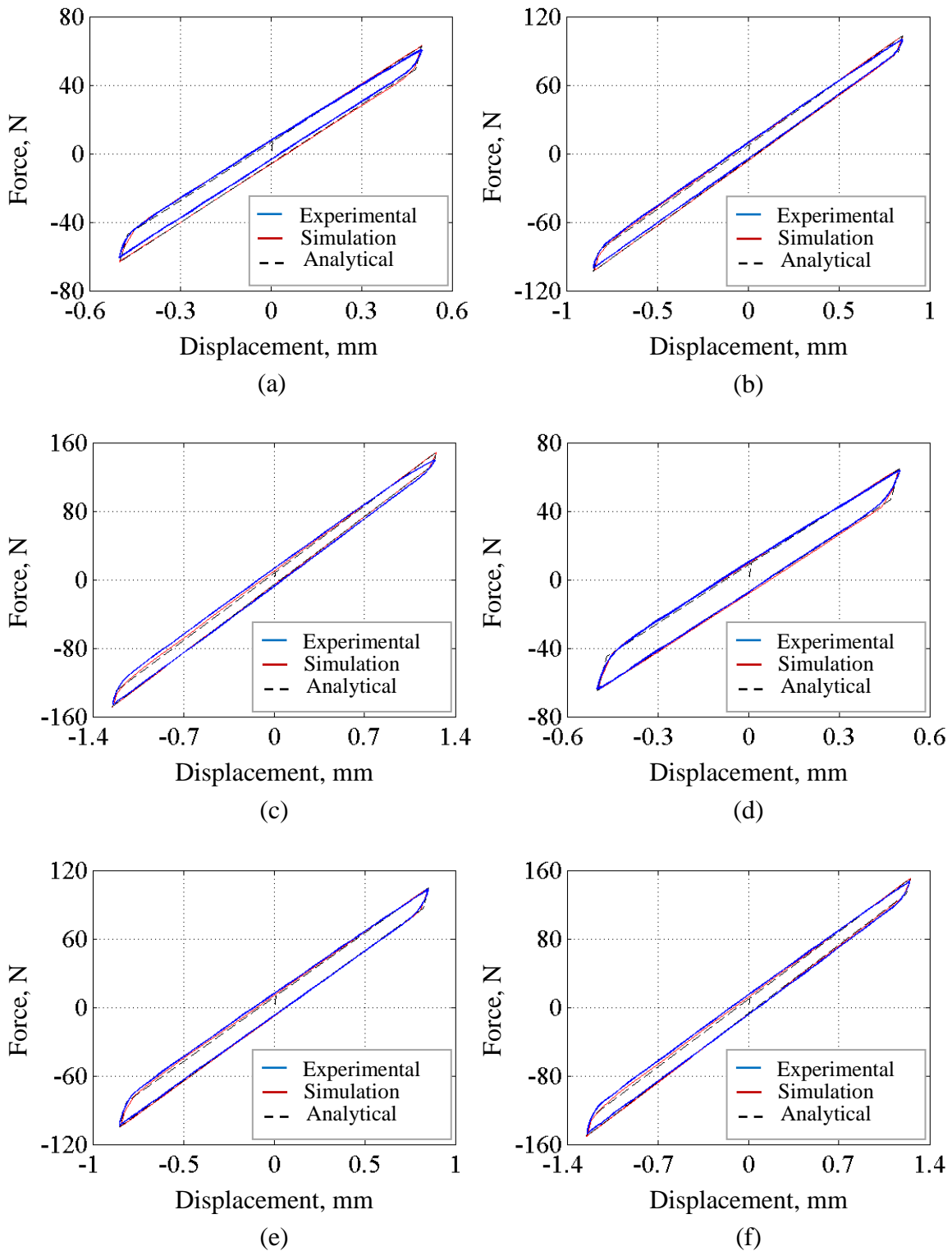
Figure F.6 Comparison of experimental, numerical and analytical hysteresis loops for Configuration sb11 at PK-PK loading of (a) 1.0 mm, (b) 1.7 mm, (c) 2.5 mm and for Configuration sb12 at PK-PK loading of (d) 1.0 mm, (e) 1.7 mm and (f) 2.5 mm
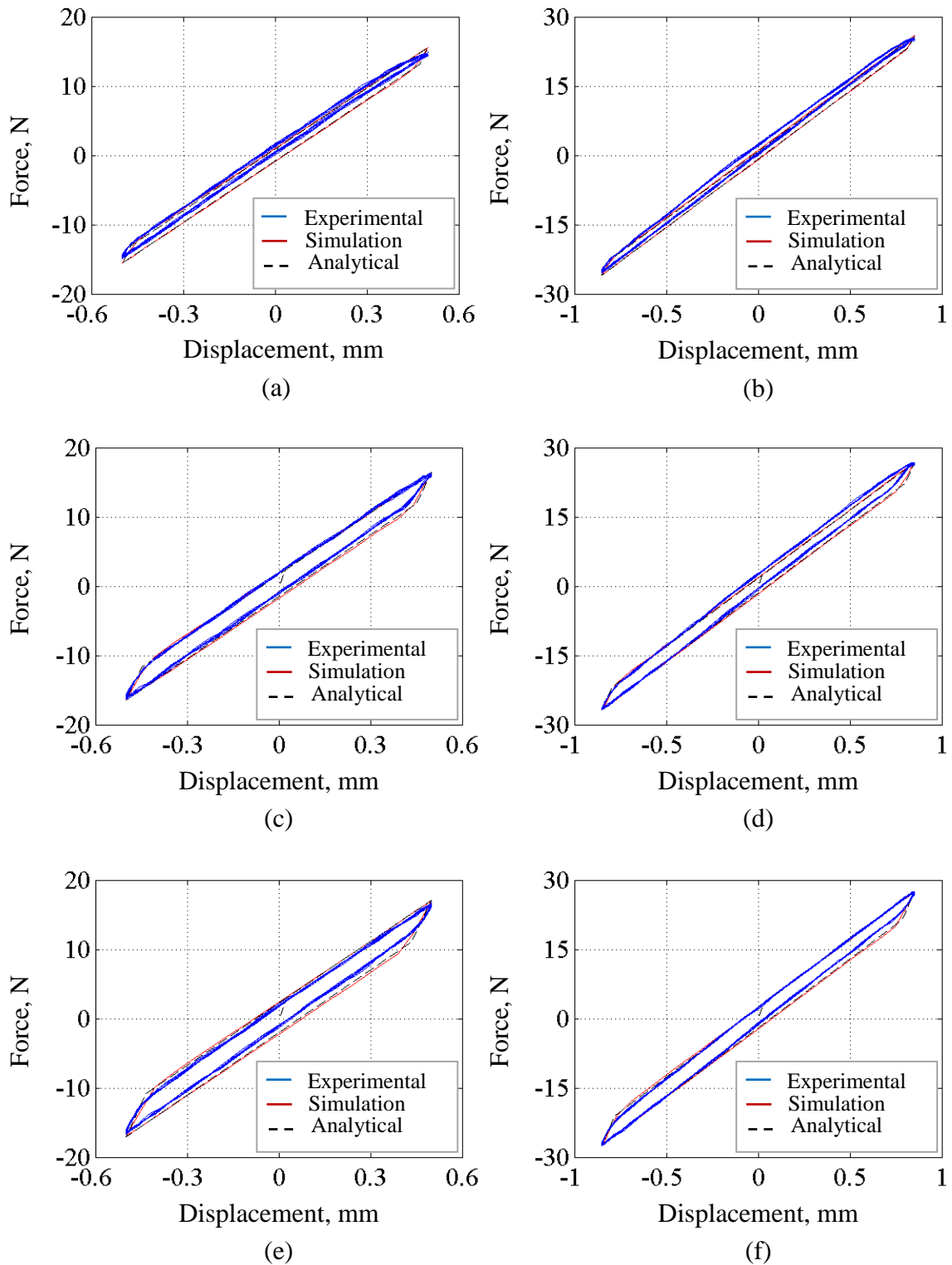
Figure F.7 Comparison of experimental, numerical and analytical hysteresis loops for Configuration sb13 at PK-PK loading of (a) 1.0 mm, (b) 1.7 mm and for Configuration sb14 at PK-PK loading of (c) 1.0 mm, (d) 1.7 mm and for Configuration sb15 at PK-PK loading of (e) 1.0 mm and (f) 1.7 mm
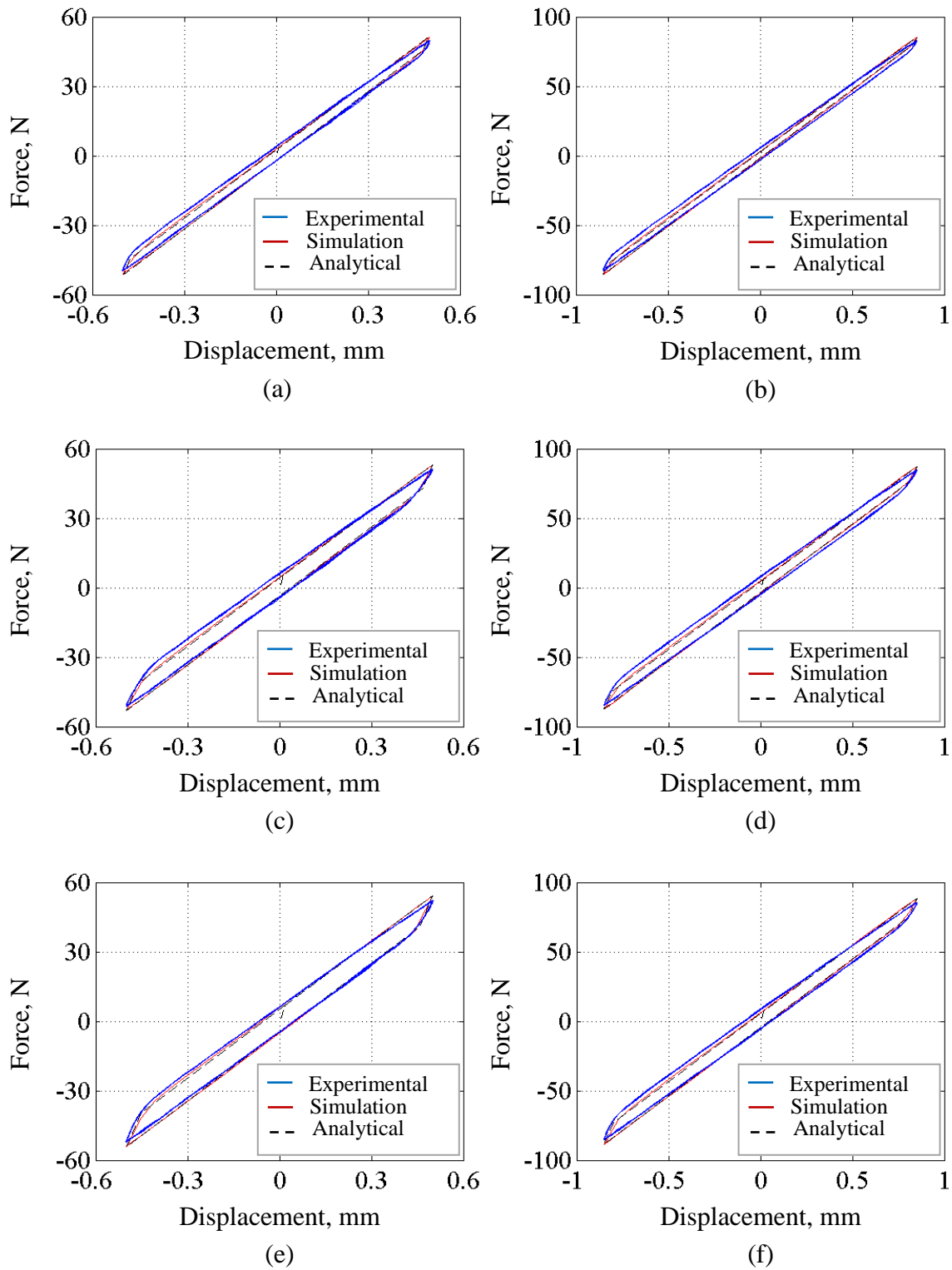
Figure F.8 Comparison of experimental, numerical and analytical hysteresis loops for Configuration sb16 at PK-PK loading of (a) 1.0 mm, (b) 1.7 mm and for Configuration sb17 at PK-PK loading of (c) 1.0 mm, (d) 1.7 mm and for Configuration sb18 at PK-PK loading of (e) 1.0 mm and (f) 1.7 mm
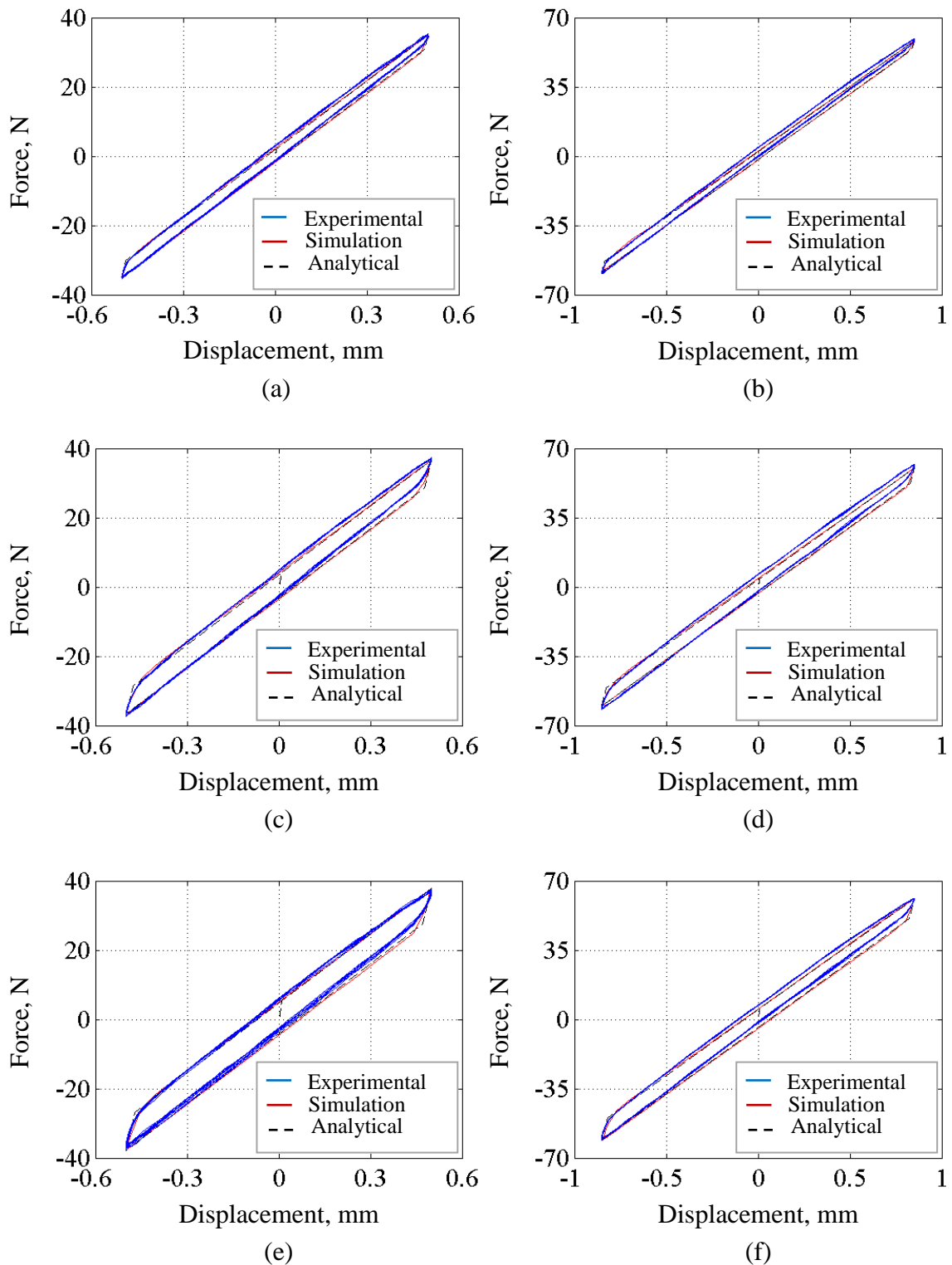
Figure F.9 Comparison of experimental, numerical and analytical hysteresis loops for Configuration sb19 at PK-PK loading of (a) 1.0 mm, (b) 1.7 mm and for Configuration sb20 at PK-PK loading of (c) 1.0 mm, (d) 1.7 mm and for Configuration sb21 at PK-PK loading of (e) 1.0 mm and (f) 1.7 mm

Appendix G

G.1 Thermal effects in diagonal multi-strand beams (DMSB)

In frictional systems, the friction between the contact surfaces converts the kinetic energy (work) of two bodies that are moving relative to each other, based on the first thermodynamic law, into thermal energy (heat). When two solid bodies slide against each other, the normal force acting in the interface region is supported by the asperities (at micro scale) that exist within the contact surfaces. As the shear stress increases (to start sliding), the interlocked asperities start to break at the weakest points and new asperities come into contact where this action generates heat [111].

For the DMSB used in this study, square key steel strands were used in order to provide damping over a large range of operation temperatures. Excessive heat can result in changes to the local interface mechanical properties of metal strands.

This section describes the experimental investigations performed to check that the generated heat from the flexural behaviour of the DMSB was within an acceptable operating temperature range (0°C–200°C). The heat generated from the frictional behaviour of Configurations db01, db03, db04 and db06, Table 5.1, was measured using an infrared camera (thermoIMAGER MICRO-EPSILON TIM 400). This camera can measure temperatures between 20°C and 900°C and record a real-time image with up to 80 Hz. The real-time images for the tests presented in Figure G.1 through Figure G.4 show that the heat generated from the DMSB during the flexural loading was in the normal limits (approximately 25°C) and would not be expected to affect the mechanical properties of the key steel strands.
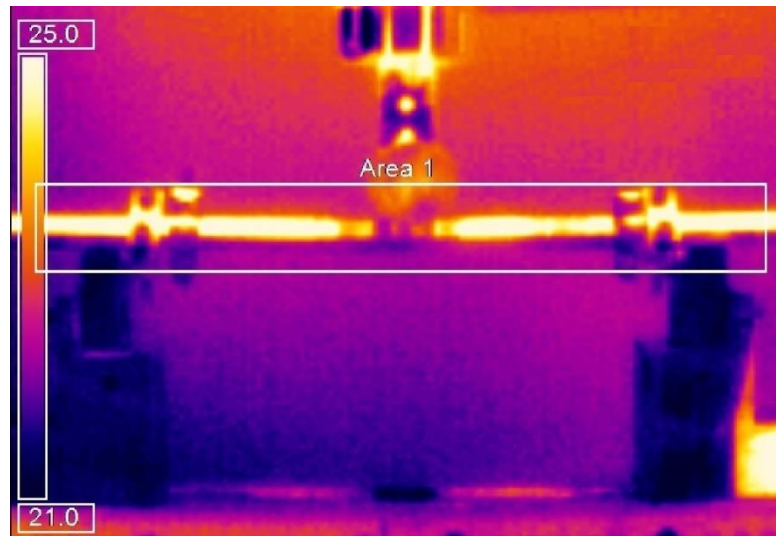
Figure G.1 Thermal effect during the flexural loading for Configuration db01
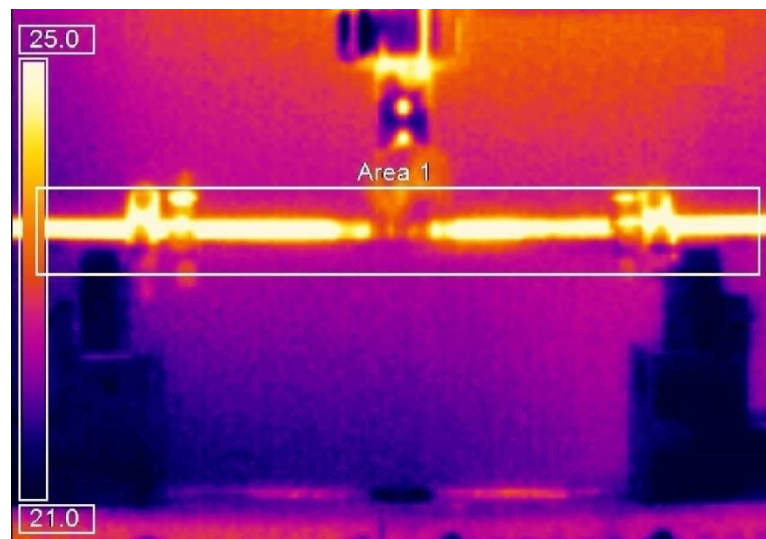
Figure G.2 Thermal effect during the flexural loading for Configuration db03
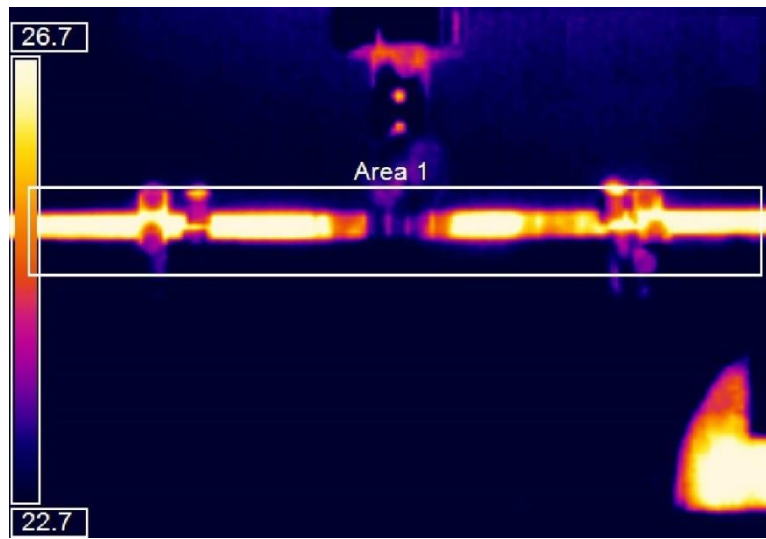
Figure G.3 Thermal effect during the flexural loading for Configuration db04
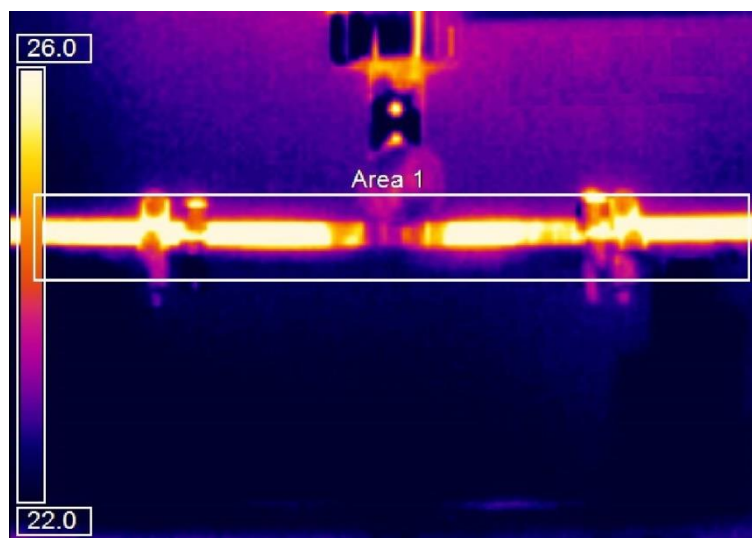
Figure G.4 Thermal effect during the flexural loading for Configuration db06

Appendix H

H.1 Comparison of experimental, numerical and analytical hysteresis loops for diagonal multi-strand beams (DMSB)
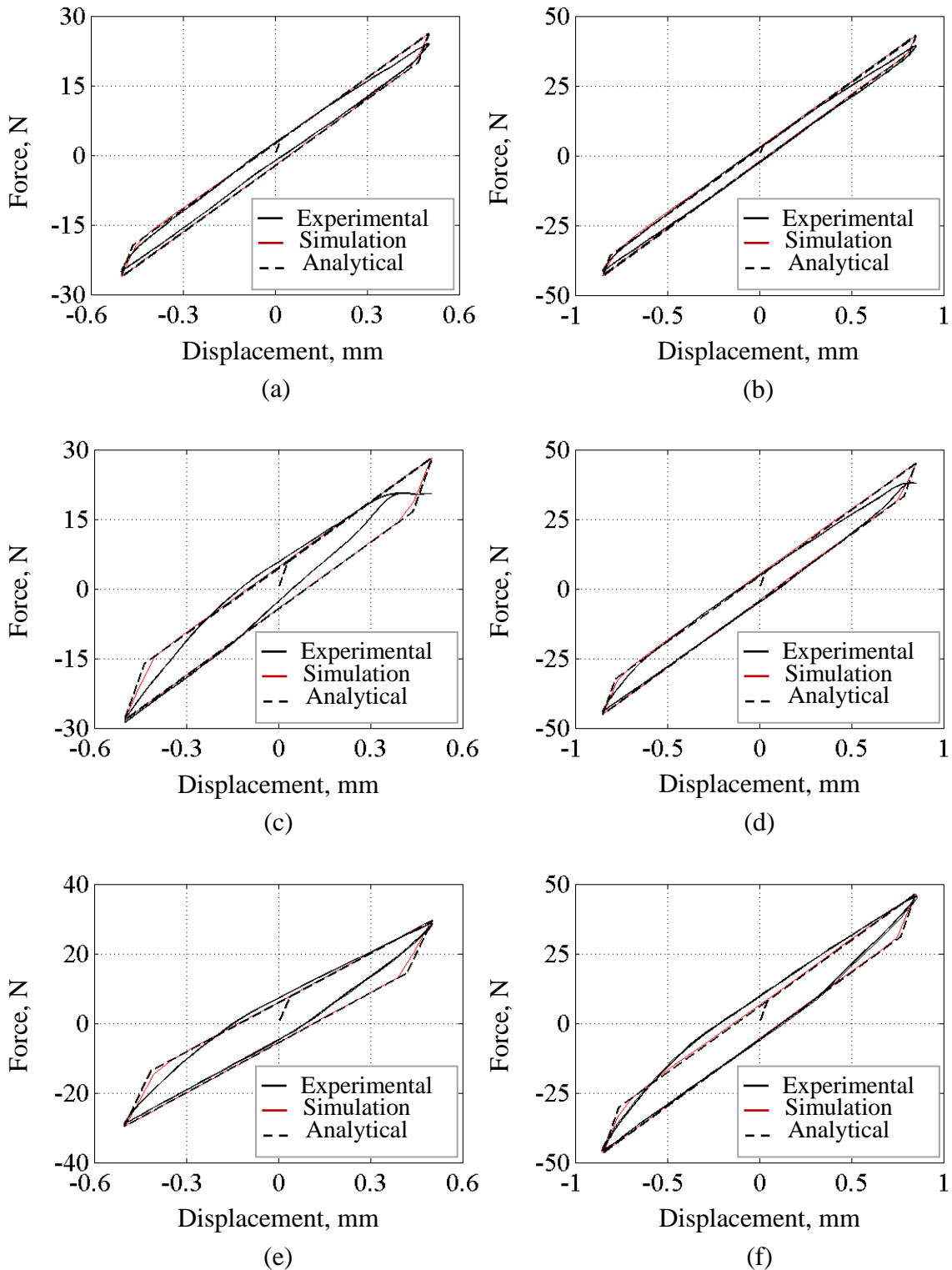
Figure H.1 Comparison of experimental and numerical and analytical hysteresis loops for Configuration db01 at PK-PK displacement of (a) 1.0 mm and (b) 1.7 mm and for Configuration db02 at PK-PK displacement of (c) 1.0 mm and (d) 1.7 mm and for Configuration db03 at PK-PK displacement of (e) 1.0 mm and (f) 1.7 mm
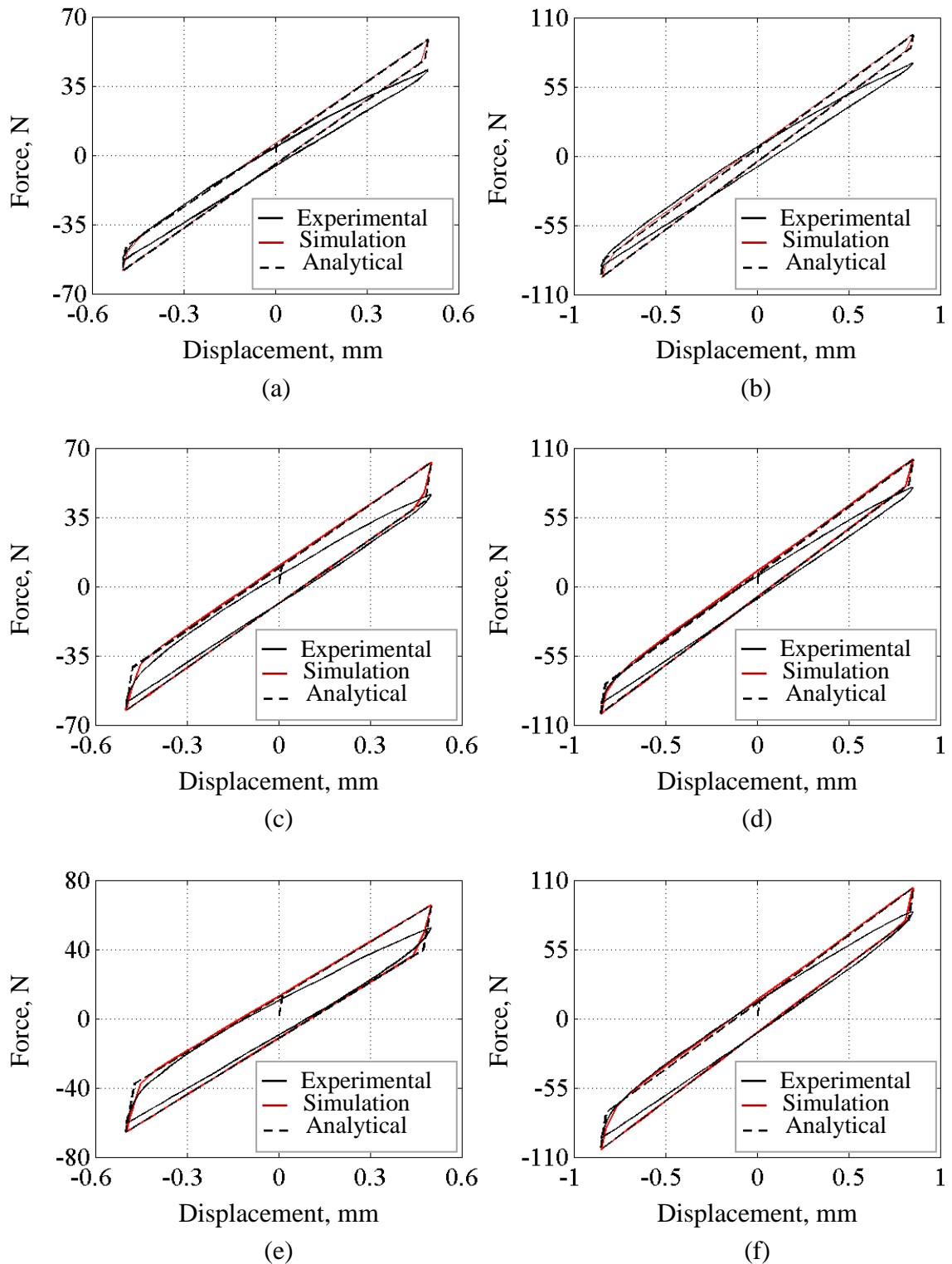
Figure H.2 Comparison of experimental and numerical and analytical hysteresis loops for Configuration db04 at PK-PK displacement of (a) 1.0 mm and (b) 1.7 mm and for Configuration db05 at PK-PK displacement of (c) 1.0 mm and (d) 1.7 mm and for Configuration db06 at PK-PK displacement of (e) 1.0 mm and (f) 1.7 mm
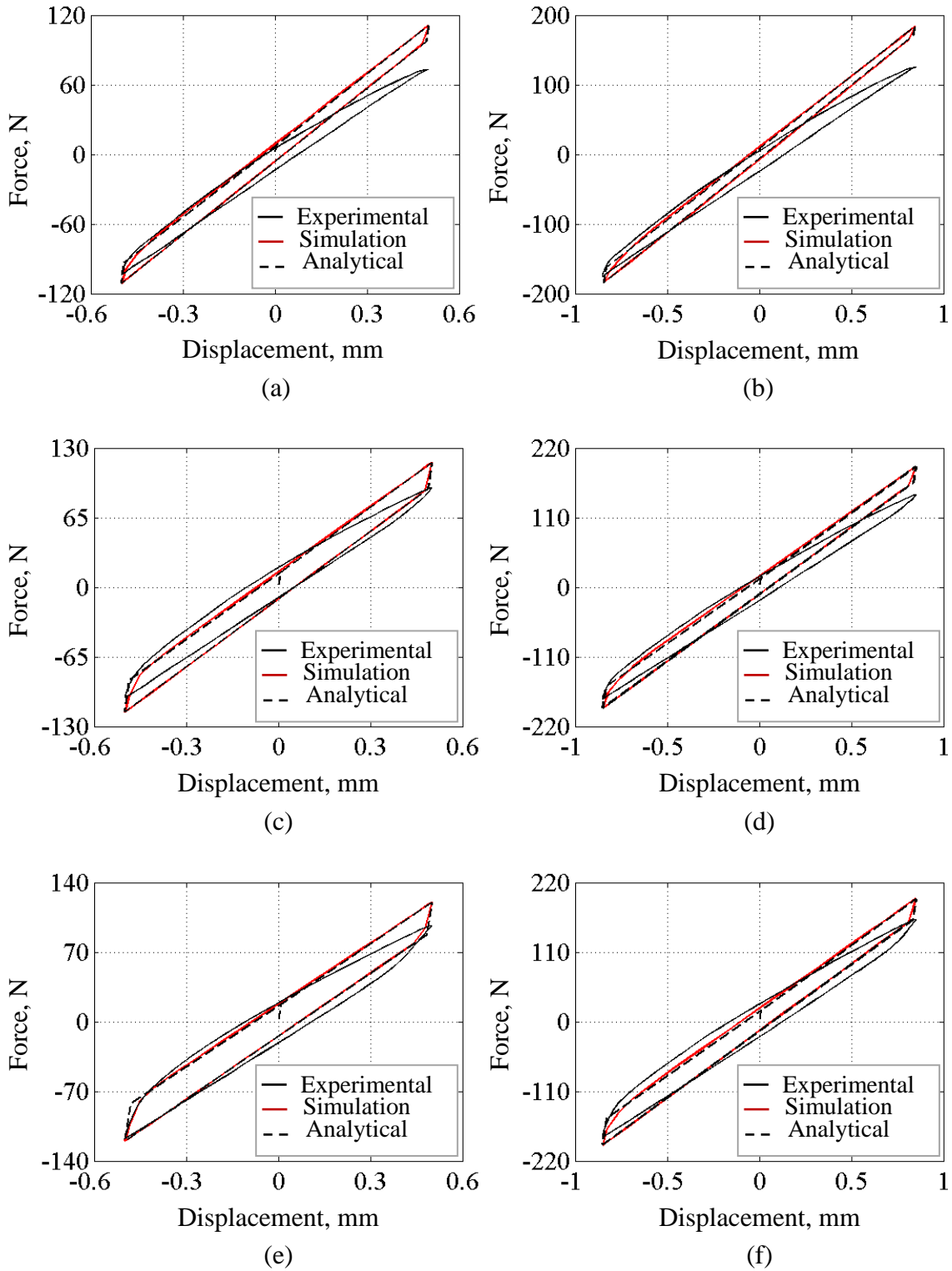
Figure H.3 Comparison of experimental and numerical and analytical hysteresis loops for Configuration db10 at PK-PK displacement of (a) 1.0 mm and (b) 1.7 mm and for Configuration db11 at PK-PK displacement of (c) 1.0 mm and (d) 1.7 mm and for Configuration db12 at PK-PK displacement of (e) 1.0 mm and (f) 1.7 mm

Appendix I

I.1 Analytical, numerical and experimental Damping characteristics of the diagonal multi-strand beams (DMSB)

Table I.1 Analytical damping characteristics for Configuration db01 through Configuration db12

Configuration	Loading, mm	Analytical			
		Loss factor	Energy dissipation / cycle, mJ	Strain energy, mJ	Stiffness, N/mm
db01	1.000	0.126	4.768	12.07	52.19
	1.700	0.079	8.655	34.88	50.46
db02	1.000	0.219	8.461	12.28	56.36
	1.700	0.138	15.19	35.14	52.97
db03	1.000	0.275	10.78	12.48	59.15
	1.700	0.175	19.41	35.38	54.64
db04	1.000	0.126	10.78	27.33	116.5
	1.700	0.082	20.44	79.09	113.0
db05	1.000	0.223	18.78	26.82	122.3
	1.700	0.137	34.20	79.45	118.2
db06	1.000	0.276	24.00	27.63	130.5
	1.700	0.172	43.42	80.20	121.6
db07	1.000	0.088	6.486	23.55	98.75
	1.700	0.057	12.20	68.18	96.71
db08	1.000	0.151	11.28	23.73	104.0
	1.700	0.096	20.56	68.45	99.88
db09	1.000	0.191	14.37	23.91	107.5
	1.700	0.121	26.03	68.68	102.0
db10	1.000	0.093	15.60	53.51	221.1
	1.700	0.065	31.29	153.3	218.1
db11	1.000	0.152	25.74	53.78	232.2
	1.700	0.100	48.98	155.5	223.6
db12	1.000	0.191	32.43	53.91	239.2
	1.700	0.124	60.50	155.8	227.9

Table I.2 Numerical damping characteristics for Configuration db01 through Configuration db12

Configuration	Loading, mm	Numerical			
		Loss factor	Energy dissipation / cycle, mJ	Strain energy, mJ	Stiffness, N/mm
db01	1.000	0.121	4.559	11.99	47.42
	1.700	0.078	8.467	34.54	48.30
db02	1.000	0.208	8.021	12.28	45.98
	1.700	0.134	14.69	34.89	47.23
db03	1.000	0.258	10.18	12.54	45.26
	1.700	0.169	18.70	35.19	46.50
db04	1.000	0.118	9.935	26.84	110.3
	1.700	0.077	18.78	77.45	108.6
db05	1.000	0.205	17.45	27.15	110.8
	1.700	0.131	32.08	77.98	111.0
db06	1.000	0.260	22.35	27.38	106.5
	1.700	0.168	41.18	78.13	111.8
db07	1.000	0.083	6.066	23.32	93.48
	1.700	0.055	11.63	67.32	93.76
db08	1.000	0.143	10.58	23.58	90.89
	1.700	0.092	19.52	67.75	93.40
db09	1.000	0.179	13.40	23.86	89.44
	1.700	0.115	24.68	68.08	92.45
db10	1.000	0.083	13.58	52.28	211.8
	1.700	0.057	26.59	149.2	209.5
db11	1.000	0.141	23.32	52.67	215.4
	1.700	0.092	43.47	151.12	210.6
db12	1.000	0.177	29.51	52.97	214.3
	1.700	0.115	54.87	152.2	214.9

Table I.3 Experimental damping characteristics for Configuration db01 through
Configuration db12

Configuration	Loading, mm	Experimental			
		Loss factor	Energy dissipation / cycle, mJ	Strain energy, mJ	Stiffness, N/mm
db01	1.000	0.090	3.338	11.80	46.19
	1.700	0.069	7.245	33.56	47.27
db02	1.000	0.140	5.754	13.05	52.36
	1.700	0.118	12.66	34.14	45.53
db03	1.000	0.192	8.920	14.78	58.15
	1.700	0.175	19.85	36.01	45.02
db04	1.000	0.107	7.780	23.23	93.42
	1.700	0.093	19.63	66.94	92.19
db05	1.000	0.150	11.58	24.64	95.31
	1.700	0.111	24.42	70.03	97.66
db06	1.000	0.214	17.21	25.57	100.7
	1.700	0.156	35.11	71.57	98.51
db07	1.000	0.100	7.026	22.33	85.40
	1.700	0.076	15.06	63.48	87.47
db08	1.000	0.175	12.71	23.18	90.44
	1.700	0.122	24.66	64.32	87.39
db09	1.000	0.194	15.17	24.89	92.58
	1.700	0.161	33.12	65.40	86.81
db10	1.000	0.102	13.95	43.48	172.7
	1.700	0.094	37.28	125.6	173.3
db11	1.000	0.153	22.12	45.90	180.8
	1.700	0.123	50.62	130.5	176.6
db12	1.000	0.220	33.06	47.90	184.7
	1.700	0.173	73.02	134.4	181.5